

PACIFIC EARTHQUAKE ENGINEERING RESEARCH CENTER

A Bayesian Network Methodology for Infrastructure Seismic Risk Assessment and Decision Support

Michelle T. Bensi

Department of Civil and Environmental Engineering
University of California, Berkeley

Armen Der Kiureghian

Department of Civil and Environmental Engineering
University of California, Berkeley

Daniel Straub

Engineering Risk Analysis Group
Technical University of Munich

Disclaimer

The opinions, findings, and conclusions or recommendations expressed in this publication are those of the author(s) and do not necessarily reflect the views of the study sponsor(s) or the Pacific Earthquake Engineering Research Center.

A Bayesian Network Methodology for Infrastructure Seismic Risk Assessment and Decision Support

Michelle T. Bensi

Department of Civil and Environmental Engineering
University of California, Berkeley

Armen Der Kiureghian

Department of Civil and Environmental Engineering
University of California, Berkeley

Daniel Straub

Engineering Risk Analysis Group
Technical University of Munich

PEER Report 2011/02

Pacific Earthquake Engineering Research Center

College of Engineering

University of California, Berkeley

March 2011

ABSTRACT

A Bayesian Network (BN) methodology is developed for performing infrastructure seismic risk assessment and providing decision support with an emphasis on immediate post-earthquake applications. A BN is a probabilistic graphical model that represents a set of random variables and their probabilistic dependencies. The variables may represent demand or capacity values, or the states of components and systems. Decision and utility nodes may be added that encode various decision alternatives and associated costs, thus facilitating support for decision-making under uncertainty.

BNs have many capabilities that make them well suited for the proposed application. Most important among these is the ability to update the probabilistic states of the variables upon receiving relevant information. Evidence on one or more variables, e.g., measured component capacities or demands, or observed states of components, can be entered into the BN and this information propagates throughout the network to provide up-to-date probabilistic characterizations of the infrastructure components and system as well as optimal ordering of the decision alternatives. This can be done in near-real time and under the uncertain and evolving state of information that is characteristic of the post-event period. As is the case with most computational methods, BNs have their limitations: calculations can be highly demanding when the BN is densely connected, or when the infrastructure system is complex and large. This study addresses these challenges.

The proposed methodology consists of four major components: (1) a seismic demand model of ground motion intensity as a spatially distributed random field, accounting for multiple sources and including finite fault rupture and directivity effects, (2) a model for seismic performance of point-site and distributed components, (3) models of system performance as a function of component states, and (4) models of post-earthquake decision-making for inspection and operation or shutdown of components.

Two example applications demonstrate the proposed BN methodology. The second of these employs a hypothetical model of the proposed California high-speed rail system subjected to an earthquake.

ACKNOWLEDGMENTS

This work was supported by the State of California through the Transportation Systems Research Program of the Pacific Earthquake Engineering Research Center (PEER). Additional support was provided by the Taisei Chair in Civil Engineering at the University of California, Berkeley. The first author also acknowledges financial support from a National Science Foundation Graduate Research Fellowship and CITRIS Bears Breaking Boundaries competition award. Any opinions, findings, and conclusions or recommendations expressed in this material are those of the authors and do not necessarily reflect those of the funding agencies.

CONTENTS

1.	Introduction	1
1.1	Motivation.....	1
1.2	Goals, methodology, and scope	4
1.3	Existing resources	6
1.3.1	HAZUS ^{MH}	6
1.3.2	ShakeMap/ShakeCast	7
1.3.3	REDARS.....	8
1.3.4	Additional resources	9
1.4	Study outline	9
2.	Introduction to Bayesian Networks	13
2.1	Background.....	13
2.2	Brief introduction to Bayesian networks	16
2.2.1	Bayesian network terminology	16
2.2.2	Constructing Bayesian networks.....	17
2.2.3	Inference in Bayesian networks	22
2.2.3.1	The elimination algorithm	25
2.2.3.2	The junction tree algorithm	29
2.3	Use of BNs in civil engineering applications	32
3.	BN-Based Seismic Demand Models	35
3.1	Introduction.....	35
3.2	Hazard due to ground shaking	36
3.2.1	Existing models.....	37
3.2.2	Proposed model.....	40
3.2.2.1	Source characterization and source-to-site distance.....	41
3.2.2.1.1	Point-source model and formulation.....	41
3.2.2.1.2	Finite-rupture model and formulation.....	47
3.2.2.2	Ground motion intensity.....	59
3.2.2.3	Rupture directivity effects	61

3.2.2.3.1	Directivity BN based on Abrahamson (2000).....	63
3.2.2.3.2	Directivity BN based on Shahi and Baker (2010).....	69
3.2.2.3.3	Directivity BN based on Bray and Rodriguez-Marek (2004)	72
3.3	Hazard due to liquefaction.....	72
3.3.1	Existing Bayesian network-based liquefaction models	74
3.3.2	Proposed formulation.....	75
3.4	Hazard due to fault rupture	79
3.5	Appendix: Earth-Centered Earth-Fixed coordinate system	80
4.	Bayesian Network Modeling of Gaussian Random Fields.....	83
4.1	Introduction.....	83
4.2	Bayesian network modeling of random fields	84
4.3	Construction of approximate transformation matrix T	88
4.3.1	Decomposition using eigenvalue expansion.....	89
4.3.2	Decomposition using Cholesky factorization	90
4.3.3	Node and link elimination using optimization.....	91
4.3.4	Qualitative comparison of methods for constructing T	93
4.4	Numerical investigation of approximation methods.....	94
4.5	Effect of correlation approximations on system reliability.....	101
5.	Modeling Component Performance with BNs.....	111
5.1	Introduction.....	111
5.2	Seismic fragility of point-site components	113
5.3	Seismic fragility of distributed components	122
5.4	Examples of available fragility functions	124
6.	Modeling System Performance with BNs.....	127
6.1	Introduction.....	127
6.2	Conventional methods of modeling system performance.....	127
6.2.1	Qualitative methods	128
6.2.1.1	Failure modes and effects analysis	128
6.2.1.2	Reliability block diagrams.....	128
6.2.1.3	Fault trees	129

6.2.1.4	Event trees	131
6.2.2	Quantitative methods	132
6.2.2.1	Minimal link sets and cut sets	133
6.2.2.2	Additional methods	134
6.3	Existing works using BNs to model system performance	134
6.4	BN formulations for modeling system performance	136
6.4.1	Naïve formulation	136
6.4.2	Explicit formulations	138
6.4.2.1	Explicit connectivity formulation.....	138
6.4.2.2	Explicit disconnectivity formulation.....	141
6.4.3	Minimal link set and minimal cut set formulations	143
6.4.3.1	Minimal link set formulation.....	143
6.4.3.2	Minimal cut set formulation.....	146
6.4.4	Extension to multistate problems.....	147
6.5	Efficient minimal link set and minimal cut set formulations.....	148
6.5.1	Construction of efficient BN formulations for series and parallel systems	150
6.5.2	General systems	153
6.5.2.1	Efficient MLS formulation.....	153
6.5.2.2	Efficient MCS formulation.....	157
6.6	Optimal ordering of efficient MLS and MCS formulations	162
6.7	Heuristic augmentation	167
6.7.1	Heuristic based on super components.....	167
6.7.2	Second heuristic for reducing the number of permutations	172
6.8	Example applications	177
6.8.1	Example application 1.....	177
6.8.2	Example application 2.....	180
6.9	Appendix: Modeling “either-or” and “ <i>k</i> -out-of- <i>n</i> ” constraints.....	184
7.	Decision Support.....	187
7.1	Introduction.....	187
7.2	Introduction to decision trees and influence diagrams	189

7.2.1	Overview of limited memory influence diagrams	192
7.2.2	Computations in limited memory influence diagrams.....	192
7.3	Post-earthquake inspection and closure decision.....	193
7.3.1	Component-level decision-making	194
7.3.2	System-level decision-making	197
7.4	Value-of-information heuristic	199
7.4.1	Example application.....	202
7.4.2	Assumed utilities.....	205
7.4.3	Numerical results	206
7.5	Appendix: Example calculation of the value of perfect and imperfect information.....	211
8.	Example Applications	215
8.1	Introduction.....	215
8.2	Example 1: Connectivity of a transportation network	216
8.2.1	Using BN for conventional site-specific PSHA.....	216
8.2.2	Using BN for system-level PSHA	228
8.2.3	Incorporating component performance in assessing system seismic risk.....	230
8.2.4	Incorporating system performance in assessing system seismic risk	232
8.2.5	Using BNs in post-event applications.....	236
8.3	Example 2: Proposed California high-speed rail system	242
8.3.1	Model assumptions	244
8.3.2	Illustrative results.....	254
9.	Conclusions	263
9.1	Summary of major contributions	263
9.2	Future research and development	265
	References.....	269

LIST OF FIGURES

Figure 2.1: A simple BN.....	17
Figure 2.2: Graphical representation of d-separation properties. Gray nodes are observed.....	19
Figure 2.3: Example of construction of CPTs by Monte Carlo simulation	20
Figure 2.4: Mechanics of computing $\phi(x_2, x_3, x_4)$	26
Figure 2.5: Graphs obtained during elimination algorithm: (a) moral graph corresponding to BN in Figure 2.1; graphs after elimination of (b) node X_1 , (c) node X_2 , and (d) node X_5	27
Figure 2.6: Illustration of the elimination algorithm for the BN in Figure 2.1 using elimination order X_5, X_2, X_1, X_3, X_4	29
Figure 2.7: Illustration of clique creation using the BN in Figure 2.1 with elimination order X_4, X_1, X_5, X_3, X_2	30
Figure 2.8: Junction tree for BN in Figure 2.1 with elimination order X_4, X_1, X_5, X_3, X_2	31
Figure 2.9: Illustration of cliques created using the BN in Figure 2.1 with elimination order X_5, X_4, X_2, X_3, X_1	31
Figure 2.10: Junction tree for BN in Figure 2.1 with elimination order X_5, X_4, X_2, X_3, X_1	31
Figure 3.1: Bayraktarli et al. (2005) BN framework for seismic risk management	38
Figure 3.2: Kuehn et al. (2009) BN of ground motion intensity obtained by structure learning..	39
Figure 3.3: BN model of point-source characteristics and source-to-site distances.....	42
Figure 3.4: Fault-specific local coordinate system for line-fault idealization and point-source model.....	43
Figure 3.5: Source-dependent distribution of L_{eq} for example	44
Figure 3.6: Illustration of (a) multisegment fault in three-dimensional space and (b) alignment of all fault segments consecutively along the x' -axis.....	46
Figure 3.7: Fault and rupture in the local coordinate system for the finite-rupture model.....	48

Figure 3.8: BN modeling rupture length and location as a function of earthquake source, epicenter location, and magnitude	49
Figure 3.9: Geographically distributed sites in vicinity of a fault	51
Figure 3.10: Example illustrating geometric inconsistencies due to discretization.....	52
Figure 3.11: (a) BN modeling relationship in Equation (3.12) and (b) BN modeling relationship after addition of a link between X_e and X_d to account for geometric inconsistencies due to discretization.....	52
Figure 3.12: Algorithm for generating CPTs of \mathbf{Xd}, \mathbf{i} and \mathbf{Ri} to address geometric inconsistencies due to discretization	54
Figure 3.13: BN modeling of source-to-site distance as a function of earthquake source and location.....	55
Figure 3.14: Parameters required for multi-segment finite-rupture length formulation.....	57
Figure 3.15: Configurations of site location relative to fault segment crossed by the rupture	58
Figure 3.16: BN model of ground motion intensity using point-source assumption.....	59
Figure 3.17: BN model of ground motion intensity using finite-rupture model.....	60
Figure 3.18: Illustration of directivity effects	62
Figure 3.19: Directivity parameters for (a) strike-slip fault and (b) dip-slip fault.....	65
Figure 3.20: Geometric cases considered for computing directivity amplification factor	66
Figure 3.21: BN model of ground motion intensity at multiple sites accounting for directivity effects according to Abrahamson (2000) model.....	68
Figure 3.22: BN model of ground motion intensity at multiple sites accounting for directivity effects using the model of Shahi and Baker (2010) and Bray and Rodriguez-Marek (2004)	71
Figure 3.23: Liquefaction BN developed by Bayraktarli (2006).....	74
Figure 3.24: BN modeling seismic demands resulting from liquefaction	76
Figure 3.25: Liquefaction modeling seismic demands resulting from liquefaction with converging structure in Figure 3.24 at node $\rho_{v,i}$ replaced by a chain structure	78

Figure 3.26: Preliminary fault rupture BN.....	80
Figure 4.1: BN model of vector Z drawn from Gaussian random field $Z(x)$	85
Figure 4.2: BN model of decomposition of vector Z drawn from Gaussian random field $Z(x)$...	86
Figure 4.3: BN model of approximate decomposition $\mathbf{Z} = \mathbf{SV} + \mathbf{TU}$	87
Figure 4.4: BN model of Dunnett-Sobel class of random variables	88
Figure 4.5: BN corresponding to transformation matrix obtained by Cholesky decomposition ..	91
Figure 4.6: Iterative algorithm for determining \mathbf{T} through node and link elimination.....	93
Figure 4.7: Generic configurations considered in numerical investigation	94
Figure 4.8: Error in approximating correlation matrix for 10-site line layouts	96
Figure 4.9: Error in approximating correlation matrix for 10-site circle layouts	97
Figure 4.10: Error in approximating correlation matrix for nine-site grid layouts.....	97
Figure 4.11: Example cluster layouts with $d = 1, 5,$ and 10	98
Figure 4.12: Error in approximating correlation matrix for nine-site cluster layouts.....	99
Figure 4.13: Nine-link BN approximations for nine-site cluster layouts using ILOA (top) and NOA (bottom).....	99
Figure 4.14: (a) BN approximation using ILOA with 20 links; (b) illustration of sites linked by common U -node for 10-site line layout with $d = 5$	100
Figure 4.15: (a) BN approximation using ILOA with 20 links; (b) illustration of sites linked by common U -node for 10-site circle layout with $d = 5$	101
Figure 4.16: (a) BN approximation using ILOA with 18 links; (b) illustration of sites linked by common U -node for nine-site grid layout with $d = 5$	102
Figure 4.17: BN model of system performance.....	104
Figure 4.18: Percent error in estimating failure probability for a 10-site line series system when (a) $\zeta_R = 0.3$ and (b) $\zeta_R = 0.6$	106
Figure 4.19: Percent error in estimating failure probability for a 10-site line parallel system when (a) $\zeta_R = 0.3$ and (b) $\zeta_R = 0.6$	107

Figure 5.1: BN model of component capacities with uncertain distribution parameters.....	115
Figure 5.2: BN model of component performances assuming exact limit-state functions.....	116
Figure 5.3: BN model of component performance including uncertainty in functional form of limit state functions.....	118
Figure 5.4: BN model of component performance including uncertainty in functional form of limit state functions after eliminating nodes representing $R_{c,ij}$ and $\boldsymbol{\varepsilon}_{i,j}(\mathbf{1})$	119
Figure 5.5: Example of fragility curves and state probabilities for a five-state component.....	120
Figure 5.6: BN modeling performance of point-site components neglecting statistical uncertainty and correlation in component response other than through seismic demands.....	122
Figure 5.7: BN modeling performance of distributed components neglecting statistical uncertainty and correlation in component states other than through demands.....	124
Figure 6.1: Example reliability block diagram	128
Figure 6.2: Example operational fault tree corresponding to traffic signal failure problem	130
Figure 6.3: Fault tree corresponding to RBD in Figure 6.1	131
Figure 6.4: Example event tree corresponding to signal failure problem.....	132
Figure 6.5: BN corresponding to fault tree in Figure 6.3.....	135
Figure 6.6: Naïve BN system formulation.....	137
Figure 6.7: Naïve formulation for example system	138
Figure 6.8: Examples of possible EC formulations for system in Figure 6.1	140
Figure 6.9: Illustration of upper and lower paths through example system used for construction of EC BN formulations in Figure 6.1.....	141
Figure 6.10: Example EDC BN formulation for system in Figure 6.1	142
Figure 6.11: System performance BN using MLS BN formulation	144
Figure 6.12: MLS formulation for example system in Figure 6.1	144
Figure 6.13: MLS BN formulation for example system in Figure 6.1, with intermediate nodes introduced to keep number of parents to a node to no more than three.....	145

Figure 6.14: System performance using MCS BN formulation	146
Figure 6.15: MCS formulation for example system in Figure 6.1	147
Figure 6.16: BNs with (a) converging structure and (b) chain structure	149
Figure 6.17: Comparison of computational demands associated with converging and chain BN topologies when components have (a) two states and (b) five states	149
Figure 6.18: Comparison of computational demands associated with converging and chain BN topologies for binary nodes with one or more common parent demand nodes	150
Figure 6.19: BN using SPEs to define performance of a series system.....	151
Figure 6.20: BN using SPEs to define performance of a parallel system.....	152
Figure 6.21: BN using FPEs to define a parallel system	153
Figure 6.22: BN using FPEs to define a series system	153
Figure 6.23: Efficient MLS BN formulation for system in Figure 6.1 with distinct SPSs.....	155
Figure 6.24: Efficient MLS BN formulations for example system with coalesced SPEs associated with components 7 and 8 using converging structure.....	156
Figure 6.25: Efficient MLS BN formulations for example system with coalesced SPEs associated with components 7 and 8 using chain structure	157
Figure 6.26: Efficient MCS BN formulation for system in Figure 6.1 with distinct FPSs.....	158
Figure 6.27: Efficient MCS BN formulation for example system with coalesced FPEs associated with components 1, 2, and 3 using converging structure.....	159
Figure 6.28: Efficient MCS formulations for example system with coalesced SPEs associated with components 1, 2, and 3 using chain structure	160
Figure 6.29: BNs illustrating constraint that no SPS may exist that is not strictly an MLS.....	166
Figure 6.30: System in Figure 6.1 with super components replacing components C4 , C5 , and C6 and components C7 and C8	168
Figure 6.31: System in Figure 6.30 with super component replacing components C1 , C2 , C3 , and SC1	168

Figure 6.32: BN constructed for system in Figure 6.1 using super component heuristic.....	169
Figure 6.33: Example system illustrating noncontiguous components that can be combined in a super component.....	169
Figure 6.34: Example application 1	177
Figure 6.35: Efficient MCS formulation without heuristics for example application 1	178
Figure 6.36: Illustration of FPSs corresponding to MCSs for example application 1	179
Figure 6.37: Example application 2.....	180
Figure 6.38: Efficient MCS formulation obtained using optimization algorithm with use of super components	181
Figure 6.39: Illustration of FPSs corresponding to MCSs for example application 2.....	182
Figure 6.40: Efficient MCS formulation obtained using optimization algorithm with chain structure.....	183
Figure 6.41: Efficient MCS formulation obtained using optimization algorithm with both heuristics	183
Figure 6.42: Illustration of FPSs corresponding to multicomponent MCSs for example application 2 using both heuristics.....	184
Figure 7.1: Types of links in limited memory influence diagrams.....	192
Figure 7.2: IDs modeling shutdown/operation decision based on (a) no information, (b) perfect information, and (c) imperfect information about damage state of component i	195
Figure 7.3: ID modeling an inspection-shutdown decision at component level.....	196
Figure 7.4: ID modeling joint inspection-shutdown decision at system level.....	198
Figure 7.5: Example infrastructure system	202
Figure 7.6: System configurations for example inspection-shutdown decisions.....	204
Figure 8.1: Example transportation network	217
Figure 8.2: Location of transportation system relative to three active faults.....	217

Figure 8.3: Prior probability mass functions of (a) source, (b) magnitude, and (c) epicenter location.....	219
Figure 8.4: Distribution of ground motion intensity at site 1	221
Figure 8.5: Example hazard curve for site 1	222
Figure 8.6: Joint distribution of magnitude and source-to-site distance.....	224
Figure 8.7: Conditional probability that spectral acceleration is equal to the state (0.55–0.6 g) or greater at site 1 for various magnitudes and source-to-site distances.....	224
Figure 8.8: Hazard deaggregation for site 1.....	225
Figure 8.9: Distribution of spectral acceleration at site 1 given evidence cases.....	226
Figure 8.10: Updated distributions of (a) earthquake source and (b) magnitude given evidence cases	227
Figure 8.11: Hazard curves for all sites for unconditional case.....	229
Figure 8.12: Hazard curves for all sites for earthquakes on each source.....	229
Figure 8.13: Site-specific hazard curves for earthquakes on each source	231
Figure 8.14: Fragility function for different realizations of model error.....	231
Figure 8.15: Probability of component failure given an earthquake	232
Figure 8.16: BN modeling system performance in example 1 using converging MLS formulation	233
Figure 8.17: BN modeling system performance in example 1 using efficient MLS formulation	234
Figure 8.18: System failure probabilities for example 1.....	235
Figure 8.19: Distribution of spectral acceleration at sites 2, 4, and 6 for evidence cases 1–3 ...	238
Figure 8.20: Distributions of earthquake location parameters for evidences cases 1–3.....	239
Figure 8.21: Distributions of random field intra-event error terms for evidence cases 1–3.....	240
Figure 8.22: Approximate random field model	240

Figure 8.23: Distributions of spectral accelerations at sites 2, 4, and 6 for evidence cases 4–7	241
Figure 8.24: Distribution of spectral acceleration at site 1 for evidence case 7	242
Figure 8.25: Google Earth map of northern California portion of proposed California High-Speed Rail system route (blue) (CA HSR 2010) and nearby faults (red and pink) (Bryant 2005)	243
Figure 8.26: Google Earth map with idealizations of Calaveras, Hayward, and a portion of the San Andreas faults	245
Figure 8.27: Ground motion prediction points along HSR alignment	246
Figure 8.28: Approximated random field model for HSR	247
Figure 8.29: Locations of major distributed components of HSR alignment (CA HSR 2010)	248
Figure 8.30: BN modeling system performance of HSR	251
Figure 8.31: LIMID for solving inspection-shutdown decision for link 1 of HSR system	253
Figure 8.32: Distributions of ground motion intensities at GMPPs 1, 6, 11, and 16 for four evidence cases	256
Figure 8.33: Distributions of normalized intra-event error terms ($z_{r,i} = \varepsilon_{r,i}/\sigma_{r,i}$) for GMPPs 1, 6, 11, and 16 and the normalized inter-event error term ($z_m = \varepsilon_m/\sigma_m$)	257
Figure 8.34: Distributions of parameters defining rupture location (\mathbf{Xr}, \mathbf{RL}) for four evidence cases	258
Figure 9.1: Summary of Bayesian network methodology for seismic infrastructure risk assessment and decision support	264

LIST OF TABLES

Table 3.1: CPT of $X_{d,i}$ given R_L and X_r showing geometric inconsistencies due to discretization	54
Table 4.1: Number of links required to achieve less than 10% error in estimate of failure probability for series system when $\zeta_R = 0.3$ (left) and $\zeta_R = 0.6$ (right) (Bold numbers indicate minimum number of links obtained with any approximation method)	109
Table 4.2: Minimum number of links required to achieve less than 10% error in estimate of failure probability for parallel system when $\zeta_R = 0.3$ (left) and $\zeta_R = 0.6$ (right) (Bold numbers indicate minimum number of links obtained with any approximation method).....	109
Table 6.1: Comparison of computational complexity.....	162
Table 7.1: Component classes.....	203
Table 7.2: System configurations for example inspection-shutdown decisions.....	203
Table 7.3: Assumed utility values for cases 1–4.....	205
Table 7.4: Assumed utility values for cases 5–8.....	206
Table 7.5: Value of information and prioritization rankings for cases 1–4 given (a) no evidence and (b) component 1 has been perfectly inspected and found to be damaged (VoI = value of information)	207
Table 7.6: Value of information and prioritization rankings for cases 5–8 given (a) no evidence and (b) component 1 has been perfectly inspected and found to be damaged (VoI = Value of information)	209
Table 8.1: Most-probable source node state configuration corresponding to evidence scenario in which spectral acceleration is in the state 0.55–0.6 g or greater.....	228
Table 8.2: Most probable node state configuration of (a) component states and (b) source characteristics for evidence scenario in which city A is disconnected from the hospital.....	236

Table 8.3: Assumed component types, length, and associated GMPPs of the HSR.....	249
Table 8.4: Assumed component inspection costs and liabilities.....	254
Table 8.5: Component state probabilities for states no damage and moderate or severe damage under different evidence cases	259
Table 8.6: System state probabilities under different evidence cases.....	260
Table 8.7: Prioritization order associated with each links under evidence cases	261
Table 8.8: Value of information and prioritization order associated with components along link 1 under evidence case 2	261

1. Introduction

1.1 Motivation

Civil infrastructure systems are the backbones of modern societies, and ensuring their reliability and resilience is critical to the health, safety, and security of communities. In many countries around the world, civil infrastructure systems face increasing service demands while they deteriorate as a result of inadequate maintenance, material degradation, and increasing exposure to overloads. In addition, these systems are subject to a variety of natural and man-made hazards. If lifelines are not operational after an extreme event, such as an earthquake or hurricane, entire communities may have to be displaced. With limited resources available to address these deficiencies, there is need for infrastructure-specific decision support tools that will help facility owners allocate scarce funds. Unfortunately, for many years, research has focused primarily on improving the performance and reliability of individual structures or components, and relatively little effort has been dedicated to examining infrastructure systems as a whole.

Risk assessment and management of infrastructure systems differs substantially from the typical risk analysis done for individual infrastructure components (Der Kiureghian 2009). Consider four major differences:

Hazard characterization: Infrastructure systems are spatially distributed and thus their rate of hazard exposure is greater than that of single-site facilities. Furthermore, they are exposed to a wider variety of failure modes. This is particularly true of infrastructure systems exposed to geographically distributed loads, such as earthquakes, which require the modeling of hazard as a spatially distributed random field. Neglecting the correlation in demands arising from the random field nature may result in incomplete hazard

characterization and overestimates of the reliability of infrastructure systems that are generally redundant.

System-level effects: System-level management activities, such as the prioritization of component inspections and repairs after a hazard event, require that lifelines be analyzed using systems analysis techniques. Failing to properly account for the systems effect may result in wasting resources on components that have little influence on overall system reliability and neglecting components that are crucial for the system's performance.

Complexity and interactions in infrastructure systems: Lifelines do not operate independently, and the performance of one infrastructure system often depends on the operation of other systems. Failing to account for such dependency may result in overestimation of system reliability. For example, retrofitting a water distribution system may help it withstand loads imposed by a large hazard event, but this investment is worthless if the electrical grid required to power the pumps is out of service.

Evolving nature of information: The infrastructure information that is available to managers and decision-makers is generally uncertain and continuously evolving in time. Under normal operating conditions, for example, components go in and out of service due to degradation and scheduled repairs, and rehabilitation and retrofit actions change the system's reliability. The evolving nature of information is particularly important in the aftermath of a hazard event, when information becomes available incrementally from a variety of sources such as structural health monitoring sensors, hazard reports, and human observation. A decision support system for managing infrastructure should be able to incorporate the flow of uncertain and evolving information.

Earthquakes pose the dominant risk to infrastructure systems in many regions. However, sound engineering and decision-making can mitigate this risk. With respect to earthquakes, infrastructure systems must be managed during three distinct stages: normal operating conditions, immediate post-event, and longer-term post-event. Each stage is associated with acquisition of information that is both uncertain and evolving in time, and that must be incorporated into hazard and component/system performance models. The aforementioned three phases are further described below.

Decision-making under normal operating conditions: In earthquake-prone regions, it is necessary to assess earthquake risks by identifying critical components and bottlenecks in the system, and then taking actions to minimize the risk exposure. These actions may include retrofitting or replacing components and modifying the system configuration. Actions also must be taken to maximize system reliability under normal conditions, e.g., by selecting types and timing of inspection, maintenance and rehabilitation actions. Decisions that improve system reliability under normal operating conditions and resilience to extreme events should ideally be made in tandem because many failures occur when damaged/deteriorated structures are subjected to abnormal loads.

Immediate post-event response: Immediately after an earthquake, decisions must be made to reduce the severity of post-event consequences. Often, at this stage, emphasis is placed on life safety and restoration of critical services. Post-event decisions include the dispatching of rescue, inspection, and repair crews as well as deciding to open or close facilities. These decisions are made under the competing demands to maintain operability (preventing revenue loss) while not sacrificing safety (avoiding death and injury, as well as liability). This phase is characterized more than the others by an environment in which information is both uncertain and quickly evolving. Sources of information at this phase may include ground motion intensity measurements, data from structural health monitoring sensors, inspection results, and observations reported by citizens and infrastructure facility employees. To aid decision-making, such information should be incorporated into hazard and component/system response models in near-real time to provide up-to-date probabilistic characterizations of the performance of the system.

Longer-term post-event recovery and recalibration: In the longer term after an earthquake, actions aim to minimize long-term economic consequences. Such actions may include prioritizing replacement and retrofitting of damaged facilities and reconfiguring the system. Also, information gained about component and system performance and the hazard environment should be used to update and refine the hazard model as well as the component fragilities and system characterizations that are used in decision support tools to minimize risk from future earthquakes.

1.2 Goals, methodology, and scope

The goal of this study is to develop the framework for a probabilistic decision-support system for seismic infrastructure risk assessment and management. The study focuses primarily on developing a framework that can incorporate uncertain and evolving information from a variety of sources and provide support to decision-makers in immediate post-event applications. However, the framework developed here can also be applied to the other two aforementioned decision-making phases.

The actions taken immediately after an earthquake can have a significant impact on the severity and extent of consequences as well as the efficiency and speed of recovery efforts. Despite the criticality of immediate post-event actions, decisions are often made in an ad hoc manner, under great uncertainty, and in the face of information that evolves rapidly. Decision makers, acting in a stressful and chaotic post-disaster environment, often have limited and uncertain information as well as their personal experience to draw upon. For near-real-time applications, decision-makers require estimates of reliabilities of the system and its components conditioned on the available information, e.g., partially or precisely known magnitude and location of the earthquake, measurements of shaking intensity at recording stations, and observed performance of components and subsystems. Additionally, the output of a management tool must provide rankings of decision alternatives. Thus, post-event decision-makers need a tool that (1) can be employed in near-real time after a major disaster; (2) can synthesize incoming information with existing probabilistic models; and (3) can properly account for uncertainties in both the incoming information as well as in the analytical and empirical models that are used to assess the demands on and the damage states of various components of an infrastructure system. Recent advances in technology, computer science, learning techniques, risk assessment, and hazard modeling have yielded knowledge and methodologies that can be integrated to create such a tool to aid post-event decision-making.

Bayesian networks may provide the ideal tool to meet these challenges. The following characteristics make Bayesian networks well-suited for the proposed application:

- (1) They are efficient and intuitive graphical tools for the representation and assessment of systems under uncertainty.

- (2) They can be used to model multiple hazards and their interdependencies resulting from common causes and characteristics.
- (3) They provide an efficient framework for probabilistic updating and the assessment of component/system performance in light of uncertain and evolving information, particularly for near-real time, post-event applications.
- (4) They can use a max-propagation algorithm to identify critical components in a system and most-probable hazard scenarios.
- (5) Their graphical interface makes them an excellent tool for interaction with and use by practitioners and end users, who may not be experts in probabilistic systems analysis.
- (6) Their ability to update information makes them an excellent tool for scenario evaluation for design purposes as well as for emergency response training and exercises.
- (7) They can be extended to include utility and decision nodes, thus providing a decision tool for ranking alternatives based on expected utility.
- (8) They provide an ideal platform for linking interdisciplinary modules to provide a comprehensive decision-support framework.

Assessing the seismic risk to civil infrastructure systems requires: (1) characterization of earthquake sources and associated properties; (2) an accurate and adaptable seismic demand model that provides estimates of ground motion intensities and related local hazards at distributed locations throughout the geographic domain of the infrastructure system, while properly accounting for the relevant spatial correlation structures; (3) models of component performance under seismic loadings; and (4) models of the infrastructure system performance in terms of the component performances. Furthermore, given fully updateable models of seismic hazard and system response, it is necessary to have an explicit framework for providing decision support.

In this study, we develop a methodology for using Bayesian networks to perform seismic infrastructure risk assessment and provide decision support. We aim to lay the foundation of a comprehensive framework by addressing issues such as the integration of existing knowledge related to seismic hazard modeling and assessment, component performance modeling, and system analysis into a Bayesian network. Furthermore, we address issues related to computational efficiency to help make the method more viable for use for realistic infrastructure

systems, which are large and complex. Although developing a final product for end users is outside the scope of this study, the work presented here provides the foundation necessary to eventually develop applied tools.

1.3 Existing resources

Before detailing the approach proposed in this study, we briefly describe the resources currently available to decision-makers. These facilitate tasks ranging from analysis of earthquake risk at the component level to portfolio risk management. The resources described here are primarily useful for risk assessment and are predominantly employed in pre-event applications for understanding seismic hazard and identifying potential weak points. Often, they provide guidance for considering representative earthquake scenarios to accomplish these tasks. However, none is able to facilitate near-real-time Bayesian updating, or provide decision support while fully accounting for the time-evolving and uncertain nature of available information and models.

1.3.1 HAZUS^{MH}

Hazards U.S. Multi-Hazard (HAZUS^{MH}) (FEMA 2008) is a widely used methodology and software program developed by the Federal Emergency Management Agency (FEMA) for estimating losses from multiple hazards, such as earthquakes, hurricane winds, and floods. It uses geographic information systems (GIS) to provide hazard map data and allows users to estimate the impact of hazards on buildings and infrastructure components by mapping and displaying damage data and economic loss estimates. HAZUS^{MH} is designed to aid decision-makers by providing loss estimates that inform mitigation plans, emergency preparedness, and response/recovery planning. HAZUS^{MH} involves a five-step process: (1) identify hazards, (2) profile hazards, (3) inventory assets, (4) estimate losses, and (5) evaluate mitigation options. HAZUS^{MH} is geared toward use before a disaster strikes to inform mitigation actions (FEMA 2008). In this sense, it is a static system, without a means of updating the model and estimates as information becomes available after an event. However, given its comprehensive nature, HAZUS^{MH} is a valuable asset for infrastructure owners.

HAZUS^{MH} has several shortcomings in areas that are extensively addressed in this study. It makes simplifying assumptions with regard to modeling seismic hazard. The effects of these simplifying assumptions are not detrimental when assessing single-site facilities, but become important when assessing the hazard on a spatially distributed system. Its characterization of lifeline systems is “necessarily incomplete and oversimplified” (DHS 2003). It also lacks an ability to update risk estimates based on evolving and uncertain information. In some areas, HAZUS^{MH} goes beyond the scope of this study by addressing a wider range of hazards as well as providing specialized guidance for specific classes of infrastructure systems. To that end, HAZUS^{MH} is a valuable risk assessment tool that can be viewed as complementary to the system proposed in this study.

1.3.2 ShakeMap/ShakeCast

Immediately after each significant earthquake, the United States Geological Survey (USGS) Earthquake Hazards Program produces a ShakeMap. A ShakeMap is a map providing estimates of ground motion and shaking intensity in a region due to an earthquake (USGS 2008). ShakeMaps are used in response and recovery efforts and information dissemination to scientists, the public, and news agencies. Scenario earthquakes can be also considered for disaster preparedness exercises and planning. ShakeMaps are determined by combining measurements of ground motion intensity collected during an earthquake with knowledge about earthquake source characteristics and local site conditions (USGS 2008). However, for seismic infrastructure risk assessment, ShakeMap has several shortcomings: (1) Interpolations between points for which measurements are available require use of empirical relations, but ground motions and intensities can vary significantly over short distances. Thus, at small scales and away from observation points, results obtained from ShakeMap can be unreliable. (2) A ShakeMap is not a complete or certain descriptor of ground motion at a site and thus may not be sufficient for predicting the severity of damage at the site (USGS 2008). (3) ShakeMaps only minimally address issues of uncertainty and neglect random field effects. (4) ShakeMaps only depict seismic intensities and do not provide information about component or system performance.

ShakeCast (short for ShakeMap Broadcast) is a “fully automated system for delivering specific ShakeMap products to critical users and for triggering established post-earthquake response protocols” (USGS 2007). Used primarily for emergency response, loss estimation, and public information, ShakeCast sends automatic notifications of earthquake shaking information (e.g., by cell phone, pager, email) at specific facilities based on preset thresholds (USGS 2007). Using pre-established damage thresholds, ShakeCast provides estimates of the likelihood of damage at locations affected by an earthquake; it also converts HAZUS structure type information to structural damage levels. (USGS 2008, 2007). ShakeCast has greater capabilities than ShakeMap and HAZUS^{MH} with regard to near-real time applications, but it falls short of the objectives outlined in this study. For example, it does not permit Bayesian updating nor does it model system performance. Nevertheless, integration of the methodology described in this study within an existing platform such as ShakeMap or ShakeCast can prove highly useful in near-real-time post-earthquake applications.

1.3.3 REDARS

REDARS (**R**isks from **E**arthquake **D**Amage to **R**oadway **S**ystems) is a seismic risk analysis tool designed to assess risks posed to highway systems (Werner et al. 2006). REDARS is a scenario-based analysis tool. For a given earthquake scenario (deterministic assessment) or for a simulated suite of earthquake realizations in which uncertainty is included (probabilistic assessment), REDARS estimates: (1) seismic hazards due to ground shaking, liquefaction, and fault rupture; (2) predicted damage to components in the system; (3) damage consequences including repair costs, downtime, and ability of the system to carry traffic as post-event repairs progress; and (4) economic losses and travel time increases. Network analysis procedures are applied to each damage scenario to determine how closures affect system wide travel times and traffic flows. REDARS is designed for use in pre- and post-earthquake applications and to provide design guidance.

Prior to the occurrence of an earthquake, REDARS can be used to estimate the effect of seismic improvement options based on the ability of the retrofit to reduce expected economic losses. It compares expected costs and benefits of available improvement options. In post-earthquake

applications, REDARS can incorporate data corresponding to realized damages and use the information to assess the relative abilities of repair strategies or priorities as well as options for traffic management. It does not facilitate Bayesian updating. The treatment of uncertainties in REDARS is less comprehensive and rigorous than in the approach developed in this study; however, REDARS is more sophisticated than the present study in its approach to modeling traffic and economic consequences.

1.3.4 Additional resources

Other methodologies similar to or based on the HAZUS^{MH} framework are available. These include:

- RADIUS (Risk Assessment Tools for Diagnosis of Urban Areas Against Seismic Disasters) is a project to help decision-makers and other leaders in developing countries understand earthquake risk and to use public awareness as a means for reducing it (GHI 2009). As part of the project, nine city case studies were selected to develop damage scenarios and action plans as well as to perform a comparative study on understanding urban seismic risk around the world, but particularly in developing countries. The project developed tools for risk management and facilitating inter-city information exchange.
- RISK-UE is a methodology similar to HAZUS^{MH} and RADIUS for specific application to European cities, which have characteristics that differentiate them from other locations. These include the presence of historical and monumental structures, characteristic city layouts, cultural impacts, and functional/social organizations. RISK-UE provides a “modular methodology” that includes assessment of seismic hazard, system exposure, and the vulnerabilities of lifelines and modern and historical structures. Handbooks are available for each module (Mouroux and Brun 2006).

1.4 Study outline

This study develops a comprehensive Bayesian network methodology for performing seismic infrastructure risk assessment and providing decision support. Components of the Bayesian

network framework include: (1) a seismic demand model of ground motion intensity as a spatially distributed Gaussian random field accounting for multiple seismic sources with unique and potentially uncertain properties as well as finite fault rupture and directivity effects; (2) models of performance of point-site and distributed components; (3) models of system performance for connectivity and flow in terms of component states; and (4) extensions of the Bayesian network to include decision and utility nodes to aid post-earthquake decision-making.

Chapter 2 introduces Bayesian networks with a brief review of Bayesian statistics, emphasizing the value of the Bayesian approach for facilitating information updating, particularly in large and complex problems. The chapter gives a brief introduction to constructing and performing inference in Bayesian networks. Because the chapter is meant to provide only the background necessary to understand the Bayesian network models outlined in this study, wherever possible complex theoretical descriptions are replaced by intuitive and example-based explanations.

Chapter 3 describes a Bayesian network-based model that provides distributions of ground motion intensity at discrete points in the domain of a geographically distributed infrastructure system. The focus of the chapter is primarily on hazards due to ground shaking, but the framework is extended to other hazards with less detail and rigor. Both point-source and finite-rupture model formulations are considered. The formulation presented accounts for random field and directivity effects.

Chapter 4 presents methods for developing Bayesian networks that efficiently model correlated random variables drawn from a Gaussian random field. Direct modeling of correlated variables results in a Bayesian network topology that is densely connected. For such a topology, the computational and memory demands rapidly grow with the number of points drawn from the random field. This chapter develops approximate methods to minimize the number of links in the Bayesian network, while limiting the error in the representation of the correlation structure of the random field.

Chapter 5 presents Bayesian network formulations for modeling the performances of components in an infrastructure system as a function of the seismic demands placed upon them. First, a generic model is presented for describing component performance while accounting for potential sources of correlation. In many instances seismic fragility research is not sufficiently

mature, nor are there adequate data, to enable construction of the generic formulation. As a result, simplified Bayesian network-based models for point-site and distributed components are developed that reflect the current state of practice. The chapter briefly describes fragility functions available for modeling the performance of components in a variety of infrastructure systems.

Chapter 6 presents several Bayesian network formulations for modeling the performance of infrastructure systems as a function of the states of the system components. It begins with a brief overview of conventional methods of modeling system performance and compares them with the Bayesian network approach. Five Bayesian network approaches are then described, including a naïve approach, two approaches based on an intuitive interpretation of system performance, and two approaches that utilize minimal link and cut sets. The last two formulations are then adapted with the goal of minimizing computational demands using a heuristically augmented optimization-based procedure. The procedure is developed to automate the construction of efficient Bayesian network formulations for modeling system performance. Both system connectivity and flow criteria are considered. Chapter 6 ends with two example applications.

Chapter 7 extends the Bayesian network with decision and utility nodes to create a new graphical structure known as an influence diagram. This allows the Bayesian network framework described in this study to be used to solve decision problems based on the principles of expected utility maximization. An example application is presented involving post-earthquake component inspection and shutdown decisions.

Chapter 8 provides two example applications. The first example is based on a simple hypothetical transportation system and shows how Bayesian networks can be used to perform and go beyond conventional probabilistic seismic hazard assessment. The second application is based on the preliminary schematics of the proposed California high-speed rail system. Because the system is still under design, the example is based on hypothetical assumptions and idealizations. The application is used to demonstrate the value of using Bayesian networks for near-real time, post-earthquake hazard assessment and decision support.

Chapter 9 summarizes the study and discusses the outlook for continued research and development in this area.

2. Introduction to Bayesian Networks

2.1 Background

Statistical inference is the process of drawing a conclusion, such as estimating the value of an uncertain quantity, using data or observations. More formally, it is the process of distinguishing systematic patterns in a set of observations from the random noise intrinsic to almost all data sets (Gill 2002). The two primary schools of thought relating to statistical inference are the frequentist approach and the Bayesian approach.

The frequentist approach is based on the frequency notion of probability. It specifies that the probability of an event is the limit of its relative frequency of occurrence as the number of event trials becomes large, theoretically infinite. It is thus an empirical approach to computing probabilities. Unfortunately, in many research disciplines (including earthquake engineering), a sufficiently large sample of events is rarely available. For this reason, Bayesian methods, which are generally more robust in situations of data scarcity (Koop 2003), have grown in popularity since the mid-20th century. Under the frequentist approach, unknown parameters are treated as fixed deterministic values to be estimated rather than as random variables. The Bayesian approach instead treats unknown parameters as random variables and argues that uncertainty can be expressed as a probability distribution that reflects the relative likelihoods of outcomes. Specifically, Bayesian statistics is concerned with determining the conditional probability of an unknown quantity given observations. It uses observations to test assumptions made prior to statistical analysis, such as those based on subjective expert opinion, engineering judgment, or physical models. Bayesian statistical models can be updated continuously as new observations become available and thus represent the probabilistic modeling of an accumulation of knowledge (Congdon 2003). As the amount of available data increases, conclusions based on a Bayesian

analysis will approach the results obtained using a frequentist approach because the influence of the prior assumptions diminishes.

The use of the term *Bayesian* to describe this approach comes from the well-known Bayes' rule, attributed to the 18th-century mathematician and philosopher Thomas Bayes:

$$\Pr(A|B) = \frac{\Pr(AB)}{\Pr(B)} = \frac{\Pr(B|A)}{\Pr(B)} \Pr(A) \quad (2.1)$$

$\Pr(AB)$ is the probability of joint occurrence of events A and B , $\Pr(A)$ is the marginal probability of event A , $\Pr(A|B)$ is the conditional probability of event A given that event B has occurred, and $\Pr(B)$ is the marginal probability of event B . The quantity $\Pr(B|A)$ is known as the *likelihood* of the observed event B . Note that the probability of event A appears on both sides of Equation (2.1). Bayes' rule describes how the probability of event A changes given information gained about the occurrence of event B . Typically, $\Pr(A)$ is known as a *prior probability* and represents a belief about the probability of A prior to knowing anything about B . Analogously, $\Pr(A|B)$ is called the *posterior probability* of A because it represents a belief about the probability of A after observing the occurrence of event B . The dominator $\Pr(B)$ is a normalizing factor obtained using the Theorem of Total Probability (Box and Tiao 1992):

$$\Pr(B) = \Pr(BA) + \Pr(B\bar{A}) = \Pr(B|A) \Pr(A) + \Pr(B|\bar{A}) \Pr(\bar{A}) \quad (2.2)$$

where \bar{A} is the complement A . It is seen that Bayes' rule facilitates the *updating* of beliefs about event A given evidence about event B .

More generally, let X be a random variable and $\mathbf{E}_x = \{E_{x,1}, \dots, E_{x,n}\}$ be a set of observations that provides information about X (e.g., $X_i = x_i$, $X_i \leq x_i$, or $X_i > x_i$). Let Θ be an unknown parameter or a set of parameters describing the probability distribution of X . Equation (2.1) is adapted to yield an expression for the updated conditional probability distribution of the unknown parameter Θ given the vector of observations on X :

$$f(\theta | \bigcap E_{x,i}) = \frac{\Pr(\bigcap E_{x,i} | \theta)}{\Pr(\bigcap E_{x,i})} f(\theta) \quad (2.3)$$

In Equation (2.3), $f(\theta)$ is the prior probability density function (PDF) representing the analyst's belief about the relative likelihoods of the possible outcomes θ of the unknown parameter Θ in the absence of observations \mathbf{E}_x . The prior distribution does not depend on the observations. $f(\theta | \cap E_{x,i})$ is referred to as the *posterior distribution* of θ , and $\Pr(\cap E_{x,i} | \theta)$ is once again referred to as the likelihood function. In this case, the likelihood gives the probability of observing the data given that θ is the true value of the unknown parameter Θ . Assuming the observed events $E_{x,i}$ are statistically independent, the likelihood can be expressed as

$$\Pr\left(\bigcap E_{x,i} \mid \theta\right) = \prod_i [\Pr(E_{x,i} \mid \theta)]. \quad (2.4)$$

Thus, the likelihood is based on observations whereas the prior comes from other, typically subjective, sources. The denominator in Equation (2.3) is obtained by normalization using the Theorem of Total Probability (Box and Tiao 1971):

$$\Pr\left(\bigcap E_{x,i}\right) = \int_{\theta} \Pr\left(\bigcap E_{x,i} \mid \theta\right) f(\theta) d\theta \quad (2.5)$$

The normalizing factor in Equation (2.5) is often difficult to compute. However, the availability of conjugate priors (Fink 1997) facilitates convenient solutions for certain known distributions. Markov-chain Monte Carlo simulation (Gamerman and Lopes 2006) provides an efficient numerical method to perform Bayesian updating.

Bayesian methods are popular in a wide variety of applications requiring efficient and practical solutions. They have also given rise to a class of graphical models known as Bayesian networks, which facilitate efficient Bayesian updating in large and complex problems.

A *Bayesian network* (BN) is a probabilistic graphical model that represents a set of random variables and their probabilistic dependencies. In the context of this study, the variables may represent demand or capacity values or other variables that define them, or the states of components and systems. BNs are graphical, facilitate information updating, can be used to identify critical components within a system, and can be extended by decision and utility nodes to solve decision problems. In particular, the facility for information updating renders the BN an excellent tool for infrastructure risk assessment and decision support. Evidence on one or more

variables, e.g., observed component capacities, demands, or component/system states, is entered into the BN, and this information propagates throughout the network to yield an up-to-date probabilistic characterization of the performance of the infrastructure system in light of the new observations, following the principles of Bayes' rule. This dynamic system characterization is particularly critical for post-event, near-real-time applications when the available information is uncertain and rapidly evolving.

Graphical models are intuitively appealing for encoding dependence relations because they provide a transparent language for communicating the relations among variables (Kjaerulff and Madsen 2008) and the flow of information between them. Thus, they facilitate communication of model configuration among interested parties. Because the BN is a graphical representation of random variables and dependencies, it permits probability and graph theories to be linked and is thus an intuitive means for dealing with uncertainties in complex systems (Friis-Hansen 2004).

2.2 Brief introduction to Bayesian networks

This section introduces BNs with the goal of providing knowledge sufficient to understand the models and methods presented in this study. Comprehensive coverage of BNs is available in textbooks (Jensen and Nielsen 2007; Kjaerulff and Madsen 2008).

2.2.1 Bayesian network terminology

A BN is a directed acyclic graph consisting of a set of *nodes* (circles) representing random variables and a set of *directed links* (arrows) representing probabilistic dependencies, which often also indicate causal relationships. Consider the simple BN shown in Figure 2.1, which models five random variables $\mathbf{X} = \{X_1, \dots, X_5\}$ and their probabilistic dependencies. For example, random variable X_3 is probabilistically dependent on variables X_1 and X_2 , as represented by arrows going from nodes X_1 and X_2 to node X_3 . In the BN terminology, X_3 is a *child* of X_1 and X_2 , and X_1 and X_2 are the *parents* of X_3 . Likewise, X_4 is defined conditionally on its parent node X_1 and X_5 is defined conditionally on X_4 . For discrete X_i , each node is associated with a set of mutually exclusive and collectively exhaustive states. To utilize exact inference algorithms, it is

generally necessary to discretize all continuous random variables in the BN (with the exception of linear functions of continuous Gaussian nodes without discrete children). BNs with continuous nodes are briefly addressed in this section; additional details can be found in Lauritzen (1992), Lauritzen and Jensen (2001), Shenoy (2006), Madsen (2008), and Langseth et al. (2009). For discrete nodes, a *conditional probability table* (CPT) is attached to each node that provides the conditional probability mass function (PMF) of the random variable represented by the node, given each of the mutually exclusive combinations of the states of its parents. For nodes without parents (e.g., X_1 and X_2 in Figure 2.1), known as *root nodes*, a marginal probability table is assigned.

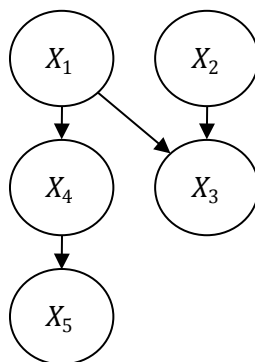


Figure 2.1: A simple BN

2.2.2 Constructing Bayesian networks

A BN generally is constructed in two steps: (1) definition of the graphical model representing the probabilistic dependence structure of the problem, i.e., its *d-separation* properties (see below); and (2) construction of the CPTs that together define the joint distribution over all random variables in the BN.

When constructing a BN, care must be taken to ensure that models are not misleading, unverifiable, unnecessarily complex, or computationally intractable. Accurate modeling with a BN requires thorough understanding of the problem and the ability to identify the primary elements that influence it. Modeling complex problems and systems with a BN may require trade-offs between transparency (verifiability), computational complexity, and detail of modeling

(Friis-Hansen 2004). In many applications, statistical data are available to develop robust models to relate random variables in a BN. In earthquake engineering and infrastructure system analysis, data are often scarce or unavailable. Thus, dependence relations between parents and children and the probabilities of root nodes may be based instead on theoretical models, empirical relations, expert opinion, and engineering judgment.

When constructing BNs, it is not required that links represent causal relations, although that is typically preferred. Rather, the conditional relations must be specified such that the *d-separation properties* of the model correspond to those of the real-world problem being modeled. Conditional (in)dependencies should not be included in the model if they do not hold in reality (Jensen and Nielsen 2007).

The concept of d-separation is important when working with BNs. Consider two distinct sets of variables X and Y in a BN. These two variable sets are considered *d-separated* by a third set of variables Z if X and Y are independent given the variables in Z , i.e., if $p(x, y|z) = p(x|z)p(y|z)$. D-separation corresponds to a blockage of the flow of information between X and Y (Bayes Nets 2007). Figure 2.2 shows three types of connections that occur in BNs: (1) *serial* (head-to-tail), (2) *diverging* (tail-to-tail), and (3) *converging* (head-to-head). For each type of connection, the path from X to Y is or is not blocked (d-separated) based on whether or not Z is *instantiated*, i.e., its value has been observed. Instantiated nodes are shaded in Figure 2.2. The path between X and Y is blocked for serial and diverging connections when Z is instantiated. That is, information about X only updates a belief about Y when Z is unobserved, and vice versa. A converging connection is blocked when Z is not instantiated, that is, information about X provides information about Y only when Z is observed. A more extensive discussion of d-separation can be found in Pearl (2000) and Jensen and Nielsen (2007).

The state space of the random variables in a BN (the set of all possible combinations of variable outcomes) grows exponentially with the number of variables in the BN. However, through the use of conditional relations, the joint distribution is factored into the product of local conditional PMFs (CPTs), which are simpler to specify and facilitate more efficient calculations. The joint PMF of all random variables \mathbf{X} in the BN is constructed as the product of the conditional PMFs:

$$p(\mathbf{x}) = \prod_{i=1}^n p(x_i | \text{Pa}(x_i)) \quad (2.6)$$

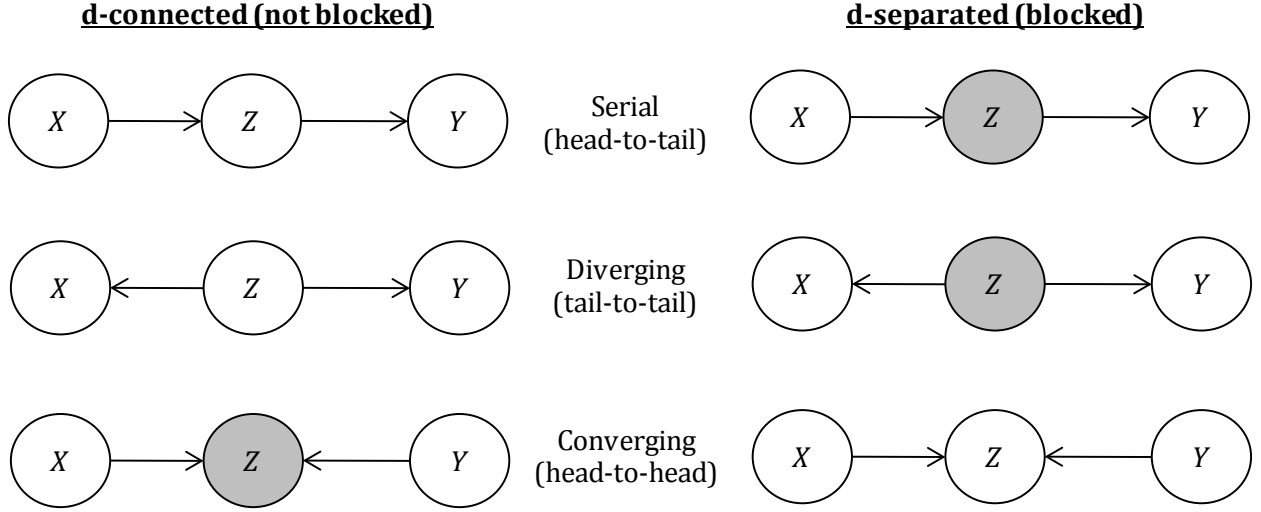


Figure 2.2: Graphical representation of d-separation properties. Gray nodes are observed.

where $\text{Pa}(x_i)$ is the set of parents of node X_i , $p(x_i | \text{Pa}(x_i))$ is the CPT of X_i , and n is the number of random variables (nodes) in the BN. Thus, for the BN in Figure 2.1, the joint PMF is

$$p(x_1, x_2, x_3, x_4, x_5) = p(x_5 | x_4) p(x_4 | x_1) p(x_3 | x_1, x_2) p(x_1) p(x_2). \quad (2.7)$$

Having the ability to model a problem using conditional distributions is convenient in civil engineering applications, where often only conditional relationships are available. For example, physical models or empirical relations establish the probability of a load exceeding a specific value given an event of a certain size. Similarly, fragility curves specify the probability of damage to a structure given a particular demand value.

In this study, conditional probability tables of nodes are typically generated using Monte Carlo simulation. To demonstrate the generation of CPTs, consider a node Y with three parent nodes, X_1 , X_2 , and X_3 , as shown in Figure 2.3. Node X_1 is a discrete node with m_1 categorical states and an arbitrary number of parents. Node X_2 is an interval node without parents. The term *interval node* describes a node that results from discretization of a continuous random variable. Node X_2 has m_2 states, which correspond to mutually exclusive collectively exhaustive intervals over the

entire range on which the continuous random variable is defined. X_3 is also an interval node but with m_3 states and an arbitrary number of parents.

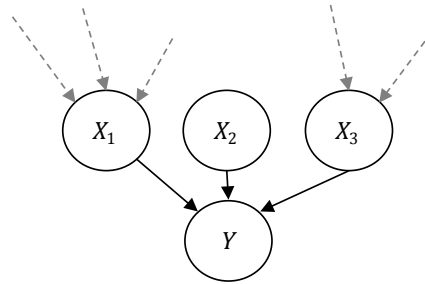


Figure 2.3: Example of construction of CPTs by Monte Carlo simulation

If Y is defined as a real-valued function of X_1 , X_2 , and X_3 , then the discrete interval states of Y must be defined over a range that contains all admissible values of Y for all combinations of the states of its parent nodes. Once the admissible range of Y has been determined, it must then be discretized into states representing mutually exclusive, collectively exhaustive intervals within this range. In many instances, certain interval states within the range of admissible values of Y will be found to be associated with a large amount of the posterior probability mass of Y . In those cases it is preferable to use a more refined discretization over the portions of the range associated with high probability mass. Note that the posterior PMF of Y will differ based on the evidence case considered. Because the posterior distribution of Y is not known a priori, it may be necessary to modify how Y is discretized after constructing the initial BN by considering representative evidence cases and studying the resulting posterior distributions of Y . Additional information on dynamic discretization is contained in other references, e.g., Neil et al. (2007).

If Y is defined using a classification function on X_1 , X_2 , and X_3 , then the states of Y are defined according to the classes associated with the classification function. An example of a classification function is a component damage function (e.g., a fragility model), which specifies a damage state given values of X_1 , X_2 , and X_3 that represent, for example, the demands placed on the component. It may be necessary to consolidate multiple classes if computational demands are of concern.

To demonstrate the generation of the CPT of Y , let Y be a deterministic function of random variables X_2 and X_3 with the form of the function defined by the categorical states of X_1 , i.e.,

$Y = f(X_1, X_2, X_3) = g_i(X_2, X_3)$ when $X_1 = x_1^i$ (where x_1^i indicates the i th categorical state of X_1). Note that the range of Y must include all admissible values of Y when considering all possible functional forms associated with the categories of X_1 . The conditional distribution of Y must be defined for each combination of the $m_1 * m_2 * m_3$ states of its parents. We use the convention that a combination of parent states corresponds to a column of the CPT associated with Y . Let x_i^j indicate the j th state of X_i , $i = 1, 2, 3$, and for $i = 2, 3$, let that state define the interval $[x_{i,L}^j, x_{i,U}^j]$. Consider the construction of the CPT of Y for a single combination of the states $X_1 = x_1^i$, $X_2 = x_2^j$ (which corresponds to an outcome of X_2 in the interval $[x_{2,L}^j, x_{2,U}^j]$ of the domain of the continuous random variable), and $X_3 = x_3^k$ (which corresponds to an outcome of X_3 in the interval $[x_{3,L}^k, x_{3,U}^k]$). To obtain the distribution of Y for this combination, N_{sim} draws are taken from distributions with probability density functions defined $f_{X_2}^j(x_2)$ and $f_{X_3}^k(x_3)$ within each of the respective intervals $[x_{2,L}^j, x_{2,U}^j]$ and $[x_{3,L}^k, x_{3,U}^k]$. For each draw, Y is computed using the functional form associated with x_1^i . Then, a normalized histogram is computed to obtain the required column of the CPT, with bins defined corresponding to the discrete interval states of Y specified based on its admissible range. Because X_2 is a root node, the form of its distribution is known. Therefore, the N_{sim} draws from within a particular interval for this variable can be taken from a normalized distribution with the correct shape. For example, suppose X_2 is distributed according to the probability density function $f_{X_2}(x_2)$. The N_{sim} draws for state x_2^j are taken from the renormalized distribution

$$f_{X_2}^j(x_2) = \frac{f_{X_2}(x_2)}{\int_{x_{2,L}^j}^{x_{2,U}^j} f_{X_2}(z) dz} \quad x_{2,L}^j < x_2 \leq x_{2,U}^j. \quad (2.8)$$

On the other hand, because X_3 has arbitrary parents, the functional form of its distribution is not known. As a result, it is suggested to sample uniformly from the interval $[x_{3,L}^k, x_{3,U}^k]$. An exception to this rule is when an interval is located in the tail of the distribution of X_3 and extends to $-\infty$ or $+\infty$. In that case, an exponential distribution over the infinite interval may be used to better capture the tail behavior. The reader is referred to Straub (2009) for additional details.

2.2.3 Inference in Bayesian networks

There are three principal tasks that can be performed using BNs: (1) probabilistic inference of unobserved values given evidence, (2) parameter learning, and (3) structure learning.

Probabilistic inference in BNs begins with a complete model of random variables and their probabilistic dependencies, typically defined using expert knowledge of causal relations, engineering judgment, physical models, or predefined empirical relationships. It may be viewed conceptually as the efficient application of Bayes' rule on a large scale when a problem contains complex dependencies. That is, the distributions of a subset of variables in the BN are updated given observations on another subset of variables in the model. The use of the word *inference* comes from the notion that "the probability of a cause can be inferred when its effect has been observed" (Kjaerulff and Madsen 2008).

Parameter and structure learning are data-driven processes. In parameter learning, conditional distributions in the BNs have unknown parameters that are estimated from data so as to maximize their likelihood, e.g., using the expectation-maximization algorithm (Moon 1996). In structure learning, the topological form of the BN is not known a priori, as is the case when BNs are used for probabilistic inference or parameter learning. In structure learning, algorithms are used to determine the topology of the BN, i.e., where and in which direction arrows exist between nodes (Heckerman 2008). In the applications considered in this study, BNs are used for probabilistic inference, with probabilistic relationships between variables determined using physical and empirical models as well as engineering judgment. Observations are then used to update these prior assumptions.

Probabilistic inference in BNs takes two forms: forward (predictive) analysis and backward (diagnostic) analysis. Forward analysis calculates the probability distribution of any node in the BN based on the assumed prior marginal PMFs of the root nodes and the conditional PMFs of all other nodes. Backward analysis involves computing the posterior probability distribution of any node given observations on one or more nodes in the BN, i.e., instantiation of any subset of the variables to one or more of their admissible values (Bobbio et al. 2001). Although many techniques can perform forward analysis, the true power in using BNs comes from the ease with which they facilitate information updating, i.e., backward analysis.

Bayesian networks efficiently compute the conditional distribution of any subset \mathbf{X}' of the variables, given evidence about the states of any other subset \mathbf{X}^e of the variables. The ease with which BNs facilitate the calculation of the conditional distribution $p(\mathbf{X}'|\mathbf{X}^e = \mathbf{x}^e)$ is the main feature that so well suits the BN framework for near-real-time seismic risk assessment and decision support. For example, suppose observations have been made on nodes X_3 and X_5 in Figure 2.1 and that the conditional distribution $p(x_2|X_3 = x_3, X_5 = x_5)$ is of interest. This posterior distribution can be computed by first marginalizing the joint distribution in Equation (2.7) to obtain the joint distributions over subsets of the variables:

$$\begin{aligned}
 p(x_2, x_3, x_5) &= \sum_{x_1, x_4} p(x_1, \dots, x_5) \\
 p(x_3, x_5) &= \sum_{x_1, x_2, x_4} p(x_1, \dots, x_5).
 \end{aligned}
 \tag{2.9}$$

The desired conditional distribution is then obtained as

$$p(x_2|X_3 = x_3, X_5 = x_5) = \frac{p(x_2, x_3, x_5)}{p(x_3, x_5)}.
 \tag{2.10}$$

Although it is possible to obtain updated distributions as shown above, this is not a computationally efficient approach to perform probabilistic inference in nontrivial BNs. Instead, *inference engines or algorithms* are available that efficiently perform calculations in BNs, including exact and approximate methods. In general, exact inference in BNs is an NP-hard (nondeterministic polynomial-time hard) task (Cooper 1990). Because a rigorous explanation of NP-hard is outside the scope of this study (see Wilson 2010 for an intuitive explanation), we simply point out that classifying a problem as NP-hard implies that it does not have a structure that will, in general, lead to a solution in a reasonable amount of time. Heuristics can make many NP-hard problems tractable by looking for patterns or structure. Tools for solving NP-hard problems often include multiple heuristics because it is uncommon that a single heuristic works for all classes of problems. Furthermore, heuristics often slow the search for a solution (Wilson 2010). Many BN algorithms use heuristics to find a structure in the BN and aid the discovery of a more optimal elimination ordering.

Exact inference in a complex and densely connected BN with many nodes may require an intractably large amount of computer memory and/or computation time. In response to the computational demands of exact inference, approximate algorithms have been developed. These methods include: approximations to exact algorithms, e.g., bounded conditioning (Horvitz et al. 1989) and mini-bucket elimination (Dechter and Rish 2003); variational approaches (Jordan et al. 1999); and sampling-based procedures such as likelihood weighting (Fung and Chang 1990; Shachter and Peot 1990), Markov-chain Monte Carlo methods (MacKay 1999), and importance-sampling (Yuan and Druzdzel 2006). Variational approaches provide bounds on the probabilities of interest using approximation procedures that take advantage of known phenomena to simplify graphical models, but for general BNs with unique and complex dependencies, derivations of variational approximations may be difficult (Jordan et al. 1999). More common approximation algorithms are based on stochastic sampling. In theory, sampling-based procedures converge to the true solution given a sufficiently large sample. In general, sampling methods offer good performance for forward analysis. However, with many sampling-based algorithms, backward analysis often yields poor convergence, particularly when evidence is entered into the BN that is a priori unlikely. Recent advances in use of importance sampling for inference in BNs increase the accuracy of sampling algorithms for both forward and backward analysis without significant degradation in convergence times (Cheng and Druzdzel 2000; Yuan and Druzdzel 2006).

Given the shortcomings of many approximate methods, particularly in lieu of unlikely evidence scenarios, we focus here on exact inference algorithms. Exact inference algorithms predominate in multipurpose BN software (Hugin Expert A/S 2008), although sampling algorithms are also used in some packages (DSL 2007). Murphy (2007, 2010) describes and compares BN software packages. Though we focus on exact algorithms here, it is anticipated that sampling algorithms will become more robust and more commonly used as an inference tool in the future. The results of this study, though focused primarily on exact inference, should also be useful when dealing with approximate inference procedures, as some of the same problems are encountered. For example, nodes with many parents result in large CPTs that must be stored in memory, posing problems to both exact and approximate inference algorithms. The memory problem, which becomes especially acute when working with large infrastructure systems, is one of the issues addressed in this study.

2.2.3.1 The elimination algorithm

One of the most basic exact inference algorithms is the *elimination algorithm*, which is also known as the *variable* or *bucket elimination algorithm*. While not used heavily in practice, it forms a basis for other, more efficient algorithms. The elimination algorithm determines the distribution of a subset of random variables in the BN by incrementally eliminating nodes from the BN that do not belong to the subset of interest. The elimination of a node has both a mathematical and a graphical interpretation.

Mathematically, elimination of a node corresponds to summing the joint distribution of the random variables over all states of the node to be eliminated. Consider the BN in Figure 2.1 with the joint distribution in Equation (2.7) and suppose that the joint distribution of X_3 and X_4 is of interest. The nodes X_1 , X_2 , and X_5 must be eliminated from the BN to obtain this quantity. Thus, the joint distribution must be summed over all states of X_1 , X_2 , and X_5 . The elimination of X_1 results in the joint distribution of the remaining variables X_2, \dots, X_5 :

$$\begin{aligned}
 p(x_2, x_3, x_4, x_5) &= \sum_{x_1} p(x_5|x_4)p(x_4|x_1)p(x_3|x_1, x_2)p(x_1)p(x_2) \\
 &= p(x_5|x_4)p(x_2) \sum_{x_1} p(x_4|x_1)p(x_3|x_1, x_2)p(x_1) \quad (2.11) \\
 &= p(x_5|x_4)p(x_2)\phi(x_4, x_3, x_2).
 \end{aligned}$$

Note that the summation operator in the second line of Equation (2.11) has been moved as far to the right as possible. This means that the summation need only be performed over the product of CPTs that include the variable X_1 . The result of the sum is a table or *potential* over the remaining variables: $\phi(x_4, x_3, x_2) = p(x_3, x_4|x_2)$. Figure 2.4 shows an example of the mechanics of computing the product of CPTs and performing the summation required to determine the potential $\phi(x_4, x_3, x_2)$ in Equation (2.11). For the sake of simplicity, each variable is assigned only two states.

conditional probability tables

$p(x_4 x_1)$		
	$x_{1,1}$	$x_{1,2}$
$x_{4,1}$	0.2	0.3
$x_{4,2}$	0.8	0.7

$p(x_1)$	
$x_{1,1}$	0.35
$x_{1,2}$	0.65

$p(x_3 x_1,x_2)$				
	$x_{2,1}$		$x_{2,2}$	
	$x_{1,1}$	$x_{1,2}$	$x_{1,1}$	$x_{1,2}$
$x_{3,1}$	0.4	0.1	0.25	0.45
$x_{3,2}$	0.6	0.9	0.75	0.55

compute product of CPTs containing X_1



$p(x_4 x_1)*p(x_1)*p(x_3 x_1,x_2)$								
	$x_{2,1}$				$x_{2,2}$			
	$x_{3,1}$		$x_{3,2}$		$x_{3,1}$		$x_{3,2}$	
	$x_{4,1}$	$x_{4,2}$	$x_{4,1}$	$x_{4,2}$	$x_{4,1}$	$x_{4,2}$	$x_{4,1}$	$x_{4,2}$
$x_{1,1}$	0.028	0.112	0.042	0.168	0.018	0.070	0.053	0.210
$x_{1,2}$	0.020	0.046	0.176	0.410	0.088	0.205	0.107	0.250

sum over states of X_1



$\phi(x_2, x_3, x_4)$							
$x_{2,1}$				$x_{2,2}$			
$x_{3,1}$		$x_{3,2}$		$x_{3,1}$		$x_{3,2}$	
$x_{4,1}$	$x_{4,2}$	$x_{4,1}$	$x_{4,2}$	$x_{4,1}$	$x_{4,2}$	$x_{4,1}$	$x_{4,2}$
0.048	0.158	0.218	0.578	0.105	0.275	0.160	0.460

Figure 2.4: Mechanics of computing $\phi(x_2, x_3, x_4)$

Next, consider the graphical interpretation of the elimination algorithm. The first step in graphical elimination is to create a *moral graph* through a process known as *moralization*. In the moral graph, nodes that share a common child (e.g., nodes X_1 and X_2 in Figure 2.1) are connected by adding an undirected link, in a process referred to as *marrying parents*. Then, all directed links in the graph are turned into undirected links. The moral graph corresponding to the BN in Figure 2.1 is shown in Figure 2.5a. The link introduced due to moralization is shown by a dashed line.

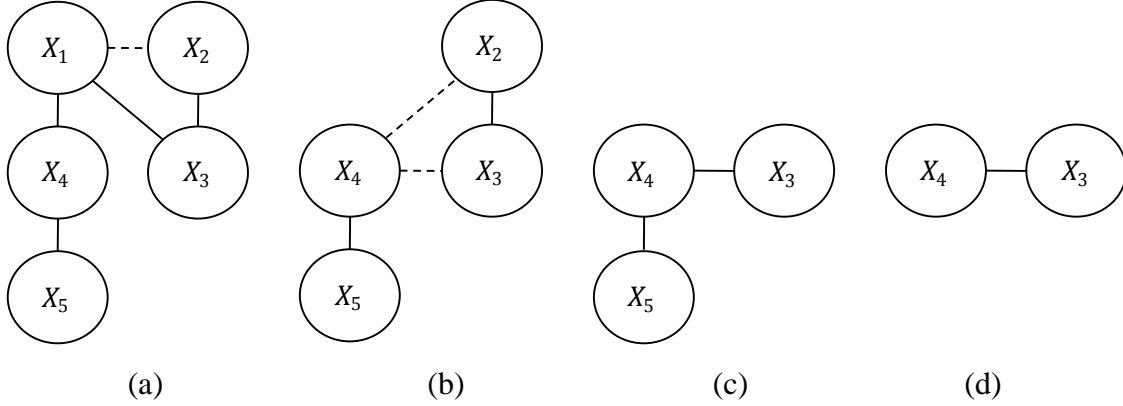


Figure 2.5: Graphs obtained during elimination algorithm: (a) moral graph corresponding to BN in Figure 2.1; graphs after elimination of (b) node X_1 , (c) node X_2 , and (d) node X_5

Next, node X_1 is eliminated from the BN as shown in Figure 2.5b. The graphical elimination of a node requires that all neighbors of the eliminated node be connected by undirected links (if they are not already connected). In Figure 2.5a, node X_1 has nodes X_2 , X_3 , and X_4 as neighbors. When X_1 is eliminated, undirected links are introduced between nodes X_2 and X_4 as well as X_3 and X_4 (Figure 2.5b). This connectivity is reflected mathematically in the potential in Equation (2.11) which contains variables X_2 , X_3 , and X_4 , though they did not exist together in a single CPT in the original joint distribution in Equation (2.7).

The above process is repeated for the elimination of X_2 and X_5 , resulting in the graphs in Figure 2.5c and Figure 2.5d, respectively. The corresponding mathematical operations are given below.

$$\begin{aligned}
 p(x_2, x_3, x_4, x_5) &= p(x_5|x_4)p(x_2)\phi(x_4, x_3, x_2) \\
 p(x_3, x_4, x_5) &= p(x_5|x_4) \sum_{x_2} p(x_2)\phi(x_4, x_3, x_2) \\
 &= p(x_5|x_4)\phi(x_3, x_4) \\
 p(x_3, x_4) &= \phi(x_3, x_4) \sum_{x_5} p(x_5|x_4) \\
 &= \phi(x_3, x_4)(\phi(x_4) = 1)
 \end{aligned} \tag{2.12}$$

Note that in performing this elimination algorithm, the product over all CPTs defining the joint distribution (as in Equation (2.7)) was not required. By requiring local products only over CPTs

containing the variable to be eliminated, memory demands are reduced. The order of computational complexity of the elimination algorithm is a function of the dimension of the largest potential that must be computed at any step and as reflected, in part, by the number of links added at any step. The larger the dimensions of the CPTs/potentials that must be multiplied, the larger the memory demand. Thus, to reduce computational demand it is necessary to keep the dimension of CPTs as small as possible. This is done by ensuring that nodes have as few parents as possible or by reducing the number of states associated with each node. More generally, the graphical structure of the BN can also result in large potentials being created during the elimination process.

The order in which the variables are eliminated significantly affects the size of the CPTs/potentials that must be multiplied at each stage of the elimination algorithm. In the above example, the largest memory demand comes from the product of three CPTs (involving four nodes) when eliminating X_1 : $p(x_4|x_1)p(x_3|x_1, x_2)p(x_1)$. If, instead, X_5 is eliminated first, the X_2 and then X_1 , the number of variables in the products involved is no more than three at any step:

$$\begin{aligned}
p(x_1, x_2, x_3, x_4) &= \sum_{x_5} p(x_5|x_4)p(x_4|x_1)p(x_3|x_1, x_2)p(x_1)p(x_2) \\
&= p(x_4|x_1)p(x_3|x_1, x_2)p(x_2)p(x_1) \sum_{x_5} p(x_5|x_4) \\
&= p(x_4|x_1)p(x_3|x_1, x_2)p(x_2)p(x_1)(1) \\
p(x_1, x_3, x_4) &= p(x_4|x_1)p(x_1) \sum_{x_2} p(x_3|x_1, x_2)p(x_2) \\
&= p(x_4|x_1)p(x_1)\phi(x_3, x_1) \\
p(x_3, x_4) &= \sum_{x_1} p(x_4|x_1)p(x_1)\phi(x_3, x_1) \\
&= \phi(x_3, x_4).
\end{aligned} \tag{2.13}$$

The graphical interpretation of the calculations in Equation (2.13) is shown in Figure 2.6. Only two additional links are introduced, one of which is introduced in the moralization step. Note that links introduced during the moralization step are governed by the structure of the BN and not by the elimination order. This demonstrates that the order in which variables are eliminated has a

significant impact on the computational demand. However, for complex BNs, determination of the optimal elimination order is NP-hard, therefore in practice heuristics and sampling-based procedures are used to determine the best elimination order. Dechter (1996) presents additional details on the elimination algorithm.

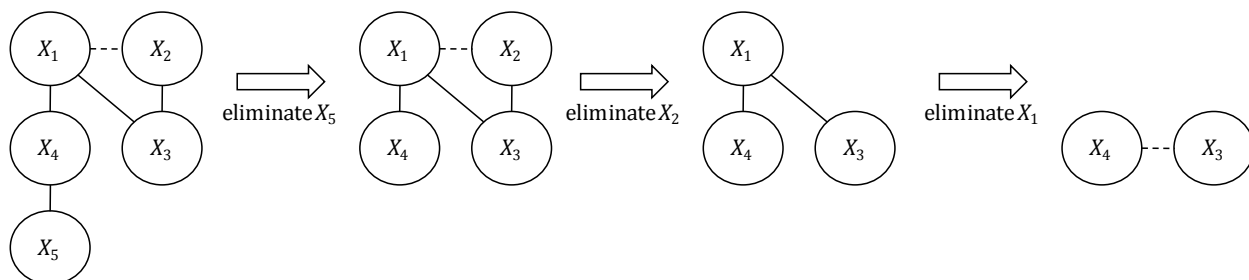


Figure 2.6: Illustration of the elimination algorithm for the BN in Figure 2.1 using elimination order X_5, X_2, X_1, X_3, X_4

The elimination algorithm is “query sensitive,” i.e., the entire algorithm must be rerun for each quantity of interest. This is because the nodes corresponding to this quantity must be the only nodes not eliminated and therefore must be the last ones in the elimination order. In the above example, if we were next interested in the joint distribution of X_1 and X_5 given $X_4 = x_4$, the algorithm would need to be performed again. The calculations used to compute the joint distribution of X_3 and X_4 are of no use for determining the joint distribution of X_1 and X_5 . Thus, the elimination algorithm is efficient from the viewpoint of computer memory, but inefficient in terms of computation time because it does not reuse computations when considering different combinations of evidence or desired posterior distributions. An alternative option that facilitates such reuse is the junction tree algorithm, described next.

2.2.3.2 The junction tree algorithm

The junction tree algorithm (JTA) can be thought of as a generalization of the elimination algorithm. It creates a data structure known as a junction tree, which contains subsets of random variables in the BN known as *cliques*. These cliques are reused to facilitate efficient inference for many quantities of interest without rerunning the algorithm.

Like the elimination algorithm, the JTA begins with a moral graph and specification of the elimination order. In the JTA, nodes are eliminated schematically and links are introduced to

record induced relations, but summations are not performed. Instead, cliques and clique potentials are recorded as each node is eliminated. The recorded cliques and associated potentials are used to create the junction tree. When a node is eliminated, the clique that is formed consists of the eliminated node and its neighbors. A single junction tree is constructed to facilitate inference for all quantities of interest. However, the structure of this junction tree depends on the elimination order used to construct it.

Consider the simple BN in Figure 2.1 and specify the elimination order: X_4, X_1, X_5, X_3, X_2 . In first eliminating X_4 , a clique is formed containing X_4 and its neighbors X_1 and X_5 , as shown by a box with dashed lines in the second diagram in Figure 2.7. Assuming that all nodes have 10 states, the size of the potential associated with this clique is 10^3 . As in the elimination algorithm, the neighbors of X_4 are connected after it is eliminated from the BN. Next, X_1 is eliminated, creating a clique consisting of itself and its neighboring nodes. The clique comprising nodes X_1, X_2, X_3 , and X_5 is shown in the third diagram of Figure 2.7. The size of the associated clique potential is 10^4 (once again assuming 10 states per node). In eliminating the remaining nodes, no additional cliques must be recorded because they contain nodes that all occur together as a subset of a previously created clique.

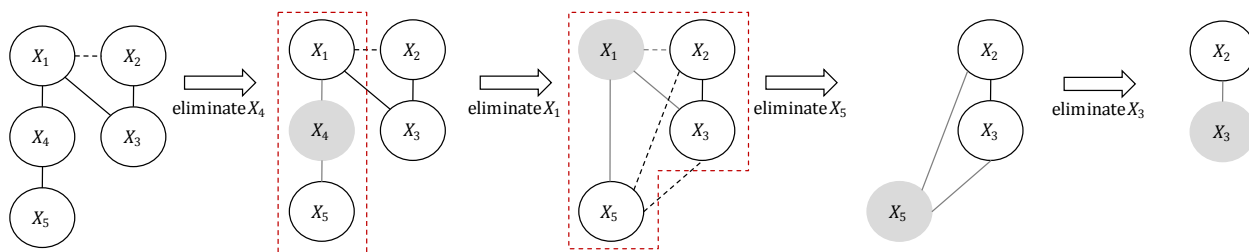


Figure 2.7: Illustration of clique creation using the BN in Figure 2.1 with elimination order X_4, X_1, X_5, X_3, X_2

The junction tree resulting from the above elimination order consists of two cliques and is shown in Figure 2.8. Each clique is shown in an oval with a *separator set* shown as a rectangle. The separator set assigned to each branch of a junction tree includes nodes that are in common to the cliques at the ends of the branch. This junction tree can now be used to answer any probabilistic inquiry on the variables within the BN.

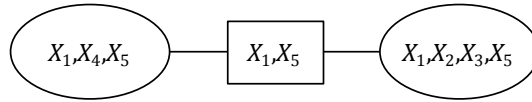


Figure 2.8: Junction tree for BN in Figure 2.1 with elimination order X_4, X_1, X_5, X_3, X_2

If, instead, the elimination order X_5, X_4, X_2, X_3, X_1 is used to create an alternate junction tree, the size of the largest clique created is smaller. This elimination order is the optimal order, which can be found because the dimension of the problem is small. Figure 2.9 shows the cliques formed as nodes are eliminated in this order, and Figure 2.10 shows the corresponding junction tree.

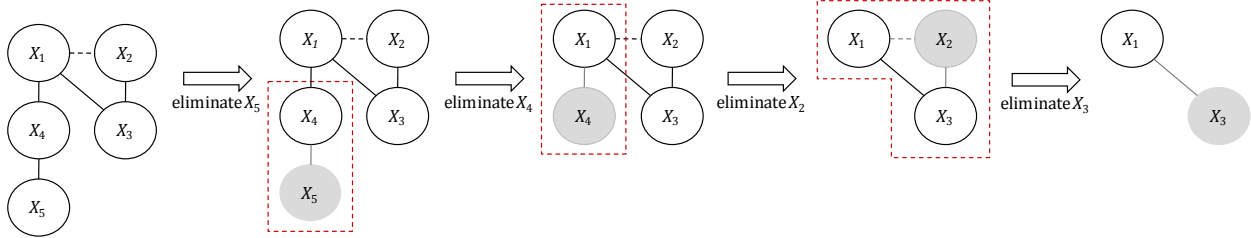


Figure 2.9: Illustration of cliques created using the BN in Figure 2.1 with elimination order X_5, X_4, X_2, X_3, X_1

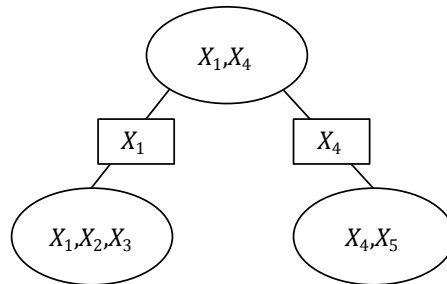


Figure 2.10: Junction tree for BN in Figure 2.1 with elimination order X_5, X_4, X_2, X_3, X_1

A junction tree is constructed that maintains three properties: (1) the graph is singly connected, with only one path between each pair of cliques; (2) each clique created when performing elimination must exist in the tree or be a subset of another clique; and (3) if a pair of cliques C_i and C_j both contain node X_k , then each clique on the path between C_i and C_j must also contain X_k (Paskin 2003).

Propagation of probabilistic information in a junction tree to obtain posterior distributions on all variables uses a message-passing algorithm involving the bidirectional exchange of information between cliques by performing operations over the variables or nodes in the separator sets.

Specifically, the joint distribution of the variables that exist in two adjacent cliques is equal to the product of the clique potentials divided by the separator potentials (Friis-Hansen 2004). A detailed explanation of the mechanics of this propagation algorithm can be found in textbooks (e.g., Jensen and Nielsen 2007), but for purposes of this study it is only necessary to understand how the growth in computational complexity is related to the sizes of cliques. In particular, two measures of computational complexity are used in this study: (1) the largest clique table size, which is the size of the potential associated with the largest clique in the junction tree, and (2) the total clique table size, which is the sum of the sizes of all potentials associated with cliques in a junction tree. For the junction tree in Figure 2.10, the largest clique contains X_1, X_2, X_3 . Assuming 10-state nodes, its potential has size 10^3 . The total clique table size for the junction tree is $10^3 + 10^2 + 10^2$, where 10^2 is the size of the potentials of the two-node cliques. Note that the size of the largest clique table has a dominating contribution to the total clique table size. The memory demand associated with the junction tree based on the optimal ordering (Figure 2.10) is an order of magnitude smaller than that for the suboptimal ordering in Figure 2.7, which has a total clique table size of $10^4 + 10^3$. The order of computational complexity of the JTA is exponential in the size of the largest clique table for BNs with discrete nodes; for BNs with continuous Gaussian nodes, the order of computational complexity of the JTA is cubic in the size of the largest clique table (Paskin 2003).

2.3 Use of BNs in civil engineering applications

The use of BNs for engineering risk and reliability analysis has been growing in recent years, especially in certain topical areas. A literature survey by Medina Oliva et al. (2009) relating to the use of BNs for risk analysis, dependability, and maintenance modeling found that the use of BNs for dependability analysis was the largest portion of the literature (64%) and references focusing on risk analysis and maintenance applications were fewer (23% and 13%, respectively). The survey found that the use of BNs for dependability analysis increased by a factor of eight between 2001 and 2007, while the use of BNs for risk analysis increased by a factor of four and their application to maintenance increased by a factor of three over the same period.

The use of BNs for natural hazard assessment has likewise grown. For example, Straub (2005) presented a generic framework for assessing risks associated with natural hazards using BN and applied it to an example involving rockfall hazard. BNs have also been applied to the modeling of risks due to typhoon (Nishijima and Faber 2007) and avalanches (Grêt-Regamey and Straub 2006). The use of BNs for management of water resources and ecological risk was the subject of a special issue of the journal *Environmental Modeling and Software* (Castelletti and Soncini-Sessa 2007), with topics including sustainable withdrawal of water from aquifers, use of financial incentives to induce water-saving, and effects of environmental changes on fish populations. Smith (2006) used BNs to analyze geotechnical and hydrological risks posed to a single-embankment dam. BNs have also been used for assessing infrastructure risks posed by anthropogenic hazards (Jha 2006).

The use of BNs in seismic applications is relatively limited. Bayraktarli et al. (2005) outlined a general BN-based framework for earthquake risk management composed of three components: (1) an exposure model indicating hazard potential (e.g., ground motion intensity and associated return periods), (2) a vulnerability model indicating direct, immediate consequences of a particular hazard (e.g., distribution of component damage given an earthquake of a particular intensity), and (3) a robustness model to quantify indirect consequences. The paper did not address many of the details complicating the application of BNs to seismic hazard assessment that are treated in this study, e.g., efficient modeling of random fields or directivity and finite rupture effects. A continuation of this work by Bayraktarli et al. (2006) integrated the BN framework with a GIS-based system for considering large inventories of buildings. Because it focused on structural modeling, that paper also did not consider random field effects or issues associated with modeling performance of systems, thus its approach is not directly applicable to seismic risk assessment of infrastructure systems. However, the integration of the BN with GIS systems represents a novel and valuable technological integration that is particularly useful in near-real-time applications. Kuehn et al. (2009) used a learning algorithm to determine the “best” BN to model the joint probability distribution of ground motion, site, and earthquake parameters, directly using data from the Next Generation Attenuation (NGA) database (PEER 2005). Their result was a BN that models ground motion intensity at a single site as a function of source and site characteristics. It represents an alternative to regression-based methods such as those

developed under the NGA project (Abrahamson et al. 2008). Other applications of BNs to seismic hazard include liquefaction modeling (Bayraktarli 2006), tsunami early warning (Blaser et al. 2009), modeling stochastic dependence between earthquake occurrences (Agostinelli and Rotondi 2003), and post-earthquake consequence assessment (Faizian et al. 2005).

3. BN-Based Seismic Demand Models

3.1 Introduction

Being typically distributed over large geographic regions, infrastructure systems have a greater exposure to seismic hazard than single-site facilities and are subject to a wider range of hazards. Some of these effects are spatially distributed in nature and must be considered as random fields. For example, the ground motion intensity at distributed points throughout a geographic region constitutes a random field. Random field effects must be included to account for the statistical dependence between the seismic demands on components of the infrastructure system, particularly components near one another.

This chapter describes BN-based models for selected seismic hazards at discrete points in the domain of a geographically distributed infrastructure system. The focus is primarily on the hazard due to ground shaking. Intensity of ground shaking can be measured using a variety of metrics including: spectral acceleration (SA), peak ground acceleration (PGA), peak ground velocity (PGV), and peak ground displacement (PGD). The seismic performance of structural systems (e.g., buildings, bridges) is often expressed as a function of SA. Liquefaction hazard is typically expressed as a function of PGA. The performance of distributed components in an infrastructure system (e.g., pipelines, highway embankments) is typically defined based on PGV. Other metrics that are occasionally used (e.g., Arias intensity) are not considered in this study. Besides addressing ground shaking, this chapter also includes preliminary and less rigorous BN models for liquefaction-induced ground deformation and displacement due to fault rupture.

The chapter begins with a description of BN models for hazard due to ground shaking and briefly summarizes existing works. Next a more general model of ground motion intensity at different points in an infrastructure system is developed. Proposed models for point-source and finite-

rupture idealizations are presented, including formulations for including directivity effects. Finally, preliminary BN-based models for liquefaction and hazard due to fault rupture are developed.

3.2 Hazard due to ground shaking

A BN model of ground motion intensity can be constructed using physical relations and empirically derived ground motion prediction equations, also known as attenuation laws. These equations are based on regressions of observed data that relate ground motion intensity at a site to earthquake source and site characteristics (e.g., Abrahamson et al. 2008). Ground motion prediction equations typically have the form

$$\ln S_i = \ln \bar{S}_i + \varepsilon_m + \varepsilon_{r,i}, \quad (3.1)$$

where $\ln \bar{S}_i = f(M, R_i, \Theta_{st,i}, \Theta_{sc})$ is the natural logarithm of the median ground motion intensity at site i expressed as a function of the earthquake magnitude M , the distance between the site and earthquake source R_i , a vector of site properties $\Theta_{st,i}$ (e.g., site shear wave velocity, depth to significant impedance contrast); and a vector of source characteristics, Θ_{sc} (e.g., faulting mechanism); ε_m is an inter-event error term; and $\varepsilon_{r,i}$ is an intra-event error term. Both errors describe variability in the logarithmic intensity value $\ln S_i$ relative to the median $\ln \bar{S}_i$. The inter-event error term captures the variability from earthquake to earthquake that is common to all sites, and the intra-event error term captures the variability from site to site for a single earthquake. Both error terms are zero-mean and normally distributed. Furthermore, the $\varepsilon_{r,i}$ terms for different sites are correlated due to the random-field nature of the ground motion.

In developing the proposed BN, several challenges are encountered, including the need to account for the correlation structure of a random field and the effects of finite rupture and directivity. These issues are not addressed in the limited literature on application of BNs to seismic hazard assessment. After a review of existing work related to modeling hazard due to ground shaking, new and more general models are developed applicable to modeling ground motion intensity at sites distributed over a geographic region.

3.2.1 Existing models

Bayraktarli et al. (2005) presented a general BN framework for management of risks due to earthquakes. The framework consists of three components: (1) an exposure model representing the hazard potential (e.g., ground motion intensity associated with a particular return period), (2) a vulnerability model representing immediate consequences (e.g., structural damage) conditioned on an exposure event, and (3) a robustness model representing indirect consequences (e.g., loss of life) dependent on the vulnerability. The associated BN model is shown in Figure 3.1. The first of these, the exposure model, is pertinent to this chapter. The seismic demand measure considered in the study is spectral displacement. It is computed as a function of earthquake magnitude, source-to-site distance (modeled by the node *Earthquake Distance*), soil type, and the fundamental period of the structure, using a software application that provides time histories consistent with a response spectrum obtained using the Boore et al. (1997) attenuation relationship. The authors made several simplifying assumptions in developing the exposure model, neglecting finite rupture and directivity effects and not explicitly accounting for uncertainties in the attenuation models. Their exposure model can thus be considered as a special case of the more comprehensive seismic demand model developed in this chapter.

Bayraktarli et al. (2006) expanded upon the model of Bayraktarli et al. (2005). The 2006 exposure model quantifies seismic demands using two intensity measures: spectral displacement (for estimating vulnerability of buildings) and peak ground acceleration (for estimating vulnerability of soils). The spectral displacement at a site is specified, as in the 2005 study, as a function of earthquake magnitude, source-to-site distance, fundamental period, and site class. The node *Earthquake Magnitude* is discretized into four states, each corresponding to a discrete magnitude value, with the probabilities specified using the Gutenberg-Richter magnitude-recurrence relationship (Gutenberg and Richter 1944). The node *Earthquake Distance* has four states, each corresponding to a single distance value. Distances are computed by assuming the earthquake source is a point. Peak ground acceleration is obtained from simulated time histories that are generated for combinations of magnitudes and distances.

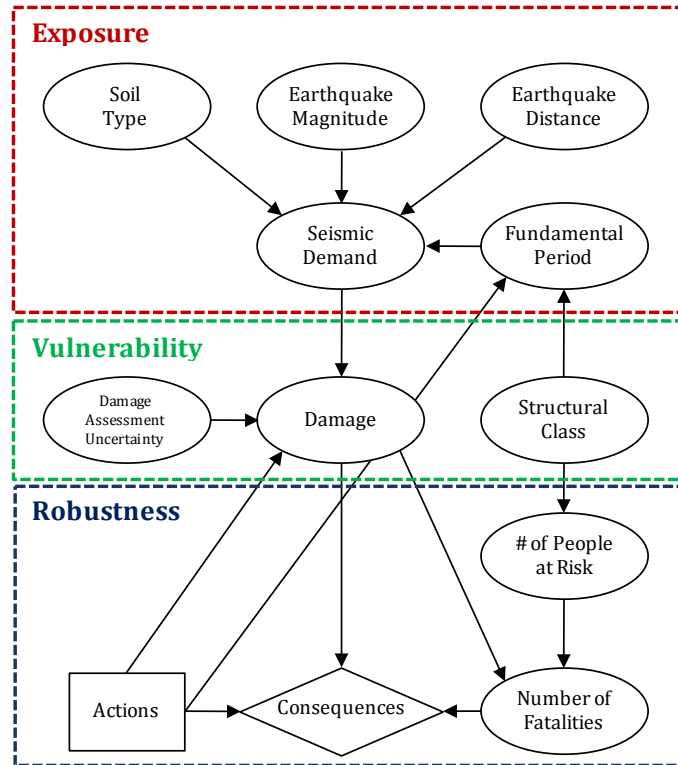
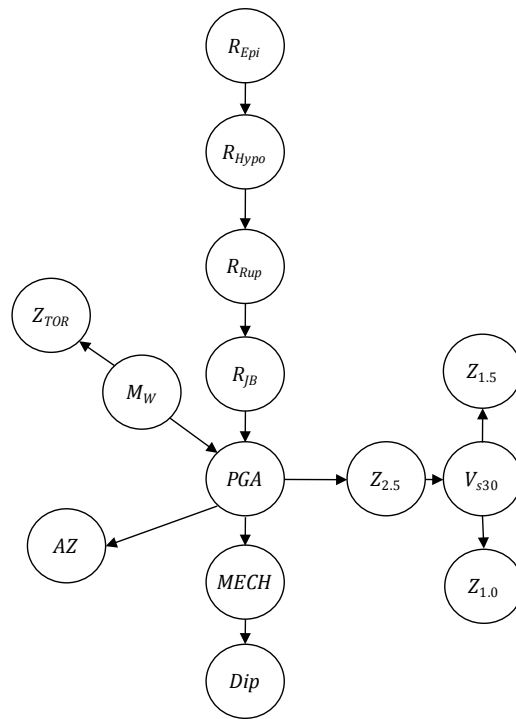


Figure 3.1: Bayraktarli et al. (2005) BN framework for seismic risk management

Kuehn et al. (2009) used structural learning to determine the “best BN topology” for modeling dependencies between ground motion intensity and source/site characteristics. The BN was learned directly from data available in the PEER NGA database (PEER 2005). Their approach offers an alternative to regression-based methods, such as those developed under the NGA project (Abrahamson et al. 2008). The resulting BN is shown in Figure 3.2 along with the definition of variables used in the model. Consistent with the NGA models, *PGA* is causally dependent on earthquake magnitude and source-to-site distance (Joyner-Boore distance). Furthermore, there is an induced relationship between all source-to-site distance measures that are available in the PEER NGA database and which appear in ground motion prediction equations. Although there are important intuitive similarities between the empirically and theoretically derived ground motion prediction equations and the learned BN, the directions of links in Figure 3.2 are not always consistent with the directions suggested by the mathematical form of the NGA models. For example, the BN in Figure 3.2 has a link going from *PGA* to $Z_{2.5}$, indicating that the depth to shear-wave velocity horizon of 2.5 km/s is probabilistically

dependent on PGA , which is not consistent with a causal interpretation. However, it is important to note that although BNs developed using a priori knowledge (e.g., physical models, empirical relations, and expert opinion) are typically constructed using a causal interpretation, BNs developed using structural learning algorithms need not reflect such an intuitive approach. The algorithms find dependencies that are likely to be consistent with the d-separation properties of the problem, as supported by data, rather than reflecting direct causality. Thus, the directed links between $Z_{2.5}$, $Z_{1.5}$, $Z_{1.0}$, and V_{s30} indicate probabilistic dependencies rather than causal relations.



- | | |
|---|--|
| PGA : horizontal peak ground acceleration (g) | R_{JB} : shortest distance from site to the horizontal projection of the rupture plane (Joyner-Boore distance) |
| M_W : moment magnitude | R_{Rup} : shortest distance from site to rupture plane (rupture distance) |
| $MECH$: focal mechanism of earthquake | AZ : source-site-azimuth (measure of directivity) |
| Dip : dip of the fault where the earthquake occurred | V_{s30} : Average shear-wave velocity in upper 30 meters |
| Z_{TOR} : depth-to-the-top-of-the-rupture of the earthquake | $Z_{1.0}$: Depth to shear-wave horizon of 1.0 km/s. |
| R_{Epi} : shortest distance from site to epicenter | $Z_{1.5}$: Depth to shear-wave horizon of 1.5 km/s. |
| R_{Hypo} : shortest distance from site to hypocenter | $Z_{2.5}$: Depth to shear-wave horizon of 2.5 km/s. |

Figure 3.2: Kuehn et al. (2009) BN of ground motion intensity obtained by structure learning

Several important observations follow from the form of the BN in Figure 3.2 that provide insight into variables affecting ground motion intensity (PGA) at a site. Notice that $Z_{2.5}$ mediates between PGA and V_{S30} . The d-separation properties of the learned BN indicate that, when the value of $Z_{2.5}$ is known, knowledge of V_{S30} supplies no additional information about the PGA. Kuehn et al. (2009) suggested that this observation supports claims that V_{S30} is not a good proxy for site effects. Similarly, the authors noted that variables DIP and Z_{TOR} , which have been incorporated in some of the most recent NGA models, are only indirectly related to PGA . As seen in Figure 3.2, the mediating variables M_w and $MECH$, when observed, d-separate Z_{TOR} and DIP from PGA . Last, notice that AZ , which is a measure of directivity, is a child of node PGA . As the authors noted, this suggests that directivity effects are present in the records of the NGA database. Kuehn et al. (2009) also showed how the results obtained from the BN can be used to generate hazard curves. However, as with Bayraktarli et al. (2005, 2006), the BN of Kuehn et al. (2009) is not directly applicable to describing correlated seismic demands on the components of a spatially distributed infrastructure system because it is formulated for evaluating a single site. To enable information updating in near-real time such that observations at one location in the system update the distributions of the ground motion intensity at other sites, it is necessary to include a model of the correlation of seismic demands. Furthermore, for highly redundant systems, neglecting correlation in demands results in an overestimation of the system reliability. These issues are addressed in the formulations developed in this chapter.

3.2.2 Proposed model

Here we describe a BN-based formulation for modeling seismic demands on an infrastructure system. It provides the distribution of ground motion intensity at discrete points in the geographic domain of a spatially distributed infrastructure system for a future earthquake of unknown characteristics on one of multiple potential seismic sources. We then develop models for characterizing the source as well as accounting for correlation in levels of ground motion intensity at spatially distributed locations.

We begin with the geometric derivations necessary to define the location of an earthquake on a fault and the consequent source-to-site distance for each site in the infrastructure system. The

ground motion intensity at each location is then defined as a function of the source-to-site distance, earthquake magnitude, and other factors. Finally, we extend the resulting seismic demand model to account for directivity effects.

3.2.2.1 Source characterization and source-to-site distance

Because existing works do not explicitly address issues related to source characterization and geometry, we develop physically derived representations for modeling earthquake source characteristics and idealized geometry that then lead to conditional definitions of the source-to-site distance. For all formulations, a fault is idealized as a straight line or a collection of contiguous straight line segments. More complex fault characterizations is left as an area of future study. A point-source model is presented first, followed by a finite-rupture source formulation.

3.2.2.1.1 Point-source model and formulation

The point-source assumption results in a topologically simple BN and relatively simple mathematical relations necessary to conditionally define the distance between the source and each site.

Consider the BN in Figure 3.3, which models source characteristics and source-to-site distances assuming an earthquake occurs as a point in space. This BN model is valid conditional on the occurrence of an earthquake. The highest level root node in the BN, S_C , represents the source of the earthquake and is an ancestor to all other nodes in the BN. The marginal probability table assigned to node S_C defines the probability that an earthquake in the region occurs on each of the sources included in the model. This probability is obtained as a function of the mean rate of occurrence of earthquakes of engineering significance on each source. Let ν_j define this mean rate for source j . Then

$$P(\text{earthquake on source } j | \text{earthquake has occurred}) = \frac{\nu_j}{\sum_{k=1}^{N_{sc}} \nu_k} \quad (3.2)$$

where N_{sc} denotes the number of seismic sources included in the model.

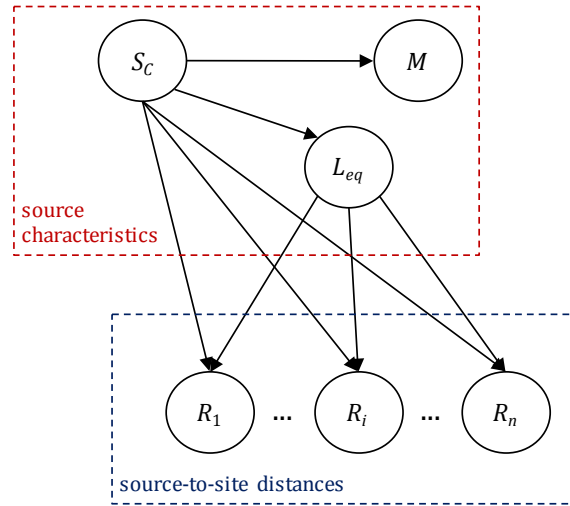


Figure 3.3: BN model of point-source characteristics and source-to-site distances

Node M , representing earthquake magnitude, is a child of S_c , indicating that the probability of experiencing an earthquake of a certain magnitude differs depending on the source. This is consistent with most earthquake magnitude recurrence relationships. Furthermore, the largest earthquake magnitude generated by a source depends on the size of the source. Common magnitude-recurrence relations include the truncated Gutenberg-Richter law and the characteristic earthquake model (Gutenberg and Richter 1944; Youngs and Coppersmith 1985). (Throughout this study, all references to the magnitude of an earthquake should be taken to mean the moment magnitude.) Although node M has no children, it is included in the BN because it will be used in later descriptions. Care should be taken when discretizing M because the energy released by an earthquake increases exponentially with the magnitude. Specifically, a one-unit increase in moment magnitude is associated with approximately 30 times more energy; an increase by a value of two is associated with a three-order of magnitude increase in energy. Thus, the difference in energy released between $M = 8.5$ and $M = 9.0$ is much larger than the difference between $M = 4.5$ and $M = 5.0$. For this reason, it is recommended to use smaller discretization intervals at larger magnitude values.

In Figure 3.3, node L_{eq} represents the point-source location of the earthquake. L_{eq} is a child of node S_c , indicating the dependence of the earthquake location on its source. In absence of contrary information, it is common to assume that the uncertain location of the earthquake is

uniformly distributed within each source. For analysis of earthquakes on each source, it is convenient to use a source-specific coordinate system. The location of seismic sources is often specified by latitude, longitude, and altitude. This information is easily converted to the Cartesian Earth-center Earth-fixed (ECEF) coordinate system (Clynch 2006). Then, a transformation into the local coordinate system for each source is necessary (described in Appendix 3.1 at the end of this chapter). Consider a line-fault idealization of the j th earthquake source. Using a source-specific coordinate system with the fault lying on the x -axis and the origin centered at one end of the fault (see Figure 3.4), the conditional distribution of the location of the earthquake is defined uniformly on the interval $[0, L_F^j]$, as described below.

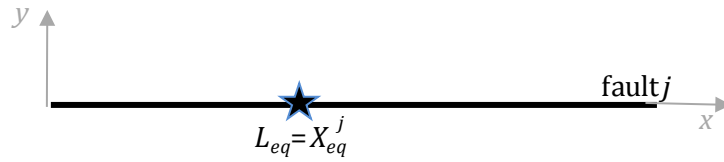


Figure 3.4: Fault-specific local coordinate system for line-fault idealization and point-source model

As mentioned earlier, in this study we choose to discretize all continuous random variables. When considering multiple sources, the states of L_{eq} must be defined to span the range $[0, \max L_F]$, where $\max L_F = \max_{i=1, \dots, N_{sc}} L_F^i$ and L_F^i is the length of fault i . The conditional PMF of L_{eq} for all sources with $L_F^i < \max L_F$ has zero values for states with $L_{eq} > L_F^i$. For illustration, consider two faults with lengths of 5 and 8 units (in an arbitrary unit system). Crudely discretize L_{eq} into four states: $[0,2]$, $[2,4]$, $[4,6]$, and $[6,8]$. Assuming that L_{eq} is equally likely to occur anywhere within each fault, the source-dependent distributions of L_{eq} are shown in Figure 3.5. Note that for source 1, the last state, $[6,8]$, is associated with zero probability mass and that the probability mass associated with state $[4,6]$ is half of the mass associated with lower states. This is because the length of source 1 (5 units) falls halfway within the third interval state.

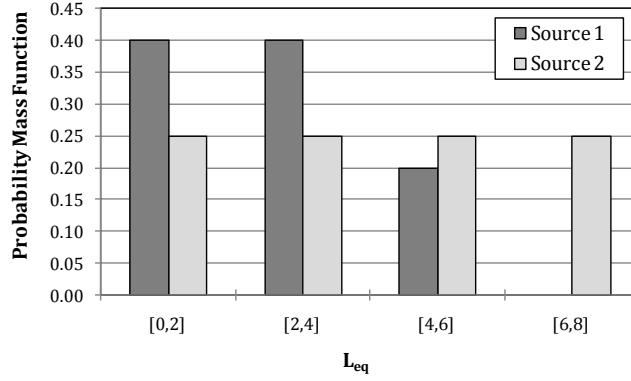


Figure 3.5: Source-dependent distribution of L_{eq} for example

To account for differences in fault length, the source-dependent PMF for L_{eq} is defined using the expression

$$P_{L_{eq}}^{(j,k)} = \left\{ \mathbb{I} \left[0 < L_{eq,U}^{(k)} \cap L_{eq,U}^{(k)} < L_F^j \right] \left(\frac{L_{eq,U}^{(k)}}{L_F^j} \right) + \mathbb{I} \left[L_F^j < L_{eq,U}^{(k)} \right] \right\} \quad (3.3)$$

$$- \left\{ \mathbb{I} \left[0 < L_{eq,L}^{(k)} \cap L_{eq,L}^{(k)} < L_F^j \right] \left(\frac{L_{eq,L}^{(k)}}{L_F^j} \right) + \mathbb{I} \left[L_F^j < L_{eq,L}^{(k)} \right] \right\},$$

where $P_{L_{eq}}^{(j,k)}$ is the probability mass associated with the k th state of node L_{eq} , given an earthquake on source j . The k th state of L_{eq} is associated with the interval $[L_{eq,L}^{(k)}, L_{eq,U}^{(k)}]$ consistent with the notation convention used previously. $\mathbb{I}[a]$ is an indicator variable defined such that $\mathbb{I}[a] = 1$ if a is true and $\mathbb{I}[a] = 0$ if a is false. Equation (3.3) is based on the assumption that the earthquake is equally likely to occur anywhere along a fault.

The distance between site i and the location of the point-source earthquake on fault, R_i^j , is easily computed in the source-specific coordinate system as

$$R_i^j = \sqrt{(x_{s,i}^j - X_{eq}^j)^2 + (y_{s,i}^j)^2 + (z_{s,i}^j)^2}, \quad (3.4)$$

where $x_{s,i}^j$, $y_{s,i}^j$ and $z_{s,i}^j$ are the x -, y -, and z -coordinates of site i in the coordinate system defined by source j . X_{eq}^j is the coordinate of the earthquake source (L_{eq}) along the x -axis in the j th

source-specific coordinate system (see Figure 3.4). Nodes representing the distance between site i and an earthquake on source j are shown in Figure 3.3. Nodes corresponding to the site coordinates are not shown because, for a given source, they are considered deterministic. The CPTs of nodes R_i are defined based on the above relations using Monte Carlo simulation.

For infrastructure systems distributed over large areas, sometimes it is necessary to model bends in faults. For this purpose we extend the above formulation for a fault idealize as a continuous set of multiple line segments. The BN in Figure 3.3 does not change for such a fault. Only the relations required to construct the CPTs must be revised.

Figure 3.6a shows a three-segment fault defined by the four points $\mathbf{P}_{f,i} = (x_{f,i}, y_{f,i}, z_{f,i})$, $i = 0, \dots, 3$, in three-dimensional space. Again we convert latitude/longitude/altitude data to ECEF coordinates, then shift the origin of the coordinate system to one end of the source, and finally orient the coordinate system such that the x -axis lies along the first fault segment. For convenience, the superscript j , which previously denoted the source index, is dropped in the following description. It is assumed that all points are defined within the coordinate system associated with the fault on which the earthquake occurs.

Define N_{seg} as the number of discrete segments comprising the fault and $l_{f,i}$, $i = 1, \dots, N_{seg}$, as the length of the i th segment computed using the coordinates of the segment ends:

$$l_{f,i} = \sqrt{(x_{f,i} - x_{f,i-1})^2 + (y_{f,i} - y_{f,i-1})^2 + (z_{f,i} - z_{f,i-1})^2}. \quad (3.5)$$

It follows that the total length of the fault is $L_F = \sum_{i=1}^{N_{seg}} l_{f,i}$. Consider that the segments of the fault are aligned to form a single straight line of length L_F , as illustrated in Figure 3.6b. A one-to-one mapping exists between the location of the point source in space, $\mathbf{P}_{eq} = (X_{eq}, Y_{eq}, Z_{eq})$, and the coordinate X'_{eq} on the x' -axis. This coordinate is represented by node L_{eq} in the BN in Figure 3.3. X'_{eq} is assumed to be distributed uniformly on the interval $[0, L_F]$ unless information supports a different assumption. For each state of L_{eq} (i.e., each value of X'_{eq}), the source-to-site distance, R_i , is computed as follows. First, compute the coordinates of the earthquake point-source \mathbf{P}_{eq} as a function of X'_{eq} :

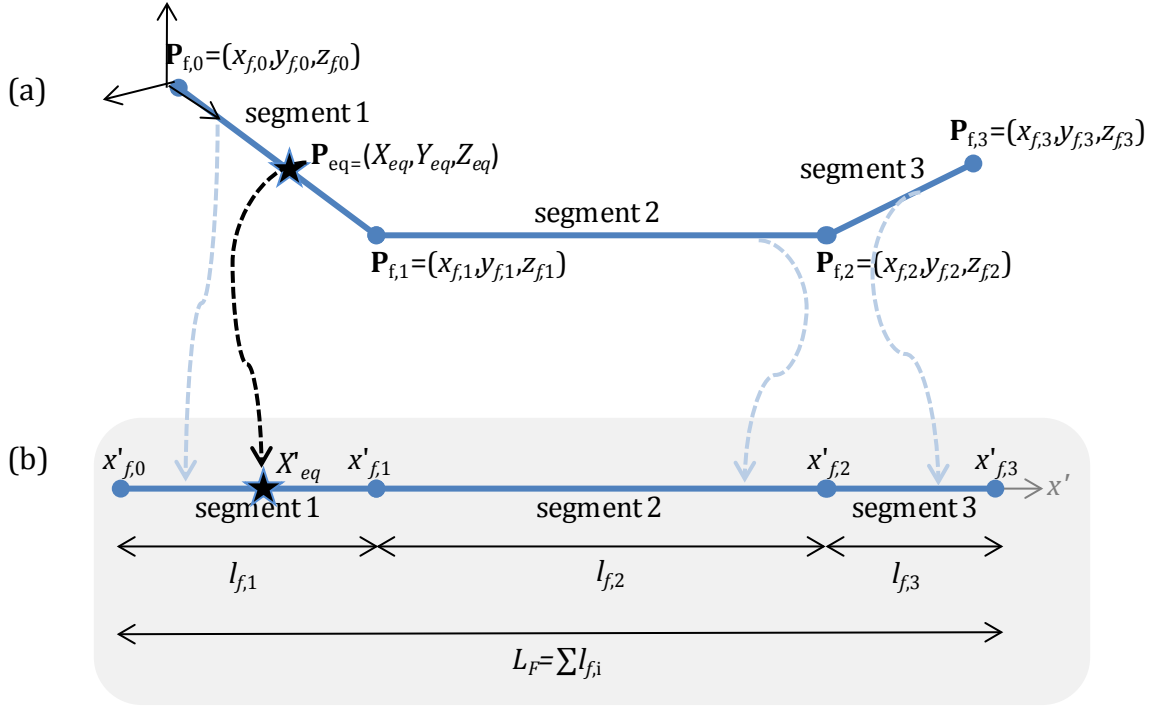


Figure 3.6: Illustration of (a) multisegment fault in three-dimensional space and (b) alignment of all fault segments consecutively along the x' -axis

$$\mathbf{P}_{eq} = \sum_{i=1}^{N_{seg}} \mathbb{I}[x'_{f,i-1} \leq X'_{eq} < x'_{f,i}] \left(\mathbf{P}_{f,i-1} + (X'_{eq} - x'_{f,i-1}) \frac{\mathcal{D}(\mathbf{P}_{f,i-1}, \mathbf{P}_{f,i})}{|\mathcal{D}(\mathbf{P}_{f,i-1}, \mathbf{P}_{f,i})|} \right), \quad (3.6)$$

where $\mathbb{I}[a]$ is again an indicator variable defined such that $\mathbb{I}[a] = 1$ if a is true and $\mathbb{I}[a] = 0$ otherwise, $x'_{f,i} = \sum_{j=1}^i l_{f,j}$ and $x'_{f,0} = 0$. $\mathcal{D}(\mathbf{P}_{f,i-1}, \mathbf{P}_{f,i})$ is a direction vector defined as

$$\mathcal{D}(\mathbf{P}_{f,i-1}, \mathbf{P}_{f,i}) = \begin{bmatrix} x_{f,i} - x_{f,i-1} \\ y_{f,i} - y_{f,i-1} \\ z_{f,i} - z_{f,i-1} \end{bmatrix}. \quad (3.7)$$

Given the location of the earthquake point source in three-dimensional space, the source-to-site distance is computed as

$$R_i = \sqrt{(x_{s,i} - X_{eq})^2 + (y_{s,i} - Y_{eq})^2 + (z_{s,i} - Z_{eq})^2}. \quad (3.8)$$

The CPTs of the nodes in Figure 3.3 are defined based on the above relationships using Monte Carlo simulation as described in Section 2.2.2.

The above relations permit the use of multi-segment fault idealizations without complicating the topology of the BN. Because multi-segment faults do not change the topology of the BN, they do not impose a computational penalty unless the number of states associated with any node needs to be increased as a result of including the bends in faults.

3.2.2.1.2 Finite-rupture model and formulation

Consider the more realistic idealization of an earthquake as a finite rupture on the fault rather than a single point. We begin again with the special case in which a fault is idealized as a straight line. The source-specific local coordinate system has the fault oriented along the x -axis and its left end at the origin (Figure 3.7). In this coordinate system, the epicenter is defined as a point on the fault. The rupture is assumed to occur anywhere along the fault with uniform likelihood, while containing the epicenter and not extending beyond the known ends of the fault. The formulations defined below assume that all coordinates and source parameters are defined within the j th fault-specific coordinate system. The superscript j is again omitted for convenience and clarity.

The following notation is used for the finite-rupture formulation (Figure 3.7):

X_e = location of the epicenter along the x -axis in the fault-specific coordinate system

$x_{f,1}; x_{f,2}$ = x -direction coordinates of the ends of the fault in the source-specific coordinate system. It follows from Figure 3.7 that $x_{f,1} = 0$ and $x_{f,2} = L_F$.

$A_L; A_R$ = the amount of the rupture that propagates to the left (toward the origin) and right (away from the origin) of the epicenter, respectively.

X_r = x -direction coordinate of the end of the rupture closest to the origin, hereafter referred to as the *rupture reference coordinate*.

R_L = length of the rupture = $A_L + A_R$. Note that, in general, $R_L < L_F$.

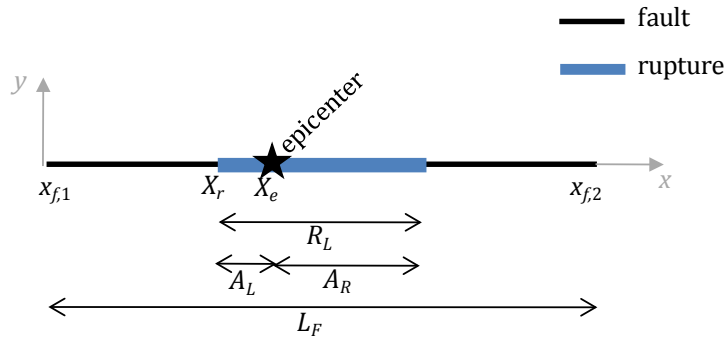


Figure 3.7: Fault and rupture in the local coordinate system for the finite-rupture model

The uncertain location of the epicenter is often assumed to be distributed uniformly along the fault. Although this assumption is used here, the derivations that follow are applicable for any probability distribution used to define the uncertain location of the epicenter. The distribution of X_e is defined by modifying Equation (3.3).

For a given epicenter location, the rupture may propagate to the left and right along the fault in uncertain proportions but constrained by the finite fault geometry. Assuming that the amount of rupture to the left is distributed uniformly within the physical boundaries (any other distribution can be used if available information supports it, but the following expressions would require adaptation), the distribution of A_L is

$$A_L \sim \text{unif}(\max(0, R_L - L_F + X_e), \min(R_L, X_e)) \quad (3.9)$$

This expression bounds the amount of rupture propagating to the left of the epicenter at a maximum of the length that can “fit” to the left side and at a minimum of the length that cannot fit on the right side. The amount of rupture that propagates to the right is simply the remainder of the rupture length, i.e., $A_R = R_L - A_L$.

The rupture reference coordinate X_r is then equal to $X_e - A_L$, and it follows that the conditional distribution of X_r is

$$X_r \sim \text{unif}[X_e - \min(R_L, X_e), X_e - \max(0, R_L - (L_F - X_e))] \quad (3.10)$$

Figure 3.8 shows a BN model of these relationships. For each fault, there is a source-dependent distribution of the earthquake magnitude and epicenter location. The rupture length on the fault

is a function of the earthquake magnitude and source characteristics (Wells and Coppersmith 1994). The distribution of R_L is typically truncated at a maximum considered value, often one-half the fault length. In the BN, nodes M and X_e are specified as children of node S_C . Node R_L is a child of nodes M and S_C , modeling the source-dependent magnitude–rupture length relationship. Consistent with Equation (3.10), X_r is a child of nodes X_e and R_L as well as node S_C , which captures the dependence of X_r on fault length and the maximum rupture length considered on the source.

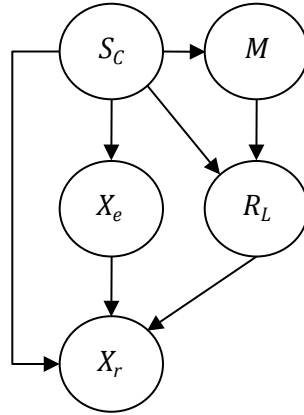


Figure 3.8: BN modeling rupture length and location as a function of earthquake source, epicenter location, and magnitude

To compute the CPT of X_r for each combination of the states of X_e and R_L , N_{sim} draws are taken from the associated intervals. For each simulation, a value of X_r is drawn from the distribution in Equation (3.10) based on the drawn values of X_e and R_L . Then, a normalized histogram is computed to obtain the required column of the CPT for X_r , with bins defined corresponding to the discrete interval states specified based on the admissible range of X_r . The range associated with X_r is typically the same as the admissible range of X_e . The sampling intervals for X_e and R_L must account for source-specific differences in the fault length as well as the assumed maximum considered rupture length on each fault. Define $maxR_L = \max_{i=1,\dots,N_{S_C}} maxR_{L,i}$, where $maxR_{L,i}$ is the maximum considered rupture length on source i . Define $R_L^{(k)}$ as the k th state associated with node R_L , which corresponds to the interval $[R_{L,L}^{(k)}, R_{L,U}^{(k)}]$. Similarly, define $X_e^{(k)}$ as the k th state representing the interval $[X_{e,L}^{(k)}, X_{e,U}^{(k)}]$. To account for fault-specific geometric constraints

given an earthquake on source i , $R_L^{(k)}$ should be sampled uniformly from the interval $\left[\min\left(\max R_{L,i}, R_{L,L}^{(k)}\right), \min\left(\max R_{L,i}, R_{L,U}^{(k)}\right)\right]$. Similarly $X_e^{(k)}$ should be sampled uniformly from the interval $\left[\min\left(L_F^i, X_{e,L}^{(k)}\right), \min\left(L_F^i, X_{e,U}^{(k)}\right)\right]$. For example, consider two faults of lengths 5 and 8 in arbitrary units. Assume that the maximum considered rupture length for each fault is equal to one-half of the fault length; thus $\max R_{L,1} = 2.5$ and $\max R_{L,2} = 4$. Crudely discretize R_L to have states $[0,2]$ and $[2,4]$ and X_e to have states $[0,2]$, $[2,4]$, $[4,6]$, and $[6,8]$. Given an earthquake on source 1, the sampling interval for the first state of R_L is $[\min(2.5,0), \min(2.5,2)] = [0,2]$ and the sampling interval for the second state is $[\min(2.5,2), \min(2.5,4)] = [2,2.5]$. Note that, for the second state, values above the maximum considered rupture length (2.5 units) are not included. For the same source, the sampling intervals for X_e are $[\min(0,5), \min(2,5)] = [0,2]$, $[\min(2,5), \min(4,5)] = [2,4]$, $[\min(4,5), \min(6,5)] = [4,5]$, and $[\min(6,5), \min(8,5)] = [5,5]$. Note that, for the third state, epicenter locations beyond the length of the fault (greater than 5 units) are not considered. The chosen sampling interval for the last state of X_e (i.e., $[6,8]$) is irrelevant given an earthquake on source 1 because it is associated with zero probability.

For a given rupture length, the source-to-site distance R_i is defined for each site within the source-specific coordinate system. See Figure 3.9 for examples of this distance for various site-rupture configurations. The distance between the i th site and a rupture on the fault is computed as

$$R_i = \sqrt{(X_{d,i})^2 + (y_{s,i})^2 + (z_{s,i})^2}, \quad (3.11)$$

where $y_{s,i}$ and $z_{s,i}$ are the coordinates of site i in the fault-specific coordinate system and $X_{d,i}$ is the x -direction distance between site i and the nearest point on the rupture on the source.

For the straight-line idealization of a fault, $X_{d,i}$ is expressed using simple geometry as

$$X_{d,i} = \max[X_r - x_{s,i}, x_{s,i} - \min(X_r + R_L, L_F), 0], \quad (3.12)$$

where $x_{s,i}$ is the x -direction coordinate of site i . The term $\min(X_r + R_L, L_F)$ specifies the coordinate of the right end of the rupture. From a geometric perspective, including the expression $\min(X_r + R_L, L_F)$ instead of $(X_r + R_L)$ is redundant because in Equation (3.10) the rupture

reference coordinate can only assume values that limit the rupture to within the fault. However, in the BN, a conditional distribution of $X_{d,i}$ must be defined for all combinations of its parent nodes, even for physically impossible combinations of $X_r + R_L$. To avoid introducing additional states, the value L_F is assigned to $X_{d,i}$ for combinations in which $X_r + R_L > L_F$. Because physically impossible combinations of $X_r + R_L$ have probability zero, this assignment has no effect on the results. It should be clear that node R_i must be a child of nodes S_C , R_L , and X_r and a function of the site coordinates as well.

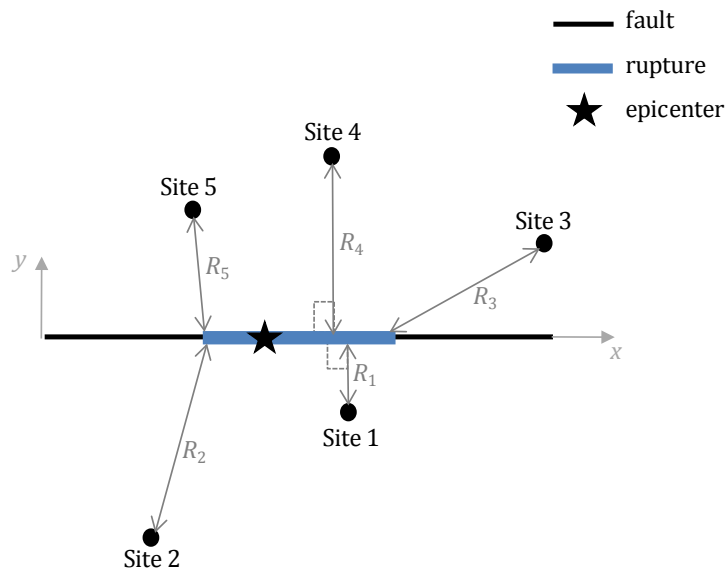


Figure 3.9: Geographically distributed sites in vicinity of a fault

In computing the CPT of R_i using the above expressions in conjunction with Monte Carlo simulation, errors may arise due to inconsistencies resulting from discretization. For example, consider a fault of length 30 (arbitrary) units and a site located at coordinate $(8, -5)$ as shown in Figure 3.10. Let the location of the epicenter be a deterministic quantity (i.e., node X_e has only one state) with value of 15. Additionally, let the rupture length be a deterministic quantity with a value of 10 units, but an uncertain location. Consider that we are interested in the x -direction distance between the site and the nearest point on the rupture, $X_{d,i}$. The BN computing this quantity using the formulation in Equation (3.12) is shown in Figure 3.11a.

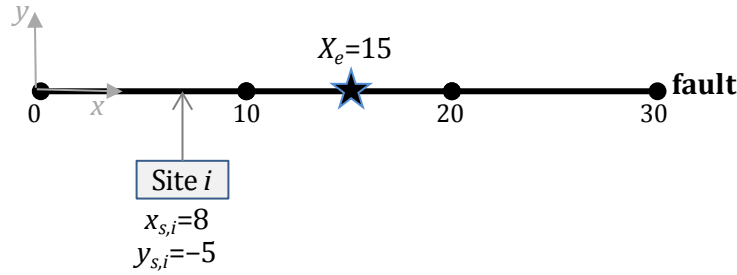


Figure 3.10: Example illustrating geometric inconsistencies due to discretization

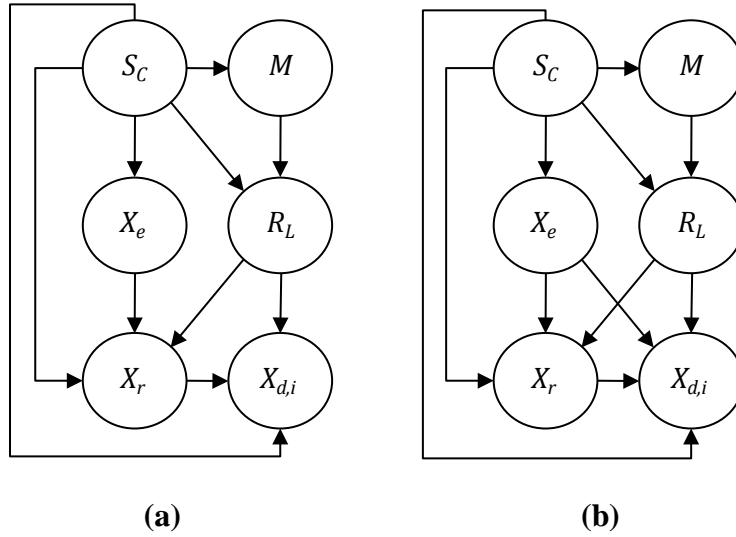


Figure 3.11: (a) BN modeling relationship in Equation (3.12) and (b) BN modeling relationship after addition of a link between X_e and X_d to account for geometric inconsistencies due to discretization

For this example, assume that X_r is crudely discretized into three states: $[0,10]$, $[10,20]$, $[20,30]$, and $X_{d,i}$ is arbitrarily discretized into three states: $[0,5]$, $[5,10]$, $[10,15]$. (In actual applications, the states of $X_{d,i}$ should be carefully defined based on the geometry of the problem.) The geometry in Figure 3.10 makes it clear that the maximum value $X_{d,i}$ can assume is $X_e - x_{s,i} = 7$. Thus, the probabilistic weight of the last state assigned to $X_{d,i}$, $[10,15]$, should always be zero.

For the known epicenter and rupture length, and using the expression in Equation (3.10), X_r falls in the range $[5,15]$ according to the uniform distribution. Half of this admissible range falls in state 1 (i.e., $[0,10]$) and the other half in state 2 (i.e., $[10,20]$). Therefore, there is a 0.5

probability that X_r will fall in each of its first two states and a zero probability of falling in the last state.

Generating the CPT of $X_{d,i}$ using Monte Carlo simulation based on the expression in Equation (3.12) results in the CPT shown in Table 3.1. The first column of this table corresponds to a true result: $X_{d,i}$ is certain to fall in the range $[0,5]$ because X_r is located in the range $[0,10]$. The last column is inconsequential because there is zero probability that X_r will fall into the state $[20,30]$. However, the distribution in the second column is erroneous due to the nonzero probability that $X_{d,i}$ is in the state $[10,15]$, which conflicts with our earlier observation that $X_{d,i}$ can be at most equal to $X_e - x_{s,i} = 7$. This inconsistency arises from the discretization of the random variables describing the geometry of the problem.

Recall from Section 2.2.2 that when generating the CPT for a node that has interval nodes as parents, values are drawn *uniformly* from within the intervals associated with each combination of its parent nodes states. Thus, when generating the second column of the CPT associated with node $X_{d,i}$, values of X_r are drawn uniformly from within the range $[10,20]$ even though values of $X_r > 15$ are not geometrically admissible given the known epicenter location. The inconsistencies due to the coarse discretization resulted in the large errors in Table 3.1. When a more refined discretization is used (say, one with six states), this effect becomes negligible and no remedial action need be taken. However, if large errors arise and a more refined discretization is not an option, the inconsistency problem can be addressed by adding a link from node X_e to $X_{d,i}$ and adapting the Monte Carlo simulation scheme to compute the CPT of $X_{d,i}$ and R_i as described in Figure 3.12. The resulting BN is shown in Figure 3.11b. The procedure in Figure 3.12 is a conceptual and generic scheme that has not been optimized for computational efficiency. Also note that, in this algorithm, $X_{i,L}^{m_j}$ and $X_{i,U}^{m_j}$ denote the lower and upper bounds of the j th state of interval node X_i . m_{X_e} , m_{X_r} , and m_{R_L} are defined as the number of states associated with nodes X_e , X_r , and R_L , respectively.

Table 3.1: CPT of $X_{d,i}$ given R_L and X_r showing geometric inconsistencies due to discretization

R_L	10		
X_r	0-10	10-20	20-30
0-5	1	0.28	0
5-10	0	0.52	0
10-15	0	0.2	0.28
15-20	0	0	0.52
20-25	0	0	0.2

for $i = 1, \dots, m_{X_e}, j = 1, \dots, m_{X_r}, k = 1, \dots, m_R$,

for $n = 1, \dots, N_{sim}$ (number of Monte Carlo simulations used to generate the CPT)

1. Generate $X_e \sim \text{unif}[X_{e,L}^i, X_{e,U}^i]$
2. Generate $X_r \sim \text{unif}[j, \min(X_{r,U}^j, X_e)]$
3. Generate $X_L \sim \text{unif}[R_{L,L}^k, R_{L,U}^k]$
4. Calculate $X_{d,i}$ using Equation (3.12)
5. Calculate R_i using Equation (3.11)

end

Determine normalized histogram of $X_{d,i}$

end

Figure 3.12: Algorithm for generating CPTs of $X_{d,i}$ and R_i to address geometric inconsistencies due to discretization

The BN computing the source-to-site distance must likewise be modified to account for the dependence of $X_{d,i}$ on X_e (which implies that R_i is dependent on X_e). The resulting BN is shown in Figure 3.13. The algorithm in Figure 3.12 describes the construction of the CPTs of R_i by Monte Carlo simulation. Note that, in node $X_{d,i}$ in Figure 3.11b and node R_i in Figure 3.13 have four parents. As a general rule, the number of parents to a node should not exceed three, so potential computational inefficiencies may arise from this formulation.

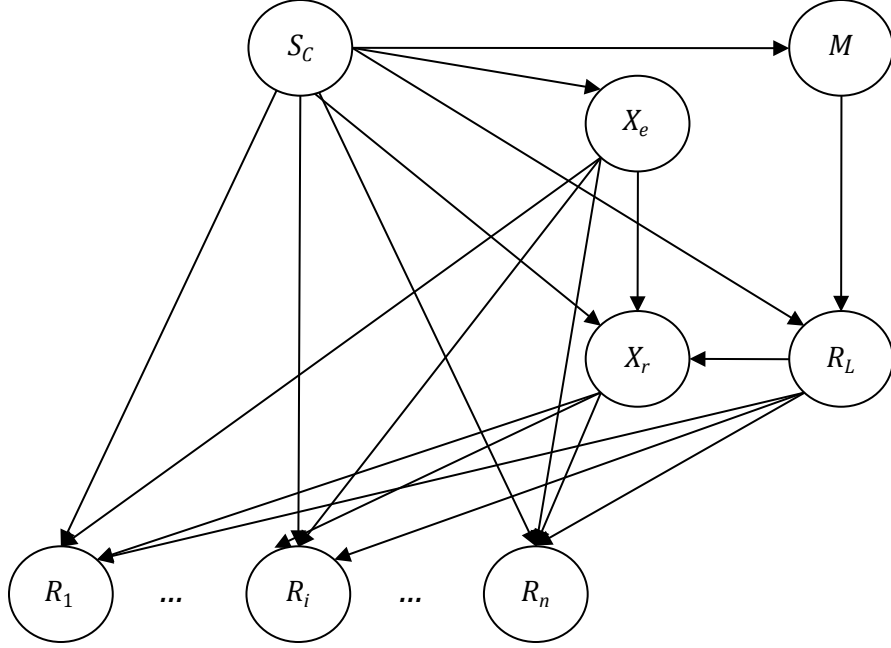


Figure 3.13: BN modeling of source-to-site distance as a function of earthquake source and location

As with the point-source case, we next extend the above formulation to the case in which a fault is idealized as a set of connected line segments. The multi-segment fault formulation only affects the computation of CPTs, not the topology of the BN in Figure 3.13. To facilitate the required derivations, we define the following additional variables:

$\mathbf{P}_{s,i} = [x_{s,i}, y_{s,i}, z_{s,i}]$ = vector containing the x -, y -, and z -coordinates of site i in three-dimensional space.

$r_{i,k}$ = distance between site i and the rupture on segment k of the source, if the rupture crosses the segment.

$\mathbf{P}_{f,k} = [x_{f,k}, y_{f,k}, z_{f,k}]$ = vector containing the x -, y -, and z -coordinates of a point defining the location of the end of a segment of the fault.

$\mathbf{P}_r = [X_r, Y_r, Z_r]$ = vector defining the location of the rupture reference coordinate in three-dimensional space.

For the finite-rupture case, we use the same method used for the point-source formulation in which the N_{seg} fault segments are aligned to form a single line of length L_F lying on the x' -axis,

as illustrated in Figure 3.6. The earthquake epicenter and rupture reference coordinate are both mapped from the three-dimensional space onto a coordinate along the x' -axis. Define X'_e and X'_r to be the coordinates of the epicenter and rupture reference coordinate on this axis.

Define $K_{rup} \subset \{1, \dots, N_{seg}\}$ as the set of segment indices corresponding to segments crossed by the rupture. The rupture crosses fault segment k if $X'_r < x'_{f,k}$ and $(X'_r + R_L) > x'_{f,k-1}$, where $x'_{f,k}$ is the x' -coordinate of the fault corresponding to $\mathbf{P}_{f,k}$ and is computed as

$$x'_{f,k} = \sum_{i=1}^k l_{f,i}. \quad (3.13)$$

It follows that the rupture reference coordinate in the three-dimensional source-specific coordinate system is

$$\mathbf{P}_r = \sum_{k=1}^{N_{seg}} \mathbb{I}[x'_{f,k-1} \leq X'_r \leq x'_{f,k}] \left(\mathbf{P}_{f,k-1} + (X'_r - x'_{f,k-1}) \frac{\mathcal{D}(\mathbf{P}_{f,k-1}, \mathbf{P}_{f,k})}{|\mathcal{D}(\mathbf{P}_{f,k-1}, \mathbf{P}_{f,k})|} \right). \quad (3.14)$$

The coordinate of the other end of the rupture, i.e., the point in the three-dimensional source-specific coordinate system that corresponds to the point $(X'_r + R_L)$ on the x' -axis, is

$$\mathbf{P}_{r+R_L} = \sum_{k=1}^{N_{seg}} \mathbb{I}[x'_{f,k-1} \leq (X'_r + R_L) \leq x'_{f,k}] \left(\mathbf{P}_{f,k-1} + (X'_r + R_L - x'_{f,k-1}) \right. \\ \left. * \frac{\mathcal{D}(\mathbf{P}_{f,k-1}, \mathbf{P}_{f,k})}{|\mathcal{D}(\mathbf{P}_{f,k-1}, \mathbf{P}_{f,k})|} \right). \quad (3.15)$$

For each fault segment crossed by the rupture define $\tilde{\mathbf{P}}_{k,1}$ and $\tilde{\mathbf{P}}_{k,2}$ as the ends of the rupture within each segment. These quantities are illustrated in Figure 3.14, which shows that the rupture crosses segments 2, 3, and 4. Points $\tilde{\mathbf{P}}_{k,1}$ and $\tilde{\mathbf{P}}_{k,2}$ are associated with the ends of the portion of the rupture that lies on each segment $k \in K_{rup}$. For example, the left end of the rupture lies on segment 2 and propagates past the right end of the segment. Therefore, $\tilde{\mathbf{P}}_{2,1} = \mathbf{P}_r$ and $\tilde{\mathbf{P}}_{2,2} = \mathbf{P}_{f,2}$ as shown in Figure 3.14. In general, $\tilde{\mathbf{P}}_{k,1}$ and $\tilde{\mathbf{P}}_{k,2}$ are defined mathematically as a function of the rupture and fault coordinates on the x' -axis:

$$\begin{aligned}
\tilde{\mathbf{P}}_{k,1} &= \mathbf{P}_r \text{ if } (x'_{f,k-1} \leq X'_r \leq x'_{f,k}) \cap ((X'_r + R_L) > x'_{f,k}) \\
&= \mathbf{P}_{f,k-1} \text{ if } (X'_r \leq x'_{f,k-1}) \cap (x'_{f,k-1} \leq (X'_r + R_L) \leq x'_{f,k}) \\
&= \mathbf{P}_{f,k-1} \text{ if } (X'_r < x'_{f,k-1}) \cap ((X'_r + R_L) > x'_{f,k}) \\
&= \mathbf{P}_r \text{ if } X'_r \geq x'_{f,k-1} \cap ((X'_r + R_L) \leq x'_{f,k}) \\
&= \emptyset \text{ if } (X'_r > x'_{f,k}) \cup ((X'_r + R_L) < x'_{f,k-1}) \\
\tilde{\mathbf{P}}_{k,2} &= \mathbf{P}_{f,k} \text{ if } (x'_{f,k-1} \leq X'_r \leq x'_{f,k}) \cap ((X'_r + R_L) > x'_{f,k}) \\
&= \mathbf{P}_{r+R_L} \text{ if } (X'_r \leq x'_{f,k-1}) \cap (x'_{f,k-1} \leq (X'_r + R_L) \leq x'_{f,k}) \\
&= \mathbf{P}_{f,k} \text{ if } (X'_r < x'_{f,k-1}) \cap ((X'_r + R_L) > x'_{f,k}) \\
&= \mathbf{P}_{r+R_L} \text{ if } X'_r \geq x'_{f,k-1} \cap ((X'_r + R_L) \leq x'_{f,k}) \\
&= \emptyset \text{ if } (X'_r > x'_{f,k}) \cup ((X'_r + R_L) < x'_{f,k-1})
\end{aligned} \tag{3.16}$$

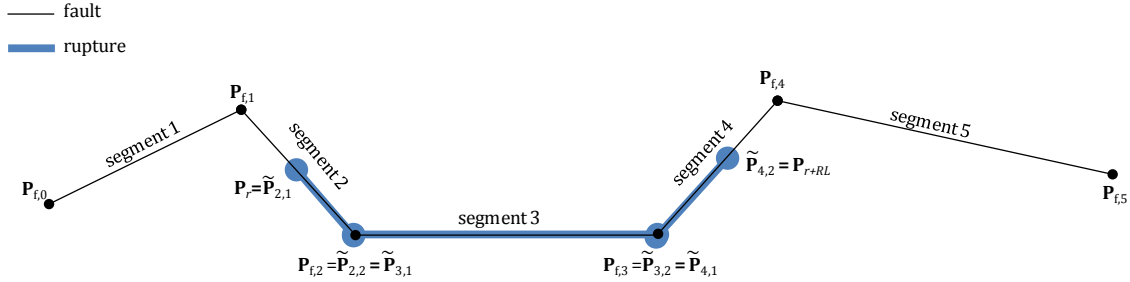


Figure 3.14: Parameters required for multi-segment finite-rupture length formulation

The source-to-site distance R_i is determined by computing the shortest distance between site i and each fault segment crossed by the rupture and then selecting the minimum length among these values, i.e.,

$$R_i = \min_{k \in K_{rup}} r_{i,k}, \tag{3.17}$$

where $r_{i,k}$ is the minimum distance between site i and the rupture on each segment $k \in K_{rup}$. This quantity is computed using different formulas depending on the location of the site relative to the ends of the rupture on the fault segment. The three possible configurations are shown in

Figure 3.15. For configuration (a), $r_{i,k}$ is equal to the distance between $\mathbf{P}_{s,i}$ and $\tilde{\mathbf{P}}_{k,1}$; for configuration (b), $r_{i,k}$ is equal to the distance between $\mathbf{P}_{s,i}$ and the point corresponding to the projection of $\mathbf{P}_{s,i}$ onto the rupture segment; and for configuration (c), $r_{i,k}$ is equal to the distance between $\mathbf{P}_{s,i}$ and $\tilde{\mathbf{P}}_{k,2}$.

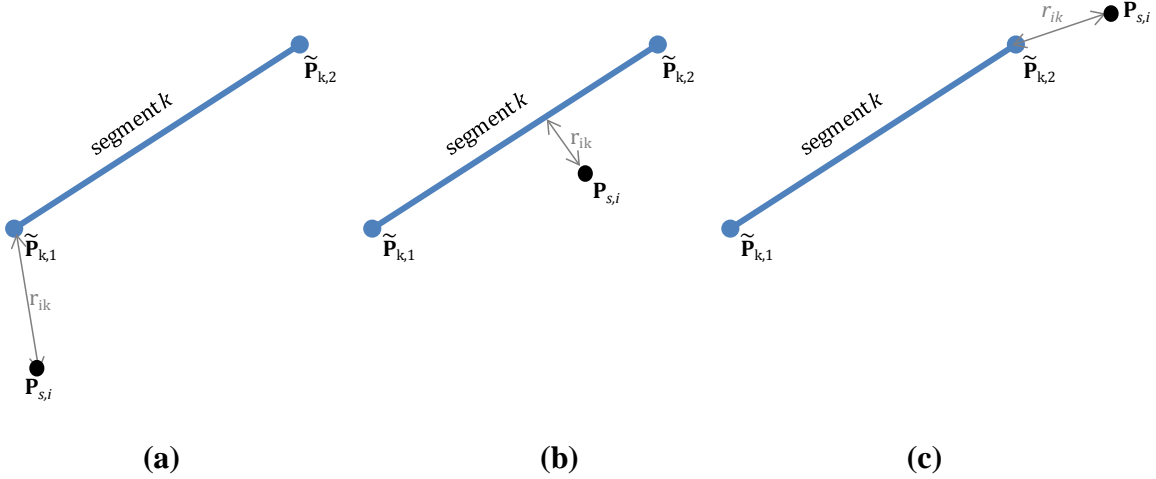


Figure 3.15: Configurations of site location relative to fault segment crossed by the rupture

The above description is written mathematically as

$$\begin{aligned}
 r_{ik} &= |\mathbf{P}_{s,i} - \tilde{\mathbf{P}}_{k,1}| \quad \text{if } \vartheta_{i,k}^j \leq 0 \\
 &= \left| \mathbf{P}_{s,i} - \left(\tilde{\mathbf{P}}_{k,1} + \vartheta_{i,k}^j * \mathcal{D}(\tilde{\mathbf{P}}_{k,1}, \tilde{\mathbf{P}}_{k,2}) \right) \right| \quad \text{if } 0 < \vartheta_{i,k}^j < 1 \\
 &= |\mathbf{P}_{s,i} - \tilde{\mathbf{P}}_{k,2}| \quad \text{if } 1 \leq \vartheta_{i,k}^j
 \end{aligned} \tag{3.18}$$

where $\vartheta_{i,k}$ is the ratio of the length of the projection of $(\mathbf{P}_{s,i} - \tilde{\mathbf{P}}_{k,1})$ on the vector $\mathcal{D}(\tilde{\mathbf{P}}_{k,1}, \tilde{\mathbf{P}}_{k,2})$ and the length of $\mathcal{D}(\tilde{\mathbf{P}}_{k,1}, \tilde{\mathbf{P}}_{k,2})$:

$$\vartheta_{i,k}^j = \frac{\mathcal{D}(\tilde{\mathbf{P}}_{k,1}, \tilde{\mathbf{P}}_{k,2}) \cdot (\mathbf{P}_{s,i} - \tilde{\mathbf{P}}_{k,1})}{\mathcal{D}(\tilde{\mathbf{P}}_{k,1}, \tilde{\mathbf{P}}_{k,2}) \cdot \mathcal{D}(\tilde{\mathbf{P}}_{k,1}, \tilde{\mathbf{P}}_{k,2})} \tag{3.19}$$

$\vartheta_{i,k}$ takes on negative values for case (a) in Figure 3.15, values between 0 and 1 for case (b), and values greater than or equal to 1 for case (c). The above relations are used to populate the CPTs of nodes R_i in Figure 3.13.

3.2.2.2 Ground motion intensity

The ground motion intensity at a site can be estimated using ground motion prediction equations. These equations express ground motion intensity at a site as a function of the median ground motion intensity (a function of magnitude, source-to-site distance, and site/source characteristics), as well as inter-event and intra-event error terms. Nodes are added to the BNs in Figure 3.3 (point-source model) and Figure 3.13 (finite-rupture model) that represent the ground motion intensity at each site as well as the site-specific median ground motion and the inter- and intra-event deviations. The resulting BNs are shown in Figure 3.16 and Figure 3.17 for point-source and finite-rupture formulations, respectively.

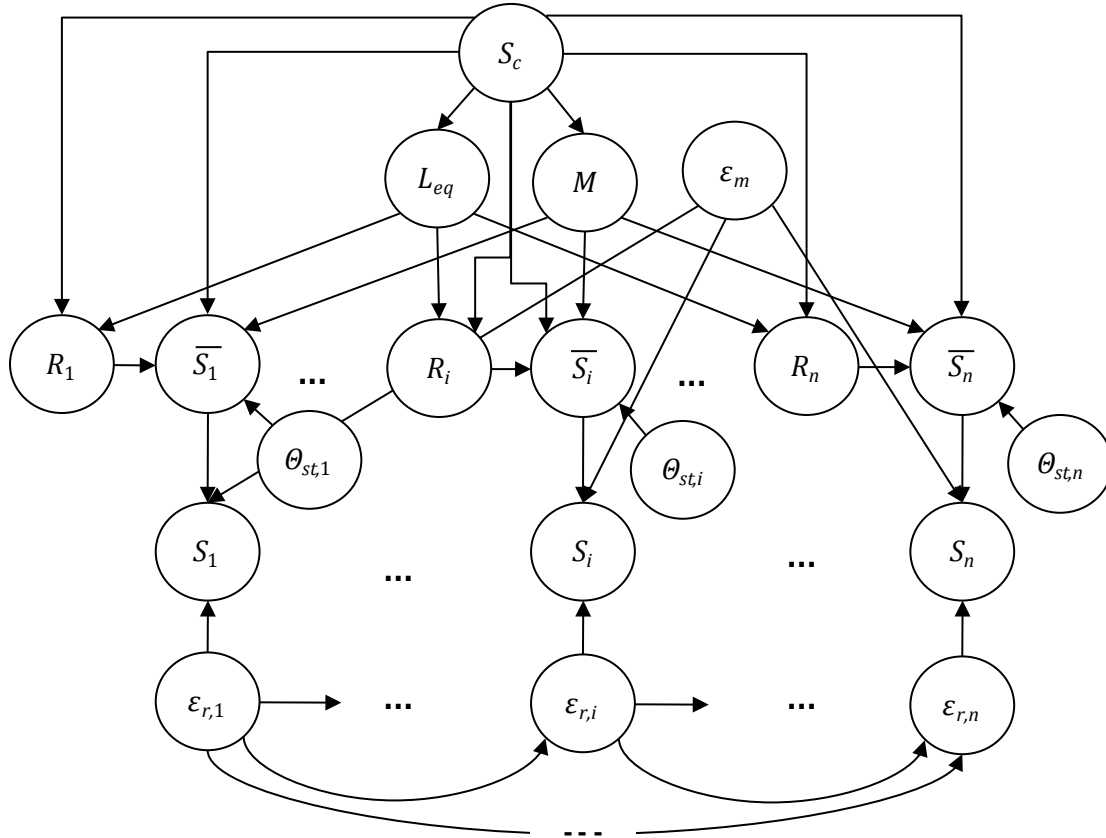


Figure 3.16: BN model of ground motion intensity using point-source assumption

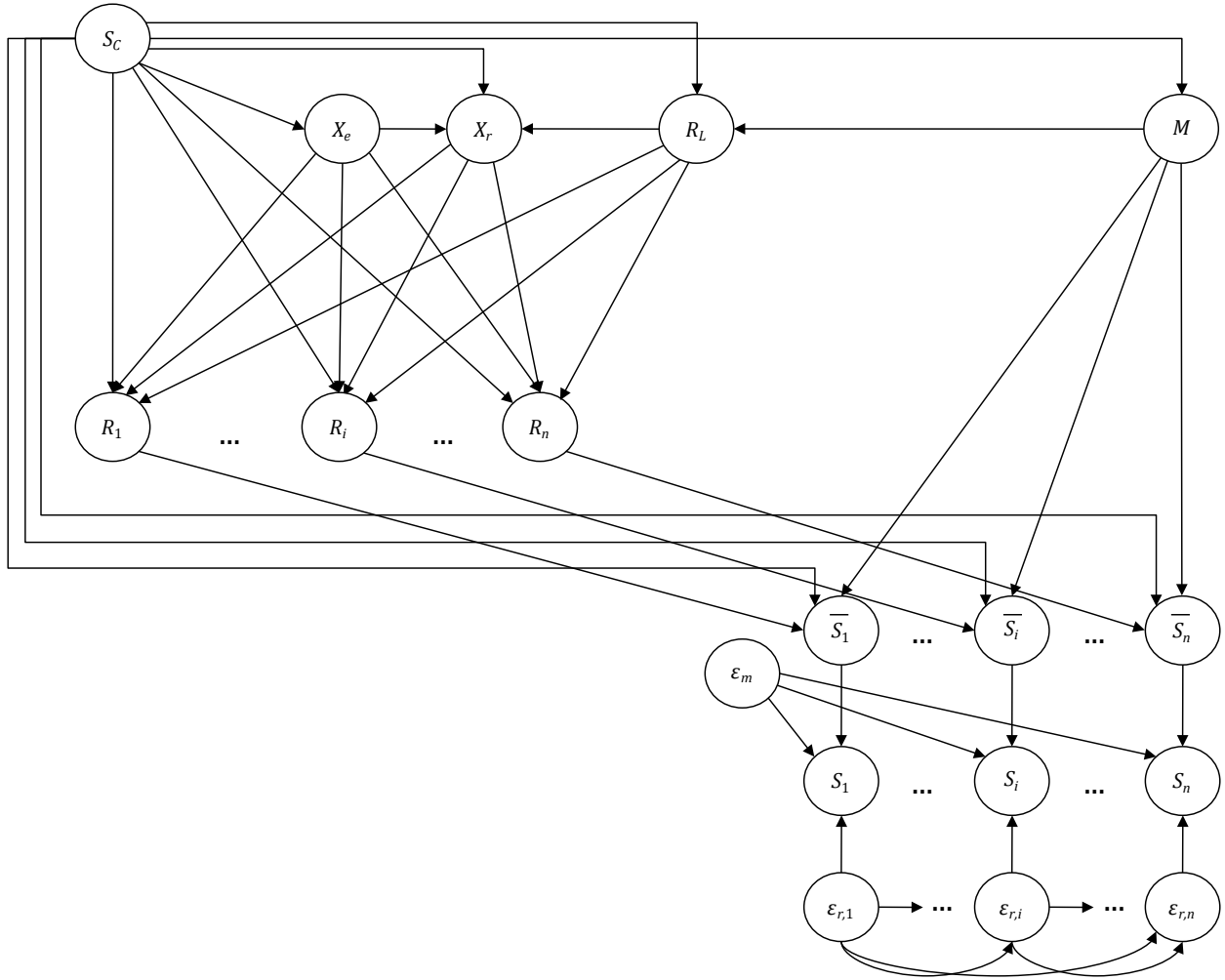


Figure 3.17: BN model of ground motion intensity using finite-rupture model

In the BN in Figure 3.16, nodes labeled S_i , $i = 1, \dots, n$ represent the ground motion intensity at n discrete sites in the region, with the earthquake idealized as a point on the fault. For reference, the sites for which ground motion intensity nodes are included in the BN are referred to as *ground motion prediction points* (GMPPs). Nodes representing the earthquake magnitude (M) and location (L_{eq}) are modeled as children of the source node (S_c) in the manner described previously. The distance between the source and site i (R_i) is expressed as a function of the site coordinates (not shown in the BN because they are assumed deterministic), the source on which the earthquake occurs, and the location of the earthquake. The median ground motion intensity at site i is represented by node \bar{S}_i , which is a child of nodes M , R_i , and source and site

characteristics. Nodes corresponding to site characteristics need not be explicitly shown if they are treated as deterministic or stochastic but unobservable; they are shown in Figure 3.16 for illustrative purposes. The actual ground motion intensity at a site, S_i , is modeled as a function of the median ground motion intensity as well as the inter- and intra-event error terms, consistent with Equation (3.1). This dependence is shown by links from nodes \bar{S}_i , ε_m , and $\varepsilon_{r,i}$ to S_i .

The inter-event deviations ε_m arise from inaccuracy or idealization in the characterization of the source and represent the earthquake-to-earthquake variability in the actual ground motion intensity from the predicted median. For a given earthquake, ε_m is the same for all sites, thus a single node ε_m is introduced that is a parent of all site-specific ground motion intensity nodes. The intra-event deviations $\varepsilon_{r,i}$ arise from uncertain wave propagation and site effects. For a particular earthquake, intra-event deviations represent the site-to-site variability in the ground motion intensity. Intra-event errors are site-specific and represent random variables drawn at discrete points in the domain of a spatially correlated zero-mean Gaussian random field. The correlation arises because, for a given earthquake, the magnitude of the difference between the actual and predicted median ground motion intensity is similar for sites near each other but can be less similar as the distance between the sites increases. A node representing $\varepsilon_{r,i}$ is added to the BN for each site. The correlation among $\varepsilon_{r,i}$ nodes is modeled with links between all pairs of the corresponding nodes, as shown in Figure 3.16. BNs with densely connected nodes, which typically arise when modeling points drawn from a random field, are highly demanding of computer memory. Methods for efficiently modeling random variables drawn from a Gaussian random field by BN are the subject of Chapter 4.

The seismic demand BN corresponding to a finite-rupture model is shown in Figure 3.17. The conditional relations used to construct this BN are the same as in the point-source case, except that nodes are added to account for the effect of the finite-rupture model on source-to-site distance consistent with the development in the previous section.

3.2.2.3 Rupture directivity effects

Ground motions at sites near a fault may differ substantially from those of sites at greater distances due to rupture directivity effects. Rupture directivity effects cause variation in ground

motion amplitude and duration at a site based on whether the direction of rupture propagation is toward (forward directivity) or away (backward directivity) from the site.

Forward directivity effects arise when the velocity of the rupture front is only slightly less than the shear wave velocity. As the rupture propagates toward the site, a shear wave front is generated as waves accumulate in front of the rupture. The waves generated between the source and the site arrive at the site at approximately the same time, and at long periods the waves constructively interfere. The result is a pulse-like ground motion of high amplitude, long period, and short duration. Forward directivity effects are most easily observed in the velocity time history. Conversely, a site may experience backward directivity when located in the direction opposite to that of rupture propagation. Such a situation arises when the rupture propagates in one direction from the epi/hypocenter. Ground motions associated with backward directivity effects are of longer duration and lower amplitude. Figure 3.18 provides a graphical representation of these directivity effects (adapted from Somerville et al. (1997)).

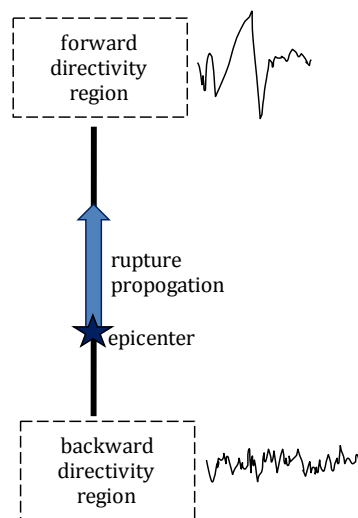


Figure 3.18: Illustration of directivity effects

The geometry of a fault relative to the location of a site is the best predictor of the potential for directivity effects. The angle between the direction of rupture and the ray path from the epi/hypocenter to the site and the amount of the rupture that lies between the epi/hypocenter and the site are good predictors of directivity potential. However, directivity is not a deterministic phenomenon. Directivity effects may not be felt at a site for which the geometry suggests it is

likely. Conversely, pulse-like motions have been measured at sites when the geometric configuration is not favorable to directivity (Shahi and Baker 2010).

Large pulse-like ground motions can result from ruptures on both strike-slip and dip-slip faults. For strike-slip faults, sites near the fault in the direction of rupture propagation typically experience directivity effects, most strongly in the strike-normal component of ground motion. For dip-slip faults, sites located on the up-dip projection of the rupture plane are most likely to experience pulse-like motions (Bray and Rodriguez-Marek 2004).

Motions arising from forward directivity place large demands on structures and earth systems and can cause greater damage than that experienced by structures not subjected to this type of loading. Thus, directivity effects are of interest when predicting intensity of ground shaking at sites near a fault.

Although it is crucial to include forward directivity effects for long-period structures near highly active faults, current ground motion prediction equations do not explicitly account for them. However, records with directivity effects are included in the databases used to derive these empirical relations. Such effects were observed by Kuehn et al. (2009) as described in Section 3.2.1. As a result, ground motion prediction equations tend to underestimate ground motion intensity in the near-fault region when pulses occur and overestimate when pulses do not occur. Adjustment factors have been proposed to correct this (Somerville et al. 1997; Abrahamson 2000; Tothong et al. 2007; Shahi and Baker 2010), some of which are modeled in this study. Abrahamson (2000) and Shahi and Baker (2010) provided directivity factors to modify the spectral acceleration obtained from conventional ground motion prediction equations. Bray and Rodriguez-Marek (2004) offered a modified attenuation relation for predicting peak ground velocity at sites where directivity pulses have occurred. BN formulations for the directivity models offered by Abrahamson (2000), Shahi and Baker (2010), and Bray and Rodriguez-Marek (2004) are developed in the following subsections.

3.2.2.3.1 Directivity BN based on Abrahamson (2000)

Abrahamson (2000), adapting an earlier relation by Somerville et al. (1997), accounted for the directivity effect by defining a factor that amplifies or diminishes the ground motion intensity at sites near a fault rupture. The model is a broadband formulation that modifies spectral

acceleration monotonically over a range of periods (Shahi and Baker 2010). The site-specific directivity amplification factor is added to the natural logarithm of the spectral acceleration in the ground motion prediction equation. Using Abrahamson (2000), we include directivity effects in the BN by adding a node, $f_{d,i}$, representing the amplification factor on ground motion intensity at site i .

Amplification factor $f_{d,i}$ is defined as a function of regression coefficients, the fraction of the rupture length that propagates toward the site, and the angle between the fault and the ray path from the earthquake source to the site. For the average horizontal component of ground motion, the Somerville et al. (1997) factor (later modified by Abrahamson (2000)) is given by

$$f_{d,i}(F_{F,mod}, \theta, T) = c_1(T) + 1.88c_2(T)F_{F,mod} \cos \theta, \quad (3.20)$$

where θ is the angle between the fault strike and the ray path to the site (azimuth angle for strike-slip faults or zenith angle for dip-slip faults), $c_1(T)$ and $c_2(T)$ are regression coefficients expressed as functions of the fundamental period T , and

$$F_{F,mod} = \begin{cases} F_F & \text{for } F_F \leq 0.4 \\ 0.4 & \text{for } F_F > 0.4 \end{cases} \quad (3.21)$$

where $F_F = D_i/R_L$ is the fraction of the rupture that propagates towards the site. D_i is the length of the rupture that falls between the epi/hypocenter and the site. The parameters of the directivity model are shown in Figure 3.19 for strike-slip and dip-slip faults. In these illustrations, R_L is the rupture length and D_i and θ are as defined above.

Abrahamson (2000) added two modifications to the Somerville et al. (1997) model in Equation (3.20). The first was added to ensure that the directivity effect reduces to zero for large source-to-site distances (greater than 60 km) and is given by

$$\begin{aligned} T_r(R_i) &= 1 \text{ for } R_i \leq 30 \text{ km} \\ &= 1 - \frac{R_i - 30}{30} \text{ for } 30 \text{ km} < R_i < 60 \text{ km} \\ &= 0 \text{ for } R_i \geq 60 \text{ km.} \end{aligned} \quad (3.22)$$

The second modification factor reduces directivity to zero for magnitudes less than 6.0. It takes the form

$$\begin{aligned}
T_m(M) &= 1 \text{ for } M \geq 6.5 \\
&= 1 - \frac{m - 6.5}{0.5} \text{ for } 6.0 < M < 6.5 \\
&= 0 \text{ for } M \leq 6.0.
\end{aligned}
\tag{3.23}$$

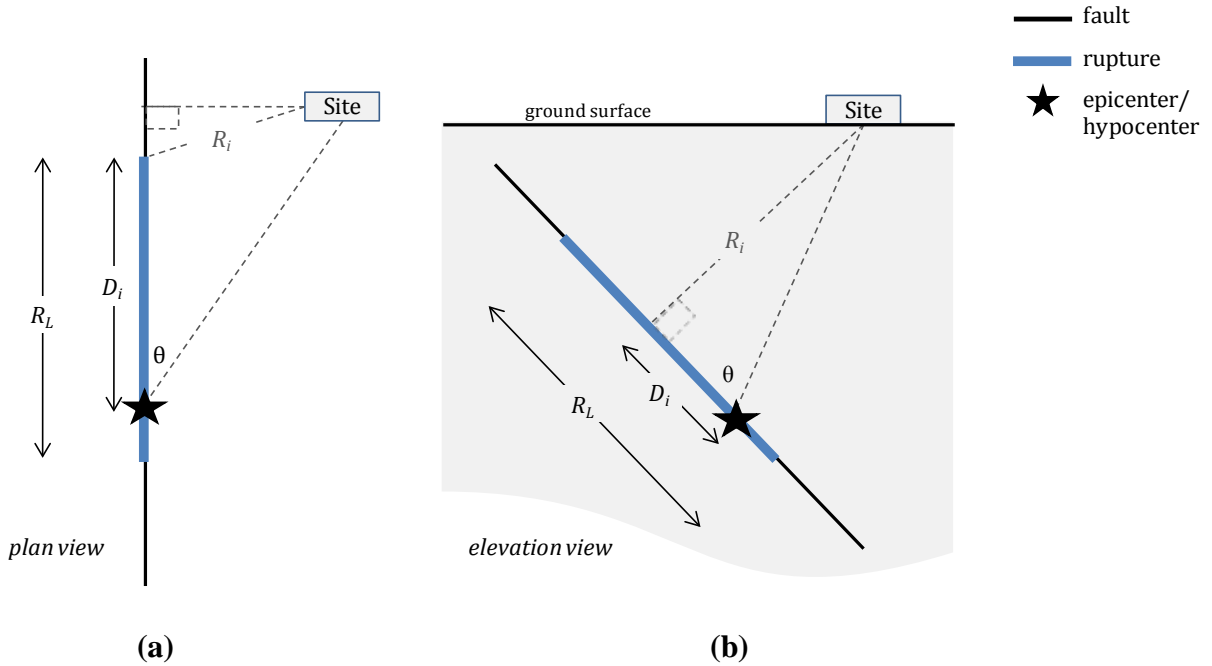


Figure 3.19: Directivity parameters for (a) strike-slip fault and (b) dip-slip fault

Two geometric expressions are necessary for computing the directivity amplification factor $f_{d,i}(F_{F,mod}, \theta, T)$: the fraction of the rupture propagating toward the site and the angle between the strike of the rupture and the ray path to the site. Four geometric cases (combinations of site and rupture locations) are considered for deriving the expressions needed for constructing the BN that includes the directivity effect:

- Case 1: the site is located to the right of the entire rupture: $x_{s,i} > (X_r + R_L)$
- Case 2: the site is located to the right of the epicenter and to the left of the right end of the rupture: $X_e < x_{s,i} < (X_r + R_L)$
- Case 3: the site is located to the left of the entire rupture: $x_{s,i} < X_r$
- Case 4: the site is located to the left of the epicenter and to the right of the left end of the rupture: $X_r < x_{s,i} < X_{epi}$

These cases are demonstrated in Figure 3.20 for a strike-slip fault. The derivations included here are based on the geometry of strike-slip faults, but similar expressions can be derived for dip-slip faults.

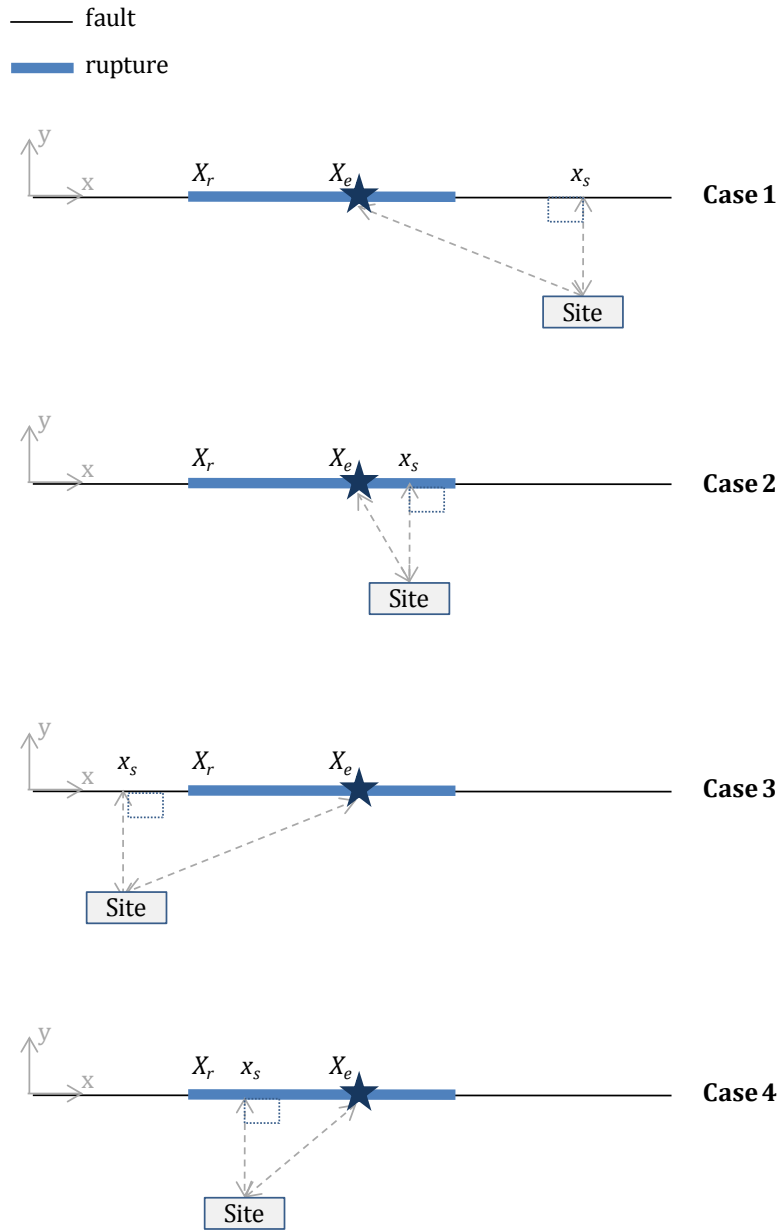


Figure 3.20: Geometric cases considered for computing directivity amplification factor

For all cases in Figure 3.20, the cosine term in Equation (3.20) is defined as

$$\cos(\theta) = \frac{|X_e - x_{s,i}|}{\sqrt{y_{s,i}^2 + z_{s,i}^2 + (X_e - x_{s,i})^2}}. \quad (3.24)$$

The fraction of the rupture that propagates toward the site, F_F , is defined for each of the geometric cases as follows:

- Case 1: $F_F = \frac{A_R}{R_L} = \frac{(X_r + R_L) - X_e}{R_L}$
- Case 2: $F_F = \frac{x_{s,i} - X_e}{R_L}$
- Case 3: $F_F = \frac{X_e - X_r}{R_L}$
- Case 4: $F_F = \frac{X_e - x_{s,i}}{R_L}$

Cases 1 and 2 correspond to the event that $X_e < x_{s,i}$ and cases 3 and 4 correspond to the event that $X_e > x_{s,i}$. Using this observation F_F is defined as

$$\begin{aligned} F_F &= \frac{\min[(X_r + R_L) - X_e, x_{s,i} - X_e]}{R_L} \quad \text{if } X_e < x_{s,i} \\ &= \frac{\min[X_e - X_r, X_e - x_{s,i}]}{R_L} \quad \text{if } X_e \geq x_{s,i}. \end{aligned} \quad (3.25)$$

Thus, the spectral acceleration at site i , when accounting for directivity effects, is computed as

$$\ln(S_{a,i}) = \ln(\overline{S_{a,i}}) + f_{d,i} * T_m(M) * T_r(R_i) + \varepsilon_m + \varepsilon_{r,i}. \quad (3.26)$$

The BN incorporating the directivity effect is shown in Figure 3.21, where node S_i represents the spectral acceleration. Node $f_{d,i}$ is a child of nodes defining the site and source geometry. Due to the modifications introduced by Abrahamson (2000), $f_{d,i}$ is affected by the earthquake magnitude and the source-to-site distance due to the factors $T_r(R_i)$ and $T_m(M)$. Thus, it is a child of nodes M and R_i as well. The CPT of node S_i is computed using Equation (3.26) and Monte Carlo simulation.

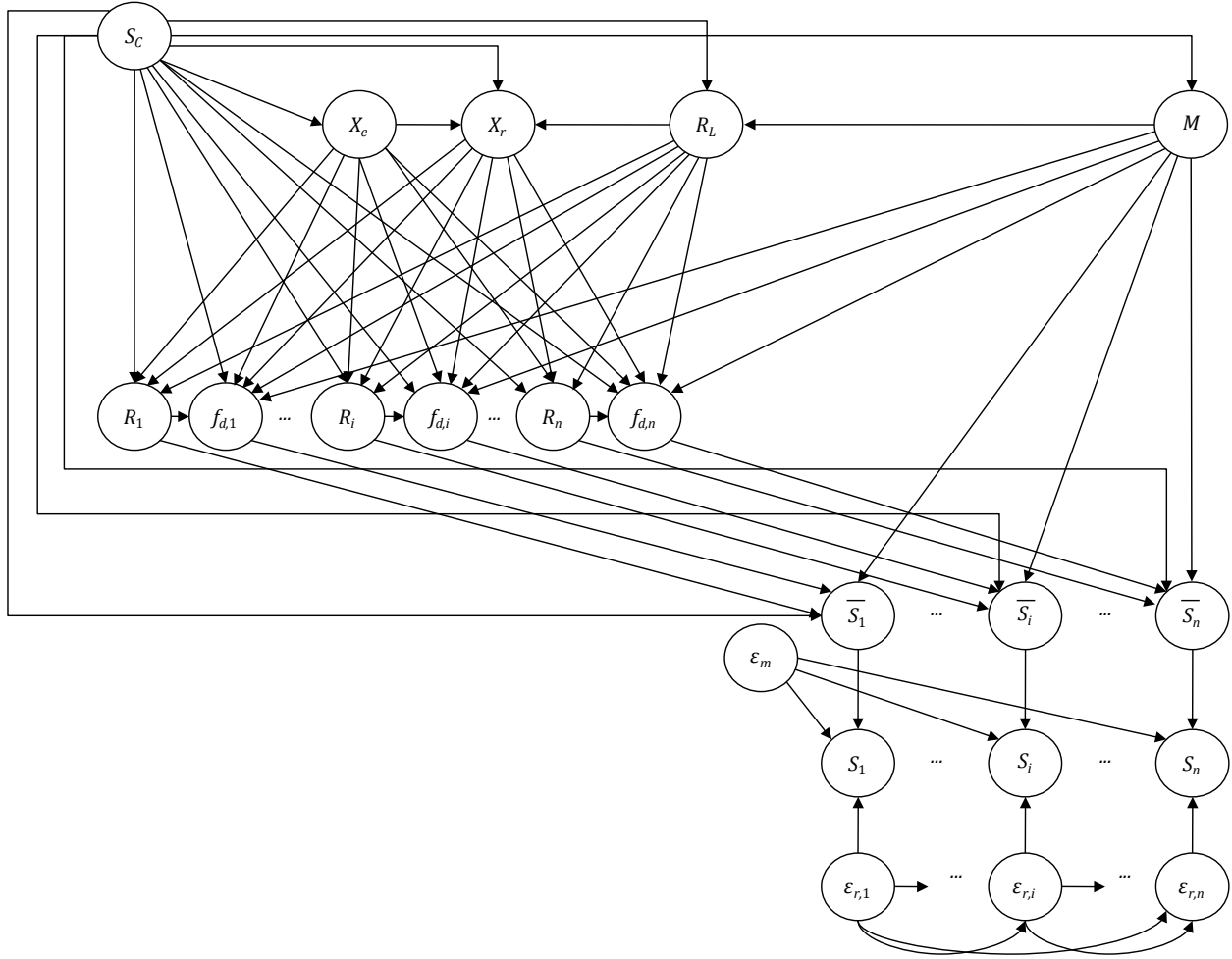


Figure 3.21: BN model of ground motion intensity at multiple sites accounting for directivity effects according to Abrahamson (2000) model

The formulations derived by Somerville et al. (1997) and Abrahamson (2000) idealize the fault as a single line segment. It is not clear how to extrapolate quantities such as $\cos \theta$ for faults with bends. Therefore, it is assumed that this directivity model and BN formulation are only applicable to faults that can be reasonably idealized as straight lines. For multi-segment faults, the Shahi and Baker (2010) model described next can be used.

3.2.2.3.2 Directivity BN based on Shahi and Baker (2010)

Shahi and Baker (2010) developed an extension to the framework of Tothong et al. (2007) for including the directivity effect in seismic hazard analysis. Unlike Somerville et al. (1997), Shahi and Baker (2010) developed a narrowband model that amplifies intensities only in the range of periods near the predominant period of the directivity pulse. Using a database of 179 pulse-like ground motions, they developed empirical models to estimate (1) the probability that a pulse-like ground motion will occur at a site, (2) the orientation of the expected pulse, (3) the pulse period, and (4) the amplification (or diminution) of the spectral acceleration resulting from the occurrence (or nonoccurrence) of a pulse-like motion.

Shahi and Baker used logistic regression to develop a model for the probability of observing a pulse-like ground motion as a function of parameters representing site/source geometry (particularly D_i , R_i and, in the case of dip-slip faults, θ). The resulting model for strike-slip faults is

$$\Pr(\text{pulse at site } i | R_i, D_i) = \frac{1}{1 + \exp(0.642 + 0.167R_i - 0.075D_i)} \quad (3.27)$$

and for dip-slip faults is

$$\Pr(\text{pulse at site } i | R_i, D_i, \theta) = \frac{1}{1 + \exp(0.128 + 0.055R_i - 0.061D_i + 0.036\theta)} \quad (3.28)$$

The amplification of spectral acceleration depends on the predominant period of the pulse, T_p . Empirical results suggest that the pulse period is dependent on the earthquake magnitude. Shahi and Baker found that $\ln T_p$ is normally distributed with mean $\mu_{\ln T_p} = -5.73 + 0.99M$ and standard deviation $\sigma_{\ln T_p} = 0.56$.

Next, they modified the spectral acceleration predicted by a ground motion prediction equation based on whether or not a pulse is observed. If a pulse is observed, then the spectral acceleration at site i ($S_{a,i}^{pulse}$) is computed as

$$\ln S_{a,i}^{pulse} = \ln A_f + \ln S_{a,i}^{GMPE}, \quad (3.29)$$

where $S_{a,i}^{GMPE}$ is the spectral acceleration predicted by a ground motion prediction equation and A_f is the amplification factor due to the occurrence of a pulse. The ground motion intensity at site i accounting for amplification due to directivity ($\ln S_{a,i}^{pulse}$) has the normal distribution with mean $\mu_{\ln A_f} + \mu_{\ln S_{a,i}^{GMPE}}$ and standard deviation $\sigma_{\ln S_{a,i}^{pulse}} = R_f \sigma_{\ln S_{a,i}^{GMPE}}$. The mathematical form of $\mu_{\ln A_f}$ is given in Shahi and Baker (2010) and is a function of T_p and the period of interest T . The term $\sigma_{\ln S_{a,i}^{GMPE}}$ is the standard deviation of the ground motion prediction equation, and R_f is a reduction factor expressed as a function of T and T_p . The reduction factor accounts for the additional refinement resulting from inclusion of a directivity factor, which decreases the uncertainty associated with the ground motion prediction equation.

Shahi and Baker (2010) provided a similar expression for the diminution of spectral acceleration in the absence of directivity:

$$\ln S_{a,i}^{no\ pulse} = \ln D_f + \ln S_{a,i}^{GMPE} \quad (3.30)$$

where $S_{a,i}^{no\ pulse}$ is the spectral acceleration at the site when a directivity pulse is not observed and D_f is a deamplification factor. $\ln S_{a,i}^{no\ pulse}$ is normally distributed with mean $\mu_{\ln D_f} + \mu_{\ln S_{a,i}^{GMPE}}$ and standard deviation $\sigma_{\ln S_{a,i}^{GMPE}}$. It was found that the standard deviation need not be altered in the absence of directivity. $\mu_{\ln D_f}$ was given in Shahi and Baker (2010) as a function of the source-to-site distance and T .

The BN seismic demand model for spectral acceleration that accounts for the directivity effect according to the Shahi and Baker (2010) model is shown in Figure 3.22. This figure shows two common representation conventions used in BNs. A rectangle with rounded corners is an object behind which a BN is hidden to reduce graphical clutter. The object in Figure 3.22 hides the random field model to be described in Chapter 4. The shaded rectangle with dotted borders represents a plate. Nodes within a plate repeat for each GMPP in the system, and outside nodes are common to all plates.

The BN in Figure 3.22 introduces a two-state node P_i as a child of nodes X_r , X_e , R_L , and S_C . Node P_i represents the existence of a pulse-like motion at site i . As described above, the Shahi

and Baker (2010) model applies adjustment factors to the median and variance of spectral acceleration to account for the presence or absence of the directivity pulse. These factors are modeled in the BN by defining the median spectral acceleration as a child of node P_i and by introducing a variance reduction factor node $R_{f,i}$ as a child of P_i and a parent of the total error term associated with the spectral acceleration. The CPTs of nodes \bar{S}_i are defined conditioned on P_i using Equations (3.29) and (3.30) as well as the conventional attenuation relationship.

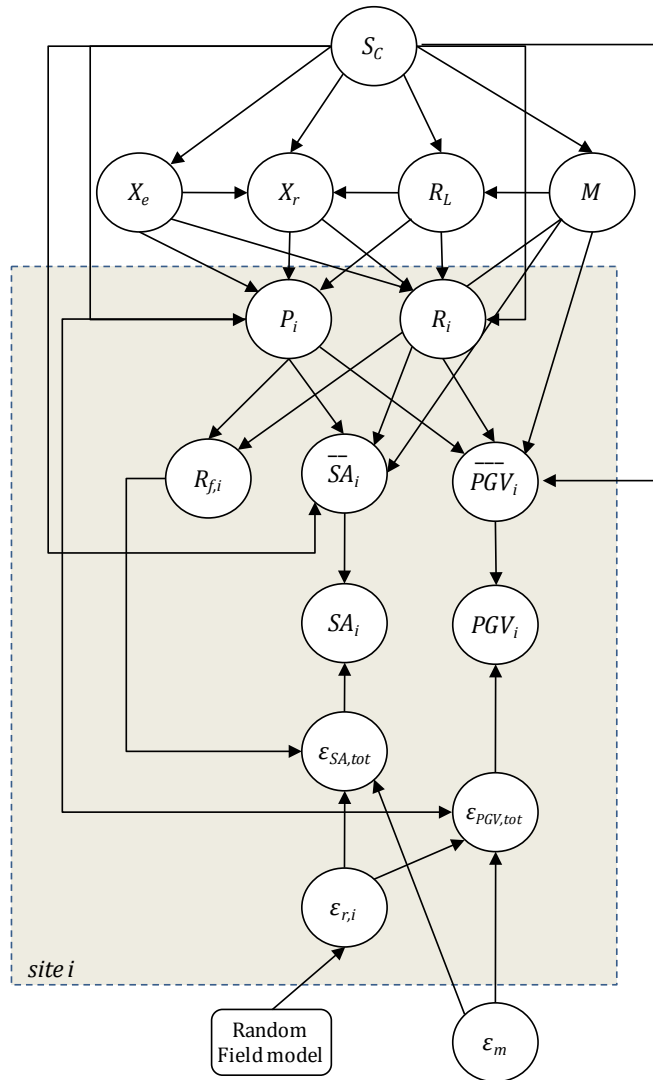


Figure 3.22: BN model of ground motion intensity at multiple sites accounting for directivity effects using the model of Shahi and Baker (2010) and Bray and Rodriguez-Marek (2004)

3.2.2.3.3 Directivity BN based on Bray and Rodriguez-Marek (2004)

For peak ground velocity, Bray and Rodriguez-Marek (2004) provided alternate prediction equations to be used when directivity effects are present, rather than modifying existing ground motion prediction equations. They did not provide prediction equations in the absence of directivity, nor did they provide estimates of the probability of experiencing directivity effects at a site for a particular earthquake. As a result, in the absence of directivity the conventional NGA prediction equations for PGV must be employed. In this study, we use the Bray and Rodriguez (2004) model for predicting PGV (for which no other models of directivity are available) when the directivity pulse is present and the conventional NGA equation for PGV when the pulse is absent, although the latter is somewhat conservative because of the “averaging” effect described earlier. The nodes required for the Bray and Rodriguez-Marek (2004) model are included Figure 3.22 along with the pulse prediction models of Shahi and Baker (2010). Because the Bray and Rodriguez-Marek (2004) model is a modified ground motion prediction, it follows the same logic as previously described for defining ground motion as a function of source and site parameters.

3.3 Hazard due to liquefaction

Liquefaction is the phenomenon in which soil turns from solid to liquid state as a result of rapid loading, including earthquake shaking. Ground shaking increases pore water pressure resulting in reduced effective stress and consequently decreased shear strength (Kramer 1996). Liquefaction occurs in two types: flow liquefaction and cyclic mobility.

Flow liquefaction is characterized by flow failures caused by a static shear stress that exceeds the shear strength of the soil. Cyclic stresses induced by ground motion bring the soil to an unstable condition at which the strength drops sufficiently to allow flow failure. Flow liquefaction occurs suddenly, and the liquefied material can travel long distances. Flow liquefaction occurs less frequently than cyclic mobility, but results in more severe consequences (Kramer 1996).

Cyclic mobility, driven by both cyclic and static stresses, occurs when the static stress does not exceed the shear strength of the soil. It develops incrementally throughout the duration of ground shaking and can occur even after shaking has stopped. Deformation induced by cyclic mobility is

called *lateral spreading* and can occur on gently sloping and flat ground. Cyclic mobility can produce surface effects known as sand boils (Kramer 1996).

Liquefaction can damage infrastructure systems in several ways (Rauch 1997): (1) foundations may experience sudden loss of load-bearing capacity resulting in irregular settlement of the supported structure; (2) differential settlement of pipelines may result from sudden loss of capacity of the supporting soil at different points along the pipe; (3) buried components in liquefied soil may float to the surface causing breakage; and (4) slope failures may cause damage to infrastructure components or structures located on the incline.

Evaluating liquefaction potential and consequences at a site involves the assessment of (1) the likelihood of initiation of liquefaction, (2) the post-liquefaction strength and stability of the soil, and (3) the deformations and displacements resulting from liquefaction (Seed et al. 2003). There is great uncertainty associated with each of these steps, but only recently have probabilistic methods been applied to this problem. Much research has been directed at specifying vulnerable soil classes. More information can be found in Seed et al. (2003) and Cetin et al. (2004).

The likelihood of liquefaction initiation is assessed on the basis of laboratory research and, more commonly, empirical relations derived from field observations. These relations are typically expressed as a function of measurements from common tests, such as the standard penetration test (SPT), the cone penetration test (CPT, not to be confused with CPT for “conditional probability table”), measurement of shear wave velocity, and the Becker penetration test (BPT).

The assessment of potential consequences when liquefaction does occur is less mature. Seed et al. (2003) noted that large deformations (> 1 m) can be estimated within a factor of two, but such accuracy is not typical with small to moderate displacements. Small to moderate displacements result from more complicated phenomena and are of more significant engineering interest, because sites prone to large deformations are typically mitigated while sites prone to smaller amounts may not be. Seed et al. (2003) present more details related to the phenomenon of liquefaction.

3.3.1 Existing Bayesian network-based liquefaction models

Bayraktarli (2006) developed a BN for liquefaction assessment that is shown in **Error! Reference source not found.**

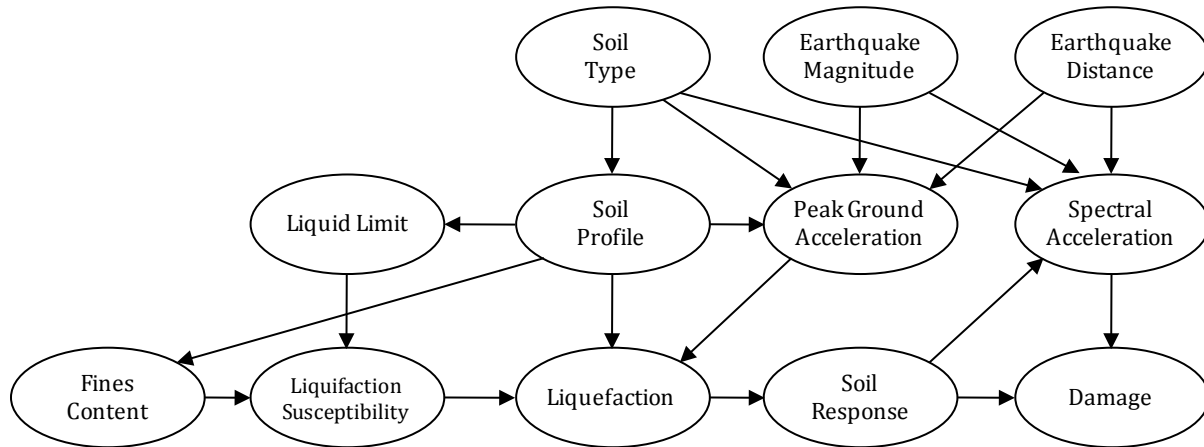


Figure 3.23: Liquefaction BN developed by Bayraktarli (2006)

The nodes for earthquake magnitude, source-to-site distance, and damage are described in Section 3.2.1. Node *Soil Type* takes on five states: rock, gravel, sand, silt, and clay. The spectral acceleration is computed as a function of the magnitude, source-to-site distance, soil type, and soil response (to account for the effect of liquefaction on ground motion experienced at the site). The node representing soil profile corresponds to the different layers of a bore profile at a site. The node *Peak Ground Acceleration* is defined as a function of nodes that represent earthquake magnitude, earthquake distance, soil type, and soil profile. The node representing liquefaction susceptibility is logically related to nodes corresponding to fines content and liquid limit using the Modified Chinese Criteria (Liam Finn et al. 1994). The probabilities required to populate the CPT for node *Liquefaction* are obtained through simulation using the limit state function $g(x) = CRR_{7.5} * MSF * K_{\sigma} - CSR = 0$, where $CRR_{7.5}$ is a function of SPT blow count $(N_1)_{60}$, MSF is a function of earthquake magnitude, K_{σ} is a correction factor, and CSR is a function of a_{max} (maximum acceleration in a soil layer, computed as a function of the PGA on rock using one-dimensional wave propagation analysis), effective stresses, and a depth reduction coefficient. Node *Soil Response* has two states: amplification and liquefaction.

3.3.2 Proposed formulation

In this section we present a preliminary BN for modeling seismic demands placed on the components of an infrastructure system due to liquefaction. Development of a more sophisticated and refined model is left as an area warranting further study. The formulation developed in this section differs from the formulation of Bayraktarli (2006) in several ways. First, it assumes that all variables related to site characteristics are either deterministic or are stochastic but unobservable. Therefore they are not explicitly modeled as nodes, as Bayraktarli (2006) did, but they influence the CPTs of nodes that appear in the BN. Nodes corresponding to these variables can be added, but at the expense of additional computational demand and increased discretization error. Second, all layers are considered simultaneously rather than layer by layer, as Bayraktarli (2006) did. Furthermore, the BN presented here assumes that the output quantities of interest are the seismic demands placed on structural and geotechnical components of the infrastructure system, and therefore nodes representing total seismic settlement are explicitly included. Finally, whereas Bayraktarli (2006) used Monte Carlo simulation to estimate the probability of liquefaction using a defined limit state function, we use published empirical relationships to estimate this probability as a function of ground motion intensity as estimated from ground shaking models. This permits us to include spatial correlation in estimating the likelihood of liquefaction at sites in close proximity. Our preliminary BN that models liquefaction-induced demands and the associated seismic settlements is presented in Figure 3.24. The construction of the CPTs it requires is described next.

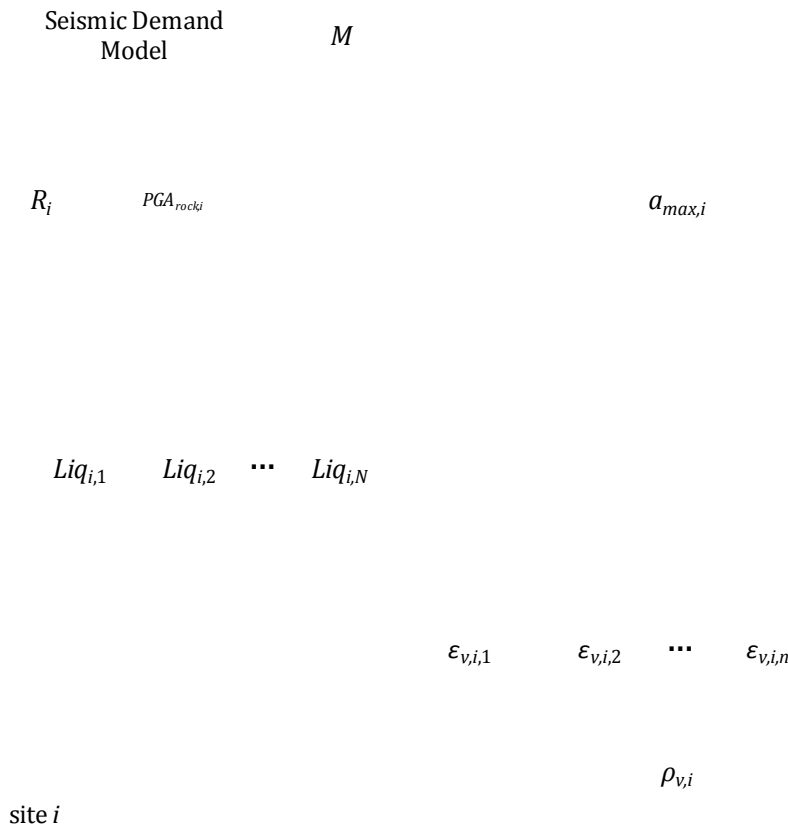


Figure 3.24: BN modeling seismic demands resulting from liquefaction

The soil profile at the site must be discretized into layers corresponding to changes in soil characteristics, e.g., soil class, SPT blow count, fines content (FC), plasticity index (PI), depth to water table, unit weight (γ), and relative density (D_R). A layer of soil experiences liquefaction if the cyclic stress ratio CSR (the demand) placed on it exceeds the cyclic resistance ratio CRR . CRR is computed using empirical relations as a function of soil tests (SPT, CPT, BPT) or shear wave velocity measurements.

The CSR for a soil layer is expressed as a function of the peak surface acceleration (a_{max}), the total and effective stresses in the layer (expressed as a function of unit weight and layer thickness), and the depth reduction coefficient r_d (available from published correlations, typically as a function of depth). a_{max} can be computed as a function of base rock acceleration using a variety of methods, including simplified procedures (Seed and Bray 1997), code-based methods (International Code Council 2006), and one-dimensional site response wave

propagation analysis (Ordenez 2009). Thus, in Figure 3.24, $a_{max,i}$ is a child of $PGA_{rock,i}$. Cetin et al. (2002) and Moss et al. (2006) provided expressions for the probability that a layer will liquefy as a function of the CSR , earthquake magnitude, and layer properties characterizing the liquefaction resistance. We use these expressions to populate the CPTs associated with the binary (liquefaction/no liquefaction) nodes $Liq_{i,k}$, $k = 1, \dots, N$ where N is the number of discrete layers at site i that are susceptible to liquefaction (e.g., as defined by the modified Chinese criteria in Liam Finn et al. 1994). The expression for probability of liquefaction given by Cetin et al. (2002) is applicable when the resistance is measured in terms of $(N_1)_{60}$ (a SPT-based correlation), whereas the expression given by Moss et al. (2006) uses a CPT-based expression. For each state of $PGA_{rock,i}$, whose value comes from the ground-shaking seismic demand model, the CPT for the node $a_{max,i}$ is computed using one of the aforementioned procedures.

The goal of the liquefaction BN in Figure 3.24 is to model the effects of liquefaction, such as soil displacement and settlement. If the k th layer liquefies, the induced volumetric strain $\epsilon_{v,i,k}$ is computed as a function of layer properties using existing relations (Tokimatsu and Seed 1987; Ishihara and Yoshimine 1992). The total settlement at site i is then computed as $\rho_{v,i} = \sum_{k=1}^N h_k * \epsilon_{v,i,k}$, where h_k is the height of layer k . These relations are used to produce the CPTs for nodes $\epsilon_{v,i,k}$ and $\rho_{v,i}$ in Figure 3.24. Because the converging structure linking $\rho_{v,i}$ with its parent nodes is computationally inefficient, it is replaced with a chain-like structure as shown in Figure 3.25. The CPT associated with node $\rho_{v,i,1}$ uses the relation $\rho_{v,i,1} = \mathbb{I}[\text{liquefaction occurs in layer 1}] * h_1 * \epsilon_{v,i,1}$, where $\epsilon_{v,i,1}$ is computed for layer 1 using relations in terms of earthquake magnitude, CSR , and layer properties (Tokimatsu and Seed 1987; Ishihara and Yoshimine 1992). For all other layers ($k = 2, \dots, N$):

$$\rho_{v,i,k} = \mathbb{I}[\text{liquefaction occurs in layer } k] * h_k * \epsilon_{v,i,k} + \rho_{v,i,k-1}. \quad (3.31)$$

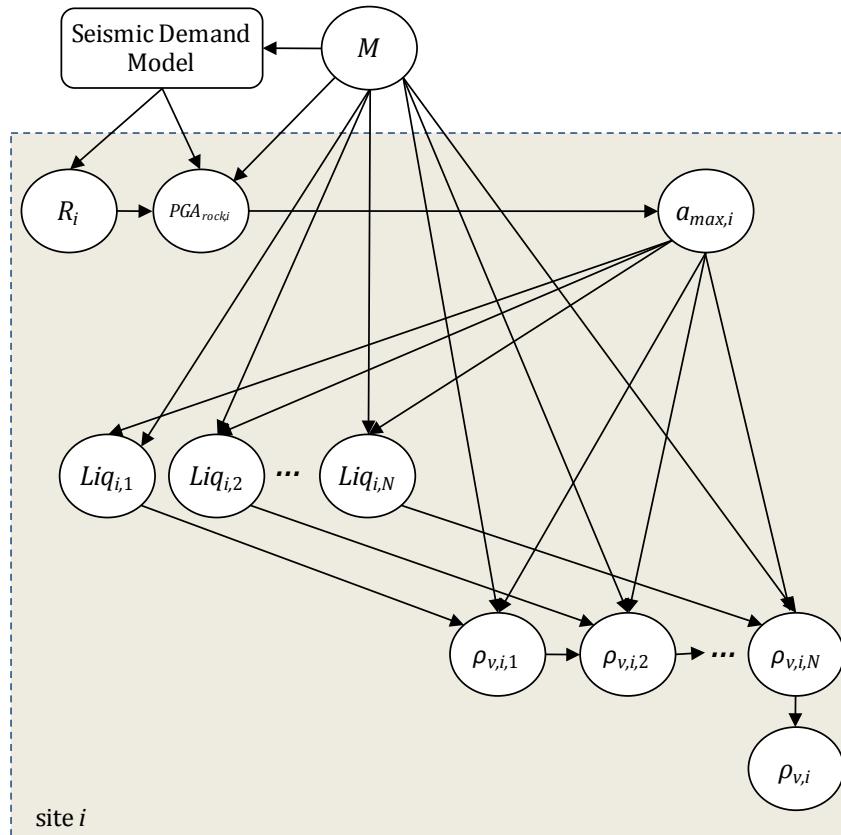


Figure 3.25: Liquefaction modeling seismic demands resulting from liquefaction with converging structure in Figure 3.24 at node $\rho_{v,i}$ replaced by a chain structure

Setting $\rho_{v,i} = \rho_{v,i,N}$ gives the total liquefaction-induced seismic settlement at the site. The liquefaction model shown in Figure 3.25 should only be added to the BN for sites vulnerable to liquefaction. Furthermore, it may be preferable to reduce computational demands by eliminating nodes $Liq_{i,j}$ and $\rho_{v,i,j}$ and computing the CPT $\rho_{v,i}$ directly as a function of $a_{max,i}$.

Similar models yield estimates of lateral spreading of sloping ground and ground with a vertical discontinuity (i.e., a free face) as a function of site and earthquake characteristics (see Youd et al. 2002). Finite-element models have also been used to assess ground stability (see Seed et al. 2003 for a summary). BN models for these hazards can be developed in a similar manner.

3.4 Hazard due to fault rupture

Hazard due to fault rupture is an important vulnerability of distributed infrastructure systems, in which long components (e.g., pipelines, bridges, embankments) may cross a fault. A generic and preliminary BN model framework is described here to address this hazard. Development of a refined model is left as future work. It is assumed that fault rupture effects need only be included when a distributed component crosses a known fault that has potential to cause permanent differential displacement of engineering significance at the surface. The effects of incoherence of ground motions on either side of the fault are not considered, although such effects may be critical for certain distributed components. Development of models to consider such effects is left as an area warranting future study.

For sites crossing faults, the BN has new nodes to account for fault rupture effects. First, a binary node RC_i is added indicating whether the rupture passes the point at which the component crosses the fault. This node is a child of nodes X_r, R_L, S_c representing the geometry of the rupture. A node SS_i is added to represent the maximum amount of surface slip associated with the fault rupture, modeled as a function of earthquake magnitude and source characteristics. The performance of the distributed component crossing the fault is computed as a function of the induced ground displacement and the deformation capacity of the component. Node C_i represents the damage stage of the component. The associated BN is shown in Figure 3.26, with nodes not applicable to the fault-rupture model omitted.

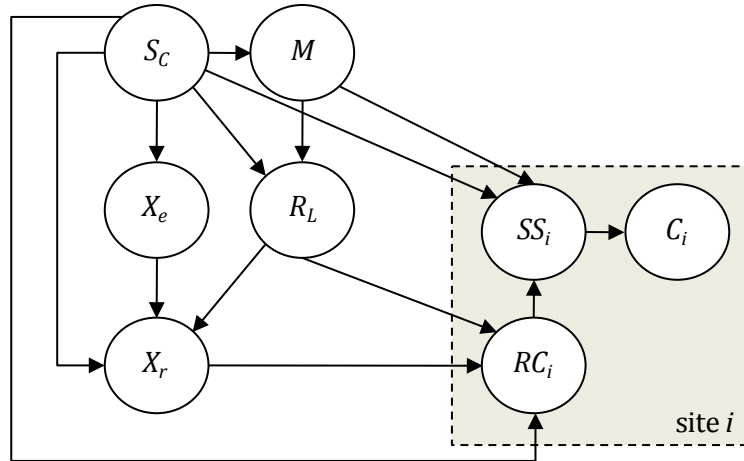


Figure 3.26: Preliminary fault rupture BN

3.5 Appendix: Earth-centered Earth-fixed coordinate system

The seismic demand model developed in this chapter requires definition of a fault-specific local coordinate systems. Typically, locations are specified using latitude, longitude, and altitude. To facilitate the conversion to a local rectangular (Cartesian) coordinate system, the latitude/longitude/altitude geographic coordinates of a location are first converted to Earth-centered Earth-fixed (ECEF) coordinates (Clynch 2006).

The ECEF coordinate system is a rectangular coordinate system with its origin (0,0,0) at the mass center of the Earth. The z-axis goes through the true North Pole, and the x-axis extends through the intersection of the Prime Meridian and the Equator. The y-axis, consistent with a “right-hand-rule” coordinate system, passes through the intersection of the Equator and the 90° longitude meridian. Using assumptions about the shape of the Earth based on the WGS84 standard coordinate frame (DoD 2000), latitude/longitude/altitude data are converted to ECEF data as described by Farrell and Barth (1999).

In this study, coordinates of all sites are defined with respect to a source-specific local coordinate system. To do this, the ECEF coordinate system is shifted from an origin at the center of the Earth to one centered at one end of the fault. Then the coordinate system is rotated so that the

first segment of the fault coincides with the x -axis, which involves a rotation about the z -axis and another about the y -axis. Thus, the coordinate transformation consists of three steps:

1. Shifting of the origin to fault-centered ECEF coordinates $(x_{f,0}, y_{f,0}, z_{f,0})$:

$$\begin{aligned}x' &= x - x_{f,0} \\y' &= y - y_{f,0} \\z' &= z - z_{f,0}\end{aligned}\tag{3.32}$$

2. Rotation about the z -axis:

$$\begin{aligned}x'' &= x' \cos(\phi_1) + y' \sin(\phi_1) \\y'' &= -x' \sin(\phi_1) + y' \cos(\phi_1) \\z'' &= z'\end{aligned}\tag{3.33}$$

where:

$$\begin{aligned}\phi_1 &= \tan^{-1}\left(\frac{y'_{f,1}}{x'_{f,1}}\right) \text{ if } x'_{f,1} > 0 \\&= \tan^{-1}\left(\frac{y'_{f,1}}{x'_{f,1}}\right) + \pi \text{ if } x'_{f,1} < 0 \text{ and } y'_{f,1} \geq 0 \\&= \tan^{-1}\left(\frac{y'_{f,1}}{x'_{f,1}}\right) - \pi \text{ if } x'_{f,1} < 0 \text{ and } y'_{f,1} < 0 \\&= \frac{\pi}{2} \text{ if } x'_{f,1} = 0 \text{ and } y'_{f,1} > 0 \\&= -\frac{\pi}{2} \text{ if } x'_{f,1} = 0 \text{ and } y'_{f,1} < 0 \\&= 0 \text{ if } x'_{f,1} = 0 \text{ and } y'_{f,1} = 0\end{aligned}\tag{3.34}$$

3. Rotation about the y -axis:

$$\begin{aligned}x''' &= x'' \cos(\phi_2) + z'' \sin(\phi_2) \\y''' &= y'' \\z''' &= -x'' \sin(\phi_2) + z'' \cos(\phi_2)\end{aligned}\tag{3.35}$$

where ϕ_2 is defined in a manner similar to Equation (3.34) but using $x''_{f,1}$ and $z''_{f,1}$ instead of $x'_{f,1}$ and $y'_{f,1}$, respectively.

4. Bayesian Network Modeling of Gaussian Random Fields

4.1 Introduction

In civil engineering applications, it is often necessary to model vectors of random variables drawn from a random field. In the current application, the earthquake-induced ground motion intensities at the locations of the system components constitute a vector of random variables drawn from the ground-motion random field. (For another example not related to this study, factors determining the progress of deterioration in elements of concrete surfaces are random variables drawn from environmental and material property random fields.) Proper modeling of the dependence structure of such vectors of random variables is essential for accurate probabilistic analysis. In the special case when the field is Gaussian or derived from a Gaussian field, the spatial dependence structure of the field is completely defined by the autocorrelation function, and the correlation matrix fully defines the dependence structure of the random vector drawn from the field. Typically, this correlation matrix is fully populated. Although this chapter only deals with Gaussian random fields, the methods developed are equally applicable to non-Gaussian fields that are derived from Gaussian fields (e.g., Grigoriu 2000).

In some applications, it is of interest to update a probabilistic model in light of available or assumed observations of the random field. In this study, we may be interested in updating the reliability of the system when ground motion intensities at one or more locations are observed. (In the case of the concrete surface, the reliability of the system would be updated when cracking is observed in some of the elements.) The BN methodology is a powerful tool for such purposes, particularly when the available information evolves in time and the updating must be done in real

or near-real time (e.g., Straub 2009). However, there is a challenge in modeling random variables drawn from a random field: due to the full correlation structure of the random variables, the BN becomes densely connected. When combining these random variables with system models that involve additional random variables, the computational and memory demands rapidly grow with the number of points drawn from the random field. In this chapter, we develop approximate methods to overcome this difficulty by selectively eliminating nodes and links to reduce the density of the BN model of the random field, while limiting the resulting error. As described earlier, continuous random variables must be discretized in order to allow use of exact BN inference algorithms. Although not explicitly discussed, such discretization will need to be performed for practical implementation of the BN models that result from the approximate methods developed in this chapter.

The chapter begins with BN models of random variables drawn from a Gaussian random field. Approximation methods are then developed to achieve computationally tractable BN models. Numerical studies using various spatial configuration models are used to compare the relative effectiveness of these approximation methods. Then the effects of the random field approximation on estimated reliabilities of example spatially distributed systems are investigated. Finally, we present recommendations for efficient BN modeling of random variables drawn from a random field.

4.2 Bayesian network modeling of random fields

Let $Y(\mathbf{x})$, $\mathbf{x} \in \Omega$, be a multidimensional Gaussian random field defined within the domain Ω with mean function $\mu_Y(\mathbf{x})$, standard deviation function $\sigma_Y(\mathbf{x})$, and autocorrelation coefficient function $\rho_{YY}(\mathbf{x}_1, \mathbf{x}_2)$, $(\mathbf{x}_1, \mathbf{x}_2) \in \Omega$. Without loss of generality, hereafter we work with the normalized random field

$$Z(\mathbf{x}) = \frac{Y(\mathbf{x}) - \mu_Y(\mathbf{x})}{\sigma_Y(\mathbf{x})} \quad (4.1)$$

where $Z(\mathbf{x})$ is a stationary Gaussian random field with zero mean, unit variance, and, because of the linearity of the transformation, autocorrelation coefficient function $\rho_{ZZ}(\mathbf{x}_1, \mathbf{x}_2) = \rho_{YY}(\mathbf{x}_1, \mathbf{x}_2)$.

Consider random variables $Z_i = Z(\mathbf{x}_i)$, $i = 1, \dots, n$, drawn from $Z(\mathbf{x})$ at selected points \mathbf{x}_i within Ω . The Gaussian vector $\mathbf{Z} = [Z_1, Z_2, \dots, Z_n]^T$ has zero means, unit standard deviations, and correlation matrix $\mathbf{R} = [\rho_{ij}]$, where $\rho_{ij} = \rho_{YY}(\mathbf{x}_i, \mathbf{x}_j)$, $i, j = 1, \dots, n$. We consider the general case where the correlation matrix is fully populated. Figure 4.1 shows a BN model of vector \mathbf{Z} . The correlation structure implies links between all pairs of Z -nodes. The particular formulation in Figure 4.1 requires the conditional distribution of each Z_i to be specified given its parent nodes Z_1, \dots, Z_{i-1} . That is, the conditional probability $\Pr(Z_i = z_i | Z_1 = z_1, \dots, Z_{i-1} = z_{i-1})$ must be specified for each combination of the mutually exclusive states of Z_1, \dots, Z_{i-1}, Z_i . It should be clear that the CPT of node Z_n can become extremely large as n increases.

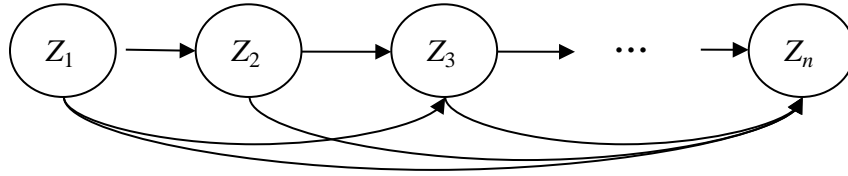


Figure 4.1: BN model of vector \mathbf{Z} drawn from Gaussian random field $Z(\mathbf{x})$

Vector \mathbf{Z} may be decomposed as a product of an $n \times n$ transformation matrix \mathbf{T} and an $n \times 1$ vector of statistically independent, standard normal random variables \mathbf{U} :

$$\mathbf{Z} = \mathbf{T}\mathbf{U} = \begin{bmatrix} t_{11} & \cdots & t_{1n} \\ \vdots & \ddots & \vdots \\ t_{n1} & \cdots & t_{nn} \end{bmatrix} \begin{Bmatrix} U_1 \\ \vdots \\ U_n \end{Bmatrix} \quad (4.2)$$

The transformation matrix \mathbf{T} may be determined using an eigenvalue (Karhunen–Loève) expansion, Cholesky factorization, or other decomposition method that diagonalizes the covariance matrix (Trefethen and Bau 1997). Alternatively, the transformation matrix may be determined approximately by numerical optimization (Song and Kang 2009; Song and Ok 2009), as described later in this chapter. The BN corresponding to the above transformation is shown in Figure 4.2, where the latent U -nodes are introduced as parents of the Z -nodes. Here, an element of the transformation matrix, t_{ij} , is interpreted as a factor on the link between U_j and Z_i . A value of $t_{ij} = 0$ corresponds to no link between U_j and Z_i . Due to the unit covariance matrix of \mathbf{U} , we have $\mathbf{R} = \mathbf{T}\mathbf{T}^T$. The CPTs required by the BN in Figure 4.2 are easier to specify than those for the BN in Figure 4.1, because each Z_i is a deterministic function of its parent U -nodes.

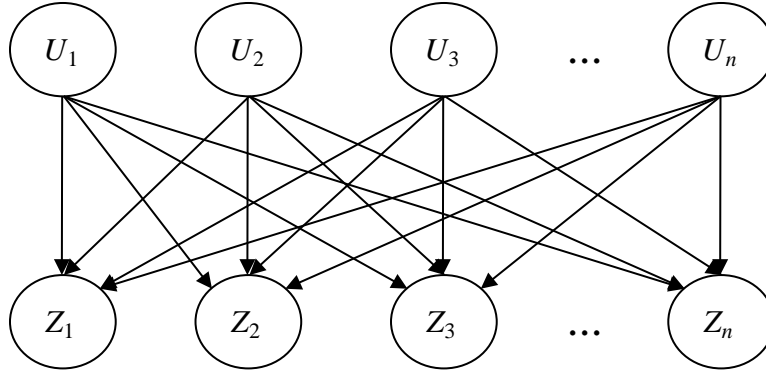


Figure 4.2: BN model of decomposition of vector \mathbf{Z} drawn from Gaussian random field $\mathbf{Z}(\mathbf{x})$

The BNs in Figure 4.1 and Figure 4.2 are densely connected and, therefore, exact inference becomes computationally intractable as the number n of random variables increases. Reducing the number of links retains computational tractability, but removing links introduces error. Hence, in developing a procedure for link elimination, the goal is to balance computational efficiency and model accuracy by removing as many links as possible without causing significant loss of accuracy. A procedure must be defined to identify and eliminate links that are least critical for accurately modeling the vector \mathbf{Z} .

Define $\hat{\mathbf{T}} = [\hat{t}_{ij}]$ as the approximate transformation matrix with some of its elements set to zero. Setting $\hat{t}_{ij} = 0$ implies removal of the link connecting U_j and Z_i . If column j of $\hat{\mathbf{T}}$ has all zero entries, then node U_j has no children and can be eliminated from the BN. The removal of links and nodes in the BN results in an approximation of the covariance matrix of \mathbf{Z} , including the on-diagonal variance terms. The errors in the variances are corrected by introducing an additional $n \times 1$ vector of statistically independent standard normal random variables \mathbf{V} and a diagonal transformation matrix \mathbf{S} ,

$$\hat{\mathbf{Z}} = \mathbf{S}\mathbf{V} + \hat{\mathbf{T}}\mathbf{U} = \begin{bmatrix} s_1 & \cdots & 0 \\ \vdots & \ddots & \vdots \\ 0 & \cdots & s_n \end{bmatrix} \begin{Bmatrix} V_1 \\ \vdots \\ V_n \end{Bmatrix} + \begin{bmatrix} \hat{t}_{11} & \cdots & \hat{t}_{1m} \\ \vdots & \ddots & \vdots \\ \hat{t}_{n1} & \cdots & \hat{t}_{nm} \end{bmatrix} \begin{Bmatrix} U_1 \\ \vdots \\ U_m \end{Bmatrix}, \quad (4.3)$$

where $\hat{\mathbf{Z}}$ denotes the approximated vector. Note that, after elimination of barren U -nodes, $\hat{\mathbf{T}}$ is an $n \times m$ matrix and \mathbf{U} is an $m \times 1$ vector, where $m \leq n$.

To achieve unit variances for $\hat{\mathbf{Z}}$, we set the condition

$$s_i = \sqrt{1 - \sum_{k=1}^m \hat{t}_{ik}^2}, \quad i = 1, \dots, n. \quad (4.4)$$

This correction does not affect the off-diagonal terms of the covariance matrix. Furthermore, the approximated correlation coefficients are given by

$$\hat{\rho}_{ij} = \sum_{k=1}^m \hat{t}_{ik} \hat{t}_{jk}, \quad i, j = 1, \dots, n. \quad (4.5)$$

The BN corresponding to the formulation in Equation (4.3) is shown in Figure 4.3. The addition of the V -nodes does not significantly increase the computational complexity of the BN.

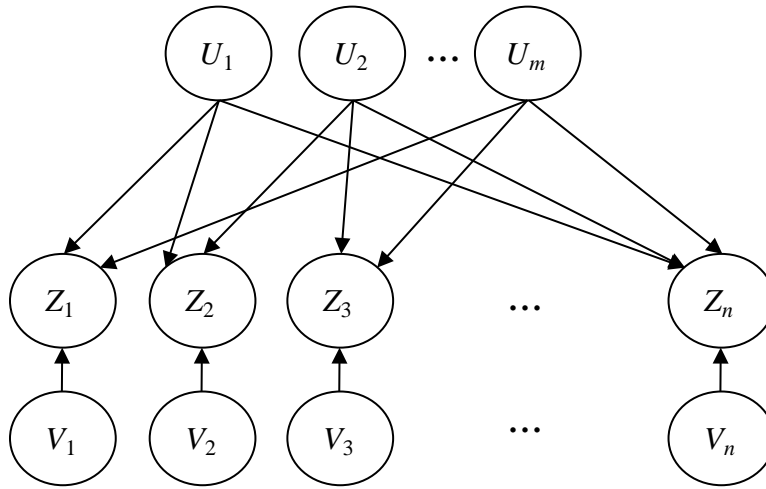


Figure 4.3: BN model of approximate decomposition $\hat{\mathbf{Z}} = \mathbf{SV} + \hat{\mathbf{T}}\mathbf{U}$

As suggested by Song and Kang (2009) and Song and Ok (2009), the transformation in Equation (4.3) may be regarded as a generalization of the Dunnett-Sobel class of Gaussian random variables (Dunnett and Sobel 1955). This class of random variables is defined by

$$Z_i = s_i * V_i + t_i * U, \quad i = 1 \dots n, \quad (4.6)$$

where V_i and U are independent standard normal random variables, and s_i and t_i are variable-specific coefficients satisfying the conditions $s_i = (1 - t_i^2)^{1/2}$ and $-1 \leq t_i \leq 1$. Note that U is

common to all Z_i and, therefore, is the source of the correlation among them. For this model, one can easily show that Z_i are standard normal random variables having the correlation coefficients $\rho_{ij} = t_i * t_j$ for $i \neq j$ and $\rho_{ij} = 1$ for $i = j$. As a special case, the Z_i are equicorrelated when all t_i are identical. The transformation in Equation (4.6) corresponds to that in Equation (4.3) with $\hat{\mathbf{T}}$ being an $n \times 1$ vector. The associated BN has a single common U -node as shown in Figure 4.4.

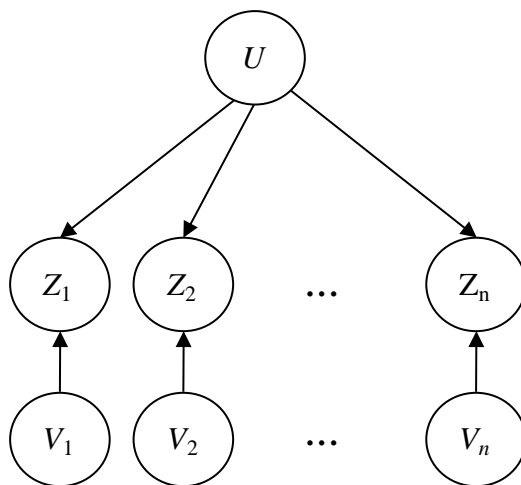


Figure 4.4: BN model of Dunnett-Sobel class of random variables

4.3 Construction of approximate transformation matrix $\hat{\mathbf{T}}$

As described above, setting elements of the transformation matrix $\hat{\mathbf{T}}$ to zero corresponds to removing links in the BN. Links may be removed by three means: (1) selectively removing U -nodes and all associated links by setting entire columns of the transformation matrix to zero, (2) selectively removing links by setting the corresponding elements of the transformation matrix to zero, or (3) doing both by first reducing the number of U -nodes and then selectively removing links from the remaining U -nodes.

To select nodes and links for elimination, we introduce node and link importance measures. For a transformation matrix \mathbf{T} (or $\hat{\mathbf{T}}$), the node importance measure (NIM) for node U_i is defined as

$$M_i = \sum_{k=1}^n \sum_{l=k}^n |\Delta_i(k, l)| \quad (4.7)$$

where $\Delta_i(k, l)$ is the (k, l) th element of the matrix

$$\Delta_i = \mathbf{t}_i \mathbf{t}_i^T \quad (4.8)$$

in which \mathbf{t}_i is the i th column of \mathbf{T} or $\hat{\mathbf{T}}$. Δ_i quantifies the contribution of U_i to the correlation matrix of \mathbf{Z} . Thus, M_i is a measure of the information contained in the correlation matrix \mathbf{R} that is lost by removing U_i . Clearly, eliminating the U -node associated with the smallest NIM will result in the least loss of accuracy. Nodes may be eliminated based on their NIM values until a preselected number of nodes remain or until a predefined threshold of NIM is exceeded.

Similarly, a link importance measure (LIM) associated with element t_{ij} of the transformation matrix \mathbf{T} or $\hat{\mathbf{T}}$ is defined as

$$m_{ij} = \sum_{k=1}^n \sum_{l=k}^n |\delta_{ij}(k, l)| \quad (4.9)$$

where $\delta_{ij}(k, l)$ is the (k, l) th element of the matrix

$$\delta_{ij} = \mathbf{t}_i \mathbf{t}_i^T - \mathbf{t}_{i,j} \mathbf{t}_{i,j}^T \quad (4.10)$$

in which \mathbf{t}_i is the i th column of \mathbf{T} or $\hat{\mathbf{T}}$ and $\mathbf{t}_{i,j}$ is equal to \mathbf{t}_i but with its j th element set equal to zero. Thus, m_{ij} is a measure of the information contained in the correlation matrix that is lost by eliminating the link from node U_j to node Z_i . It follows that eliminating the link associated with the smallest LIM will result in the least loss of accuracy. Links are eliminated based on their LIM until a preselected number remain, or until a predefined threshold of the LIM is exceeded. The node- and link-based approaches can be combined, eliminating U -nodes first on the basis of their NIMs, then eliminating links from the remaining nodes on the basis of their LIMs. Below, we describe three methods for constructing the transformation matrix \mathbf{T} and its approximation $\hat{\mathbf{T}}$ by use of the above measures.

4.3.1 Decomposition using eigenvalue expansion

Using an eigenvalue expansion, the transformation matrix can be obtained in the form (Jolliffe 2002)

$$\mathbf{T} = \mathbf{\Phi}\mathbf{\Lambda}^{1/2}, \quad (4.11)$$

where $\mathbf{\Phi} = [\boldsymbol{\phi}_1, \dots, \boldsymbol{\phi}_n]$ is the matrix of eigenvectors and $\mathbf{\Lambda} = \text{diag}[\lambda_i]$ is the diagonal matrix of eigenvalues obtained by solving the eigenvalue problem

$$\mathbf{R}\boldsymbol{\phi}_i = \boldsymbol{\phi}_i\lambda_i, i = 1, \dots, n. \quad (4.12)$$

In this case the transformation matrix is generally full and the resulting BN takes the form in Figure 4.2. The eigenvalues λ_i may be interpreted as factors associated with the U -nodes, while the elements in the eigenvectors are interpreted as factors of the links. It is well known that the order of contribution of the eigenvectors to the covariance matrix is consistent with the order of magnitudes of the corresponding eigenvalues (a property exploited by principal component analysis; see Jolliffe 2002). Our numerical investigations reveal that the order of the NIMs generally agrees with the eigenvalue ordering. Hereafter, we refer to the approach in which the transformation is defined by eigenvalue decomposition and U -nodes are eliminated based on their NIMs as the *node-based eigenvalue approach* (NEA). The approach in which individual links are eliminated based on their LIMs is referred to as a *link-based eigenvalue approach* (LEA). The use of a link-based elimination procedure in conjunction with eigenvalue decomposition was first suggested by Straub et al. (2008); however, the importance measure defined there is less general than the one introduced here as it only applies to transformation matrices obtained by eigenvalue decomposition.

4.3.2 Decomposition using Cholesky factorization

The decomposition approach using Cholesky factorization results in a transformation matrix \mathbf{T} that is triangular (Trefethen and Bau 1997). Assuming \mathbf{T} is a lower triangular matrix, the corresponding BN takes the form shown in Figure 4.5, where node Z_i has the parents U_1, \dots, U_i . By virtue of the triangular form of the transformation matrix, the BN in Figure 4.5 is less densely connected than the BN in Figure 4.3. However, the sizes of the largest CPT and the largest clique, $\{U_1, \dots, U_n, Z_n\}$, remain unchanged, making the formulations in Figure 4.2 and Figure 4.5 of the same order of computational complexity for exact inference. Using a node-elimination approach, the nodes corresponding to the rightmost columns of the transformation matrix are

typically associated with the smallest NIMs and are eliminated first. Hereafter, we refer to the elimination of nodes based on a transformation matrix determined by Cholesky decomposition as the *node-based Cholesky approach* (NCA). When individual links are eliminated by zeroing the elements in the Cholesky decomposition matrix based on their LIMs, the approach is referred to as the *link-based Cholesky approach* (LCA).

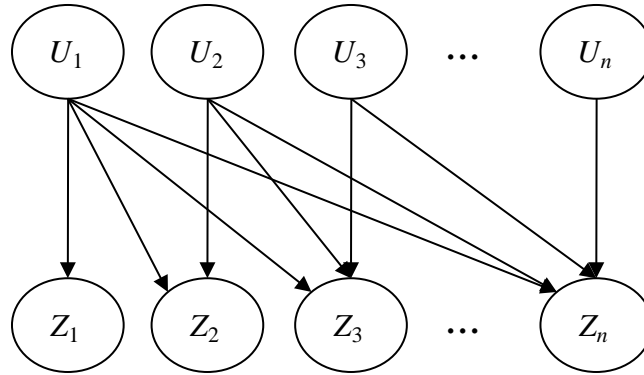


Figure 4.5: BN corresponding to transformation matrix obtained by Cholesky decomposition

4.3.3 Node and link elimination using optimization

Numerical optimization offers an alternative approach to defining the approximate transformation matrix $\hat{\mathbf{T}}$. We propose an optimization-based node-elimination approach consisting of two steps: (1) specification of the number $m \leq n$ of U -nodes to include in the BN and (2) solution of the nonlinear constrained optimization problem

$$\min \sum_{i=1}^{n-1} \sum_{j=i+1}^n \left[\rho_{ij} - \sum_{k=1}^m \hat{t}_{ik} * \hat{t}_{jk} \right]^2 \quad (4.13)$$

subject to: $\sum_{k=1}^m \hat{t}_{ik}^2 \leq 1, i = 1, \dots, n.$

The objective of the problem is to minimize the sum of squared deviations between the actual and approximated coefficients in the upper triangle of the symmetric correlation matrix (excluding the diagonal terms, which are later corrected using Equations (4.3) and (4.4)). The

constraint functions are based on Equation (4.4). The use of nonlinear constrained optimization to determine the terms of an approximate transformation matrix was earlier suggested by Song and Ok (2009) and Song and Kang (2009). Hereafter, construction of the approximate transformation matrix by use of the optimization scheme in Equation (4.13) is referred to as the *node-based optimization approach* (NOA).

Analogously, a link-based optimization problem may be formulated in which the number of links rather than nodes is specified. The result is a mixed-integer, nonlinear constrained optimization problem, which is difficult to solve in practice as it encounters problems with convergence and oversensitivity to initial values. Instead, an iterative procedure for link elimination is developed. First, the optimization problem in Equation (4.13) is solved for a prespecified m ; then the term in the resulting transformation matrix with the lowest LIM is set to zero and the remaining terms in the matrix are reoptimized. The link elimination is repeated until a preset number of links remain. The iterative algorithm is summarized in Figure 4.6. Hereafter, this procedure is referred to as the *iterative link-based optimization approach* (ILOA).

An alternative scheme is as follows: In each iteration step, all elements in the transformation matrix that have LIM values below a threshold are set to zero. The remaining elements in the matrix are then reoptimized according to Equation (4.13) and the procedure is repeated until no link has an LIM below the specified threshold. Hereafter, this procedure is referred to as the *alternative iterative link-based optimization approach* (AILOA).

For the numerical analysis reported in this chapter, the function *fmincon* in Matlab, which finds the minimum of a constrained nonlinear multivariable function, is used to solve the optimization problem in Equation (4.13).

```

INITIALIZE

Specify:
    m = maximum number of U-nodes to include
    L = number of links to eliminate
ELIMINATE NODES
1. Determine  $n \times m$  matrix  $\hat{\mathbf{T}}_0$  with elements obtained by solving the optimization problem in Equation (4.13)
ELIMINATE LINKS
for  $p = 1, \dots, L$ 
    1. Calculate LIMs for all elements of  $\hat{\mathbf{T}}_{p-1}$ 
    2. Identify  $p$  elements in  $\hat{\mathbf{T}}_{p-1}$  with the smallest LIM values. (These include elements previously set equal to zero.)
    3. Determine the  $n \times m$  matrix  $\hat{\mathbf{T}}_p$  by setting all elements identified in step 2 equal to zero and solving for the remaining elements according to Equation (4.13)
end

```

Figure 4.6: Iterative algorithm for determining $\hat{\mathbf{T}}$ through node and link elimination

4.3.4 Qualitative comparison of methods for constructing $\hat{\mathbf{T}}$

It is important to recognize a significant distinction between the decomposition methods (eigen-expansion and Cholesky factorization) and optimization methods described above. In decomposition methods, after setting selected elements to zero, the remaining elements in the transformation matrix remain unchanged. In the optimization methods, the matrix $\hat{\mathbf{T}}$ is reoptimized after each elimination step. In this sense, the optimization approaches are “dynamic” while the decomposition methods are “static.” Because of these characteristics, one can expect that the optimization approaches will generally outperform the decomposition methods.

The numerical trials in the next section demonstrate that from a practical standpoint, a node-elimination approach is preferable because the effect on the computational complexity of the BN is systematic. The modeler can easily predict the memory demands of the resulting BN before performing inference. The same cannot be said when links are individually eliminated. However, the link-elimination approach is often better able to capture the correlation structure of a given configuration of points drawn from a random field because unimportant links are eliminated selectively rather than in large groups, as is the case with the node-elimination approach.

4.4 Numerical investigation of approximation methods

In this section, a numerical investigation is performed to compare the efficiencies of the proposed methods for approximating the correlation structure of random variables drawn from a Gaussian random field in the context of BN analysis. Four generic configurations of points drawn from the random field are considered:

- (1) Points arranged along a line (Figure 4.7a)
- (2) Points arranged on a circle (Figure 4.7b)
- (3) Points arranged in a rectangular grid (Figure 4.7c)
- (4) Points arranged in clusters (Figure 4.7d)

Different sizes of the above configurations are considered by changing the number of points, n , and controlling the distance between points using a distance measure d , as defined in Figure 4.7. For the cluster configuration, the points in each cluster are distributed uniformly on the circumference of a circle of radius d centered at a predefined coordinate. For brevity, results for representative cases of the above configurations are shown and general trends are described.

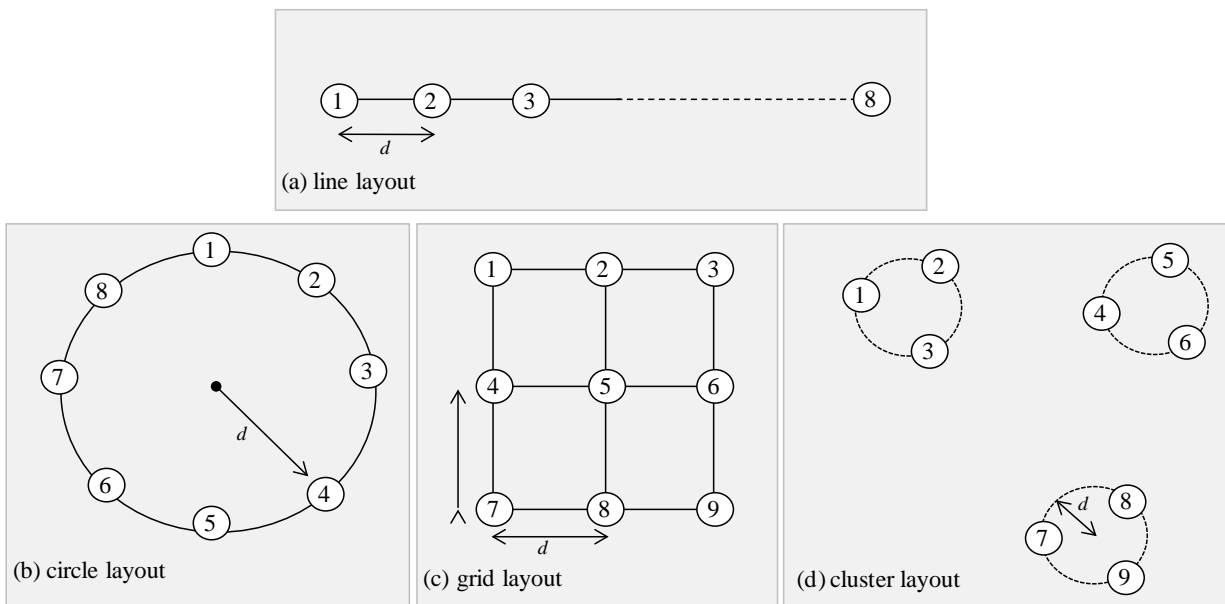


Figure 4.7: Generic configurations considered in numerical investigation

To measure the relative efficiencies of the aforementioned approximation methods (NEA, LEA, NCA, LCA, NOA, ILOA, and AILOA), the error measure

$$e = \frac{\sum_{i=1}^{n-1} \sum_{j=i+1}^n |\hat{\rho}_{ij} - \rho_{ij}|}{\sum_{i=1}^{n-1} \sum_{j=i+1}^n |\rho_{ij}|} \quad (4.14)$$

is used, where ρ_{ij} is the correlation coefficient between Z_i and Z_j and $\hat{\rho}_{ij}$ is the approximated correlation coefficient as defined in Equation (4.5). Note that the sums are over the upper triangle of the correlation matrix, excluding the diagonal terms. This error measure was selected because normalizing by the sum of absolute values of the correlation coefficients permits comparison of cases with varying sizes of vector \mathbf{Z} and a wide range of correlation values. (In section 4.5, we consider another error measure that is directly relevant to reliability assessment of an infrastructure system.) For each layout, this error is compared against a measure of the computational complexity of the resulting BN. For simplicity and intuitive appeal, we use the number of links in the BN as a proxy for computational complexity. The number of links in a BN does not perfectly match direct measures of computational complexity like the tree width, which is equal to one less than the size of the largest clique (Wainwright and Jordan 2008), but it serves our purpose of comparing alternative approximation methods.

For the numerical investigation, the Gaussian random field is assumed to be homogeneous and isotropic with the autocorrelation coefficient function

$$\rho_{VV}(\mathbf{x}_i, \mathbf{x}_j) = \exp\left(-\frac{\Delta \mathbf{x}_{ij}}{a}\right), \quad (4.15)$$

where $\Delta \mathbf{x}_{ij} = |\mathbf{x}_i - \mathbf{x}_j|$ is the distance between sites \mathbf{x}_i and \mathbf{x}_j and a is a measure of the correlation length of the random field with value $a = 6$ in units of distance. This correlation model, taken from Park et al. (2007), is motivated by our interest in applying the BN methodology to seismic risk assessment of infrastructure systems.

First consider a line layout system (Figure 4.7a) with 10 sites. For this system, an exact BN with the eigenvalue expansion method has $10^2 = 100$ links (see Figure 4.3) and with the Cholesky decomposition method it has $1 + 2 + \dots + 10 = 55$ links (see Figure 4.5). Figure 4.8 shows the error measure versus the number of links included in the BN for $d = 1, 5,$ and 10 (corresponding

to $d = \frac{1}{6}a$, $\frac{5}{6}a$, and $\frac{5}{3}a$) using the decomposition and optimization methods described above. All methods exhibit similar trends with increasing d : the error measure becomes larger and converges to zero more slowly. This is partly due to the definition of the error measure: For large d , correlations are small and therefore the error measure is magnified. For all d values and for both node- and link-elimination approaches, optimization methods consistently achieve smaller errors than decomposition methods. Among the optimization methods, ILOA and AILOA outperform NOA, particularly in speed of convergence to zero. For small d , the performances of NEA and LEA are close to those of the corresponding optimization approaches, but the performance of the eigen-expansion approaches rapidly degrades as d increases. This is because, for large d , correlation coefficients are small and eigenvalues of the resulting correlation matrix are of similar magnitude. Furthermore, LEA exhibits non-monotonic convergence. Conversely, the approaches based on Cholesky decomposition perform poorly for small distances, but their performance approaches those of the optimization methods as d increases. The above investigation was repeated for 5- and 15-site line layouts and similar trends were observed.

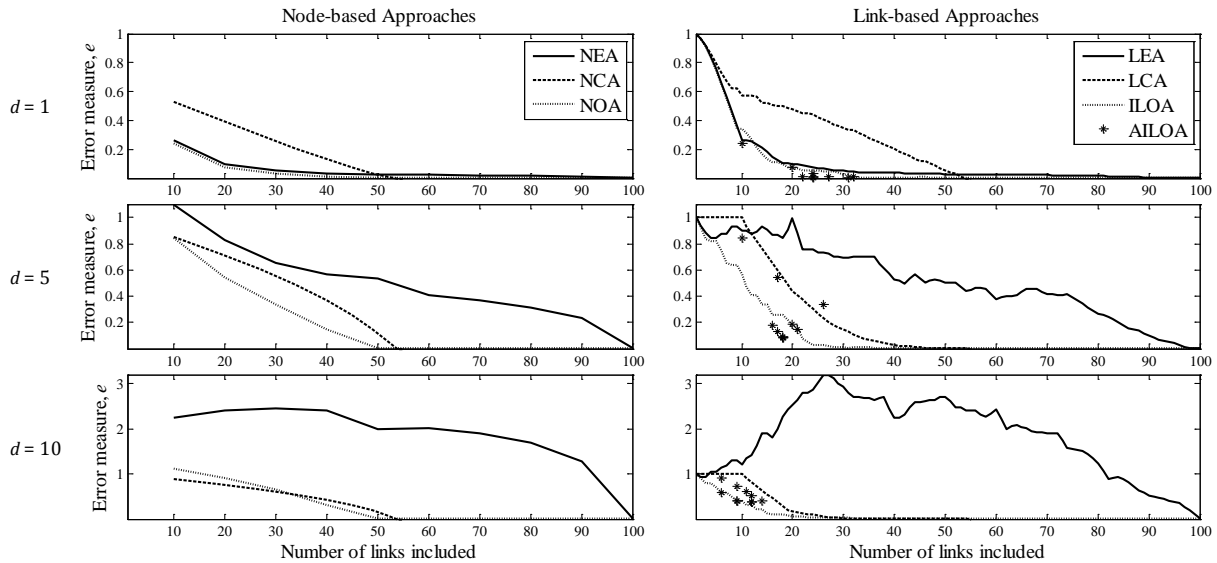


Figure 4.8: Error in approximating correlation matrix for 10-site line layouts

Figure 4.9 and Figure 4.10 respectively show the results for 10-site circle and 9-site grid layouts. As with the line layout, the optimization methods outperform the decomposition methods for all d values. For small d , all points in these layouts are closely spaced and, hence, the correlation

coefficients are large and relatively uniform in magnitude. As a result, the correlation structure is well captured by a few U -nodes, or even a single U -node. As d increases, the elements of the correlation matrix become less uniform. A larger number of nodes is then required to capture the correlation structure. In this situation, the link-based approaches exhibit better performance because they offer versatility in distributing links among different U -nodes.

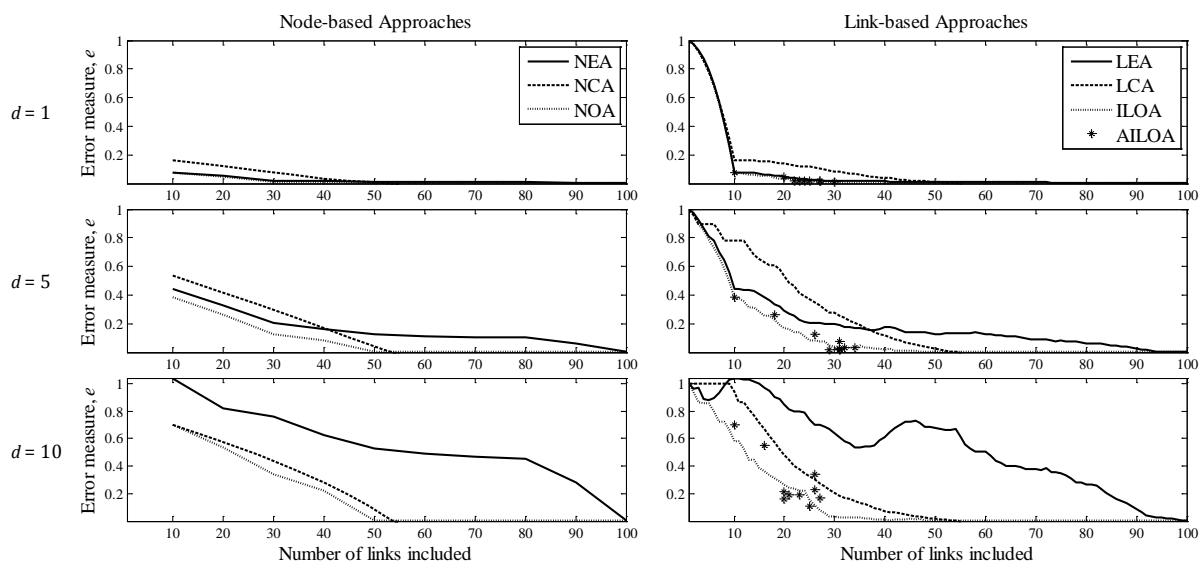


Figure 4.9: Error in approximating correlation matrix for 10-site circle layouts

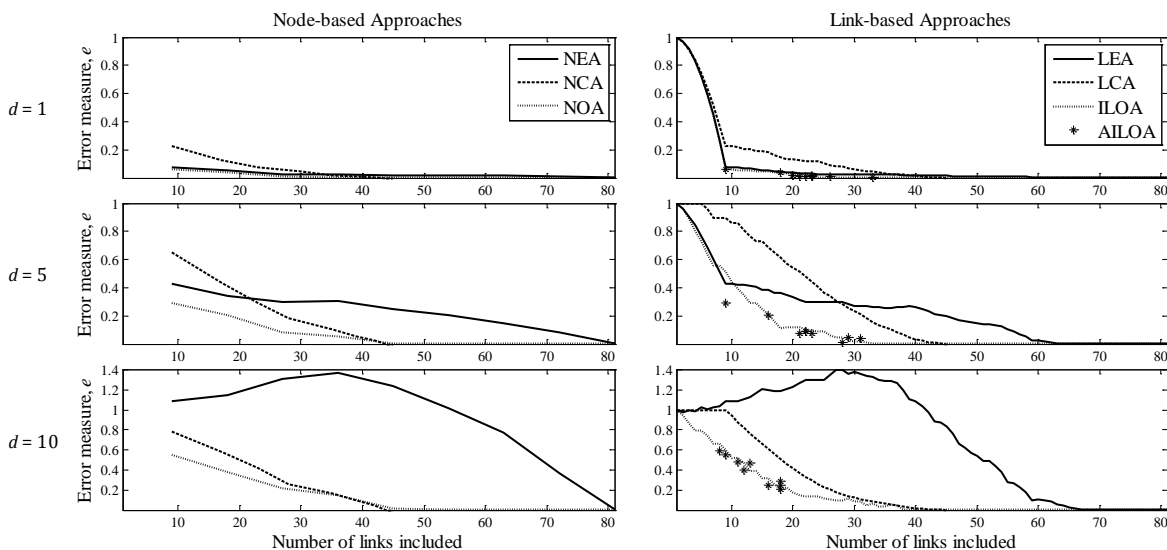


Figure 4.10: Error in approximating correlation matrix for nine-site grid layouts

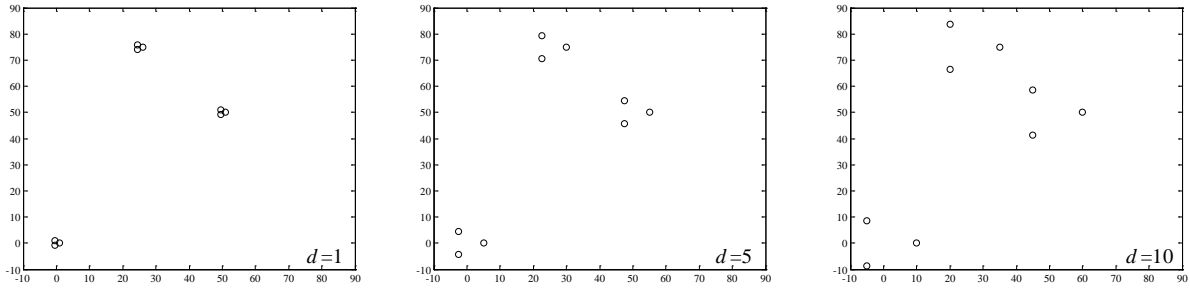


Figure 4.11: Example cluster layouts with $d = 1, 5,$ and 10

Finally, we consider the layout in which points are arranged in clusters. Figure 4.11 shows examples of nine-site layouts arranged into three three-site clusters centered at coordinates $(0,0)$, $(50,50)$, and $(25,75)$. For each cluster, points are equally distributed around a circle of radius d . Thus, d is a measure of how tightly the nodes in each cluster are arranged.

Figure 4.12 shows the errors for the 9-site cluster layouts with $d = 1, 5,$ and 10 . Among the node-based approaches, NCA and NOA perform similarly while NEA performs poorly, particularly for large d . Overall, the link-based approaches, excluding LEA, offer much better performance for the cluster layouts. This is because link-based approaches are able to distribute links among different U -nodes consistent with the geometry of the clusters. To illustrate this concept, consider the two BNs shown in Figure 4.13, which represent alternative approximations of the nine-node cluster system with nine links. The top BN uses the ILOA, which distributes the nine links such that the points in each cluster are connected to a common U -node and points in different clusters are uncorrelated. The bottom BN uses a node-based approach, in which nine links connect a single U -node to all the Z -nodes. Although both BNs in Figure 4.13 have the same number of links, ILOA distributes them more efficiently, consistent with the geometry of the layout. If clusters are sufficiently far apart, it is not necessary to include information paths (common U -nodes) between sites located in different clusters. This is why the link-based methods outperform node-based methods.

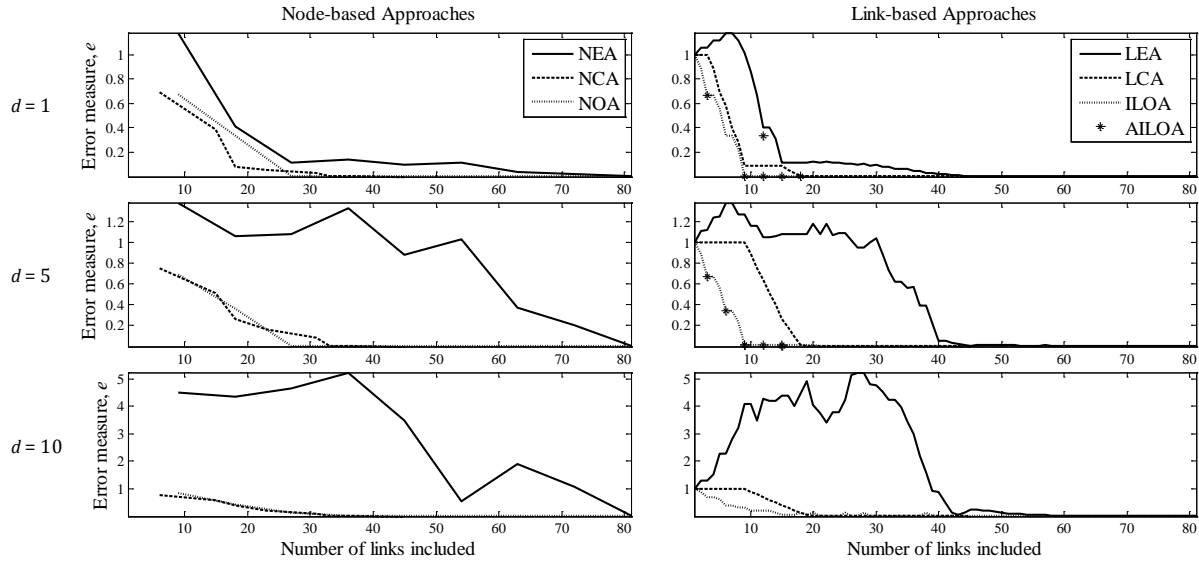


Figure 4.12: Error in approximating correlation matrix for nine-site cluster layouts

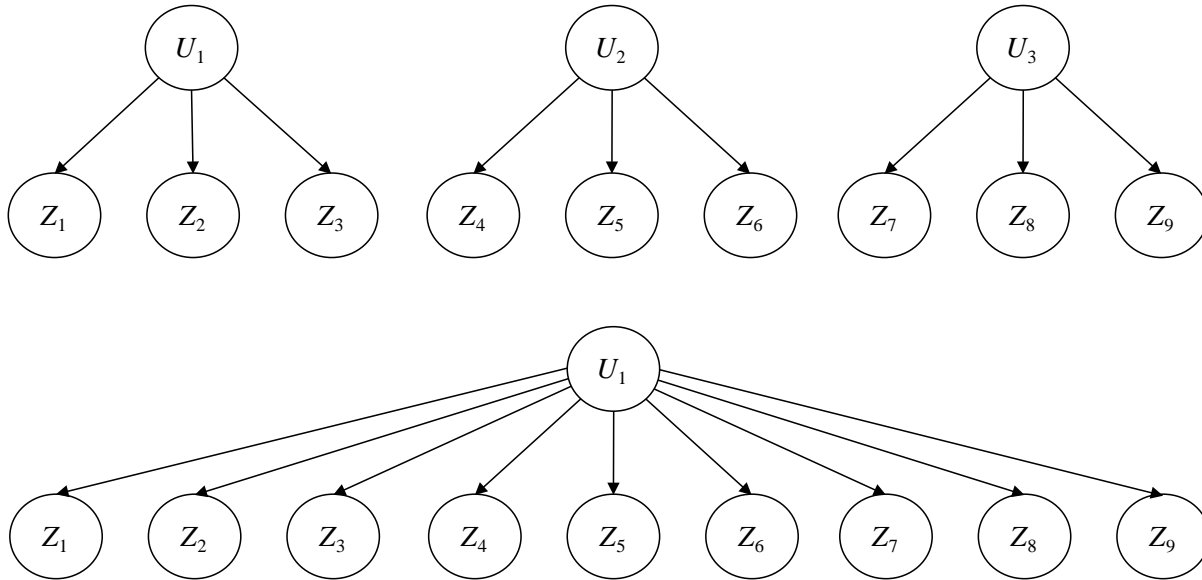
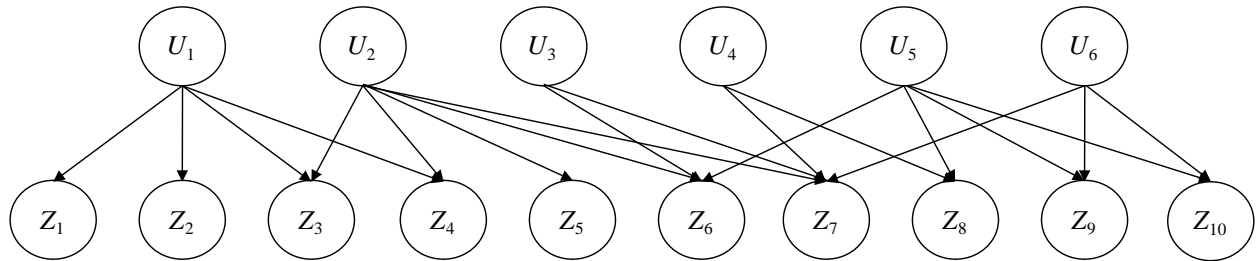


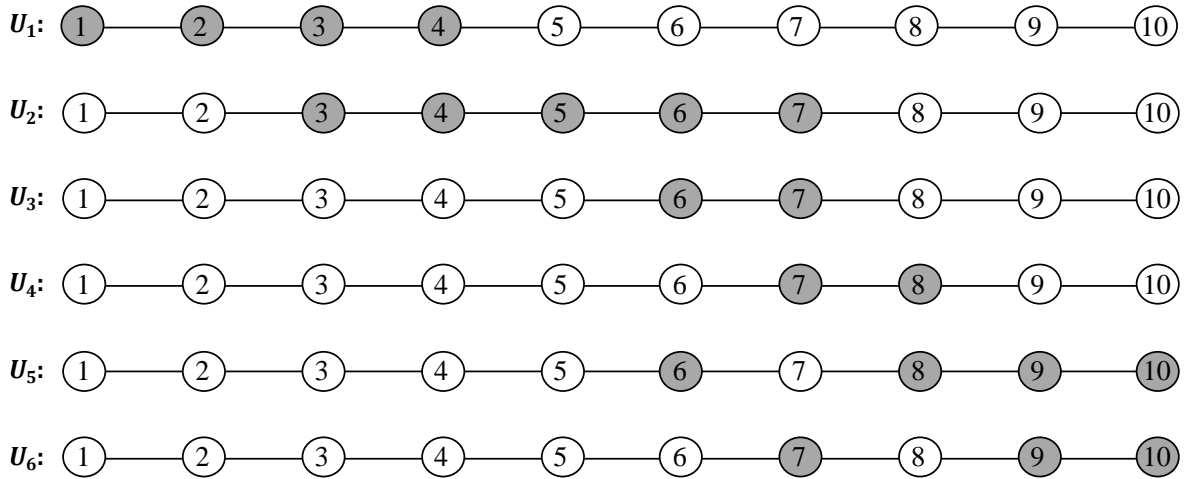
Figure 4.13: Nine-link BN approximations for nine-site cluster layouts using ILOA (top) and NOA (bottom)

For comparison, select BNs obtained using the ILOA for the 10-site line and circle and nine-site grid layouts for $d = 5$ are shown next. For the line and circle layouts, each BN contains $2n = 20$ links; the BN corresponding to the grid layout contains $2n = 18$ links. Note that the ILOA is an iterative procedure for identifying important links. The iterative procedure is used in lieu of considering the full link-based optimization problem, which is difficult to solve in practice.

Therefore, the BNs obtained from the procedure may not be globally optimal. Geometric interpretations of the resulting BNs for the line, circle, and grid layouts are not as clear as that for the cluster configuration; however, trends do exist.



(a)



(b)

Figure 4.14: (a) BN approximation using ILOA with 20 links; (b) illustration of sites linked by common U -node for 10-site line layout with $d = 5$

For the line layout, the BN using 20 links is shown in Figure 4.14a. In this BN, links are distributed so that there are overlapping information paths between nodes in close proximity. Sites located farther apart do not share a common U -node. Figure 4.14b graphically illustrates the sites that are linked by common U -nodes with shaded circles. The BN for the 10-site circle layout with 20 links is shown in Figure 4.15a and the corresponding diagram of sites sharing

common U -nodes is shown in Figure 4.15b. Because points are spaced concentrically in this layout, the sites are linked by a single common U -node when as few as 10 links are considered (see the second diagram in Figure 4.15b). When more than 10 links are included, overlapping information paths around the circle are added, similar to the trend seen for the line layout. For the grid layout, the BN containing the 18 most important links defined by ILOA is shown in Figure 4.16a and the diagram of sites sharing common U -nodes is shown in Figure 4.16b. For this layout with 18 links, links are distributed so that adjacent sites share at least one U -node.

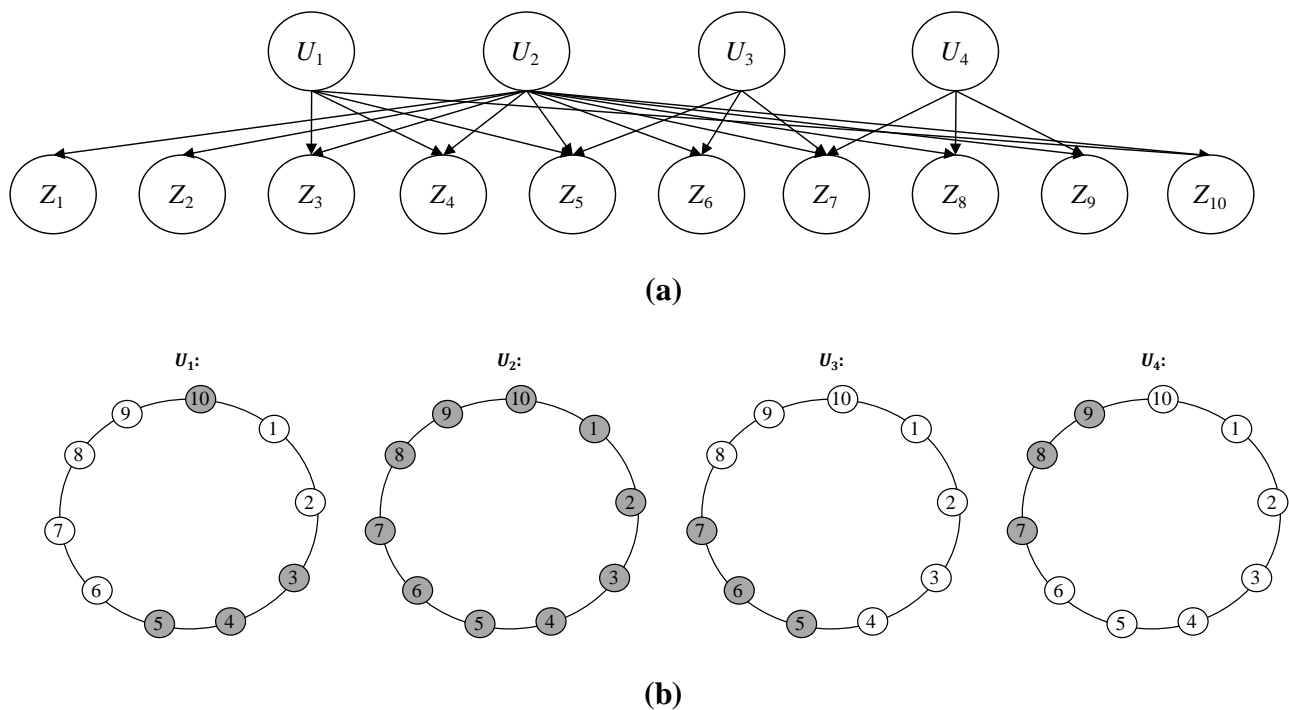


Figure 4.15: (a) BN approximation using ILOA with 20 links; (b) illustration of sites linked by common U -node for 10-site circle layout with $d = 5$

4.5 Effect of correlation approximations on system reliability

The objective in BN analysis is usually some sort of probabilistic assessment involving risk or reliability evaluation, life-cycle cost analysis, statistical inference, or expected-utility decision-making. Thus the effect of approximating the correlation structure of random variables drawn

from a Gaussian random field should be evaluated within such a context. Toward that end, we investigate the effect of the correlation approximation on the estimates of reliability of example systems. The points in the layouts in Figure 4.7 are assumed to represent the locations of components of infrastructure systems subjected to an earthquake demand. Two system performance criteria are considered: (1) all components must survive for the system to survive (series system), and (2) only one component needs to survive to ensure survival of the system (parallel system).

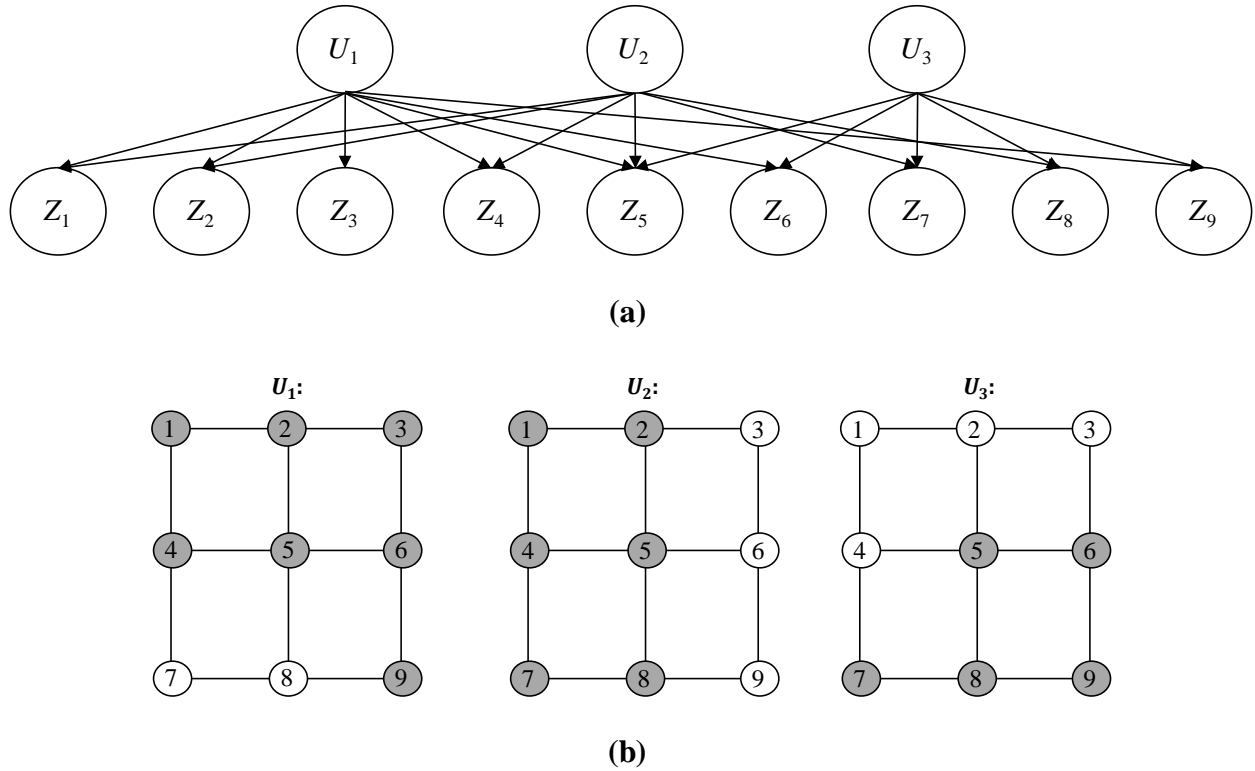


Figure 4.16: (a) BN approximation using ILOA with 18 links; (b) illustration of sites linked by common U -node for nine-site grid layout with $d = 5$

A limit-state function is assigned to each component of the system to model its performance. For component i , $i = 1, \dots, n$, the limit-state function has the form

$$g_i = \ln(R_{c,i}) - \ln(S_i), \quad (4.16)$$

where $R_{c,i}$ is the capacity of component i and S_i is the seismic demand on the component. The natural logarithms $\ln(R_{c,i})$ are assumed to be statistically independent normal random variables

with common means λ_R and common standard deviations ζ_R . Consistent with the descriptions in Chapter 3, the natural logarithm of the seismic demand on component i is expressed as

$$\ln(S_i) = \ln(\bar{S}_i) + \varepsilon_m + \varepsilon_{r,i}, \quad (4.17)$$

where \bar{S}_i is the median ground motion intensity at site i , ε_m is a normally distributed inter-event error term with zero mean and variance σ_m^2 that is common to all components in the system, and $\varepsilon_{r,i}$ is a site-specific intra-event error term drawn from a homogeneous Gaussian random field with zero mean, variance σ_r^2 , and autocorrelation function $\rho_{\varepsilon\varepsilon}(|\mathbf{x}_i - \mathbf{x}_j|)$ distributed over the spatial domain containing the system. It is assumed that \bar{S}_i is the same for all sites in the system. This assumption, as well as the earlier assumption of identical distributions for component capacities, ensures that all components have equal importance with regard to the performance of the system. This allows us to focus solely on the effect of the approximation of the correlation structure.

For a system of n components, there exist n limit state functions. Component i is in the fail state if $g_i \leq 0$. Thus, for a series system, the failure probability is given by

$$\Pr(F_{series}) = \Pr[(g_1 \leq 0) \cup (g_2 \leq 0) \cup \dots \cup (g_n \leq 0)] = \Phi_n(-\mathbf{M}_g, \mathbf{\Sigma}_{gg}) \quad (4.18)$$

and for a parallel system the failure probability is given by

$$\Pr(F_{parallel}) = \Pr[(g_1 \leq 0) \cap (g_2 \leq 0) \cap \dots \cap (g_n \leq 0)] = 1 - \Phi_n(\mathbf{M}_g, \mathbf{\Sigma}_{gg}). \quad (4.19)$$

The right-hand sides of the above equations are exact solutions of the system failure probabilities expressed in terms of the n -variate multinormal cumulative probability function $\Phi_n(\mathbf{M}_g, \mathbf{\Sigma}_{gg})$, with the mean vector \mathbf{M}_g having common elements $\lambda_R - \ln \bar{S}$ and the covariance matrix $\mathbf{\Sigma}_{gg}$ having variances $\zeta_R^2 + \sigma_m^2 + \sigma_r^2$ and covariances $\sigma_m^2 + \rho_{ij}\sigma_r^2$, where $\rho_{ij} = \rho_{\varepsilon\varepsilon}(|\mathbf{x}_i - \mathbf{x}_j|)$ is the autocorrelation coefficient function of the random field from which $\varepsilon_{S,i}$ are drawn. For the autocorrelation function, the form in Equation (4.15) is used. Furthermore, $\lambda_R = -0.9$, $\ln \bar{S} = -1.8$, $\sigma_m = 0.2$, and $\sigma_r = 0.5$ are used, while for ζ_R two values as described below are selected. The multinormal probabilities are computed by an algorithm available in the general-purpose reliability code CalREL (Der Kiureghian et al. 2006).

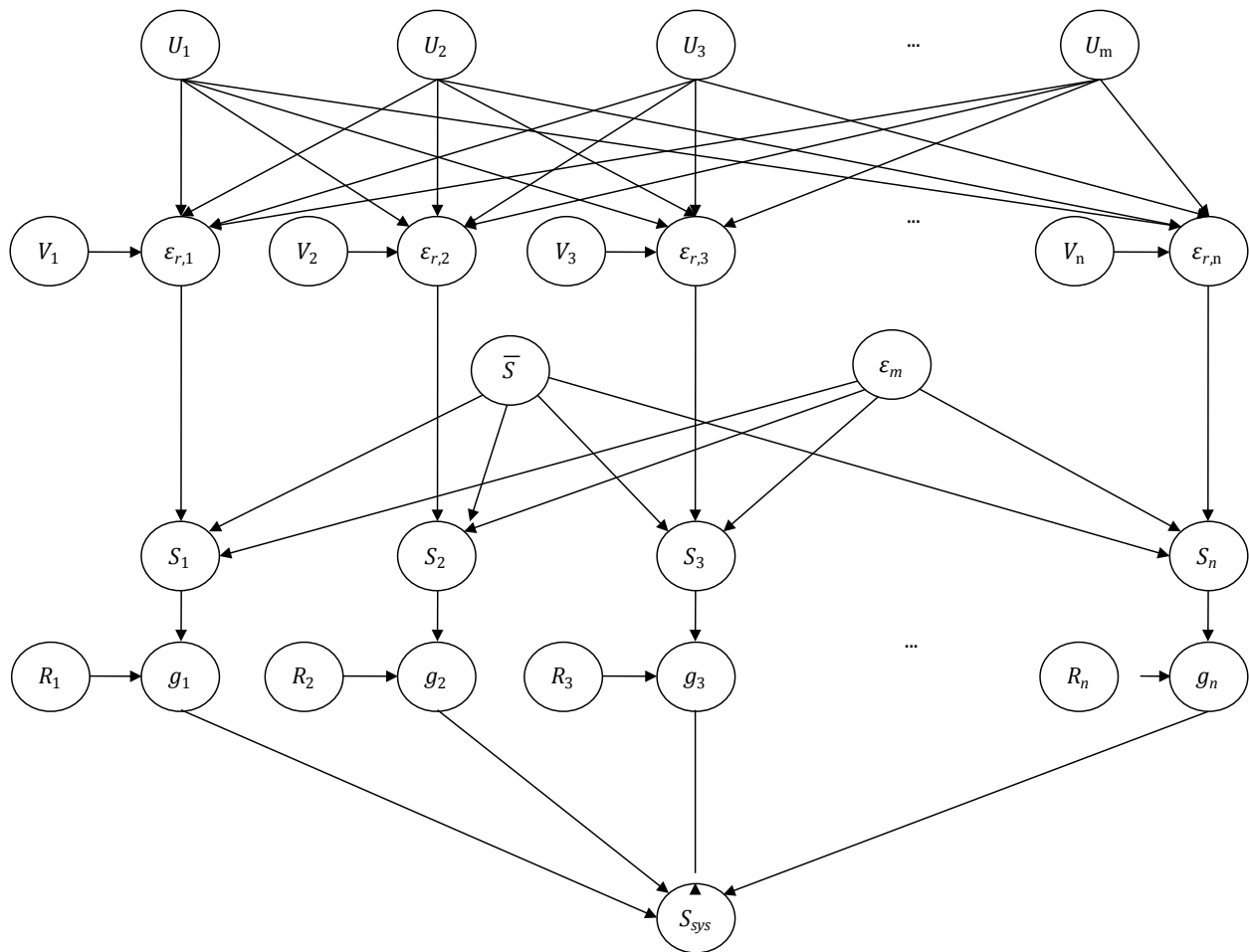


Figure 4.17: BN model of system performance

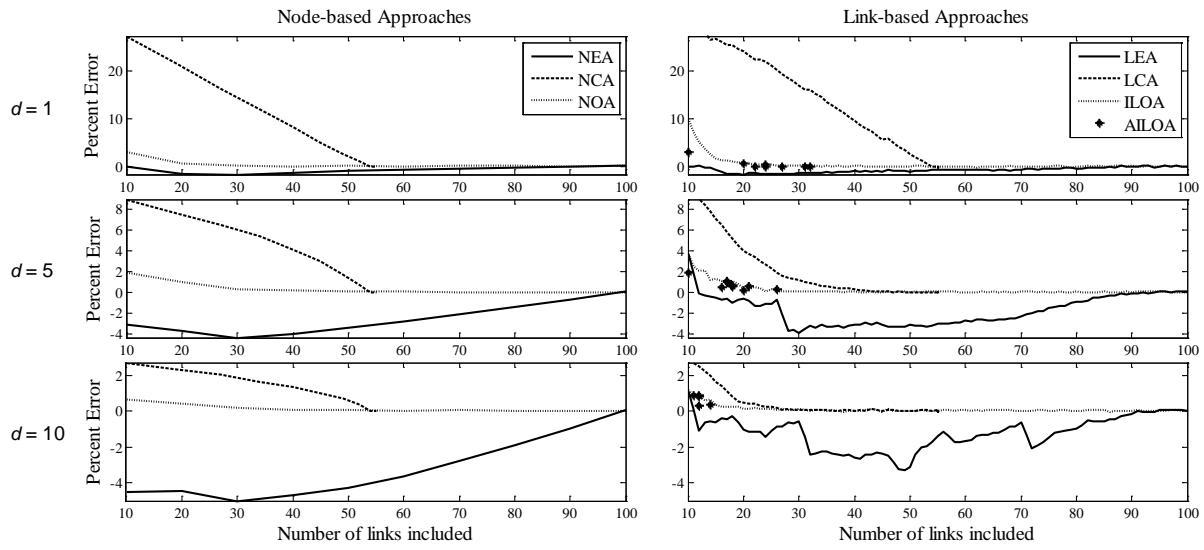
Figure 4.17 shows the BN model of the system performance. Each node g_i is binary, indicating failure or survival of component i , and is a child of nodes representing the component capacity (R_i) and demand (S_i). Node S_i is a child of nodes representing the common median demand \bar{S} , the common error term ϵ_m , and the site-specific error term $\epsilon_{r,i}$. The correlations among the site-specific error terms are accounted for through the latent U - and V -nodes according to the formulation in Equation (4.3), as exemplified in Figure 4.3. The performance of the system is represented by a single node S_{sys} , which is a child of all the component limit-state nodes g_i . Note that the converging structure of links going into node S_{sys} , as shown in Figure 4.17, is computationally inefficient. Methods for efficiently constructing the system performance portion

of the BN are contained in Chapter 6. When using the proposed approximation methods, the correlation coefficients ρ_{ij} are replaced by their approximations $\hat{\rho}_{ij}$. To avoid mixing the discretization error of the BN with the error due to elimination of nodes and links, failure probabilities are computed by the same formulas as in Equations (4.18) and (4.19) but using the approximate covariance matrix. In the following analysis, the error in computing the system failure probability is measured as

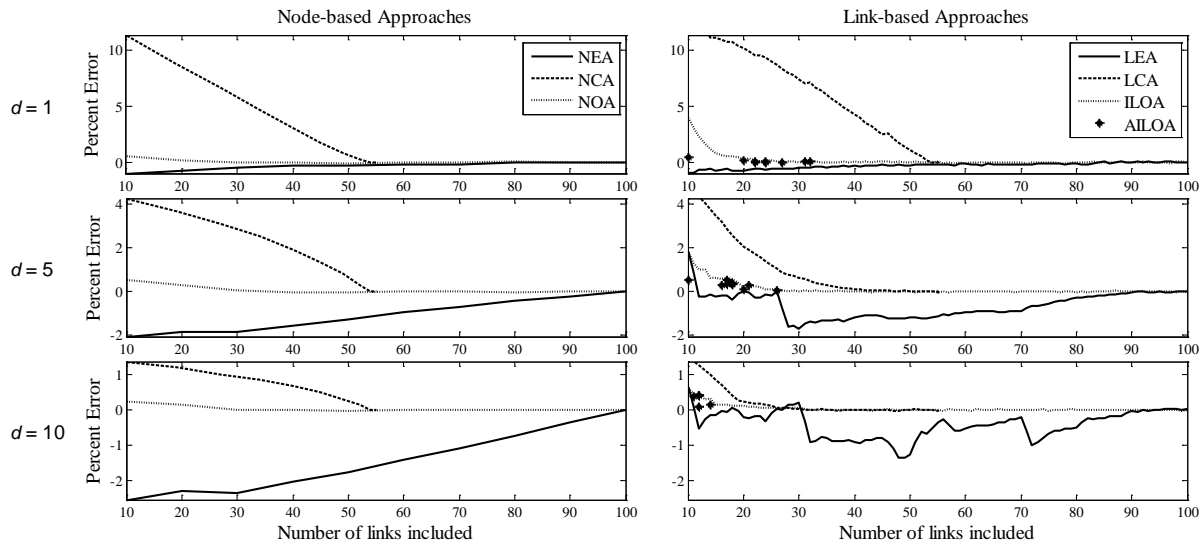
$$\text{Percent Error} = \frac{\hat{P}_{f,sys} - P_{f,sys}}{P_{f,sys}} * 100, \quad (4.20)$$

where $P_{f,sys}$ is the true system failure probability and $\hat{P}_{f,sys}$ is the approximate failure probability computed based on the approximate correlation matrix. A negative (positive) error implies underestimation (overestimation) of the system failure probability.

For a 10-site line layout system, Figure 4.18 and Figure 4.19 plot the percent errors in estimating the failure probabilities for series and parallel systems, respectively, versus the number of links included for each of the approximation methods. These are shown for two values of ζ_R , which approximately represents the coefficient of variation of the component capacities. Consistent with the results shown in the previous section, the optimization approaches outperform the decomposition approaches for both the parallel and series configurations. Among the decomposition approaches, the eigen-expansion methods are unconservative for the series system and the Cholesky factorization methods are unconservative for the parallel system. Overall, the errors associated with the series system are significantly smaller than those associated with the parallel system. This is because the failure probability for the series system is less sensitive to the correlation between component demands than that of a parallel system with the same components—a fact that has also been observed by other investigators (Grigoriu and Turkstra 1979). Comparing parts (a) and (b) of Figure 4.18 and Figure 4.19, it is evident that the error due to the approximation in the correlation matrix of the component demands becomes less critical when the uncertainty in the component capacities is large ($\zeta_R = 0.6$ versus $\zeta_R = 0.3$). Thus, accurate modeling of the correlation structure of the random field is less critical when important sources of uncertainty other than the random field are present.

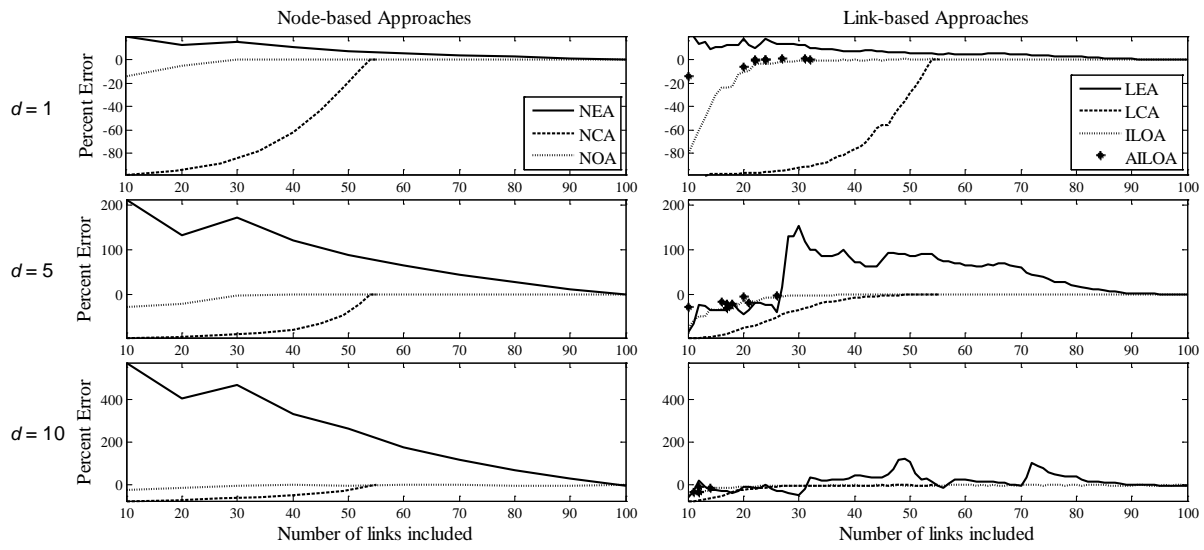


(a)

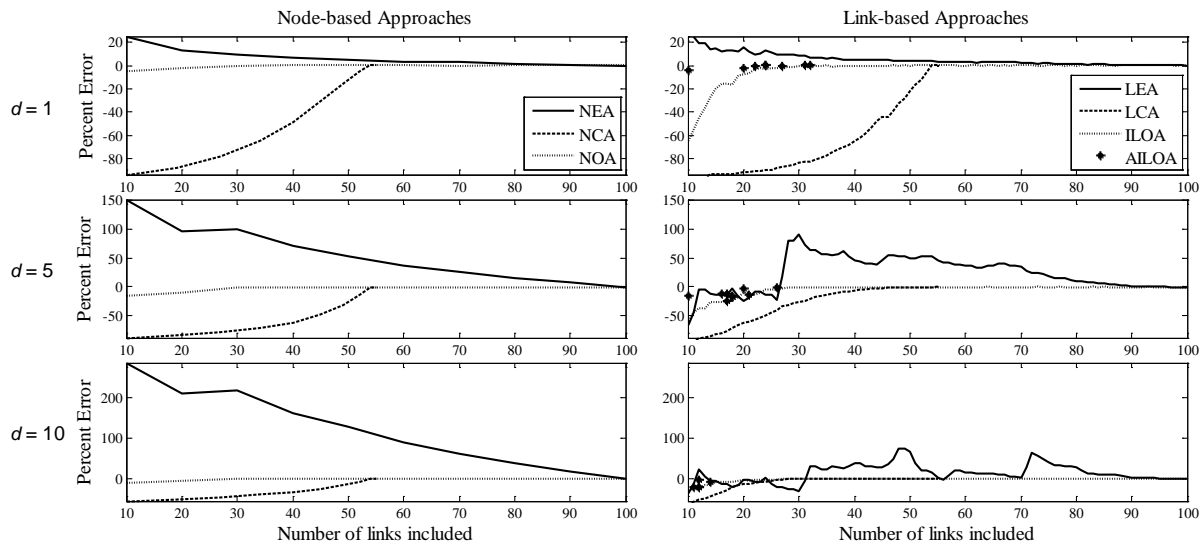


(b)

Figure 4.18: Percent error in estimating failure probability for a 10-site line series system when (a) $\zeta_R = 0.3$ and (b) $\zeta_R = 0.6$



(a)



(b)

Figure 4.19: Percent error in estimating failure probability for a 10-site line parallel system when (a) $\zeta_R = 0.3$ and (b) $\zeta_R = 0.6$

To aggregate and compare the results of the numerical investigation for the various layouts, we consider the minimum number of links required in the BN model of each layout to achieve an error less than 10% in the estimate of the system failure probability. Table 4.1 and

Table 4.2 present the required minimum number of links for series and parallel systems, respectively, for each of the layouts and each of the seven approximation methods considered. Tables on the left list the results for $\zeta_R = 0.3$, while those on the right list the results for $\zeta_R = 0.6$. Results for $d = 10$ are not shown for the series system because, for this relatively long distance, the target accuracy threshold of 10% is achieved without including random field effects. For shorter correlation lengths, similar accuracy is obtainable when neglecting random field effects for some layouts, particularly for $\zeta = 0.6$, as indicated by a symbol (*) in Table 4.1.

It is known that series systems are not strongly sensitive to neglecting correlation in demands. This observation is reflected in Table 4.1, which demonstrates that the accuracy threshold is met when considering very few links, if any. Cases in which the threshold is met without inclusion of random field effects, shown with an asterisk (*), essentially require zero links. Furthermore, for the series system, the optimization-based methods are generally not associated with significant gains in efficiency relative to the decomposition approaches, particularly LEA. Because the optimization approaches are computationally more expensive than the decomposition approaches, it may not be of value to compute transformation matrices using optimization techniques when working with series systems.

Conversely, it is well established that parallel systems are sensitive to inclusion of correlation in demands. This finding is reflected in

Table 4.2 by the relatively large number of links that are needed in each case to achieve the required threshold of accuracy in the estimate of the system failure probability. With few exceptions, the optimization approaches are more efficient than the decomposition approaches. For small values of d (high correlations), the node- and link-based optimization approaches offer similar performance, except in the case of the cluster layout system. For large d values (low correlations), NOA and AILOA are more efficient than ILOA. In most cases, more links are required to achieve a percent error below the specified threshold when $\zeta_R = 0.3$ than when $\zeta_R = 0.6$, particularly for larger systems.

Table 4.1: Number of links required to achieve less than 10% error in estimate of failure probability for series system when $\zeta_R = 0.3$ (left) and $\zeta_R = 0.6$ (right) (Bold numbers indicate minimum number of links obtained with any approximation method)

$d = 1$									$d = 1$								
Layout	N	NEA	LEA	NCA	LCA	NOA	ILOA	AILOA	Layout	N	NEA	LEA	NCA	LCA	NOA	ILOA	AILOA
Line	5	5	5	9	9	5	5	5	Line	5	5	4	5	4	5	4	5
Line	10	10	9	40	40	10	9	10	Line	10	10	7	19	21	10	8	10
Circle	5	5	5	5	5	5	5	5	Circle	5	5	4	5	4	5	4	5
Circle	10	10	10	27	22	10	10	10	Circle	10	10	9	10	9	10	9	10
Cluster	9	9	6	15	7	18	6	9	Cluster	9	*	*	*	*	*	*	*
Grid	9	9	9	17	18	9	9	9	Grid	9	9	8	9	9	9	8	9

$d = 5$									$d = 5$								
Layout	N	NEA	LEA	NCA	LCA	NOA	ILOA	AILOA	Layout	N	NEA	LEA	NCA	LCA	NOA	ILOA	AILOA
Line	5	5	2	5	6	5	2	5	Line	5	*	*	*	*	*	*	*
Line	10	10	2	10	11	10	2	10	Line	10	*	*	*	*	*	*	*
Circle	5	5	3	5	6	5	3	5	Circle	5	*	*	*	*	*	*	*
Circle	10	10	8	27	24	10	8	10	Circle	10	10	5	10	8	10	4	10
Cluster	9	9	1	6	1	9	1	3	Cluster	9	*	*	*	*	*	*	*
Grid	9	9	6	17	20	9	6	9	Grid	9	*	*	*	*	*	*	*

* Percent error below 10% achievable when neglecting random field effects.

Table 4.2: Minimum number of links required to achieve less than 10% error in estimate of failure probability for parallel system when $\zeta_R = 0.3$ (left) and $\zeta_R = 0.6$ (right) (Bold numbers indicate minimum number of links obtained with any approximation method)

$d = 1$									$d = 1$								
Layout	N	NEA	LEA	NCA	LCA	NOA	ILOA	AILOA	Layout	N	NEA	LEA	NCA	LCA	NOA	ILOA	AILOA
Line	5	10	9	14	14	5	5	5	Line	5	10	7	12	13	5	5	5
Line	10	50	14	52	53	20	21	20	Line	10	30	22	52	53	10	19	10
Circle	5	15	9	12	13	5	5	5	Circle	5	10	8	12	13	5	5	5
Circle	10	10	10	45	45	10	10	10	Circle	10	10	10	45	44	10	10	10
Cluster	9	72	35	33	18	27	9	9	Cluster	9	63	33	31	17	27	9	9
Grid	9	27	13	39	39	9	9	9	Grid	9	18	13	35	37	9	9	9

$d = 5$									$d = 5$								
Layout	N	NEA	LEA	NCA	LCA	NOA	ILOA	AILOA	Layout	N	NEA	LEA	NCA	LCA	NOA	ILOA	AILOA
Line	5	25	20	14	14	5	7	5	Line	5	25	4	14	13	5	7	5
Line	10	100	85	54	39	30	24	20	Line	10	90	12	54	38	30	20	20
Circle	5	25	19	14	14	5	5	5	Circle	5	25	17	14	14	5	5	5
Circle	10	90	71	52	50	20	13	18	Circle	10	80	61	52	49	10	10	10
Cluster	9	81	5	33	18	27	9	9	Cluster	9	81	5	31	17	27	9	9
Grid	9	81	56	42	41	9	19	9	Grid	9	72	50	42	40	9	18	9

$d = 10$									$d = 10$								
Layout	N	NEA	LEA	NCA	LCA	NOA	ILOA	AILOA	Layout	N	NEA	LEA	NCA	LCA	NOA	ILOA	AILOA
Line	5	25	20	14	10	5	7	5	Line	5	25	3	14	9	5	7	5
Line	10	100	13	54	25	30	19	12	Line	10	100	13	52	23	20	15	12
Circle	5	25	21	14	13	5	9	5	Circle	5	25	3	12	11	5	8	5
Circle	10	100	81	54	47	10	23	10	Circle	10	100	77	52	44	10	21	10
Cluster	9	81	4	23	17	27	10	■	Cluster	9	54	4	23	16	9	8	■
Grid	9	81	55	42	37	9	32	9	Grid	9	81	51	42	34	9	31	9

■ indicates method was not able to achieve a percent error below specified threshold

5. Modeling Component Performance with BNs

5.1 Introduction

This chapter presents BN formulations for modeling the performance of individual components of an infrastructure system as a function of the seismic demands placed upon them. Two types of components are considered: (1) point-site components, such as relatively short span highway bridges, buildings, culverts, pumps in a water distribution system, or transformers in an electrical grid; and (2) distributed components, such as pipelines, embankments, and rail lines.

Components of an infrastructure system are modeled as having multiple states, but in many cases binary states (e.g., fail or survive, open or closed, damaged or undamaged) are sufficient to describe their performance under seismic demands. For example, a single-lane tunnel in a transportation system will be either open or closed after an earthquake. Components of an electrical system also typically have binary states. Usually more than two states are considered when a component has a “flow” characteristic associated with its performance. Water distribution systems have components with flow characteristics; for instance, a leaking pump may exhibit decreased flow capacity but still be operable. Multistate components are also useful for distinguishing operating levels without consideration of flow. For example, in transportation systems, a bridge may be open for full capacity traffic, open only to light (non-truck) vehicles due to load restrictions associated with moderate damage, or closed to all traffic. Such a bridge has three states.

Seismic risk assessment of infrastructure requires definition of a mapping between the seismic demands placed on a component (modeled using the seismic demand BN formulation described

in Chapter 3) and the associated damage states of the component. In developing a BN framework for seismic risk assessment and decision support, it is assumed that only the demands and component damage states or operating level are observable. Nodes that are not observable and that are not required for modeling dependences between random quantities are not explicitly included in the BN, but are instead handled when constructing CPTs of nodes that are explicitly included.

A component's performance can be predicted as a function of the ground motion intensity at its site using methods such as structural reliability analysis, stochastic finite elements, and statistical analysis of experimental or field data. For a point-site component, the probabilistic mapping between site-specific ground motion intensity and component performance is expressed using a set of *fragility functions*. Each fragility function provides the probability that the component experiences a specified damage state or greater for a given level of ground motion intensity. For distributed components, similar functions give mean occurrence rates of damage of a particular state or greater for a given level of ground motion intensity.

Fragility functions are widely used in probabilistic seismic hazard assessment. However, infrastructure components are often complex systems themselves and fragility functions may oversimplify their response to seismic demands. For example, a highway bridge subjected to ground shaking may have a complex response and multiple correlated failure modes, and proper computation of its reliability may require use of nonlinear structural analysis as well as systems reliability methods. However, because our goal is to develop a framework that operates at the system level, we are interested in aggregated results. Therefore, idealizing component performance using fragility functions is both reasonable and computationally necessary. Furthermore, sophisticated approaches are becoming increasingly available for developing fragility functions that are better able to predict complex post-earthquake performance of components in an infrastructure system (e.g., Straub and Der Kiureghian (2008)). However, defining fragility functions requires care in properly accounting for uncertainties that arise from idealization of structural performance as well as possible sources of correlation between estimated performances of similar components.

In recent years, BNs have been applied in a limited way for modeling component performance. For example, Mahadevan et al. (2001) used BNs for modeling simple structural systems with multiple failure modes consisting of a node representing the overall structural performance that is a child of nodes corresponding to individual limit-state functions. However, that BN topology causes prohibitively large memory demands if used to model a large number of components in an infrastructure system. Shumuta et al. (2009) developed a BN-based damage estimation framework for electric power distribution equipment. It provides time-evolving estimates of post-earthquake damage by integrating information on the hazard and performance of components, e.g., observed power outages, using BN. They did not account for spatial correlation in demands or system effects. Bayraktarli (2006) developed vulnerability curves for original and retrofitted structures (low-rise, bare frame reinforced concrete structures) and used them to populate the CPTs for the seismic vulnerability BN model shown in Figure 3.22. More recently, Straub and Der Kiureghian (2010a,b) developed a novel and sophisticated computational framework for integrating structural reliability methods with BNs to facilitate the risk and reliability assessment of structural systems that function as components of larger infrastructure systems. Other applications of BNs have included embankment dams (Li et al. 2009) and marine structures (Friis-Hansen 2000).

5.2 Seismic fragility of point-site components

Seismic fragility is the conditional probability of failure of a component (or a point-site system) for a given measure(s) of ground motion intensity. Here failure is defined generically as an event in which a particular level of damage, or other undesirable consequence, is met or exceeded. With structural reliability methods, the failure of a component is defined in terms of a limit state function, which defines the boundary between failure and survival events in the outcome space of random variables influencing the state of the component (Ditlevsen and Madsen 1996). Other sources (Ditlevsen and Madsen 1996; Rackwitz 2001; Der Kiureghian 2005) have additional details on structural reliability methods.

Let $g(\mathbf{X}, \boldsymbol{\theta})$ define the limit state function for a given component, where \mathbf{X} is a set of random variables influencing the performance of the component and $\boldsymbol{\theta}$ is a set of model parameters

estimated from data or from theory of structural analysis. Conventionally, $\{g(\mathbf{X}, \boldsymbol{\theta}) \leq 0\}$ represents the failure event. The fragility of the component is then expressed as

$$F(\mathbf{s}, \boldsymbol{\theta}) = \Pr(\{g(\mathbf{X}, \boldsymbol{\theta}) \leq 0\} | \mathbf{S} = \mathbf{s}), \quad (5.1)$$

where \mathbf{s} is a vector of variables defining the ground motion intensity. A plot of $F(\mathbf{s}, \boldsymbol{\theta})$ versus \mathbf{s} yields a fragility surface. In the special case when \mathbf{s} is a scalar intensity measure, a plot of $F(s, \boldsymbol{\theta})$ versus s yields the conventional fragility curve (Der Kiureghian 2002). Hereafter, for the sake of simplicity, models are developed for a scalar intensity measure; however, the concepts that are developed can be easily extended to vector-valued intensity measures. Furthermore, the limit-state function is assumed to be composed of a capacity term and a demand term, though each of these in general could be functions of other random variables.

As a general case, we consider an infrastructure system that comprises multiple components in different classes (e.g., bridges of different age and construction type). The capacity of components within each class to withstand damage is thought of as having been randomly drawn from a distribution that characterizes its inherent randomness arising from, for example, natural variability in material properties, construction and manufacturing processes, and changes due to deterioration. The components in different classes are assumed to have statistically independent capacities with different distributions. Let $R_{c,i,j}$ denote the uncertain capacity of a component, where $i \in (1, \dots, n)$ is an index set defining the component numbers and $j \in (1, \dots, J)$ is an index set defining the class to which the component belongs. Capacities are measured in the same unit as the site-specific seismic demand, which is denoted as S_i for component i .

In risk analysis of infrastructure systems, it is common to assume the lognormal distribution for component capacities. This distribution has several characteristics that make it well suited for modeling capacities, and its use in many cases is supported by empirical observations. Let λ_j and ζ_j denote the parameters of the lognormal capacity distribution for class j . For each class of components, the parameters λ_j and ζ_j can be estimated using experimental or post-earthquake field observations and numerical or analytical structural models. When observations are limited in number, there is often statistical uncertainty associated with the estimates of the parameters. This implies that a distribution on the values of the parameters should be used rather than taking them to be deterministic quantities. This statistical uncertainty is common to all components

within a class and, hence, gives rise to correlations among the perceived component capacities (Der Kiureghian 2002). In the context of BN modeling, this implies that nodes corresponding to the uncertain parameters λ_j and ζ_j must be included as common parents to nodes representing capacities of all components within each class. For illustration, Figure 5.1 shows BNs of capacities of components in several classes that are correlated by common uncertain parameters.

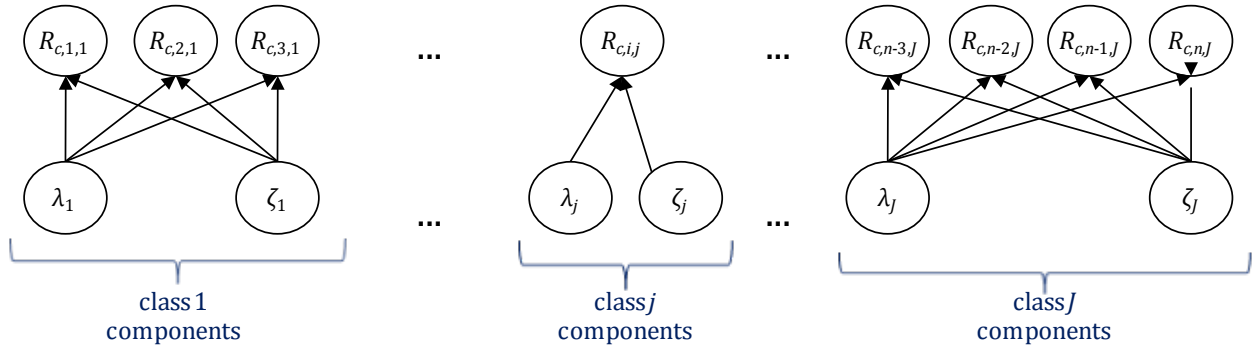


Figure 5.1: BN model of component capacities with uncertain distribution parameters

In accordance with the models described in Chapters 3 and 4, the ground motion intensity S_i is also modeled as a lognormal random variable. In that case, assuming the fragility model is exact, the limit-state function is conveniently formulated as $g_i = \ln R_{c,i,j} - \ln S_i$. This function defines the state of component i of class j for each value of $R_{c,i,j}$ and S_i . The BN corresponding to such a model is shown in Figure 5.2, where the details of the ground motion intensity model are hidden in a BN object. In this BN, each node C_i is binary indicating the state of component i . The node indicates failure if $g_i < 0$, that is, if $R_{c,i,j} < S_i$. Note that in the formulation in Figure 5.2, the ground motion prediction points (GMPPs) selected in the random field seismic demand model correspond to the locations of the point-site components in the infrastructure system.

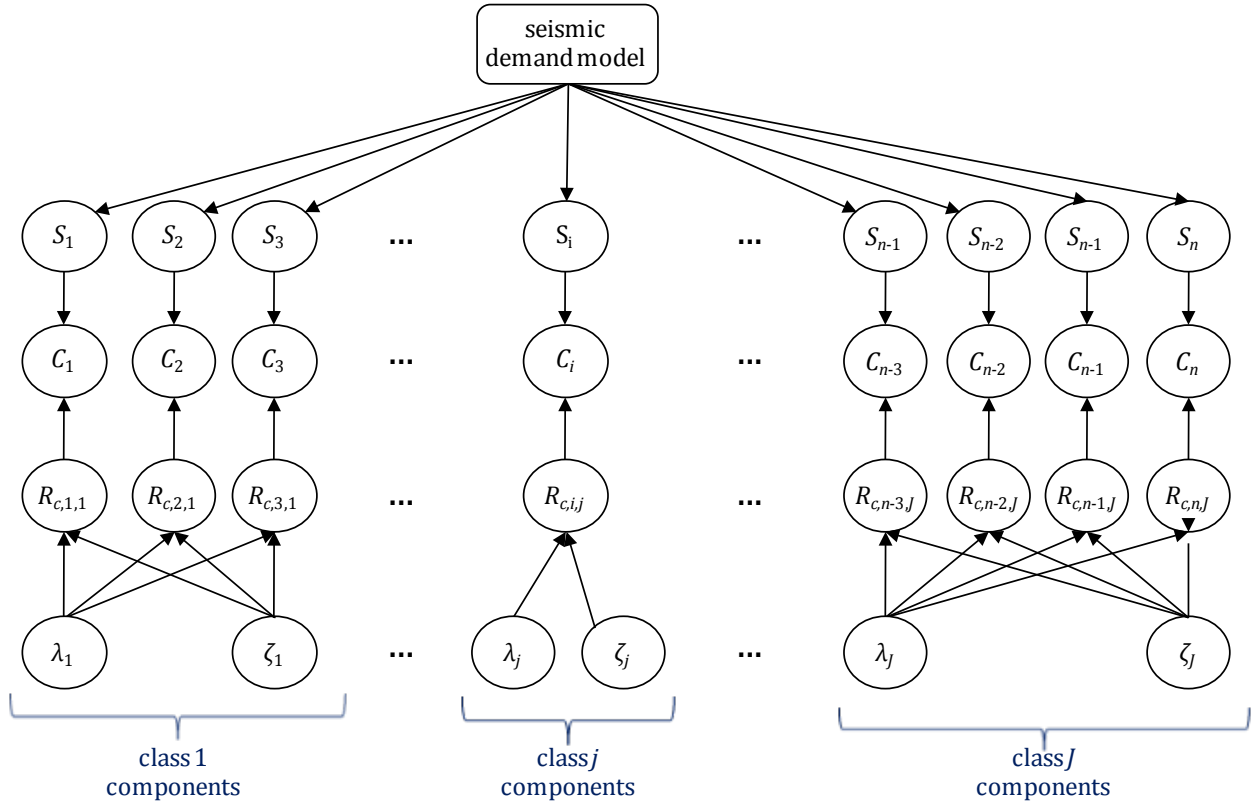


Figure 5.2: BN model of component performances assuming exact limit-state functions

Limit-state functions and fragility models are idealizations of component performance. In constructing such models based on theory and observed data, it is usually necessary to account for the model error resulting from this idealization. After an earthquake, the observed states of components differ from those predicted using a limit state function. In fact, given a set of identical components subjected to ground motions with exactly the same magnitude of ground motion intensity S , the observed performances vary from component to component because the intensity measure S does not fully characterize the ground motion at a site (Der Kiureghian 2002).

To account for the uncertainties that arise from incomplete characterization of the ground motion and other idealizations, a random correction term $\varepsilon_{i,j}$ is added to the limit state function characterizing the performance of component i of class j :

$$g_i = \ln R_{c,i,j} - \ln S_i + \varepsilon_{i,j} \quad (5.2)$$

where $\varepsilon_{i,j}$ is zero mean and normally distributed with standard deviation $\sigma_{i,j}$. The correction term captures uncertainty arising from the idealization of structural performance and missing variables, including ground motion characteristics not captured by the intensity measure and structural properties not explicitly included in the model.

At the component level, these uncertainties can be reasonably incorporated into the fragility model. As a result, a component-level fragility model should not be interpreted as a distribution on the true capacity of the component because it accounts for the aforementioned sources of uncertainty. In fact, the uncertainty in the fragility model may be larger if a different, and less informative, measure of intensity is selected. The assumptions that $R_{c,i,j}$ and S_i are lognormal random variables and $\varepsilon_{i,j}$ is normally distributed implies that $P(g_i \leq 0)$ can be easily computed using the standard normal CDF, $\Phi(\cdot)$. This is the approach taken when developing many fragility models.

When modeling the performance of systems of components, a problem arises that is not an issue with individual components. A portion of the model error $\varepsilon_{i,j}$ is random from component to component. However, some of the missing variables and a portion of the uncertainty in the form of the mathematical model are common to different components of the same class. Therefore, the estimated fragilities of these components become statistically dependent. To account for the portions of the model error that are independent, separately from the portions that are correlated from component to component, it is useful to break the model error down into two components: $\varepsilon_{i,j}^{(1)}$ and $\varepsilon_j^{(2)}$. The first term captures the uncertainty that is random from component to component of class j and the second term captures the portion of model error that is common to all components of the same class. The BN corresponding to such a model is shown in Figure 5.3. Consistent with an assumption of component exchangeability, it is assumed that the performances of all components of the same class are equicorrelated through $\varepsilon_j^{(2)}$. Thus, nodes $\varepsilon_{i,j}^{(1)}$ are component-specific and nodes $\varepsilon_j^{(2)}$ are common to all nodes C_i of the same class j .

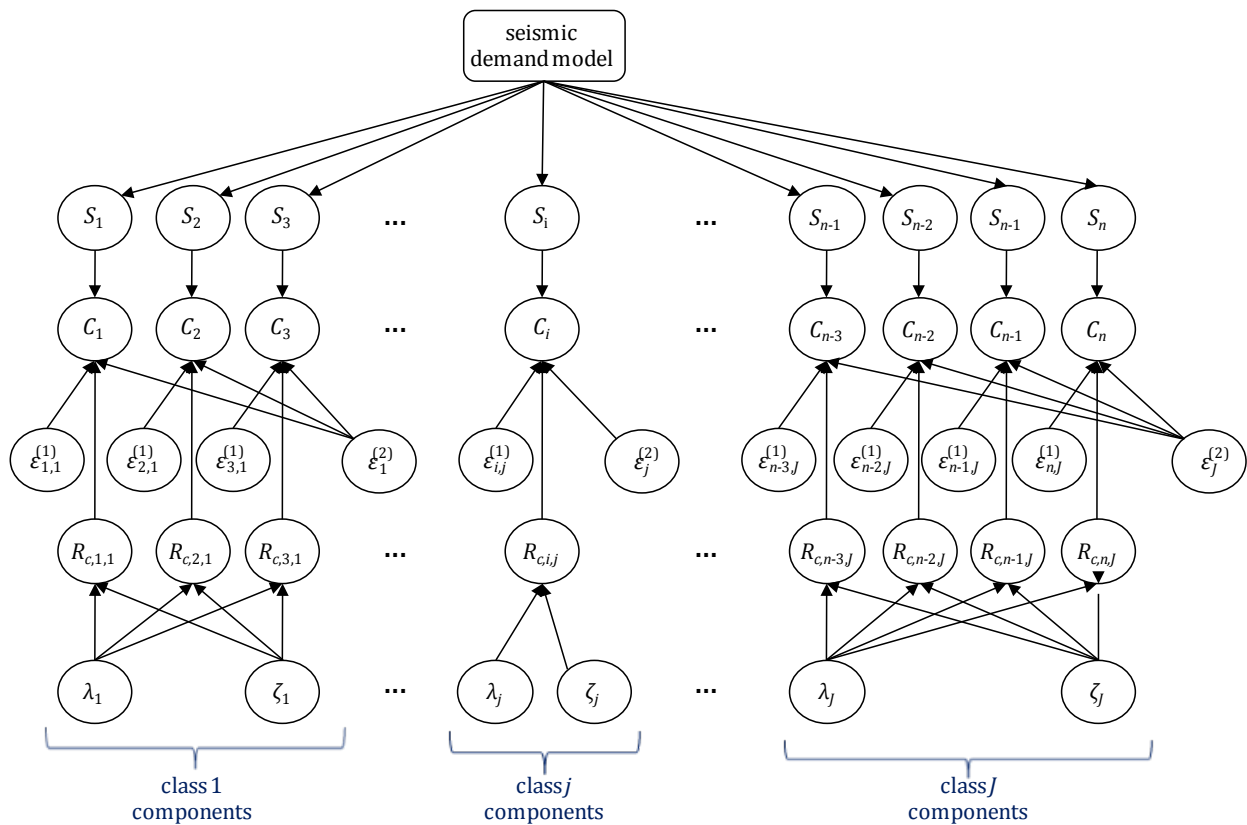


Figure 5.3: BN model of component performance including uncertainty in functional form of limit state functions

Because $\varepsilon_{i,j}^{(1)}$ and $R_{c,i,j}$ are component-specific, their uncertainties can be incorporated into the CPT of the node representing the uncertain component damage state, C_i , and it is not necessary to explicitly include nodes representing these quantities in the BN. This reduces computational demands and discretization error. The resulting BN is shown in Figure 5.4.

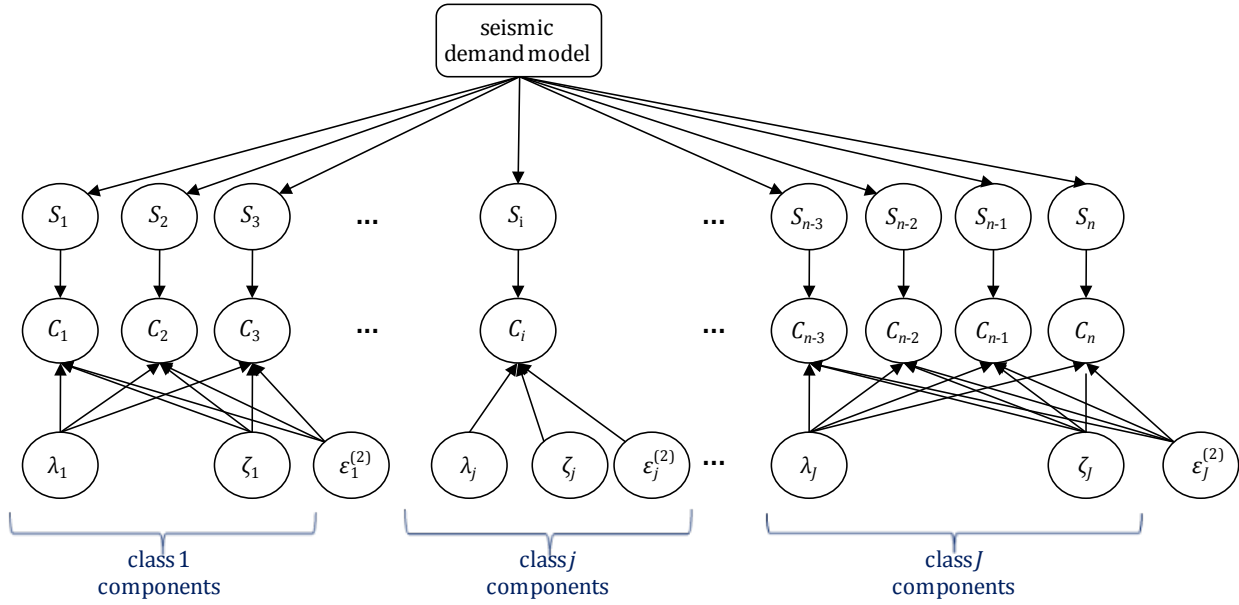


Figure 5.4: BN model of component performance including uncertainty in functional form of limit state functions after eliminating nodes representing $R_{c,i,j}$ and $\epsilon_{i,j}^{(1)}$

Recall that the concept of failure described above is general and includes any event in which an unacceptable level of damage is experienced or exceeded. Define a damage index set $k = \{0, 1, \dots, K\}$ such that $k = 0$ corresponds to the undamaged state and $k = K$ corresponds to the most severe damage state considered. Node C_i has mutually exclusive states corresponding to each element of the damage index set. It follows that the fragility of component i for state k is

$$F_{k,i}(s_i) = \Pr(\text{component } i \text{ meeting or exceeding damage state } k | S_i = s_i). \quad (5.3)$$

Note that $F_{0,i}(s_i) = 1$. The probability that component i is in damage state k is then computed as

$$P_{k,i}(s_i) = F_{k,i}(s_i) - F_{k+1,i}(s_i). \quad (5.4)$$

For illustration, Figure 5.5 shows example fragility curves and state probabilities for a five-state component (Der Kiureghian 2009).

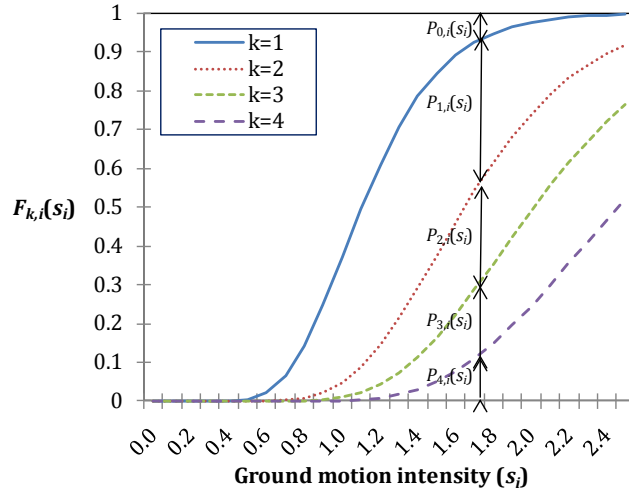


Figure 5.5: Example of fragility curves and state probabilities for a five-state component

The BN in Figure 5.4 requires that the probability of each damage state be defined for each combination of the states of the parent nodes of C_i . Let

$$g_{i,k} = \ln R_{c,i,j,k} - \ln S_i + \varepsilon_{i,j,k}^{(1)} + \varepsilon_{j,k}^{(2)} \quad (5.5)$$

be the true limit-state function defining damage of state k or greater, where $R_{c,i,j,k}$ represents the corresponding capacity and $\varepsilon_{i,j,k}^{(1)}$ and $\varepsilon_{j,k}^{(2)}$ are the associated model errors. Therefore the probability that component i will experience damage of state k or greater is

$$P(g_{i,k} \leq 0) = P(\ln R_{c,i,j,k} + \varepsilon_{i,j,k}^{(1)} \leq \ln S_i - \varepsilon_{j,k}^{(2)}). \quad (5.6)$$

As before, $\ln R_{c,i,j,k}$ is assumed to be normally distributed with parameters $\lambda_{j,k}$ and $\zeta_{j,k}$, and $\varepsilon_{i,j,k}^{(1)}$ and $\varepsilon_{j,k}^{(2)}$ are normally distributed with zero mean and standard deviations $\sigma_{i,j,k}^{(1)}$ and $\sigma_{j,k}^{(2)}$, respectively. In Equation (5.6) the error terms have been split across the inequality to facilitate the separate account of (1) the portion of the model error that is independent from component to component and that need not be modeled explicitly as a node, and (2) the portion of the model error that is common to all components of the same class and must be modeled explicitly as a node. The conditional probability that a component is in the k th damage state for a particular combination of the parent nodes of C_i is expressed as

$$\begin{aligned}
P_{k,i}(s_i) &= F_{k,i}(s_i, \varepsilon_{j,k}^{(2)}, \lambda_{j,k}, \zeta_{j,k}) - F_{k+1,i}(s_i, \varepsilon_{j,k+1}^{(2)}, \lambda_{j,k+1}, \zeta_{j,k+1}) \\
&= \Phi\left(\frac{\ln s_i - \varepsilon_{j,k}^{(2)} - \lambda_{j,k}}{\sqrt{(\zeta_{j,k})^2 + (\sigma_{i,k}^{(1)})^2}}\right) - \Phi\left(\frac{\ln s_i - \varepsilon_{j,k+1}^{(2)} - \lambda_{j,k+1}}{\sqrt{(\zeta_{j,k+1})^2 + (\sigma_{i,k+1}^{(1)})^2}}\right)
\end{aligned} \tag{5.7}$$

where $\Phi(\cdot)$ is the standard normal cumulative distribution function. This formulation imposes certain conditions on the true joint distribution of the parameters $(\lambda_{j,k}, \zeta_{j,k})$ and model error variances $\sigma_{i,j,k}$, $k = 1, \dots, K$; namely, they should be such that the probabilities computed by Equation (5.7) are non-negative. That is, the fragility curves in Figure 5.5 must be nonintersecting.

Although a few studies (e.g., Straub and Der Kiureghian (2008) for two-state components) provide enough information to populate the CPTs required for the above comprehensive formulation, many components have insufficient information to assess parameter uncertainties and components of the model error. Thus it is necessary either to use engineering judgment to define quantities that are not available or to make simplifying assumptions about the BN formulation. Lacking information or assumptions about the statistical uncertainty of parameters or the statistical dependence of estimated fragility models, the simplified BN shown in Figure 5.6 disregards uncertainty in the fragility function parameters and assumes, given ground motion intensities, that the component states are statistically independent. The probability that C_i is in each damage state k given $S_i = s_i$ is defined using the expression

$$\begin{aligned}
P_{k,i}(s_i) &= F_{k,i}(s_i) - F_{k+1,i}(s_i) \\
&= \Phi\left(\frac{\ln s_i - \lambda_{j,k}}{\sqrt{\zeta_{j,k}^2 + \sigma_{i,j,k}^2}}\right) - \Phi\left(\frac{\ln s_i - \lambda_{j,k+1}}{\sqrt{\zeta_{j,k+1}^2 + \sigma_{i,j,k+1}^2}}\right),
\end{aligned} \tag{5.8}$$

where $\sigma_{i,j,k}^2$ is the variance of the total model error.

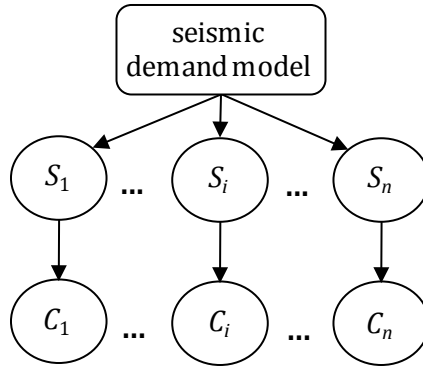


Figure 5.6: BN modeling performance of point-site components neglecting statistical uncertainty and correlation in component response other than through seismic demands

Because the dependence among the estimated states of the components of the system is not included in the BN in Figure 5.6, the result is a simpler formulation with reduced computational demand. If the uncertainty in modeling seismic demands dominates the uncertainty in capacity, if the system is not highly redundant, or if the system is heterogeneous with few components of the same class, then this omission should not significantly degrade the accuracy of probability estimates obtained from the simplified BN.

5.3 Seismic fragility of distributed components

For distributed components, such as pipelines and rail segments, it is not adequate to model performance at a single point. Instead, the seismic fragility of these linear components is expressed as a mean number of damages of state k or greater per unit length, given a level of ground motion intensity. The failures along a distributed component are often assumed to follow a Poisson process. One or more failures along the length constitute failure of the entire component (Adachi and Ellingwood 2008).

While a distributed component is continuous, the BN requires discretization of the random field, and thus estimates of ground motion intensity are only available at the discrete GMPPs represented by nodes S_i , $i = 1, \dots, n$. As a result, it is necessary to discretize a distributed component into segments. GMPPs modeled in the BN are selected to correspond with the ends of each segment. Each discretized segment is considered a “component” in the system. Define

$C_{i,i+1}$ as the segment of a distributed component between GMPPs represented by nodes S_i and S_{i+1} . Let $\eta_i^k(s_i)$ be the mean rate of damage points of state k or greater along the component when ground motion intensity $S_i = s_i$. Associated with the component segment $C_{i,i+1}$ are two mean damage rates, $\eta_i^k(s_i)$ and $\eta_{i+1}^k(s_{i+1})$. Interpolating linearly between these two values gives the mean damage rate as a function of the coordinate along the component length. The mean number of damages of state k or greater for the entire component $C_{i,i+1}$ is then

$$\mu_{i,i+1}^k(s_i, s_{i+1}) = \frac{L_{i,i+1}}{2} (\eta_i^k(s_i) + \eta_{i+1}^k(s_{i+1})), \quad (5.9)$$

where $L_{i,i+1}$ is the length of $C_{i,i+1}$. Assuming that damages occur randomly, the probability that the component experiences damage of state k or greater (i.e., the probability of at least one incident of damage of state k or greater) is computed by treating the occurrence of such events as a nonhomogeneous Poisson process. The probability that $C_{i,i+1}$ is in damage state k given ground motion intensities s_i and s_{i+1} , expressed as $p_{i,i+1}^k(s_i, s_{i+1})$, is then computed as

$$\begin{aligned} P_{i,i+1}^k(s_i, s_{i+1}) &= \exp\left(-\mu_{i,i+1}^1(s_i, s_{i+1})\right) \text{ for } k = 0 \\ &= \exp\left(-\mu_{i,i+1}^{k+1}(s_i, s_{i+1})\right) - \exp\left(-\mu_{i,i+1}^k(s_i, s_{i+1})\right), \text{ for } k = 1, \dots, K-1 \\ &= 1 - \exp\left(-\mu_{i,i+1}^K(s_i, s_{i+1})\right), \text{ for } k = K \end{aligned} \quad (5.10)$$

Once again neglecting parameter uncertainties and correlation due to common components of model error, the BN corresponding to the above description is shown in Figure 5.7. The node representing the damage state of component segment $C_{i,i+1}$ is modeled as a child of ground motion intensity nodes at either end of the segment: S_i and S_{i+1} . Note that this formulation preserves the correlation between the states of components sharing a common GMPP, even if random field effects were neglected.

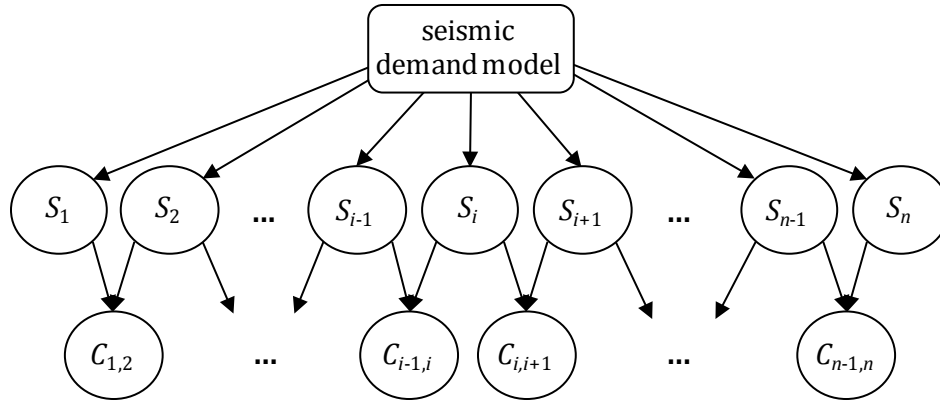


Figure 5.7: BN modeling performance of distributed components neglecting statistical uncertainty and correlation in component states other than through demands

5.4 Examples of available fragility functions

Fragility curves have been developed for a vast range of infrastructure component types using varying degrees of sophistication relating to the treatment of uncertainties. Fragility models have been developed based on (1) expert opinion or engineering judgment, (2) statistical analysis using data collected during past earthquakes, (3) simulation and modeling of component performance under earthquake loading, and (4) a combination of physical and computer models as well as empirical information. Examples of these functions are described below. However, this is not an exhaustive list and updated models continually become available.

One of the most widely used sources for fragility curves is the HAZUS^{MH} Technical Manual (DHS 2003). It provides fragility functions, typically in the form of parameters $\lambda_{j,k}$ and $\zeta_{j,k}$ for the formulation in Equation (5.8), for a large number of generic infrastructure types including transportation systems (highway, air, and rail), utility systems (potable water, waste water, oil, natural gas, electric and communications), and building stocks. Statistical uncertainty and uncertainty in the functional form of the fragility models are generally not explicitly described. Because of the large number of infrastructures included in that document, the fragility functions are based primarily on engineering judgment. As a result, they are associated with a high degree of uncertainty. While the HAZUS^{MH} Technical Manual is a good source of fragility functions for

generic systems, the models for specific classes of infrastructure components that have been developed by researchers in discipline-specific settings tend to be more accurate.

Researchers in bridge engineering have been prolific producers of fragility curves. A wide range of models is available, including older models developed using expert knowledge (e.g., Rojahn and Sharpe 1985), empirically based formulations (e.g., Basoz et al. 1999; Shinozuka et al. 2000), models based on structural analysis (e.g., Karim and Yamazaki 2003; Mackie and Stojadinovic 2004; Mackie and Stojadinovic 2006), and hybrid models that combine empirical and analysis-based methods (e.g., Gardoni et al. 2002; Kim and Shinozuka 2004). Some highly specific models provide, for example, the fragility of retrofitted structures (Padgett and DesRoches 2009), time-dependent fragility curves capturing the behavior of deteriorating structures (Gardoni and Rosowsky 2009; Sung and Su 2009), seismic fragility curves specifically for bridges in the central and southeastern United States (Nielsen and DesRoches 2007), and bridges under ground motion with spatial variation (Kim and Feng 2003). Although the majority of bridge fragility curves consider ground shaking as the hazard, models are also available that consider liquefaction and lateral spreading (Bowers 2007; Zhang et al. 2008).

Fragility curves for other components of transportation infrastructure are available, but in a more limited capacity, e.g., functions are available to estimate the mean number of post-earthquake damages per kilometer of highway embankment (Mizuno et al. 2008) and for predicting the performance of rail viaducts (Kurian et al. 2006; Yoshikawa et al. 2007). Fragility curves for transportation infrastructures other than bridges tend to be based on observations from a single earthquake or analyses of a single structure.

The American Lifelines Alliance provides fragility functions for components of water distribution systems including buried pipelines, water tanks, tunnels, and canals (Eidinger et al. 2001). The seismic hazards discussed include ground shaking, liquefaction, landslide, and fault rupture. Additional studies model the performance of underground pipelines to ground shaking and fault rupture (Jacobson and Grigoriu 2005; Shih and Chang 2006; Toprak and Taskin 2007). The majority of these pipeline studies are based on post-earthquake observations.

Fragility functions for components in electrical distribution systems are available from several authors including Vanzi (1996), who modeled the reliability of electrical networks by assessing

the fragility of microcomponents and macrocomponents. Ang et al. (1996) developed fragility functions for critical components and substations. Straub and Der Kiureghian (2008) developed empirical fragility models for components in an electrical substation, while accounting for parameter uncertainties and statistical dependence among observations. Fragility models are also available for components of hydropower systems (Lin and Adams 2007) and nuclear power facilities (Kennedy and Ravindra 1984; Nakamura et al. 2010).

Fragility functions have also been developed for other types of infrastructure components such as oil storage facilities (Fabbrocino et al. 2005) or more general on-grade steel storage tanks (O'Rourke and So 2000; Berahman and Behnamfar 2007). Furthermore, a vast literature exists relating to fragility curves for many classes of buildings (e.g., Ellingwood 2001; Ryu et al. 2008; Park et al. 2009; Rota et al. 2010).

6. Modeling System Performance with BNs

6.1 Introduction

This chapter presents BN formulations for modeling the performance of an engineered system as a function of the states of its constituent components. It begins with a brief review of conventional methods for modeling system performance, including reliability block diagrams, fault trees, event trees, and minimal link and cut sets. Then it compares these methods with the use of BNs for modeling system performance. The chapter continues with the description of several methods for modeling system performance within the context of BNs. Emphasis is placed on the computational efficiency of these methods and algorithms are developed for minimizing computational demands. The chapter concludes with example applications.

6.2 Conventional methods of modeling system performance

A system is a collection of components, each having one or more states. The state of the system is defined as a function of the states of the individual components that compose it. Critical infrastructure systems (e.g., transportation networks, water and power distribution systems) as well as structural systems (e.g., buildings and bridges) are all engineered systems for which it is important to know the system reliability. As described in previous chapters, these systems have statistically dependent component states due to several factors, including dependence in loading and in capacities.

Various methods have been developed to facilitate the performance modeling of engineered systems, all of which represent the system performance as a function of events that affect its overall state. Several of these are briefly described below.

6.2.1 Qualitative methods

The qualitative systems analysis methods described below are typically used in organizational settings to help identify failure modes, consequences, and remedial actions.

6.2.1.1 Failure modes and effects analysis

Failure modes and effects analysis is used for enumerating system failure modes. It is primarily an organizing tool listing, for example, system components that can fail, the corresponding component failure modes, the probability of occurrence for each mode, and the possible ways the governing organization can respond (Lewis 1987). The results of a failure modes and effects analysis are often used to construct graphical models such as fault trees (described below).

6.2.1.2 Reliability block diagrams

The reliability block diagram (RBD) is a graphical way of representing system topology. The blocks in an RBD represent system components or events, and links represent component relationships. The blocks are arranged in series and parallel configurations to show logical interactions between components (Pagès and Gondran 1986). An example of an RBD is shown in Figure 6.1, in which a source and a sink node are connected by eight components. Components 1, 2, and 3 are shown in parallel and components 4, 5, and 6 are constructed in series. Each of the components 1, 2, and 3 exists in series with components 7 and 8, and components 4, 5, and 6 collectively exist in series with components 7 and 8. This example system is used throughout this chapter for illustration purposes.

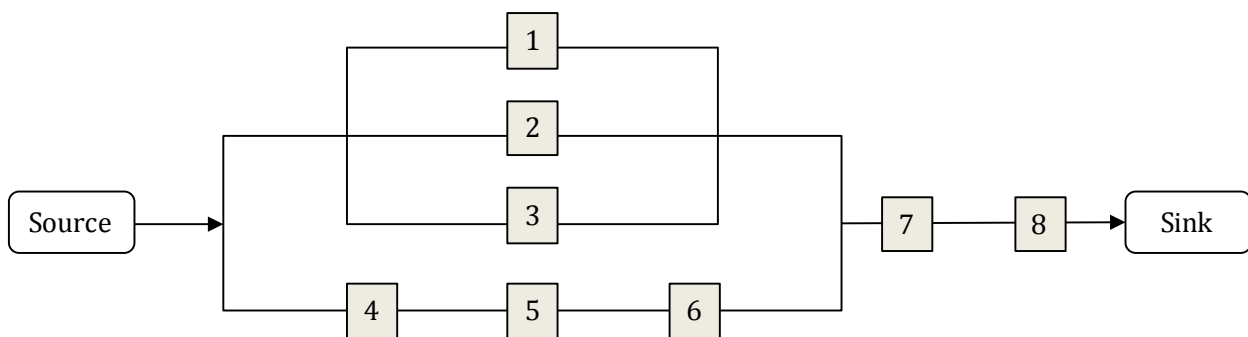


Figure 6.1: Example reliability block diagram

6.2.1.3 *Fault trees*

A fault tree is a graphical model of events that, when occurring individually (i.e., events in series) or in conjunction with other events (i.e., events in parallel), give rise to higher-level events that eventually lead to system failure. A fault tree is constructed specifically for a particular undesired event or mode of system failure. Therefore, a single fault tree cannot model all possible modes or causes of system failure. Fault trees are graphical models. They are first and foremost qualitative models, though quantitative analyses can be performed on them.

A fault tree consists of a *top event* corresponding to the undesired system event. *Gates* in a fault tree permit or inhibit the passage of fault logic up the tree. We limit ourselves here to consideration of two important types of gates: *and gates* and *or gates*. An *and gate* indicates that all input failure events must occur for the output event to indicate failure. Conversely, an *or gate* signifies that the output event is in the failure state if any of the input events is in the failure state (NRC 1981).

Fault trees are typically used to identify possible sequences of events leading to the occurrence of the undesired top event. They are used most often in operational settings, e.g., to enumerate sequences of events leading to core damage in a nuclear reactor. For example,

Figure 6.2 shows a fault tree corresponding to the undesired event of a traffic signal failure at a dangerous intersection. It is assumed that there are two possible causes for the failure: loss of power *or* damage of the signal control box due to vehicle collision. Loss of power only occurs if offsite power supply *and* emergency backup power supply both fail. The emergency power supply system fails if either the trigger that initiates the switch to backup power fails *or* the emergency batteries are dead.

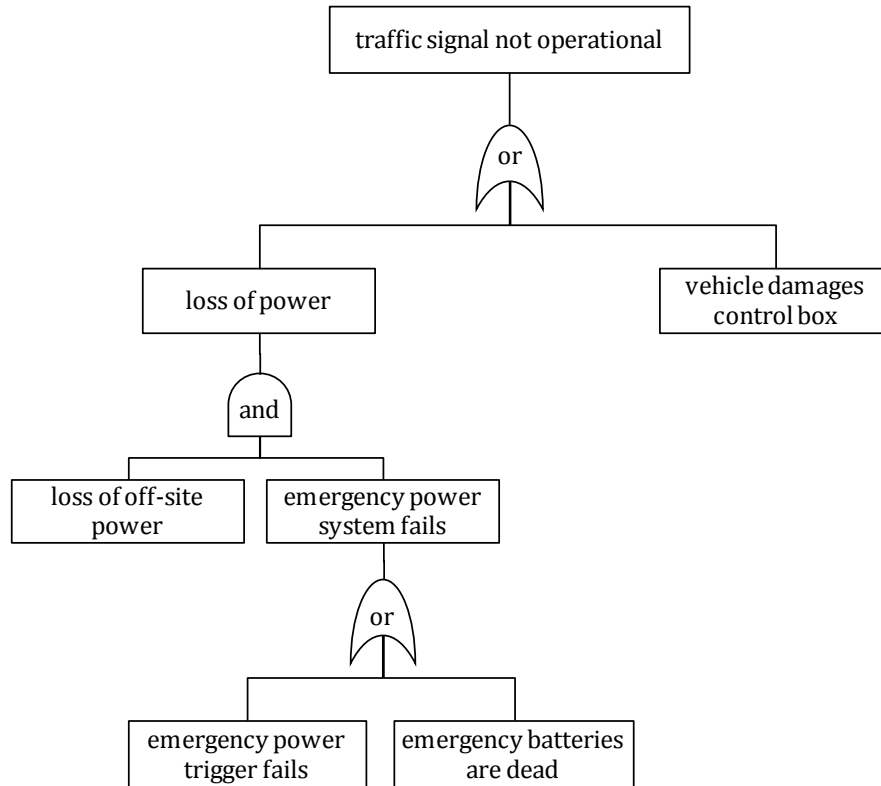


Figure 6.2: Example operational fault tree corresponding to traffic signal failure problem

It is uncommon to use fault trees to analyze topologically defined networks commonly found in civil engineering applications, such as transportation or water distribution systems. Such networks are often defined by an RBD. However, fault trees can be constructed from simple RBDs. A fault tree associated with the RBD in Figure 6.1 is shown in Figure 6.3. The circle nodes represent basic events that correspond to the failure of components C_1, \dots, C_8 . A bar over the component name denotes a failure event. For complex topological networks, direct construction of a fault tree from an RBD is difficult.

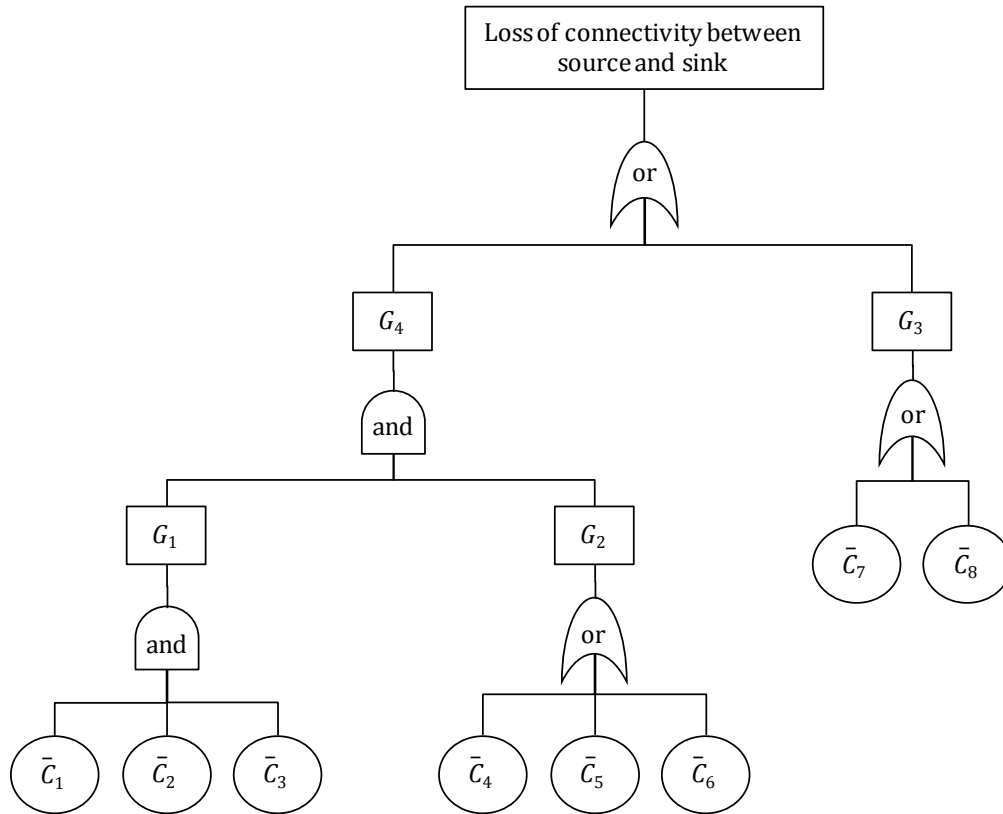


Figure 6.3: Fault tree corresponding to RBD in Figure 6.1

6.2.1.4 Event trees

An event tree is a graphical model that is used for inductive analyses. It begins with an initiating event and then branches outward following possible progressions of subsequent events, e.g., failure or nonfailure of other components (Pagès and Gondran 1986). Like fault trees, event trees are primarily qualitative tools useful for identifying failure sequences in operational settings. In the example involving a traffic signal, one possible initiating event is the loss of offsite power. The corresponding event tree is shown in Figure 6.4.

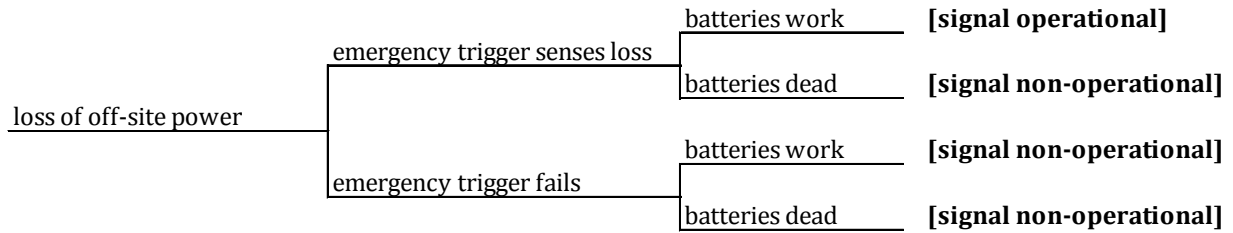


Figure 6.4: Example event tree corresponding to signal failure problem

6.2.2 Quantitative methods

Consider a system of n components. Each component $i \in [1, n]$ has d_i discrete component states. Each system configuration represents a distinct combination of component states. Therefore the number of distinct configurations of the system is $N = \prod_{i=1}^n d_i$. Clearly, for systems with either a large number of components or components with many states, the number of distinct system configurations can be large. Define s_i as an indicator variable corresponding to the state of component i , with outcomes in the set $\{1, 2, \dots, d_i\}$. Also define S as an indicator variable for the state of the system with outcomes in the set $\{1, 2, \dots, D\}$, where D indicates the number of system states. The N distinct system configurations fall into the D distinct system states in accordance to the structure of the system. In general $D \leq N$ and usually $D \ll N$ (Der Kiureghian 2006).

Quantitative system analysis methods define a mapping $S = f(s_1, \dots, s_n)$, known as the *system function*, that quantifies the relationship between the component and system states. Often the formulation of the system function is best done by individuals familiar with the disciplinary nature of a system. When the component states are random, and thus the system state is stochastic, the resulting quantitative analysis solves a *system reliability* problem (Der Kiureghian 2006). In such problems, the objective of quantitative analysis is to determine a system failure probability or, complementarily, the system reliability. When both the components and the system have binary states (e.g., on/off, open/close), the result is a special case of the system reliability problem in which $N = 2^n$ and s_i and S are Boolean random variables defined such

that $\mathcal{S}, \mathcal{s}_i \in \{0,1\}$. We use the convention that 0 and 1 respectively denote the failure (false) and survival (true) states.

6.2.2.1 Minimal link sets and cut sets

The analysis of systems with binary component and system states is often quantified through the use of *link sets* and *cut sets*. A link set is a set of components whose joint survival ensures survival of the system. Conversely, a cut set is a set of components whose joint failure constitutes system failure. A *minimal (or minimum) link set* (also referred to as a *minimal path set*) is a link set that ceases to be a link set if any component is removed from it. Similarly, a *minimal (or minimum) cut set* is a cut set containing no superfluous components.

The system failure probability is specified in terms of the minimal cut sets (MCSs) or the minimal link sets (MLSs). Using MLSs, the system failure probability is written as

$$P_f = 1 - \Pr \left(\bigcup_{1 \leq i \leq N_{MLS}} \left(\bigcap_{j \in MLS_i} \{\mathcal{s}_j = 1\} \right) \right), \quad (6.1)$$

where N_{MLS} is the number of MLSs of the system and $MLS_i, i = 1, \dots, N_{MLS}$, denotes the set of indices corresponding to the components in the i th MLS. It follows from Equation (6.1) that each MLS is a series system of its components, i.e., all components must survive for the MLS to survive. The system state is a parallel system of its MLSs, i.e., the system survives if any MLS survives.

In terms of the MCSs, the system failure probability is written as

$$P_f = \Pr \left(\bigcup_{1 \leq i \leq N_{MCS}} \left(\bigcap_{j \in MCS_i} \{\mathcal{s}_j = 0\} \right) \right), \quad (6.2)$$

where N_{MCS} is the number of MCSs of the system and $MCS_i, i = 1, \dots, N_{MCS}$, denotes the component indices of the i th MCS. Each MCS is a parallel system of its components, and the system state is a series system of the MCSs.

The enumeration of MCSs (or MLSs) is an essential part of conventional quantitative systems analysis. Qualitatively, MCSs may be interpreted as weak points in the system and sources of

false redundancy (Pagès and Gondran 1986). Algorithms for determining system MCSs/MLSs include methods ranging from inductive analysis to approaches utilizing simulation (Shin and Koh 1998; Suh and Chang 2000; Yeh 2006). MCSs can also be determined directly from fault trees (Pagès and Gondran 1986; Fard 1997).

6.2.2.2 Additional methods

The use of MLSs and MCSs is one of the most common methods for quantifying system performance, but other approaches exist. These methods include definition of Boolean *operating* and *failure functions* as well as construction of *state transition (Markov) diagrams*. Additional details on these less widely employed methods can be found in Pagès and Gondran (1986).

6.3 Existing works using BNs to model system performance

Examples of the use of BNs for modeling system performance are limited. The majority of work in this area relates to the conversion of conventional qualitative system modeling techniques into BNs. For example, Torres-Toledano and Sucar (1998) addressed converting RBDs into BNs for simple system configurations. However, they only considered simple RBDs and did not address issues related to computational efficiency or tractability, nor did they provide algorithms for automating the construction of BNs from RBDs for large and complex problems. Doguc et al. (2009) provided a generic algorithm for learning the structure of a system performance BN automatically from raw system behavior data using an algorithm that is efficient for complete systems and large data sets. They sought to eliminate the need for expert interference by constructing BNs automatically. However, for many civil engineering systems, data are sparse and the BNs resulting from such an algorithm may be inefficient, intractable, or inaccurate.

A fault tree may be considered a deterministic special case of a BN (Lampis and Andrews 2009). Because of the advantages of using BNs over fault trees, several authors have described algorithms for generating BNs from fault trees (Bobbio et al. 2001; Liu et al. 2008; Lampis and Andrews 2009). While the algorithms differ slightly from author to author, they generally consist of the following steps: (1) converting basic (bottom) events in the fault tree into root (top) nodes in the BN, (2) expressing logical gates in the fault tree as nodes in the BN, (3) assigning links in the BN consistent with the input-output relationships in the fault tree, and (4) assigning CPTs

consistent with the logic gates in the fault tree. Using such an algorithm, the fault tree in Figure 6.3 is converted to the BN in Figure 6.5.

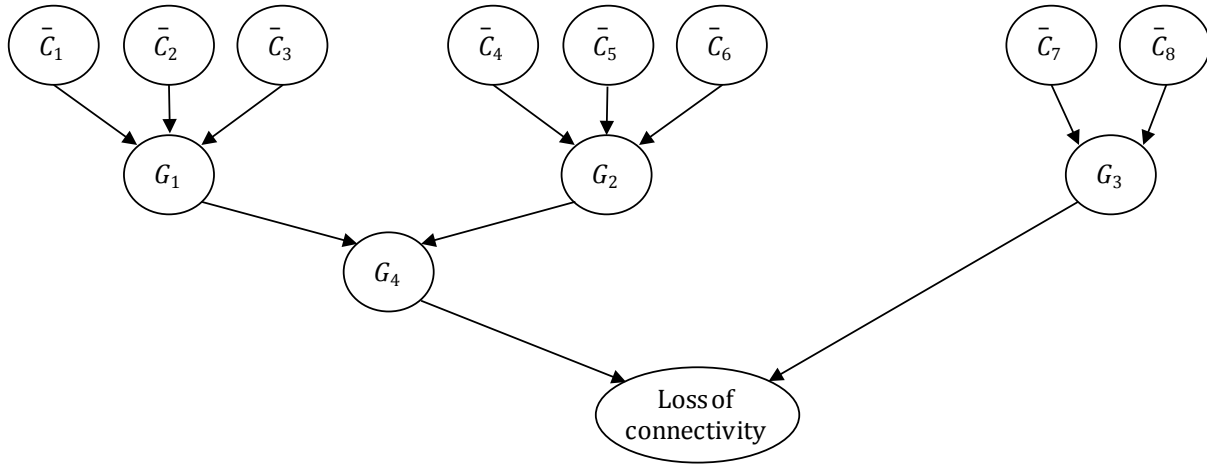


Figure 6.5: BN corresponding to fault tree in Figure 6.3

The CPTs of the nodes G_i are constructed using the logical relations

$$\begin{aligned}
 \bar{G}_1 &= \bigcap_{i=1}^3 \bar{C}_i \\
 \bar{G}_2 &= \bigcup_{i=4}^6 \bar{C}_i \\
 \bar{G}_3 &= \bar{C}_7 \cup \bar{C}_8 \\
 \bar{G}_4 &= \bar{G}_1 \cap \bar{G}_2 \\
 LC &= \bar{G}_4 \cup \bar{G}_3
 \end{aligned} \tag{6.3}$$

where G_i is the event that the output event from the gate is in the survival state and \bar{G}_i indicates its complement, the failure state. LC represents the event of loss of connectivity between the source and sink.

While both BNs and fault trees are graphical models and are useful for representing systems, BNs have capabilities that fault trees do not have:

- (1) Unlike faults trees, in BNs the dependence relations between components are not restricted to be deterministic and BNs are not limited to binary components (Bobbio et al. 2001).

- (2) The BN framework enables modeling of complex dependences among the performances of individual components.
- (3) BNs permit information to be entered at any node and this evidence propagates throughout the BN.
- (4) BNs avoid repeating nodes associated with common causes (Mahadevan et al. 2001).

6.4 BN formulations for modeling system performance

This section presents five formulations for modeling system performance using BNs. We focus first on systems with binary component and system states. The components of such a system have two states and the system itself also has two states, e.g., connectivity between the source and sink nodes exists or does not exist. The analysis for this class of systems is obviously simpler than when the components or the system have multiple states. Consideration of the multistate problem is presented in subsequent sections. We initially introduce five methods for modeling system performance: (1) naïve formulation, (2) explicit connectivity formulation, (3) explicit disconnectivity formulation, (4) MLS formulation, and (5) MCS formulation. Later, we adapt formulations (4) and (5) with the goal of optimizing computational efficiency.

6.4.1 Naïve formulation

Consider a system of n components, each component $i \in [1, n]$ having d_i discrete component states. Therefore, the number of distinct configurations of the system is $\prod_{i=1}^n d_i$. We refer to the BN formulation that corresponds to the joint consideration of all combinations of component and system states as the *naïve BN formulation*. In this formulation, a single node S_{sys} , representing the state of the system, is defined as a child of all nodes representing the states of the components forming a converging structure, as shown in Figure 6.6. For a system with n binary components and binary system state, node S_{sys} has a CPT of size 2^{n+1} . For systems with a large number of components, the size of the CPT of node S_{sys} quickly causes the BN to become computationally intractable. However, the naïve formulation is useful when the number of components is small, e.g., in the reliability assessment of simple structural systems. Mahadevan

et al. (2001) used a formulation like that in Figure 6.6, with components representing limit-state functions corresponding to the failure modes of a structural system. The number of limit-state functions in their example is small enough that the CPT associated with the system node is not prohibitively large. However, for realistic infrastructural systems, this approach is impractical. Hence, while easy to formulate, this is not a pragmatic approach for many real-world applications involving infrastructure systems, where the number of system components is often large.

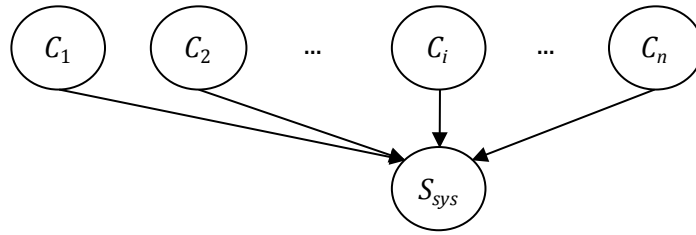


Figure 6.6: Naïve BN system formulation

Consider the example system represented by the RBD in Figure 6.1. In this system, eight components (squares) connect the system source and sink. It is assumed that only the square components in the system can fail. The required system performance is connectivity between the source and sink nodes. The naïve BN formulation for this system is shown in Figure 6.7. For binary components, the state of the system must be specified for each combination of the states of the eight components, thus the size of the CPT associated with node S_{sys} is $2^8 = 256$. Assuming each member of the CPT takes up 8 bytes of memory, the CPT requires 2 kilobytes of computer memory to store the table. If the number of states associated with each node is increased from 2 to 10, then the CPT grows to 10^8 and amount of memory required to store it increases to over 7 gigabytes and inference using exact inference algorithms cannot be done on a standard workstation. Adding just one more component node to the BN increases the memory requirement to $10^9 \times 8$ bytes (nearly 75 GB) simply to hold the CPT in memory. It is clear that the naïve formulation is computationally impractical when either the number of states associated with each node is large or the system has many components.

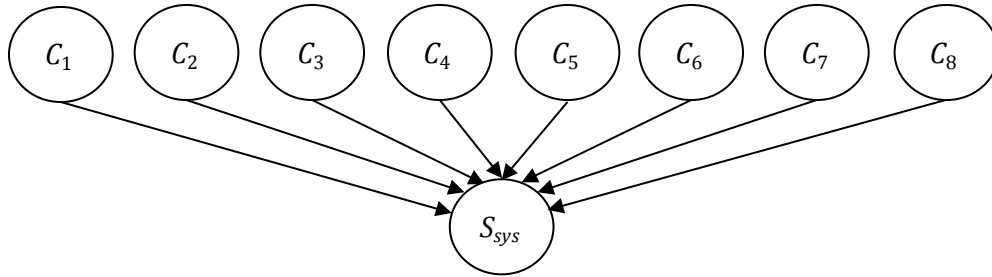


Figure 6.7: Naïve formulation for example system

6.4.2 Explicit formulations

Two intuitive approaches for modeling system performance with BN are next developed and are referred to as the *explicit connectivity* and *explicit disconnectivity* formulations. These explicit formulations use a causal rather than systematic approach, in which connectivity paths or disconnectivity sequences are constructed manually based on the topology of the system. The explicit formulations are designed to aid interaction with third-party system owners or operators; their intuitive nature allows for validation by interested parties familiar with a particular system but not with quantitative systems analysis techniques or BNs.

6.4.2.1 *Explicit connectivity formulation*

Friis-Hansen (2004) proposed a BN approach to modeling system performance in which system connectivity is modeled by exploiting causal relationships between the system components necessary for its survival. The *explicit connectivity (EC) BN formulation* defined in this study is a formalization of the approach to modeling system performance advocated by Friis-Hansen (2004). In promoting this intuitive approach, Friis-Hansen noted that when modeling complex systems, it is of utmost importance that the modeling can be validated by third parties. Therefore, the modeling approach should focus on transparency, which causal modeling helps ensure. Thus the EC BN formulation expresses system connectivity using a causal interpretation of the connectivity paths. We think of it as the optimist’s formulation (in contrast to the explicit disconnectivity formulation, which is viewed as a pessimist’s formulation), because one models the system by directly defining paths that ensure *survival* of the system. This approach does not formally require identification of MLSs, though the causal logic indirectly employs them. Due to

the encoded causal relationships, the resulting BN is likely to produce CPTs that are smaller than those of the naïve formulation. As a result, the EC formulation is typically superior to the naïve formulation in terms of computational efficiency.

The EC formulated BN must be constructed for each system of interest. Because the construction of the explicit formulation is not systematic, accuracy is not guaranteed, particularly for large or complex systems. Furthermore, there is no formal control on the computational demands of the resulting BN. To illustrate the construction of a BN using the EC formulation, Figure 6.8 shows two possible BNs that may be constructed using this approach for the RBD shown in Figure 6.1. The BN formulation in Figure 6.8a distinguishes two paths through the system: an upper path and a lower path, as shown in Figure 6.9.

Let C_i be the event that component i is in the survival state. The upper path is open only if components 7 and 8 are functioning and at least one of components 1, 2, and 3 is also working. The Boolean logic corresponding to this causal interpretation is used to construct the CPT of the node *Upper Path* in Figure 6.8a. The event in which the upper path is operational (denoted UP) is expressed as

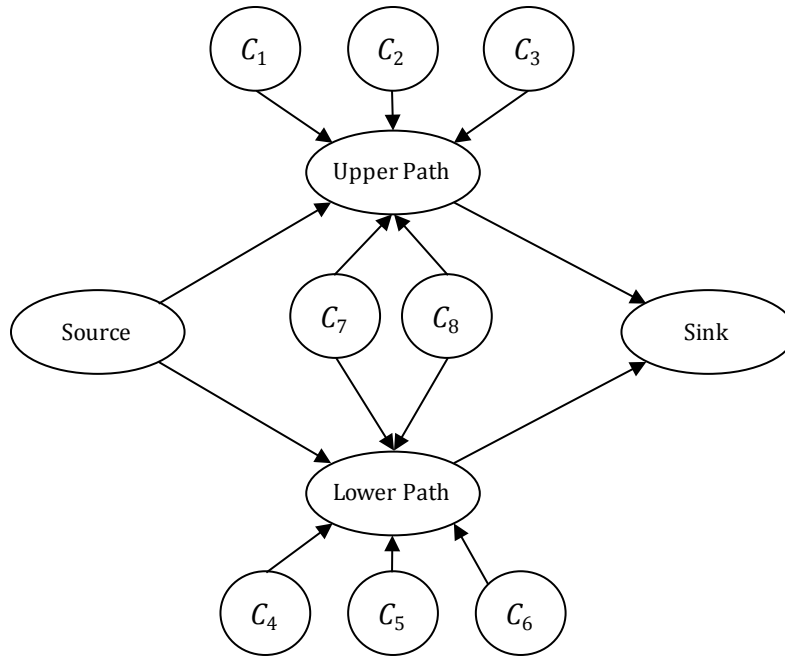
$$UP = C_7 \cap C_8 \cap (\cup_{i=1}^3 C_i). \quad (6.4)$$

Similarly, the CPT attached to the node labeled *Lower Path* is constructed using the Boolean logic

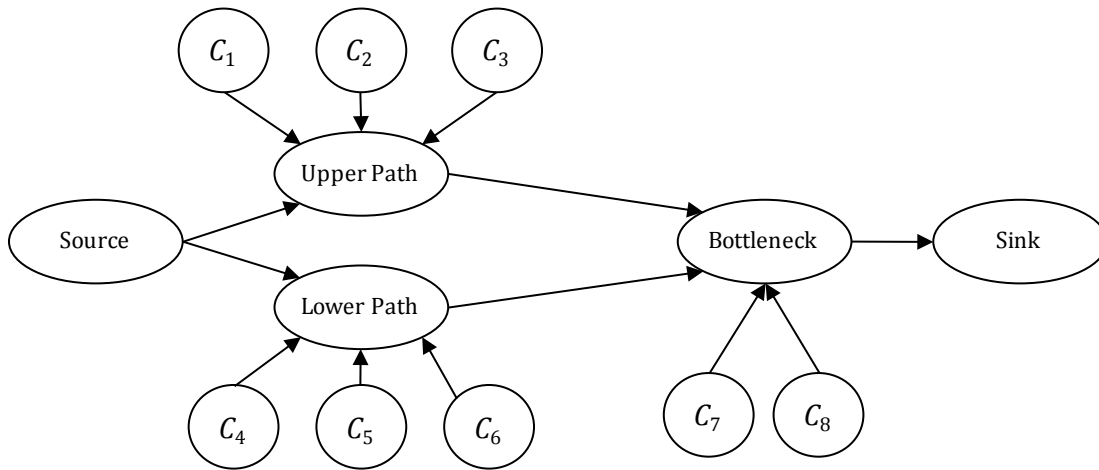
$$LP = C_7 \cap C_8 \cap (\cap_{i=4}^6 C_i), \quad (6.5)$$

where LP is the event in which the lower path is functioning. Connectivity between the source and sink is maintained if either path is functioning. Letting *Sink* be the event in which there is connectivity to the sink, the CPT attached to the corresponding node is expressed using the logic

$$Sink = UP \cup LP \quad (6.6)$$



(a)



(b)

Figure 6.8: Examples of possible EC formulations for system in Figure 6.1

Alternatively, one can model the system bottleneck explicitly while distinguishing between the upper and lower paths up to the bottleneck. The associated BN is shown in Figure 6.8b. The CPT for node *Upper Path* is constructed using the logic: $UP = \bigcup_{i=1}^3 C_i$. The CPT for node *Lower Path* is similarly constructed: $LP = \bigcap_{i=4}^6 C_i$. The node *Bottleneck* is constructed using

a causal interpretation of the connectivity paths: one is able to traverse the bottleneck only if one is first able to reach the bottleneck through either the lower or upper path *and* both components 7 and 8 are functioning. The CPT for node *Bottleneck* is thus constructed:

$$BT = (UP \cup LP) \cap C_7 \cap C_8, \quad (6.7)$$

where BT corresponds to the event in which one is able to traverse the system bottleneck. Relative to the naïve formulation, the EC formulation is advantageous because it facilitates understanding of system topology, whereas the naïve formulation aggregates all system states into a single node. Furthermore, the EC formulation is typically associated with significantly smaller CPTs, and thus lower memory demands, than the naïve formulation.

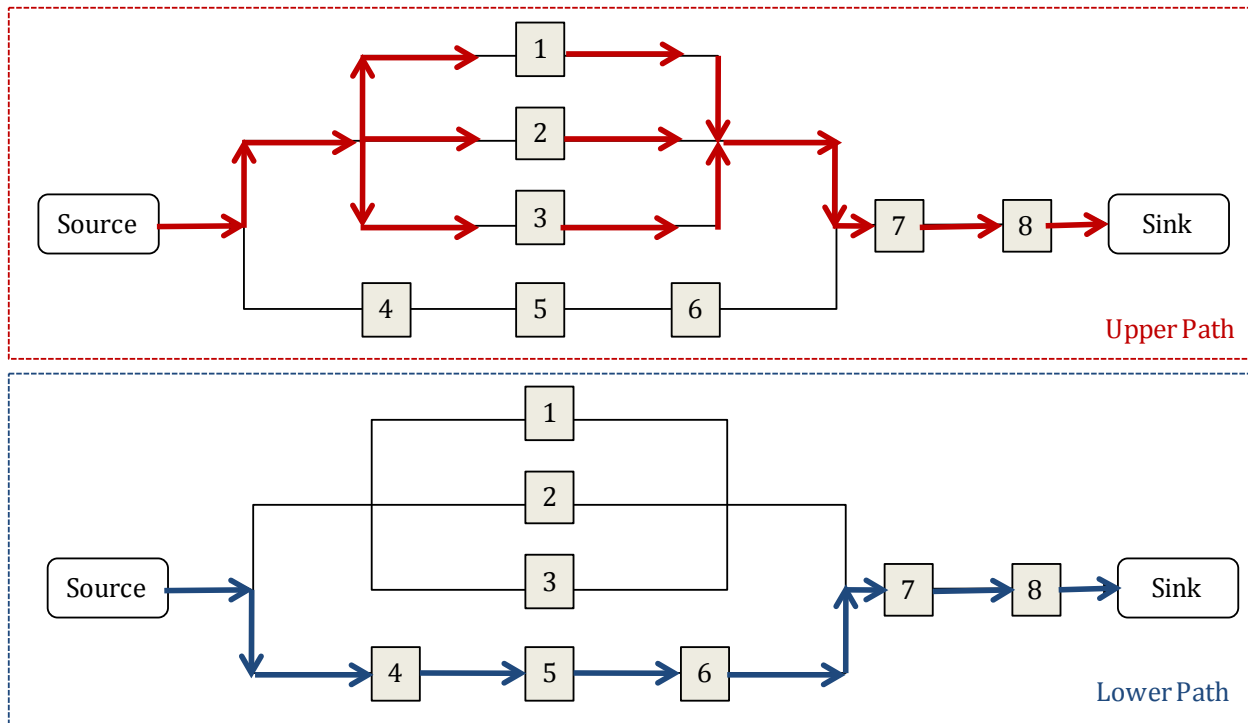


Figure 6.9: Illustration of upper and lower paths through example system used for construction of EC BN formulations in Figure 6.1

6.4.2.2 *Explicit disconnectivity formulation*

The dual of the EC formulation is defined as the *explicit disconnectivity* (EDC) *BN formulation*. Rather than tracing paths that ensure survival of the system, one pursues causal event paths that ensure failure of the system. This may be a less intuitive approach than the EC formulation as it

follows a pessimist’s perspective. The EDC formulation can often improve upon the naïve formulation, particularly when the number of failure event paths (or MCSs) is small relative to the number of components. The EDC formulation does not explicitly require the MCSs, though the causal logic indirectly employs them. The EDC formulation may be instinctual for situations in which the construction of fault and event trees is common, because these models are constructed by enumerating failure sequences.

Consider the example system in Figure 6.1. Working backward from the sink, we observe that disconnectivity will occur if the bottleneck is blocked, or if connectivity is blocked further upstream. The upstream connectivity is lost only if both the upper and lower paths through the system up to the bottleneck are closed. The lower path is not operational if any component along it fails. The upper path loses connectivity only if all components fail. The above description leads to the BN in Figure 6.10. This formulation has the same topology and conditional relationships as the BN in Figure 6.5, which was created directly from a fault tree.

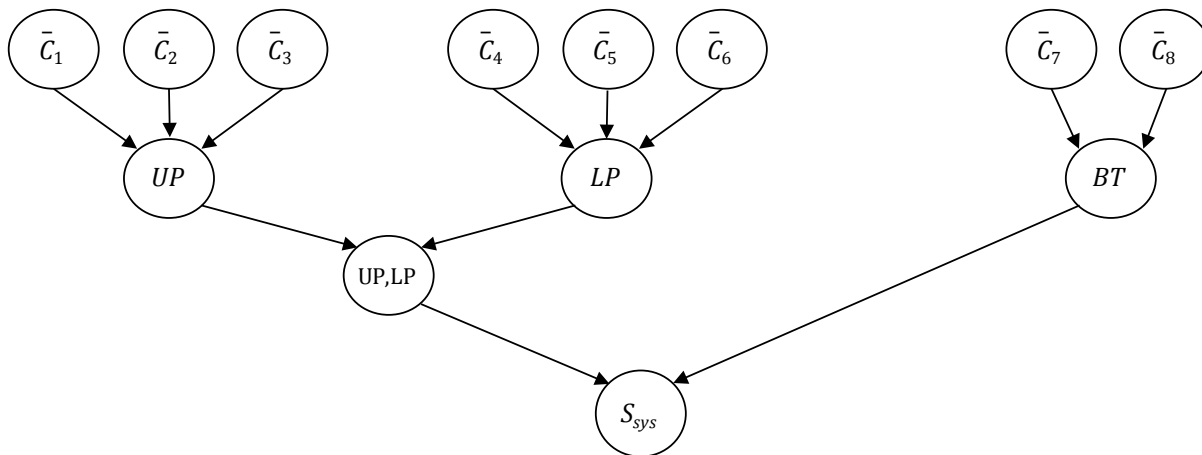


Figure 6.10: Example EDC BN formulation for system in Figure 6.1

Like the EC formulation, the EDC formulation is more computationally efficient than the naïve formulation due to the generally smaller CPT sizes. It likewise lends itself to easier interpretation than the naïve formulation.

6.4.3 Minimal link set and minimal cut set formulations

As described previously, a common approach to making systems analysis more methodical is through the use of minimal link sets and minimal cut sets. Recall that a minimal link set (MLS) is a minimum set of components whose joint survival constitutes survival of the system. The *minimal link set BN formulation* introduces intermediate nodes, between the component and system nodes in the naïve formulation, that correspond to the MLSs. Analogously, the *minimal cut set BN formulation* introduces intermediate nodes corresponding to the system MCSs. Torres-Toledano and Sucar (1998) used an MLS-based BN formulation for modeling system performance, though with less formality and generality than is described here.

6.4.3.1 Minimal link set formulation

The MLS BN formulation introduces intermediate nodes corresponding to the system MLSs between the nodes representing component and system states. In the example in Figure 6.11, the binary states of the MLS nodes are defined such that each MLS node is in the survival state only if all its constituent components have survived; otherwise it is in the failure state. The system node is in the survival state if any MLS node is in the survival state. The MLS BN formulation takes advantage of the fact that each MLS node is a series system of its components, and that the system node is a parallel system of its MLS parents. Clearly, this formulation is advantageous to the naïve formulation described above, particularly when the system has fewer MLSs than components. With binary component and system states, the size of the CPT for each MLS node is 2 to the power of the number of its constituent components plus one, and the size of the system node CPT is 2 to the power of the number of MLSs plus one. As a result, when the number of MLSs is large, the size of the CPT associated with the system node S_{sys} becomes large. A similar problem occurs for a MLS node with a large number of constituent components. To address this problem, the MLS formulation described here is adapted in later sections.

The example system in Figure 6.1 has four MLSs: $MLS_1 = \{1,7,8\}$, $MLS_2 = \{2,7,8\}$, $MLS_3 = \{3,7,8\}$, and $MLS_4 = \{4,5,6,7,8\}$. The MLS-formulated BN for the example system is shown in Figure 6.12. For this example, the largest CPT occurs at node MLS_4 and has size 2^6 . The total memory requirement associated with performing inference in this BN, measured as the total clique table size, is 208, assuming independent component states.

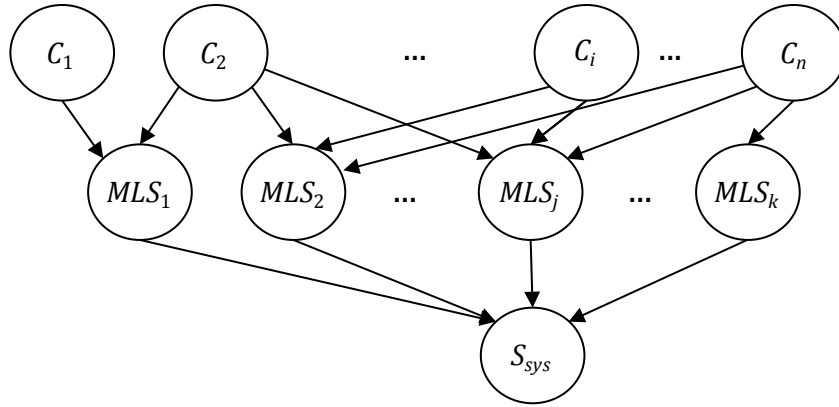


Figure 6.11: System performance BN using MLS BN formulation

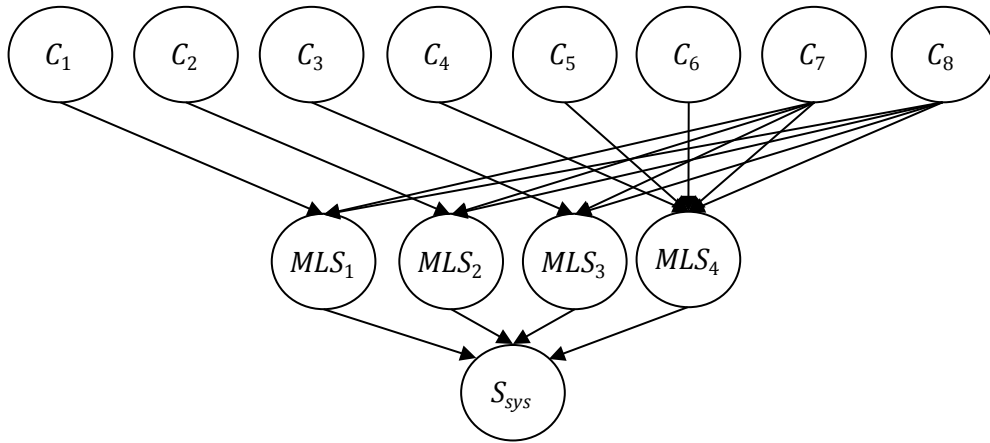


Figure 6.12: MLS formulation for example system in Figure 6.1

The CPT size can be reduced by introducing additional intermediate nodes between the component and MLS nodes or between the MLS and system nodes. A common rule when working with BNs suggests that, wherever possible, the number of parents to a node should be no more than three. For the BN in Figure 6.12, nodes MLS_4 and S_{sys} have more than three parents. Intermediate nodes are introduced into this BN to reduce the number of parents associated with any node to three or fewer, as shown in Figure 6.13.

The CPTs of the intermediate nodes $I_{MLS_4,i}, i = 1,2$, are constructed such that they are in the survival state only if all their parent nodes are in the survival state. The CPT of the child to the

intermediate nodes is constructed similarly. The CPTs of nodes $I_{sys,i}, i = 1,2$, are defined such that they are in the survival state if any of their parent MLS nodes is in the survival state. Node S_{sys} is in the survival state if any node $I_{sys,i}$ is in the survival state. The introduction of intermediate nodes in the BN decreases the size of the largest CPT to 2^4 , and the total clique table size is reduced to 176. Although the intermediate nodes result in a small computational advantage, the increase in efficiency is not significant. In later sections this MLS formulation, referred to as the *standard MLS (MCS) BN formulation*, is adapted to increase computational efficiency.

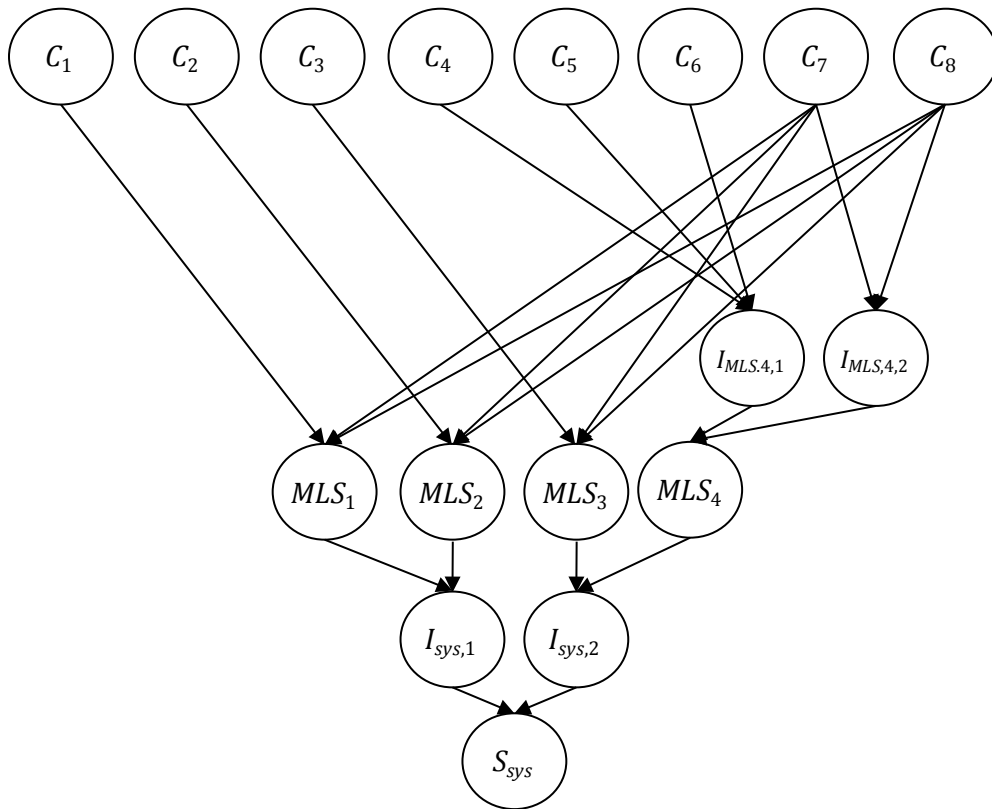


Figure 6.13: MLS BN formulation for example system in Figure 6.1, with intermediate nodes introduced to keep number of parents to a node to no more than three

6.4.3.2 Minimal cut set formulation

We define the dual of the MLS formulation as the *minimal cut set BN formulation*. In this formulation, the system node is a child of parents corresponding to MCSs, and each MCS node is a child of nodes representing its constituent components. Figure 6.14 shows a conceptual BN employing the MCS formulation. The system node is a series system of all the MCS nodes, whereas each MCS is a parallel system of its parent nodes.

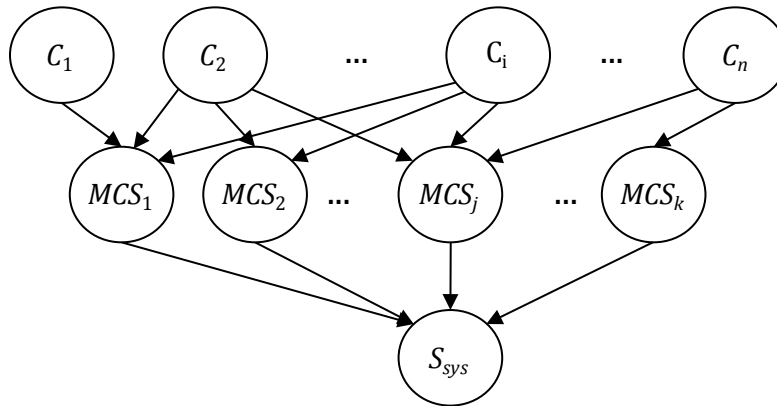


Figure 6.14: System performance using MCS BN formulation

The example system in Figure 6.1 has five MCSs: $MCS_1 = \{1,2,3,4\}$, $MCS_2 = \{1,2,3,5\}$, $MCS_3 = \{1,2,3,6\}$, $MCS_4 = \{7\}$, and $MCS_5 = \{8\}$. The MCS BN for the example system is shown in Figure 6.15. For this BN formulation, the largest CPT is associated with the system node and has size 2^6 . The total clique table size for this BN, assuming independent binary components, is 232. Introducing intermediate nodes between the MCS and system node so no node has more than three parents reduces the total clique table size to 200.

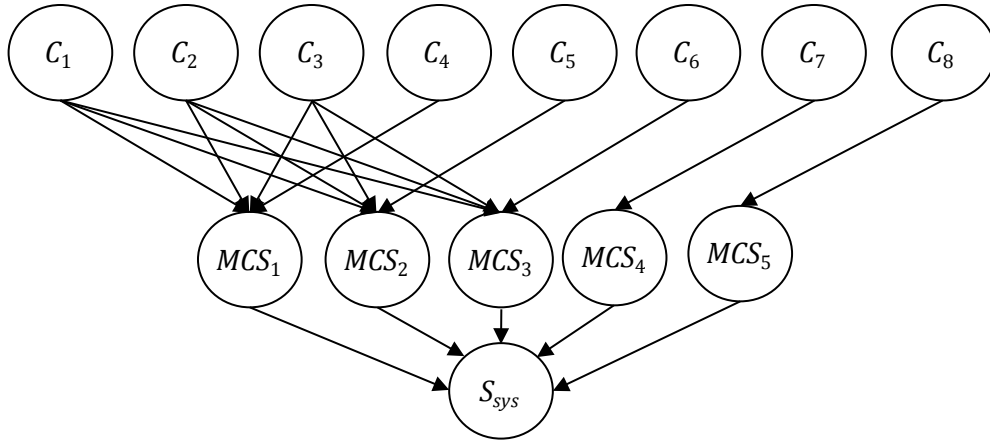


Figure 6.15: MCS formulation for example system in Figure 6.1

Generally, relative to the MLS formulation, the MCS formulation is advantageous when the number of MCSs is smaller than the number of MLSs. However, their relative advantage also depends on the number of components within the individual MLSs and MCSs. As with the MLS formulation, the CPTs in the MCS formulation become large as the number of MCSs increases or when the number of components in individual MCSs grows large.

6.4.4 Extension to multistate problems

Thus far, the BN formulations described have only considered binary-state components and systems. Multistate problems are easily handled within the MCS BN formulation through application of the max-flow min-cut theorem (Elias et al. 1956; Ford and Fulkerson 1956). We are not aware of any similar theories that allow a direct adaptation of the MLS formulation to multistate problems.

Let Cap_i denote the operating capacity of component i . Assign to each MCS a value by taking the sum of the capacities of the components in the MCS. For distributed components, one should only count the capacities going from the source side to the sink side of the cut. The max-flow min-cut theorem states that the maximum possible flow from source to sink is equal to the minimum value among all MCSs, i.e., the bottleneck in the system. The theorem allows the MCS formulation to be adapted to multistate problems, without changing the topology of the BN created when assuming components are binary. It is only necessary to (1) increase the number of

states associated with each node to correspond to the component operating levels, and (2) use arithmetic expressions rather than Boolean logic to define the relationships between the nodes.

Consider the RBD in Figure 6.1 with the MCS BN formulation in Figure 6.15. Nodes C_i are modified to contain states corresponding to operating levels of the components. If the component has flow characteristics, then the range of possible flow levels must be discretized; in such a case, node C_i will be an interval node. Similarly, nodes MCS_i must have multiple states corresponding to the values of each MCS, with CPTs defined using the relation

$$Value(MCS_i) = \sum_{C_j \in MCS_i} Cap_j. \quad (6.8)$$

Note that, because the value of MCS_i is an additive function of the capacities, the states of the system node must be modified to contain all possible system operating levels (Cap_{sys}) with CPTs defined using the relation

$$Cap_{sys} = \min_{all\ MCS_i} Value(MCS_i). \quad (6.9)$$

6.5 Efficient minimal link set and minimal cut set formulations

Because computational demands associated with the MLS and MCS BN formulations may be excessive when the number of components belonging to a MLS/MCS or the number of MLS/MCSs is large, alternative formulations are proposed here. These take advantage of the observation that BNs with nodes arranged in chain structures are generally more efficient than the converging structures characterizing the naïve and standard MLS/MCS formulations. Consider the two BN topological structures shown in Figure 6.16, in which the figure on the left shows a converging structure and the one on the right illustrates a chain structure. Both BNs model systems whose components are correlated by a common demand, D . We present a formal description of the construction of the BN in Figure 6.16b and its CPTs in the forthcoming sections.

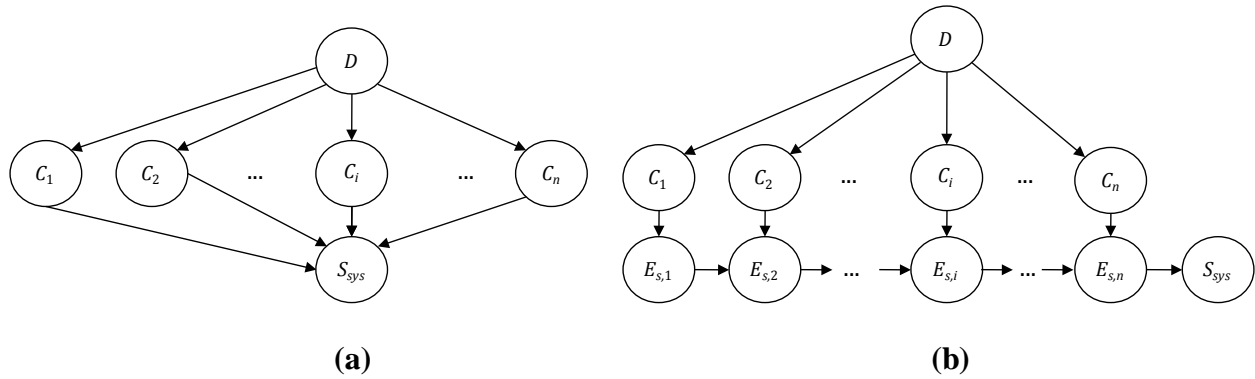


Figure 6.16: BNs with (a) converging structure and (b) chain structure

Figure 6.17 shows a comparison of the computational demands, measured in terms of the total clique table sizes, associated with binary and five-state components when the system analysis BNs are arranged in converging and chain structures as in Figure 6.16. The converging structure is associated with exponentially increasing memory demands while the complexity of the chain structure grows linearly. However, the converging structure is more efficient than the chain structure when fewer than four components are considered. Thus, when the node modeling system performance in Figure 6.16a has more than three parents, it is advantageous to model the system as in Figure 6.16b.

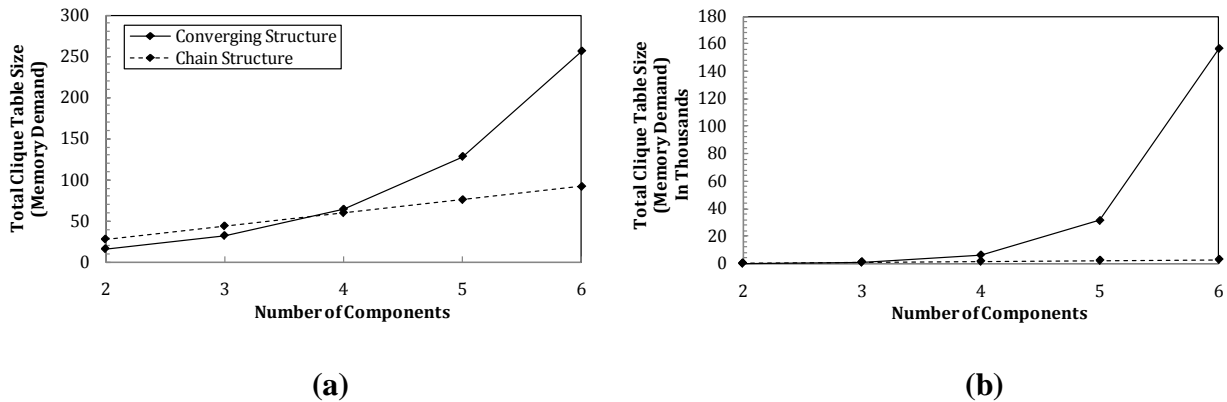


Figure 6.17: Comparison of computational demands associated with converging and chain BN topologies when components have (a) two states and (b) five states

The computational demands associated with inference are influenced not only by the system configuration, but also by the number of common parents to the component nodes in Figure 6.16.

Figure 6.19 compares computational demands associated with the converging and chain topologies for binary component nodes with one, two, and three common parent demand nodes and shows that increasing the number of common parent nodes increases the computational demands. However, the chain structure remains superior to the converging structure as the number of components increases. Note that as the number of common demand nodes increases, the point at which the converging structure is better than the chain structure moves upward slightly. For three common demand nodes, the converging structure is more efficient than the chain structure when considering up to four components. For one common demand node, the converging structure is more efficient for up to three components.

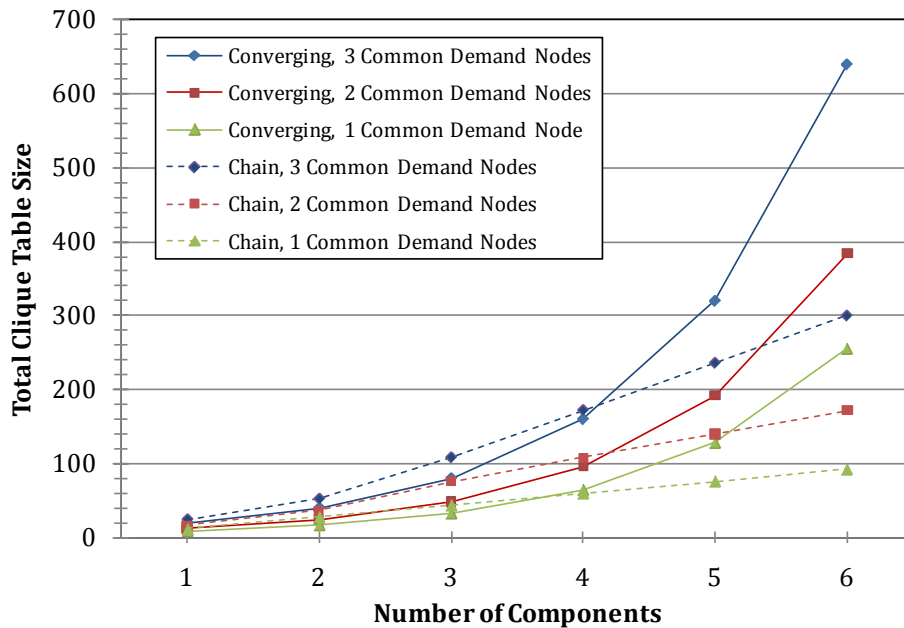


Figure 6.18: Comparison of computational demands associated with converging and chain BN topologies for binary nodes with one or more common parent demand nodes

6.5.1 Construction of efficient BN formulations for series and parallel systems

In this section, we construct efficient chain-structure BN formulations for series and parallel systems with binary states to illustrate the construction of the BN formulation. In subsequent sections, we extend the approach to more general system topologies.

Define a *survival path sequence* (SPS) as a chain of events, corresponding to an MLS, in which the terminal event in the sequence indicates whether or not all the components in the MLS are in the survival state. Note that the term “sequence” does not have any time-based implications. A series system has one MLS, and a parallel system has n MLSs. It follows that a series system has one SPS and a parallel system has n SPSs. A SPS is a chain of *survival path events* (SPEs), each of which describes the state of the sequence up to that event. SPEs are represented in the BN by nodes labeled $E_{s,i}$; the subscript i indicates that the particular SPE is associated with component i . The state of $E_{s,i}$ is defined as

$$\begin{aligned} E_{s,i} &= 1 \text{ if } E_{s,\text{Pa}(i)} = 1 \cap C_i = 1 \\ &= 0 \text{ otherwise,} \end{aligned} \quad (6.10)$$

where $E_{s,\text{Pa}(i)}$ defines the state of the SPE node that is parent to $E_{s,i}$; $E_{s,i} = 1$ indicates that the node is in the survival state and $E_{s,i} = 0$ indicates its failure. C_i denotes the state of component i with $C_i = 1$ ($C_i = 0$) indicating the survival (failure) state. Thus, for a series system, the BN formulation takes the form shown in Figure 6.19. The state of node $E_{s,1}$ is equal to the state of node C_1 . $E_{s,2}$ is in the survival state only if $E_{s,1}$ is in the survival state and C_2 is in the survival state. This pattern continues, such that $E_{s,n}$ is in the survival state only if both $E_{s,n-1}$ and C_n are in the survival state. Consequently, the state of $E_{s,n}$ describes the state of the entire SPS (i.e., it indicates whether all components in the MLS have survived) and, therefore, that of the system.

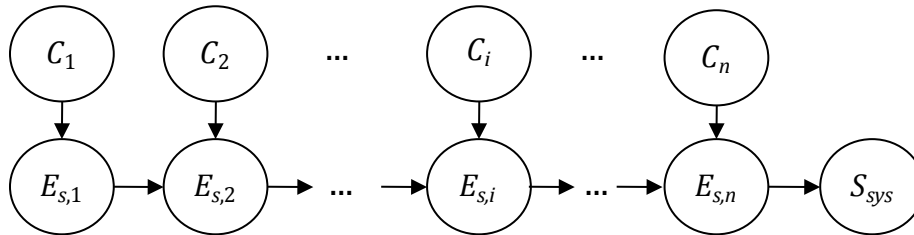


Figure 6.19: BN using SPEs to define performance of a series system

A parallel system has an SPS corresponding to each component. The resulting BN formulation is shown in Figure 6.20. The system node indicates system survival if any node $E_{s,i}$ is in the survival state. Like the naïve formulation, the exponential growth in the size of the CPT

associated with node S_{sys} renders this BN intractable when the number of components in the system is large.

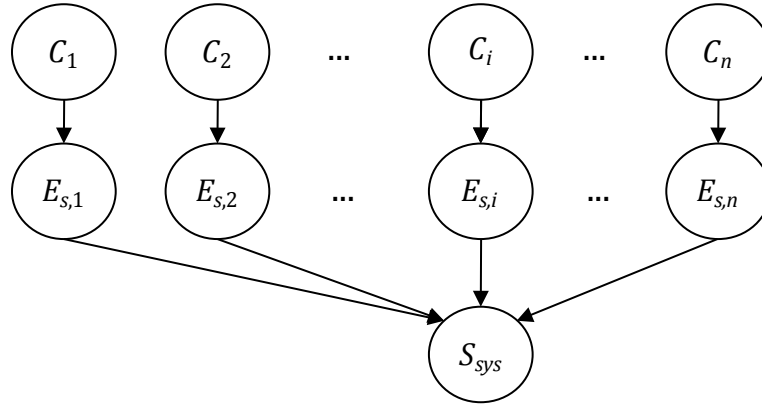


Figure 6.20: BN using SPEs to define performance of a parallel system

Define a *failure path sequence* (FPS) as a chain of events, corresponding to an MCS, in which the terminal event in the sequence indicates whether or not all the components in the MCS are in the failure state. For a parallel system, there is only one MCS and thus one FPS. For a series system with n components, there are n FPSs, one corresponding to each component. An FPS is a chain of *failure path events* (FPEs), each of which gives the state of the sequence up to that event. Let $E_{f,i}$ be the FPE associated with component i . The state of $E_{f,i}$ is expressed as

$$\begin{aligned} E_{f,i} &= 0 \text{ if } E_{f,Pa(i)} = 0 \cap C_i = 0 \\ &= 1 \text{ otherwise,} \end{aligned} \quad (6.11)$$

where $E_{f,Pa(i)}$ defines the state of the FPE node that is parent to $E_{f,i}$; $E_{f,i} = 0$ indicates that the node is in the failure state and $E_{f,i} = 1$ indicates its survival. Thus, for a parallel system, the BN formulation takes the chain form shown in Figure 6.21. The Boolean logic used to construct the CPTs in this BN is the dual of that used for SPSs, that is, $E_{f,i}$ is in the failure state only if the parent FPE is in the failure state and C_i is also in the failure state. For a series system, the BN formulation using FPSs is shown in Figure 6.22. The size of the CPT associated with S_{sys} is 2^{n+1} , and there is no computational advantage to this approach over the naïve formulation for series systems. These findings suggest that a combination of SPS and FPS formulations, described in the next section, can be used to efficiently model general systems.

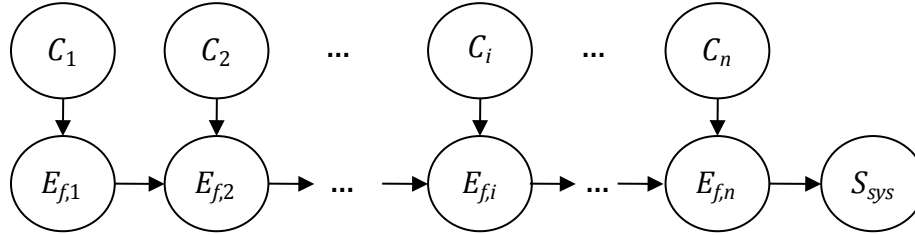


Figure 6.21: BN using FPEs to define a parallel system

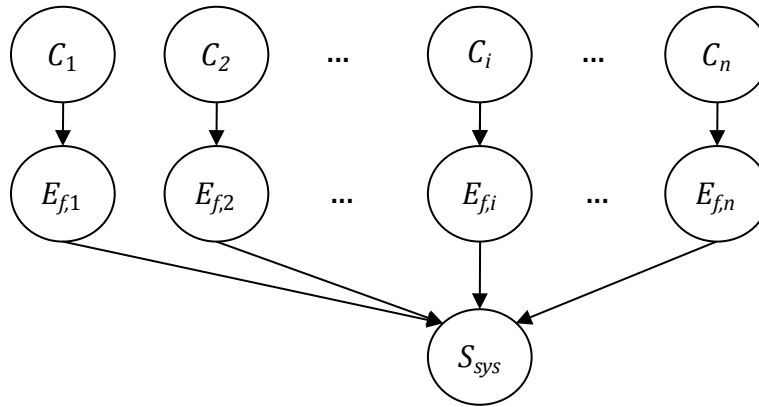


Figure 6.22: BN using FPEs to define a series system

6.5.2 General systems

This section develops efficient MLS and MCS formulations for general system topologies.

6.5.2.1 Efficient MLS formulation

As described earlier, a MLS is a series system of its constituent components. Therefore, one can construct an SPS to describe each MLS. Consider the example system in Figure 6.1, which has four MLSs: $MLS_1 = \{1,7,8\}$, $MLS_2 = \{2,7,8\}$, $MLS_3 = \{3,7,8\}$, and $MLS_4 = \{4,5,6,7,8\}$. In Figure 6.23, each MLS is modeled as an individual SPS. The SPEs, $E_{s,i}^j$, in each SPS are indexed by a subscript corresponding to the associated component i and a superscript corresponding to

SPS/MLS number j . The dependence between the SPEs corresponding to the same component is modeled through a common parent node. The system node is in the survival state if the terminal node of any SPS is in the survival state. For reference, the BN formulation in which the MLSs are arranged in chain structures is named the *efficient MLS BN formulation*. The total clique table size associated with the BN in Figure 6.23 is 224, which is higher than the demands required by the standard MLS formulation (208). This increase arises because MLSs 1–3 only have three components, and therefore it is less efficient to model them using a chain structure than a converging structure, as indicated by the graphs in Figure 6.17. Furthermore, the dependence between SPEs sharing a component increases the computational demand when performing inference in the BN. By coalescing common SPEs that appear in multiple SPSs, the number of nodes and links in the BN, and hence the computational demand, are reduced. In the example system, components 7 and 8 appear in all SPSs. We take advantage of this observation and introduce only one “instance” of the SPEs associated with these components. The resulting BN is shown in Figure 6.24. The states of SPE nodes having multiple SPEs as parents (e.g., node $E_{s,7}$ in Figure 6.24) are specified using the Boolean relation

$$\begin{aligned}
 E_{s,i} &= 1 \text{ if } \left[\bigcup \{E_{s,Pa(i)} = 1\} \right] \cap C_i = 1 \\
 &= 0 \text{ otherwise.}
 \end{aligned}
 \tag{6.12}$$

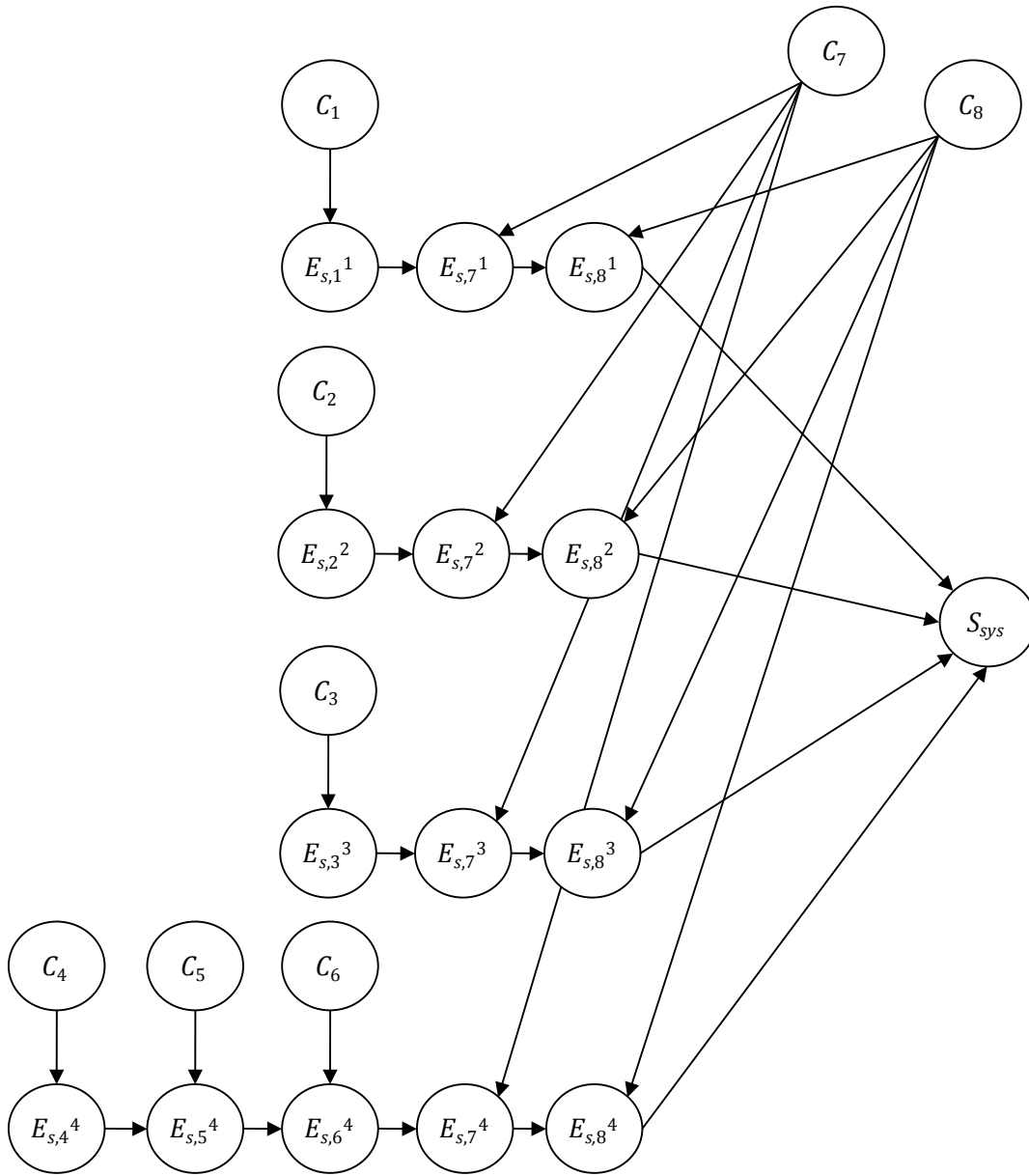


Figure 6.23: Efficient MLS BN formulation for system in Figure 6.1 with distinct SPSs

A notational change has been introduced in Figure 6.24: the superscript associated with each SPE node, which previously indicated the MLS/SPS number, now represents the *instance* of the SPE, so that if multiple SPEs are associated with the same component, they are recognized as different instances of the SPE and are distinguished through the superscript. Because in this system each component is associated with only one SPE, all superscripts in Figure 6.24 are 1.

The total clique table size associated with the BN in Figure 6.24 is 108, which is smaller than the demand associated with any other formulation.

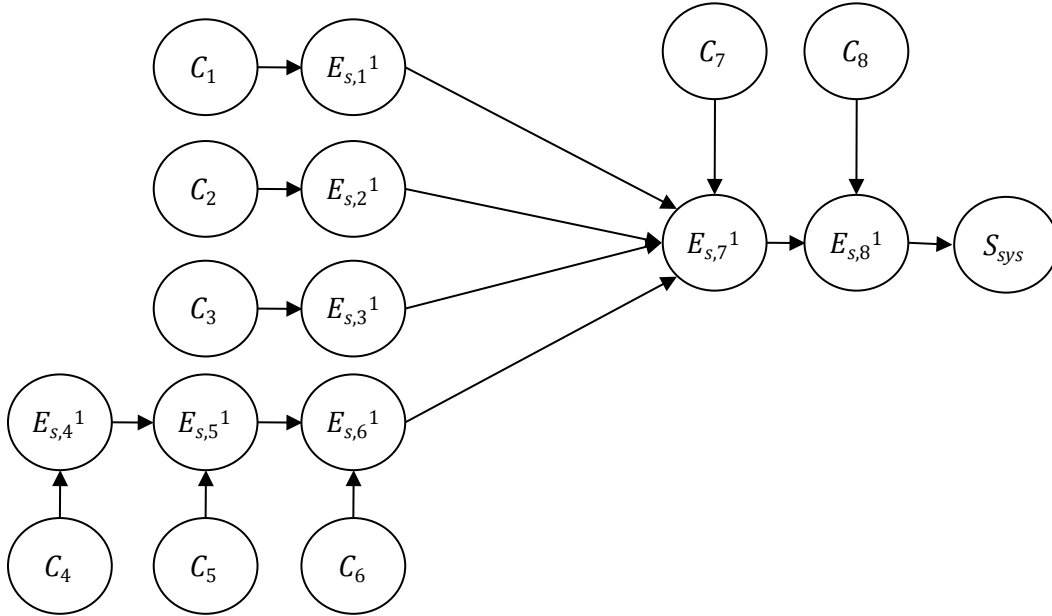


Figure 6.24: Efficient MLS BN formulations for example system with coalesced SPEs associated with components 7 and 8 using converging structure

Note that node $E_{s,7}$ in Figure 6.24 has more than three parents. Earlier, it was indicated that chain structures are more efficient than converging structures when the number of parents is greater than 3. Thus, we can further modify the BN in Figure 6.24 by replacing the parallel SPE nodes associated with components 1, 2, 3, and 6 with nodes arranged in a chain, resulting in the BN in Figure 6.25, with CPTs defined using the relation

$$\begin{aligned}
 E_{s,i} &= 1 \text{ if } [(C_i = 1) \cap (\cup \{E_{s,Pa(i)'} = 1\})] \cup \{E_{s,Pa(i)''} = 1\} \\
 &= 0 \text{ otherwise,}
 \end{aligned}
 \tag{6.13}$$

where $E_{s,Pa(i)'}$ are the SPE nodes that are parent to $E_{s,i}$ before the addition of the chain modification and which remain parents after it, and $E_{s,Pa(i)''}$ are the SPE nodes that become parents to $E_{s,i}$ after the chain structure is added (identified by dashed links in Figure 6.25). The total clique table size associated with this BN is 64.

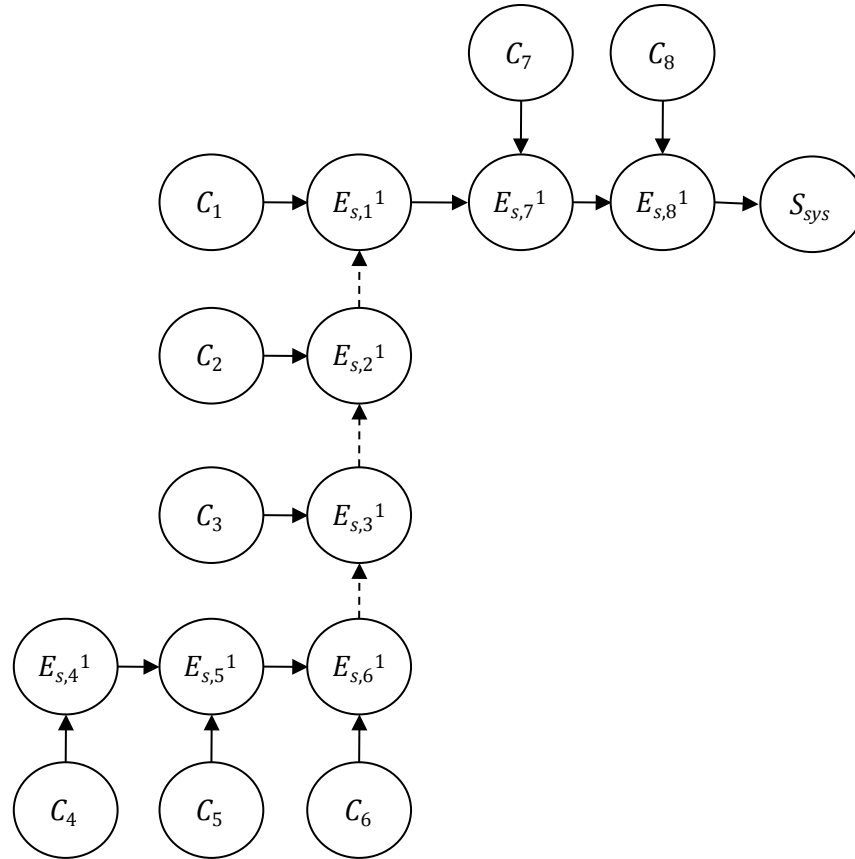


Figure 6.25: Efficient MLS BN formulations for example system with coalesced SPEs associated with components 7 and 8 using chain structure

6.5.2.2 Efficient MCS formulation

The efficient MCS formulation is constructed in a manner similar to the efficient MLS formulation, with strings of FPSs constructed corresponding to each MCS. To illustrate this formulation, return to the example system with RBD in Figure 6.1. Figure 6.26 shows a BN formulation with an FPS corresponding to each MCS and with the superscripts on the FPE nodes indicating MCS numbers. The total clique table size associated with this BN is 320. In Figure 6.27, FPSs associated with components 1, 2, and 3 are coalesced, reducing the total clique table size to 132. Once again, a notational change has been made: the superscript on each FPE node, which previously indicated the MCS number, now represents the instance of the FPE. (Because each component is associated with only one FPE, all superscripts are 1.) If the component and system states are binary, the CPTs of the FPE nodes are constructed using Boolean logic:

$$\begin{aligned}
 E_{f,i} &= 0 \text{ if } [\cup \{E_{f,Pa(i)} = 0\}] \cap [C_i = 0] \\
 &= 1 \text{ otherwise,}
 \end{aligned}
 \tag{6.14}$$

where $E_{f,Pa(i)}$ indicate the FPE nodes that are parent to $E_{f,i}$. The node representing the system state indicates failure if any of its parent FPE nodes is in the failure state.

Note that node S_{sys} in Figure 6.27 has more than three parents. To increase computational efficiency, we replace the converging connection by a chain structure, as was done previously with the efficient MLS formulation, to yield the BN shown in Figure 6.28.

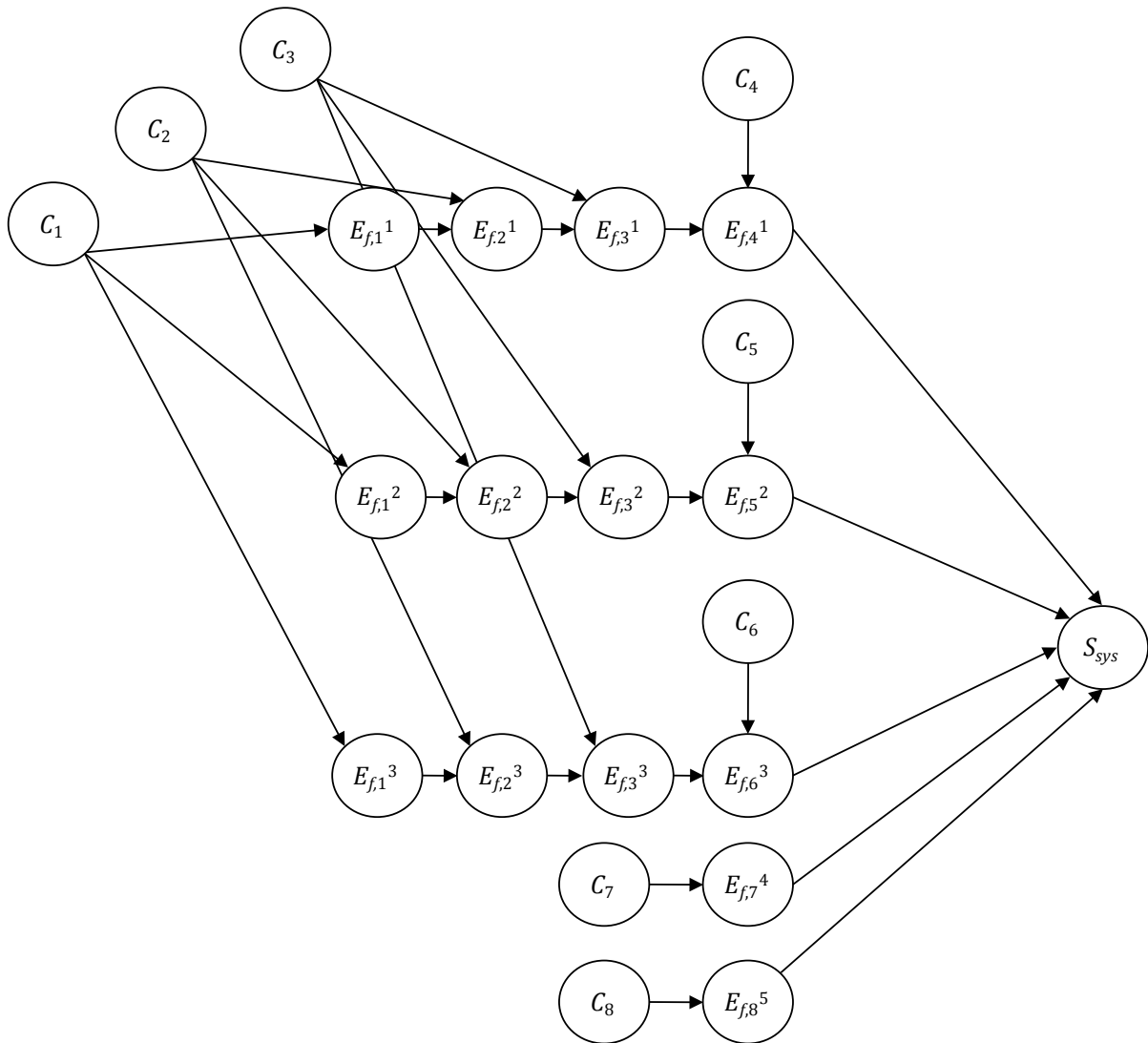


Figure 6.26: Efficient MCS BN formulation for system in Figure 6.1 with distinct FPSs

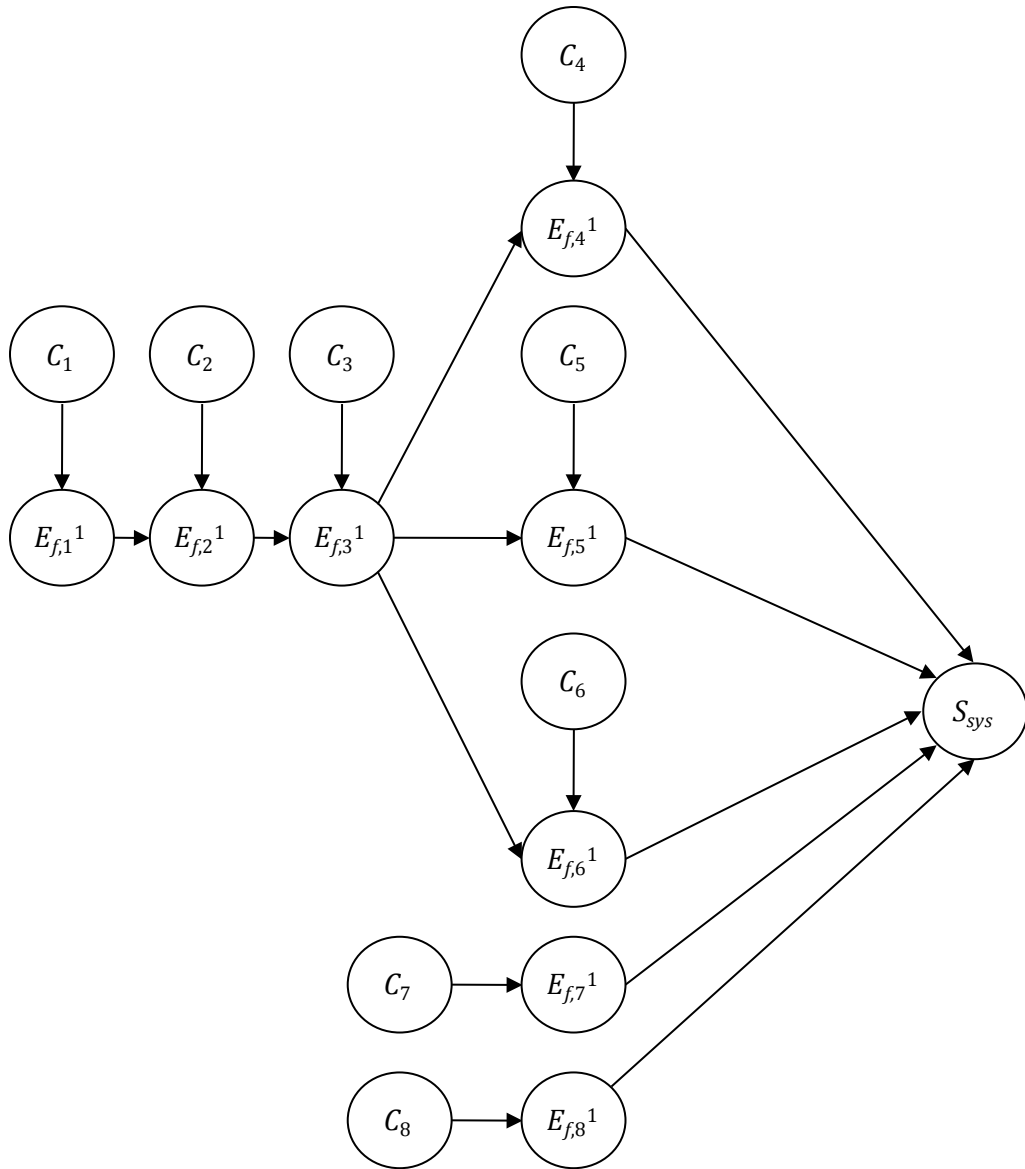


Figure 6.27: Efficient MCS BN formulation for example system with coalesced FPEs associated with components 1, 2, and 3 using converging structure

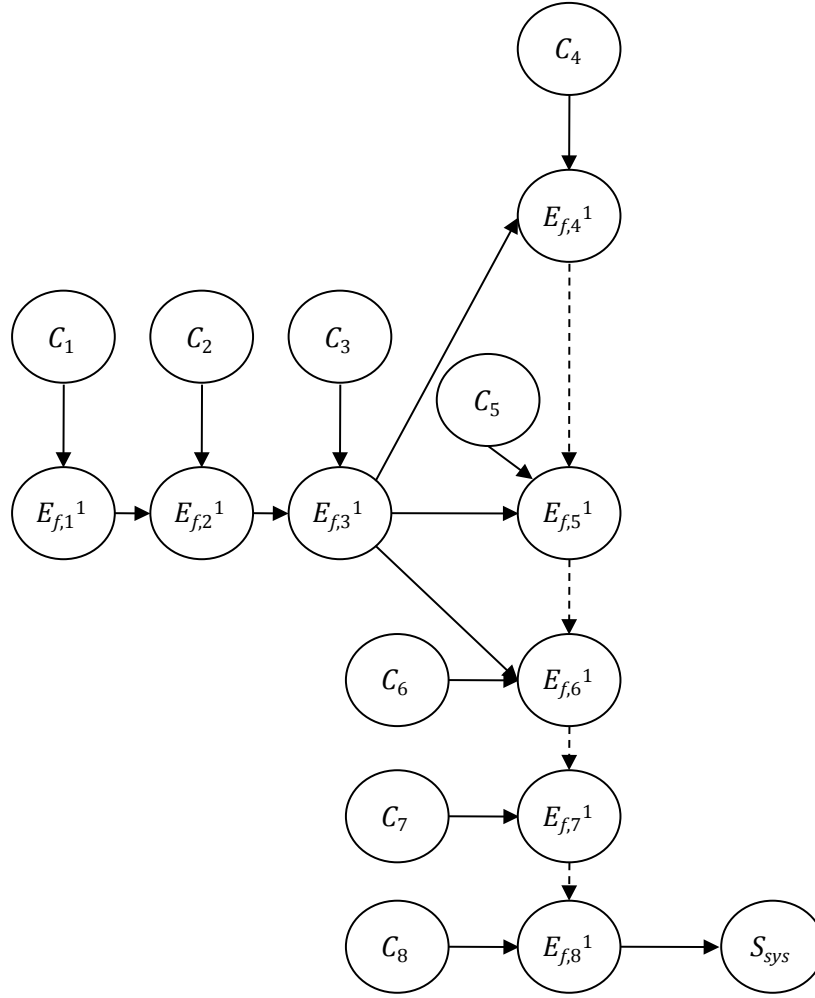


Figure 6.28: Efficient MCS formulations for example system with coalesced SPEs associated with components 1, 2, and 3 using chain structure

Returning to the special case of binary state components and system, the CPTs of the FPE nodes are defined using the relation

$$\begin{aligned}
 E_{f,i} &= 0 \text{ if } [(C_i = 0) \cap (\cup \{E_{f,Pa(i)'} = 0\})] \cup \{E_{f,Pa(i)''} = 0\} \\
 &= 1 \text{ otherwise,}
 \end{aligned} \tag{6.15}$$

where $E_{f,Pa(i)'}$ are the FPE nodes that are parents to $E_{f,i}$ before addition of the chain modification and which remain parents after it, and $E_{f,Pa(i)''}$ are the FPE nodes that become parents to $E_{f,i}$ after the chain structure is added (identified by dashed links in Figure 6.28). The total clique table size associated with this BN is 80, assuming independent binary components.

Like the standard MCS formulation, the efficient MCS formulation can be adapted to handle multistate problems through the application of the max-flow min-cut theorem. To consider multistate problems, the topology of the BN need not differ from the topology used for the binary state problem. It is only necessary to increase the number of states associated with all nodes and use arithmetic expressions instead of Boolean relations to define the CPTs. In the multistate problem, the states associated with the FPE nodes correspond to values rather than logical outcomes, similar to the values assigned to the MCS nodes when adapting the standard MCS formulation to the multistate problem. The values of the FPE nodes for the multistate problem are defined as

$$Value(E_{f,i}) = \left[\min_{E_{f,j} \in Pa(E_{f,i})} Value(E_{f,j}) \right] + Cap_i. \quad (6.16)$$

That is, the value assigned to node $E_{f,i}$ is equal to the value of any incoming node plus the capacity of the associated component. Thus, each FPE node can be thought of as representing a “running total” of the capacities of the MCSs that the current FPE is a part of. Node S_{sys} now represents the maximum operating level of the entire system rather than a Boolean outcome. Its value corresponds to the minimum value among all MCSs and thus is defined using the expression

$$Cap_{sys} = \min_{E_{f,j} \in Pa(Sys)} Value(E_{f,j}). \quad (6.17)$$

Considering the formulation modified with the addition of the chain structure to replace a converging structure (e.g., Figure 6.28), the value of a node $E_{f,i}$ is expressed as:

$$Value(E_{f,i}) = \min_{E_{f,j} \in Pa(E_{f,i})} \left[Value(E_{f,j}), \left(\left(\min_{E_{f,k} \in Pa(E_{f,i})} Value(E_{f,k}) \right) + Cap_i \right) \right]. \quad (6.18)$$

Table 6.1 shows a summary of the total clique table sizes associated with the above formulations, considering binary and statistically independent component states. It shows that all MLS/MCS-based formulations are more efficient than the naïve formulation. For this small example system, the efficient MLS and MCS formulations only offer an advantage over the standard MLS/MCS formulations if care is used with regard to the structure of chains. However, when properly

constructed, the efficient formulations are associated with lower computational demands than all other methods. The next section describes an optimization-based algorithm for determining the optimal order of the SPE or FPE nodes so as to minimize the number of links in the BN, as a proxy for minimizing total computational demands.

Table 6.1: Comparison of computational complexity

BN	Total clique table size
Figure 6.7: naïve formulation	512
Figure 6.12: standard MLS formulation	208
Figure 6.13: standard MLS formulation with intermediate nodes	176
Figure 6.15: standard MCS formulation	232
Standard MCS formulation with intermediate nodes (no figure)	200
Figure 6.23: efficient MLS formulation with distinct SPEs	224
Figure 6.24: efficient MLS formulation with coalesced SPEs	108
Figure 6.25: efficient MLS formulation with chain structure for system	64
Figure 6.26: efficient MCS formulation with distinct FPEs	320
Figure 6.27: efficient MCS formulation with coalesced FPEs	132
Figure 6.28: efficient MCS formulation with chain structure for system	80

6.6 Optimal ordering of efficient MLS and MCS formulations

Thus far, the SPEs in an SPS (FPEs in FPSs) corresponding to a particular MLS (MCS) have been arranged in an arbitrary order. However, for complex systems, the arrangement of the SPEs in the SPSs may strongly influence our ability to coalesce SPEs in multiple SPSs (and analogously for FPEs in FPSs). We showed that increases in computational efficiency are achieved only if nodes in different SPSs (FPSs) are coalesced. The order in which SPEs (FPEs) appear can be optimized such that SPEs (FPEs) in as many SPSs (FPSs) as possible are coalesced, reducing the number of nodes and links in the BN. This optimization problem is described next. For brevity, only the formulation employing SPSs is presented; a dual

formulation applies to FPSs. To obtain the dual formulation, one simply needs to replace references to MLSs with MCSs when specifying the optimization problem.

Let $L(i^m, j^n) = 1$ indicate the existence of a directed link from $E_{S,i}^m$ to $E_{S,j}^n$ in the efficient MLS BN formulation and $L(i^m, j^n) = 0$ indicate its absence, where i and j are component indices and m and n are indices denoting the instances of these SPE nodes in the BN. Similarly, let $K_i^m = 1$ indicate a directed link between the node representing component i and node $E_{S,i}^m$ and $S_i^m = 1$ indicate a directed link between $E_{S,i}^m$ and the system node (with $K_i^m = 0$ and $S_i^m = 0$ respectively denoting their absences). $L(i^m, j^n)$, K_i^m , and S_i^m are the decision variables in the optimization problem. Formulation of the optimization problem assumes the use of only SPE nodes and a converging structure at the system node. To further increase computational efficiency of the resulting BN, the converging structure at any node with more than three SPE nodes as parents is replaced by a chain structure in the manner described above.

The objective of the optimization problem is to minimize the number of links in the BN. That is, the objective function is

$$\min \left[\sum_{i=1}^{N_c} \sum_{j=1}^{N_c} \sum_{m=1}^{N_I} \sum_{n=1}^{N_I} L(i^m, j^n) + \sum_{i=1}^{N_c} \sum_{m=1}^{N_I} K_i^m + \sum_{i=1}^{N_c} \sum_{m=1}^{N_I} S_i^m \right], \quad (6.19)$$

where N_c is the number of components in the system and N_I is the maximum number of instances of any SPE. It is desirable that N_I be as small as possible, but its value is initially not known. Thus, we must pursue an iterative procedure to find the smallest N_I value for which the optimization problem is feasible.

The existence of links between the component and SPE nodes as well as between the SPE nodes and the system node is controlled by the arrangement of SPE nodes in the BN. Specifically, $K_i^m = 1$ if node $E_{S,i}^m$ exists in the BN, which occurs if the decision variables $L(j^n, i^m)$ or $L(i^m, j^n)$ indicate a link going into or out of node $E_{S,i}^m$, respectively. (A node without any links going into or out of it can be removed from the BN.) Mathematically, this constraint is written as

$$\left[\sum_{j=1}^{N_C} \sum_{n=1}^{N_I} \{L(i^m, j^n) + L(j^n, i^m)\} \geq 1 \right] \Rightarrow K_i^m = 1. \quad (6.20)$$

Techniques are available for modeling “if-then” constraints in numerical optimization, as well as “ k -out-of- n ” constraints, which are needed later (e.g., see Sarker and Newton 2008). Appendix 6.1 explains these techniques. The decision variable $S_i^m = 1$ if node $E_{S,i}^m$ is a terminal node in an SPS, that is, if $E_{S,i}^m$ exists and has no other SPE node as a child. Mathematically, this is written as

$$\left[\sum_{j=1}^{N_C} \sum_{n=1}^{N_I} L(j^n, i^m) \geq 1 \right] \cap \left[\sum_{j=1}^{N_C} \sum_{n=1}^{N_I} L(i^m, j^n) = 0 \right] \Rightarrow S_i^m = 1. \quad (6.21)$$

Two additional constraints govern the arrangement of the SPE nodes in the BN: (1) each MLS must be represented by an SPS; and (2) no SPS may exist that is not strictly an MLS. If the first constraint is violated, then one or more MLSs are excluded resulting in overestimation of the system failure probability. If the second constraint is violated, then the BN includes one or more fictitious MLSs and thus underestimates the system failure probability.

The first constraint requires that each MLS be represented as an SPS, and means that at least one *permutation* of the SPEs associated with the components in each MLS must be connected as a chain. Define MLS_i to be the set of components contained in the i th MLS and let $N_{MLS,i}$ be the number of components in MLS_i . For the system in Figure 6.1, $N_{MLS,1} = N_{MLS,2} = N_{MLS,3} = 3$ and $N_{MLS,4} = 5$. Let P_i be the set of permutations, without replacement, of the component indices in MLS_i and define $p_i^\alpha = \{p_{i,1}^\alpha, p_{i,2}^\alpha, \dots, p_{i,N_{MLS,i}}^\alpha\}$ as the α th permutation contained in the set P_i . As an example, for the system in Figure 6.1, $P_1 = [p_1^1 = \{8,7,1\}, p_1^2 = \{8,1,7\}, p_1^3 = \{7,8,1\}, p_1^4 = \{7,1,8\}, p_1^5 = \{1,7,8\}, p_1^6 = \{1,8,7\}]$.

Next, let Q_i be the set of permutations with replacement of $N_{MCS,i}$ draws from the instance index set $\{1, \dots, N_I\}$. Define $q_i^\beta = \{q_{i,1}^\beta, q_{i,2}^\beta, \dots, q_{i,N_{MCS,i}}^\beta\}$ as the set of instance indices ordered according to the β th member of Q_i . Using the same example and assuming $N_I = 2$, we have $Q_1 = \{q_1^1 = (1,1,1), q_1^2 = (1,1,2), q_1^3 = (1,2,1), q_1^4 = (1,2,2), q_1^5 = (2,1,1), q_1^6 = (2,1,2),$

$q_1^7 = (2,2,1)$, $q_1^8 = (2,2,2)$. Note that P_i has $N_{MLS,i}!$ members, whereas Q_i has $N_I^{N_{MLS,i}}$ members.

Define a set $r_i^{\alpha,\beta} = [r_{i,1}^{(\alpha,\beta)}, r_{i,2}^{(\alpha,\beta)}, \dots, r_{i,N_{MLS,i}}^{(\alpha,\beta)}]$ which combines the elements of p_i^α and q_i^β . Specifically, $r_i^{\alpha,\beta}$ includes the set p_i^α with superscripts given by the set q_i^β . For the example system, $r_1^{1,1} = \{8^1, 7^1, 1^1\}$, $r_1^{1,2} = \{8^1, 7^1, 1^2\}$, $r_1^{2,4} = \{8^1, 1^2, 7^2\}$, and so on. Overall, for this specific MLS, there are $3! * 2^3 = 48$ possible ways to arrange the component indices given by p_i^α and the instance superscripts given by q_i^β .

For convenience, define the sum $X_i^{(\alpha,\beta)} = \sum_{l=1}^{N_{MLS,i}-1} L[r_{i,l}^{(\alpha,\beta)}, r_{i,l+1}^{(\alpha,\beta)}]$, where $r_{i,l}^{(\alpha,\beta)}$ is the l th element of $r_i^{(\alpha,\beta)}$. Then $X_i^{(\alpha,\beta)} = N_{MLS,i} - 1$ only if the SPEs corresponding to the components in MLS_i form an SPS in the order specified by p_i^α and instance indices according to q_i^β . For a required SPS to exist in the BN, $X_i^{(\alpha,\beta)} = N_{MLS,i} - 1$ for *at least one* component/instance index ordering from the set $r_i^{(\alpha,\beta)}$. The constraint is written as

$$\max_{\alpha,\beta} X_i^{(\alpha,\beta)} = N_{MLS,i} - 1 \quad \alpha = 1, \dots, N_{MLS,i}!, \beta = 1, \dots, N_I^{N_{MLS,i}}, \quad \forall i. \quad (6.22)$$

The second constraint requires that no SPS exist in the BN that does not correspond to an MLS. Consider the BN shown in Figure 6.29a. Let the shaded nodes ($E_{s,1}^1 \rightarrow E_{s,2}^1 \rightarrow E_{s,3}^1 \rightarrow E_{s,4}^1$) represent a particular permutation of component/instance indices $r_i^{(\alpha,\beta)} = \{1^1, 2^1, 3^1, 4^1\}$ resulting in a valid SPS. This constraint prohibits an SPE $E_{s,j}^n$, for any n , from branching off the SPS at any point (i.e., being a child of any node in the chain), unless component j exists in an MLS with all components of the preceding SPEs in the sequence. For example, in Figure 6.29a, $E_{s,j}^n$ cannot exist as a child of $E_{s,3}^1$ unless components 1, 2, 3, and j all exist together in an MLS. If components 1, 2, 3, and j do not exist in an MLS, then the false survival path shown by nodes with dashed edges is introduced into the BN. The associated constraint is written as

$$\left[X_i^{(\alpha,\beta)} = N_{MLS,i} - 1, \forall i, \alpha, \beta \right] \Rightarrow L[r_{i,l}^{(\alpha,\beta)}, j^n] = 0, \forall j: \{p_{i,1}^{(\alpha)}, \dots, p_{i,l}^{(\alpha)}, j\} \notin MLS_m, \forall n, \forall m, \forall l. \quad (6.23)$$

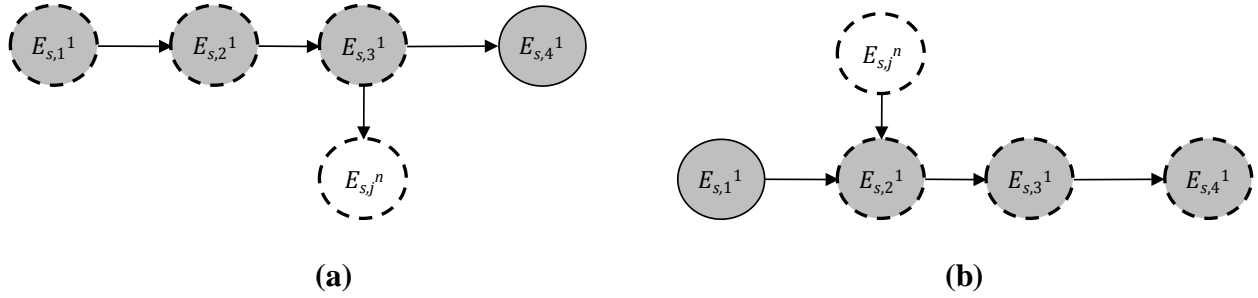


Figure 6.29: BNs illustrating constraint that no SPS may exist that is not strictly an MLS

Furthermore, the second constraint must prohibit SPE $E_{s,j}^n$, for any n , from being a parent to any node in a valid SPS, unless component i exists in an MLS with all components of the subsequent SPEs in the sequence. For example, in Figure 6.29b, $E_{s,j}^n$ cannot be a parent of $E_{2,1}$ unless components 2, 3, 4, and j all exist together in an MLS. The second constraint takes the form

$$\begin{aligned} & \left[X_i^{(\alpha,\beta)} = N_{MLS,i} - 1, \forall i, \alpha, \beta \right] \Rightarrow \\ & L \left[j^n, r_{i,l}^{(\alpha,\beta)} \right] = 0 \quad \forall j: \left\{ j, p_{i,l}^{(\alpha)}, \dots, p_{i,N_{MLS,i}}^{(\alpha)} \right\} \notin MLS_m, \forall n, \forall m, \forall l. \end{aligned} \quad (6.24)$$

The combination of these two requirements along with the objective function, the minimization of which ensures that links not necessary for constructing the required SPSs are not in the BN, prohibits invalid SPSs in the BN. Combining Equations (6.23) and (6.24) results in the constraint

$$\begin{aligned} & \left[X_i^{(\alpha,\beta)} = N_{MLS,i} - 1, \forall i, \alpha, \beta \right] \Rightarrow \\ & \sum_{m=1}^{N_{MLS}} \sum_{n=1}^{N_I} \sum_{l=1}^{N_{MLS,i}} \sum_{\forall j: \{p_{i,1}^{(\alpha)}, \dots, p_{i,l}^{(\alpha)}, j\} \notin MLS_m} L \left[r_{i,l}^{(\alpha,\beta)}, j^n \right] \\ & + \sum_{m=1}^{N_{MLS}} \sum_{n=1}^{N_I} \sum_{l=1}^{N_{MLS,i}} \sum_{\forall j: \{j, p_{i,l}^{(\alpha)}, \dots, p_{i,N_{MLS,i}}^{(\alpha)}\} \notin MLS_m} L \left[j^n, r_{i,l}^{(\alpha,\beta)} \right] = 0 \end{aligned} \quad (6.25)$$

The binary optimization problem described above requires permutations of components to be considered. Consequently, this problem is difficult to solve in practice for large systems. To overcome this problem, several heuristics have been developed to reduce the size of the optimization problem that must be considered. In one, groups of components are considered as

single “super components” to reduce the number of components in each MLS or MCS. In another, measures are taken to reduce the permutations of component indices considered in the optimization problem, without significantly affecting the optimality of the final solution.

Before describing the heuristics, note that significant differences in performance arise depending on the optimization algorithm or software used to solve the above problem in conjunction with these heuristics. For example, the Matlab-based Tomlab optimization toolbox (Holmström 2008) solved example applications described later in this chapter in less than 30 seconds on an HP xw8600 workstation with 3.00GHz Xeon processor. However, using the same computer, the native binary integer program solver in the Matlab optimization toolbox often “timed-out” at over 1500 seconds without finding a solution.

6.7 Heuristic augmentation

For systems with MLSs or MCSs with many components, the large number of permutations to be considered may make the optimization problem computationally infeasible. One way to reduce the size of the optimization problem is through the use of super components, a process used in multiscale modeling. The first heuristic discussed in this section is based on an algorithm for identifying super components. The second heuristic identifies sets of components that appear in multiple MLSs and MCSs and uses them to reduce the number of permutations that must be considered in solving the optimization problem. Both heuristics represent a “first attempt” at improving the performance of the optimization problem. Development of alternate heuristics is an area requiring further study.

6.7.1 Heuristic based on super components

Multiscale modeling is an approach by which elementary components in a system are grouped into super components (Der Kiureghian and Song 2008). Analysis is performed individually for each super component, and then results are aggregated on the system level. The super components typically are made up of simple subsystems, such as components that exist in series or parallel along a system link. In this study, only super components made up of series and

parallel components are considered. The introduction of super components reduces the size and number of MCSs and MLSs, which in turn reduces the number of permutations that must be considered in the optimization problem.

Consider the simple system shown in Figure 6.1. Components C_4 , C_5 , and C_6 exist in series as do components C_7 and C_8 . We replace these individual components with two super components SC_1 and SC_2 , as shown in Figure 6.30. The system still has four MLSs, but the number of components in them is reduced: $\{1, SC_2\}$, $\{2, SC_2\}$, $\{3, SC_2\}$, $\{SC_1, SC_2\}$.

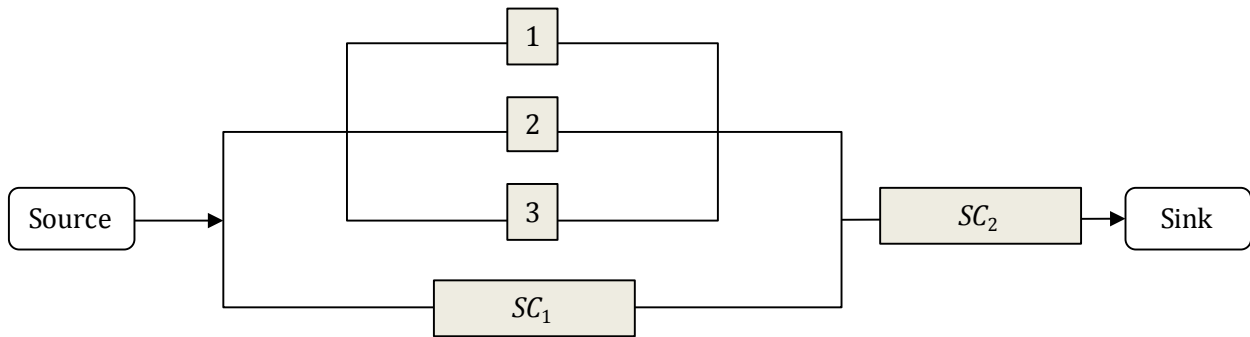


Figure 6.30: System in Figure 6.1 with super components replacing components C_4 , C_5 , and C_6 and components C_7 and C_8

Examination of Figure 6.30 reveals that components C_1 , C_2 , C_3 , and SC_1 exist in parallel. These components are next replaced by a single super component, resulting in the RBD shown in Figure 6.30. Now, components SC_2 and SC_3 exist in series and can be replaced by another super component. The BN resulting from this incremental procedure for identifying components that may be grouped and replaced by a super component is shown in Figure 6.32. For super components containing less than four constituent components, a converging structure is used. For super components with four or more constituent components, a chain structure is used.

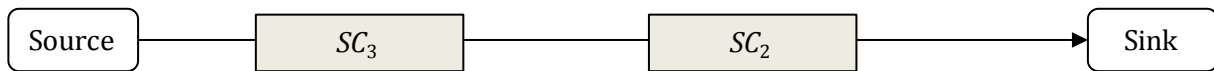


Figure 6.31: System in Figure 6.30 with super component replacing components C_1 , C_2 , C_3 , and SC_1

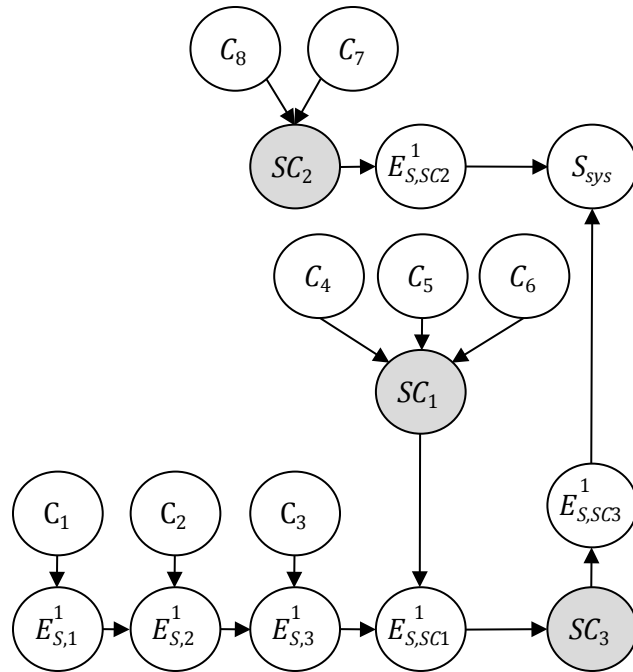


Figure 6.32: BN constructed for system in Figure 6.1 using super component heuristic

Note that components in a super component need not be contiguous. For example, consider the simple system in Figure 6.33. From an analysis perspective, components 1 and 4 can be combined because, with regard to formation of MLSs and MCSs, they have the same effect as if they physically existed in series.

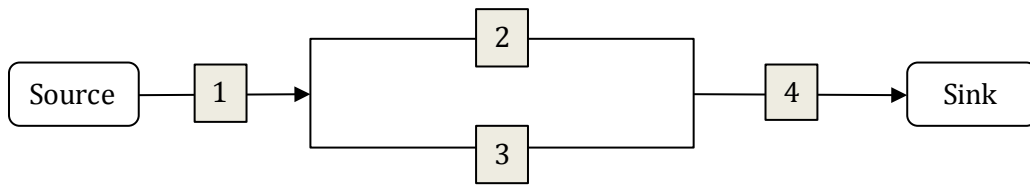


Figure 6.33: Example system illustrating noncontiguous components that can be combined in a super component

An algorithm has been developed to automate the incremental identification and replacement of elementary components by super components (or sets of super components by other super components). The first step in the algorithm is to construct an initial matrix \mathbf{M}^0 that contains a row corresponding to each MLS (MCS) and a column corresponding to each component. The elements of the initial matrix \mathbf{M}^0 , M_{ij}^0 , are defined such that

$$M_{ij}^0 = 1 \text{ if component } j \text{ is a member of MLS (MCS) } i$$

$$= 0 \text{ otherwise.} \quad (6.26)$$

For the example system in Figure 6.1, \mathbf{M}^0 has the following elements:

	Comp 1	Comp 2	Comp 3	Comp 4	Comp 5	Comp 6	Comp 7	Comp 8
MLS 1	1	0	0	0	0	0	1	1
MLS 2	0	1	0	0	0	0	1	1
MLS 3	0	0	1	0	0	0	1	1
MLS 4	0	0	0	1	1	1	1	1

Two types of super components are considered in the algorithm. Class A super components are made up of groups of components that always appear together in an MLS (MCS) and never appear separately. In an MLS-based formulation, class A super components correspond to components that exist in series. For an MCS-based formulation, class A super components represent components that exist in parallel. Define a quantity $m_j^{(A)}$ that is assigned to each component j at the p th iteration of the algorithm:

$$m_j^{(A)} = \sum_{i=1}^{N_{MLS}} 2^i M_{ij}^p \quad (6.27)$$

where M_{ij}^p is the element of \mathbf{M}^p at step p of the algorithm; for the initial step, $p = 0$. This quantity is identical only for components that always appear together in MLSs (MCSs) and do not appear separately in different MLSs (MCSs). Therefore, components having identical values of this quantity can be grouped into a super component. Returning to the example system: $m_1^{(A)} = 2$, $m_2^{(A)} = 4$, $m_3^{(A)} = 8$, $m_4^{(A)} = m_5^{(A)} = m_6^{(A)} = 16$, and $m_7^{(A)} = m_8^{(A)} = 30$ at the first iteration. Thus, components 4, 5, and 6 can be grouped into one super component and components 7 and 8 can be grouped into another. This was shown graphically in Figure 6.30.

Matrix \mathbf{M}^0 is now updated to reflect the new super components by removing columns corresponding to components that have been grouped and adding columns that correspond to the new super components. To illustrate the updating process, first consider SC_1 containing components 4, 5, and 6. Adapt the matrix \mathbf{M}^0 to produce a matrix \mathbf{M}^1 that accounts for the new super component. This is done by removing columns from \mathbf{M}^0 corresponding to components 4,

5, and 6 and adding a column that corresponds to SC_1 . Let $M^{1'}$ denote this column. Each row k of this column is defined such that

$$M_{\text{row } k}^p{}' = 1 \text{ if } \sum_{i \in C_{grp}^{p-1}} M_{ki}^{p-1} > 0$$

$$= 0 \text{ otherwise}$$
(6.28)

where C_{grp}^{p-1} is the set of components grouped into a super component at stage $(p - 1)$, that is, components 4, 5, and 6 for $(p - 1 = 0)$ in the example. For the example system, \mathbf{M}^1 is

	Comp 1	Comp 2	Comp 3	Comp 7	Comp 8	SC_1
MLS 1	1	0	0	1	1	0
MLS 2	0	1	0	1	1	0
MLS 3	0	0	1	1	1	0
MLS 4	0	0	0	1	1	1

The above procedure is repeated to construct SC_2 consisting of components 7 and 8. The resulting matrix \mathbf{M}^2 is

	Comp 1	Comp 2	Comp 3	SC_1	SC_2
MLS 1	1	0	0	0	1
MLS 2	0	1	0	0	1
MLS 3	0	0	1	0	1
MLS 4	0	0	0	1	1

The second class of super components, class B, contains components that appear in separate MLSs (MCSs), but with the same set of other components. For an MLS formulation, this corresponds to components in parallel; for an MCS formulation it corresponds to components in series. For the example in Figure 6.30, components 1, 2, 3, and SC_1 appear in separate MLSs, but with the same set of other components (7 and 8) in those separate MLSs. Define the quantity for each component j

$$m_j^{(B)} = \sum_{i=1}^{N_{MLS}} \left\{ M_{ij}^p * \left(\sum_{\substack{k=1 \\ k \neq j}}^{N_c} 2^k M_{ik}^p \right) \right\}$$
(6.29)

At iteration p , any set of components (or super components) for which the value of $m_j^{(B)}$ is the same can be grouped into a super component. For the example system in Figure 6.1, $m_1^{(B)} = m_2^{(B)} = m_3^{(B)} = m_{SC1}^{(B)} = 32$ and $m_{SC2}^{(B)} = 30$. As expected, components 1, 2, 3, and super component SC_1 have the same value of $m_j^{(B)}$ and can be grouped into a super component. The matrix \mathbf{M}^2 is adapted by removing columns corresponding to the grouped components and adding columns that correspond to the new super component. The rows of the column that is added to the matrix \mathbf{M}^2 are defined using Equation (6.28). Redundant rows of the updated \mathbf{M}^p matrix can be removed. It follows that \mathbf{M}^3 is

$$\text{MLS 1} \quad \begin{array}{|c|c|} \hline & \begin{array}{c} SC_2 \\ SC_3 \end{array} \\ \hline & \begin{array}{c} 1 \\ 1 \end{array} \\ \hline \end{array}$$

The above iterative procedure for replacing components with super components of classes A and B is repeated until no additional super components are left to be constructed. The matrix \mathbf{M}^p that corresponds to the last iteration is then used to specify the components and MLSs or MCSs required to define the optimization problem.

6.7.2 Second heuristic for reducing the number of permutations

The second heuristic identifies components that appear in many (but not all) MLSs (MCSs) and uses this observation to reduce the number of permutations to be considered in the optimization problem. This heuristic can be used after first reducing the size of the problem through identification of super components. This heuristic is likely to result in a solution to the optimization problem that is suboptimal.

To facilitate the explanation of the heuristic, an example system is used to illustrate each step of the procedure. Consider an arbitrary system with seven MLSs:

$$\begin{aligned} \text{MLS}_1 &= \{1,2,3,4\} \\ \text{MLS}_2 &= \{1,4,5,6,8\} \\ \text{MLS}_3 &= \{1,4,7\} \\ \text{MLS}_4 &= \{2,3,5\} \end{aligned}$$

$$MLS_5 = \{1,5,7\}$$

$$MLS_6 = \{1,2,9\}$$

$$MLS_7 = \{7,9\}$$

Step 1: Create an ordered list of components based on the number of times a component appears in an MLS or MCS. Call this list O . For the example system, the number of occurrences of each component within an MLS is shown in the following table:

Component	number of appearances in a MLS
1	5
2	3
3	2
4	3
5	3
6	1
7	3
8	1
9	2

The above table leads to the ordered list: $O = \{1,2,4,5,7,3,9,6,8\}$. In the case of ties in the above table, the order is arbitrarily based on component index value.

Step 2: Reorder the components within the MLSs or MCSs based on the order O . For the example system, the new MLS component orders are:

$$MLS_1 = \{1,2,4,3\}$$

$$MLS_2 = \{1,4,5,6,8\}$$

$$MLS_3 = \{1,4,7\}$$

$$MLS_4 = \{2,5,3\}$$

$$MLS_5 = \{1,5,7\}$$

$$MLS_6 = \{1,2,9\}$$

$$MLS_7 = \{7,9\}$$

Step 3a: Determine all pairwise intersecting sets between MLSs or MCSs. Define the set of components in the intersection of MLS_i (or MCS_i) and MLS_j (or MCS_j) as G_{ij} :

$$G_{ij} = MLS_i \cap MLS_j, \quad i = 1, \dots, (N_{MLS} - 1), \quad j = (i + 1), \dots, N_{MLS}. \quad (6.30)$$

For the example problem:

$$G_{12} = G_{13} = G_{23} = \{1 \ 4\}$$

$$G_{16} = \{1 \ 2\}$$

$$G_{35} = \{1 \ 7\}$$

$$G_{25} = \{1 \ 5\}$$

$$G_{14} = \{2 \ 3\}$$

$$G_{15} = G_{24} = G_{26} = G_{36} = G_{37} = G_{45} = G_{46} = G_{56} = G_{57} = G_{67} = \text{sets of cardinality 1}$$

$$G_{17} = G_{27} = G_{34} = G_{47} = \emptyset.$$

Step 3b: Define G as a set containing the unique sets $G_{ij}, \forall i, j$ with cardinality greater than 1.

For the example, $G = \{\{1 \ 4\}, \{1 \ 2\}, \{1 \ 5\}, \{1 \ 7\}, \{2 \ 3\}\}$.

Step 4: Sequentially assign to each MLS (or MCS) a set from within G that corresponds to the set whose intersection with the MLS (or MCS) has the largest cardinality. Let $g_{k,i}$ be the intersection of set i within G and the k th MLS (or MCS):

$$g_{k,i} = G_i \cap MLS_k, \quad (6.31)$$

where G_i is the i th set contained within G . Define g'_k as the set $g_{k,i}$ which has the longest length:

$$g'_k = \{g_{k,max}: |g_{k,max}| = \max_i |g_{k,i}|\}, \quad (6.32)$$

where $|\cdot|$ denotes the cardinality of a set. In the case of equal lengths, the set within G that appears first is assigned to the MLS (MCS). Once a set from within G has been assigned to a MLS (or MCS), place it in a new set G' , if it has not already been placed there. Define $g'_{c,i}$ as the number of times component i appears within the sets in G' . When a component has appeared in N_I (the parameter representing number of instances in the optimization problem described previously) sets within G' , all remaining sets containing that component are removed from G ,

unless the set is already a member of G' . This step is necessary because if $g'_c > N_l$ for any component, the optimization problem may become infeasible.

Return to the example system and assume $N_l = 2$. Begin with the first MCS. The sets within G with the longest intersection with MCS_k are $\{1,4\}$, $\{1,2\}$, and $\{2,3\}$. Because set $\{1,4\}$ appears first in G , it is assigned to the first MCS. Therefore, $g'_{k=1} = \{1,4\}$ and this set is added to G' . It follows that $g'_{c,1} = g'_{c,4} = 1$ and $g'_{c,i} = 0$ for $i = 2,3,5, \dots, 9$. These results for MLS_1 as well as the results for MLS_k , $k = 2, \dots, 7$, are shown below:

For $k = 1$, $MLS_1 = \{1,2,4,3\}$:

$$\begin{aligned} g'_1 &= \{1,4\}; G' = \{\{1,4\}\} \\ g'_{c,1} &= 1; g'_{c,4} = 1, g'_{c,i} = 0, i = 2,3,5, \dots, 9 \\ G &= \{\{1\ 4\}, \{1\ 2\}, \{1\ 5\}, \{1\ 7\}, \{2\ 3\}\} \end{aligned}$$

For $k = 2$, $MLS_2 = \{1,4,5,6,8\}$:

$$\begin{aligned} g'_2 &= \{1,4\}; G' = \{\{1,4\}\} \\ g'_{c,1} &= 1; g'_{c,4} = 1, g'_{c,i} = 0, i = 2,3,5, \dots, 9 \\ G &= \{\{1\ 4\}, \{1\ 2\}, \{1\ 5\}, \{1\ 7\}, \{2\ 3\}\} \end{aligned}$$

For $k = 3$, $MLS_3 = \{1,4,7\}$:

$$\begin{aligned} g'_3 &= \{1,4\}; G' = \{\{1,4\}\} \\ g'_{c,1} &= 1; g'_{c,4} = 1, g'_{c,i} = 0, i = 2,3,5, \dots, 9 \\ G &= \{\{1\ 4\}, \{1\ 2\}, \{1\ 5\}, \{1\ 7\}, \{2\ 3\}\} \end{aligned}$$

For $k = 4$, $MLS_4 = \{2,5,3\}$:

$$\begin{aligned} g'_4 &= \{2,3\}; G' = \{\{1,4\}, \{2,3\}\} \\ g'_{c,1} &= 1; g'_{c,4} = 1, g'_{c,2} = 1; g'_{c,3} = 1, g'_{c,i} = 0, i = 5, \dots, 9 \\ G &= \{\{1\ 4\}, \{1\ 2\}, \{1\ 5\}, \{1\ 7\}, \{2\ 3\}\} \end{aligned}$$

For $k = 5$, $MLS_5 = \{1,5,7\}$:

$$\begin{aligned} g'_5 &= \{1,5\}; G' = \{\{1,4\}, \{2,3\}, \{1,5\}\} \\ g'_{c,1} &= 2; g'_{c,4} = 1, g'_{c,2} = 1; g'_{c,3} = 1, g'_{c,5} = 1, g'_{c,i} = 0, i = 6, \dots, 9 \\ G &= \{\{1\ 4\}, \{1\ 5\}, \{2\ 3\}\} \end{aligned}$$

For $k = 6$, $MLS_6 = \{1,2,9\}$:

$$\begin{aligned} g'_6 &= \emptyset; G' = \{\{1,4\}, \{2,3\}, \{1,5\}\} \\ g'_{c,1} &= 2; g'_{c,4} = 1, g'_{c,2} = 1; g'_{c,3} = 1, g'_{c,5} = 1, g'_{c,i} = 0, i = 6, \dots, 9 \\ G &= \{\{1\ 4\}, \{1\ 5\}, \{2\ 3\}\} \end{aligned}$$

For $k = 7$, $MLS_7 = \{7,9\}$:

$$\begin{aligned} g'_7 &= \emptyset; G' = \{\{1,4\}, \{2,3\}, \{1,5\}\} \\ g'_{c,1} &= 2; g'_{c,4} = 1, g'_{c,2} = 1; g'_{c,3} = 1, g'_{c,5} = 1, g'_{c,i} = 0, i = 6, \dots, 9 \\ G &= \{\{1\ 4\}, \{1\ 5\}, \{2\ 3\}\} \end{aligned}$$

Note that, after the fifth MCS ($k = 5$) is considered, component 1 has appeared in G' two times. Because it has appeared $N_I = 2$ times, all sets containing component 1 are removed from the set G unless they already appear in G' .

Step 5: Modify the optimization problem such that the permutations on components contained within the set g'_k assigned to MLS_k are not considered. Recall that $r_k^{\alpha,\beta} = [p_{k,1}^{(\alpha,\beta)}, p_{k,2}^{(\alpha,\beta)}, \dots, p_{k,n_k}^{(\alpha,\beta)}]$ combines the elements of p_k^α and q_k^β . Specifically, $r_k^{\alpha,\beta}$ includes the set p_k^α with superscripts given by the set q_k^β . To modify the optimization problem, remove from the set of constraints all $r_k^{\alpha,\beta}$ for which the component indices do not appear in the order specified by g'_k . Furthermore, remove all $r_k^{\alpha,\beta}$ for which the superscript on component i in the set g'_k exceeds the value $g'_{c,i}$.

6.8 Example applications

Two example systems are considered to illustrate the use of the above optimization scheme, with and without the heuristics, and compare the computational complexities associated with the efficient MLS/MCS BN formulations versus the standard MLS/MCS formulations.

6.8.1 Example application 1

Consider the system shown in Figure 6.34 (e.g., a utility distribution system), in which a source and sink are connected by a series of numbered links that can fail. The system has five MCSs: $\{1,2\}$, $\{1,4,6\}$, $\{2,3,5\}$, $\{3,4,6\}$, $\{2,5,7\}$, and $\{6,7\}$. The efficient MCS formulation obtained by the optimization algorithm, without use of heuristics, is shown in Figure 6.35. The first heuristic is not useful for this problem because no component appears in series or parallel and thus no components can be grouped in super components. Furthermore, the second heuristic is not necessary because the size of the problem is small. Figure 6.36 illustrates the FPSs corresponding to each MCS, as shown in gray. The total clique table size associated with this BN is 164, which can be compared with a total clique table size of 1024 when the standard MCS formulation is used without the addition of intermediate nodes (recall Figure 6.13). The total clique table size is 680 when intermediate nodes are added to the standard MCS formulation to ensure that no node has more than three parents.

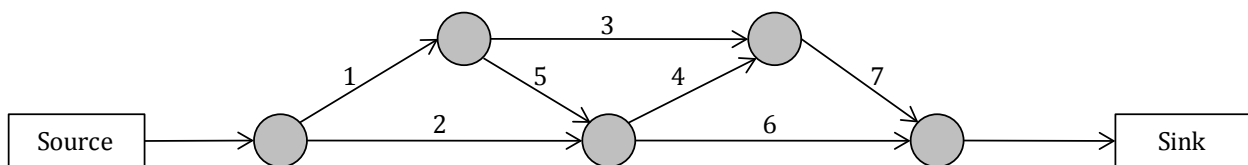


Figure 6.34: Example application 1

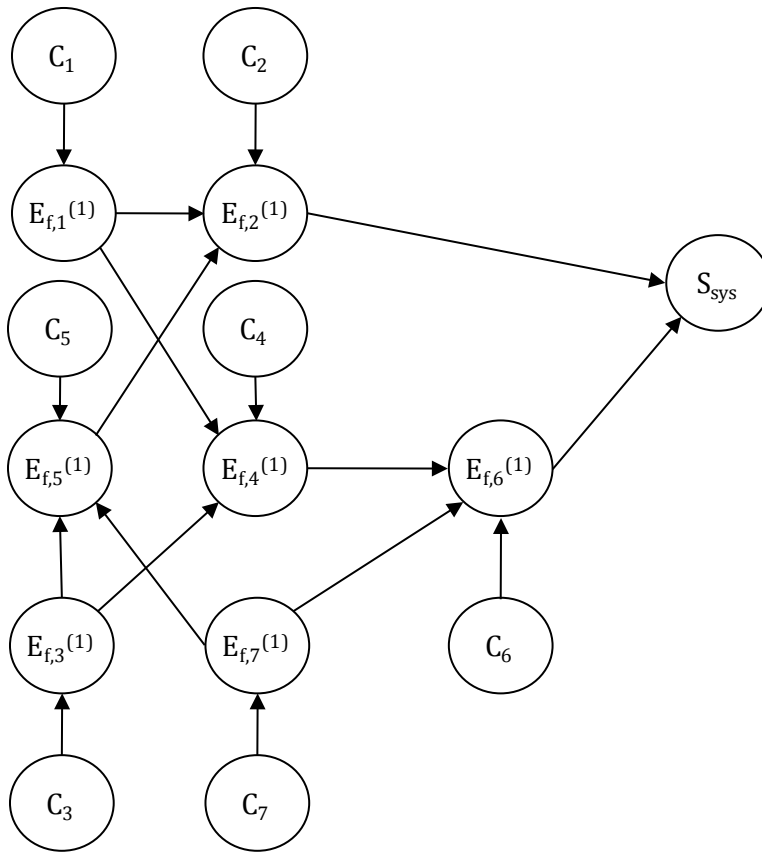


Figure 6.35: Efficient MCS formulation without heuristics for example application 1

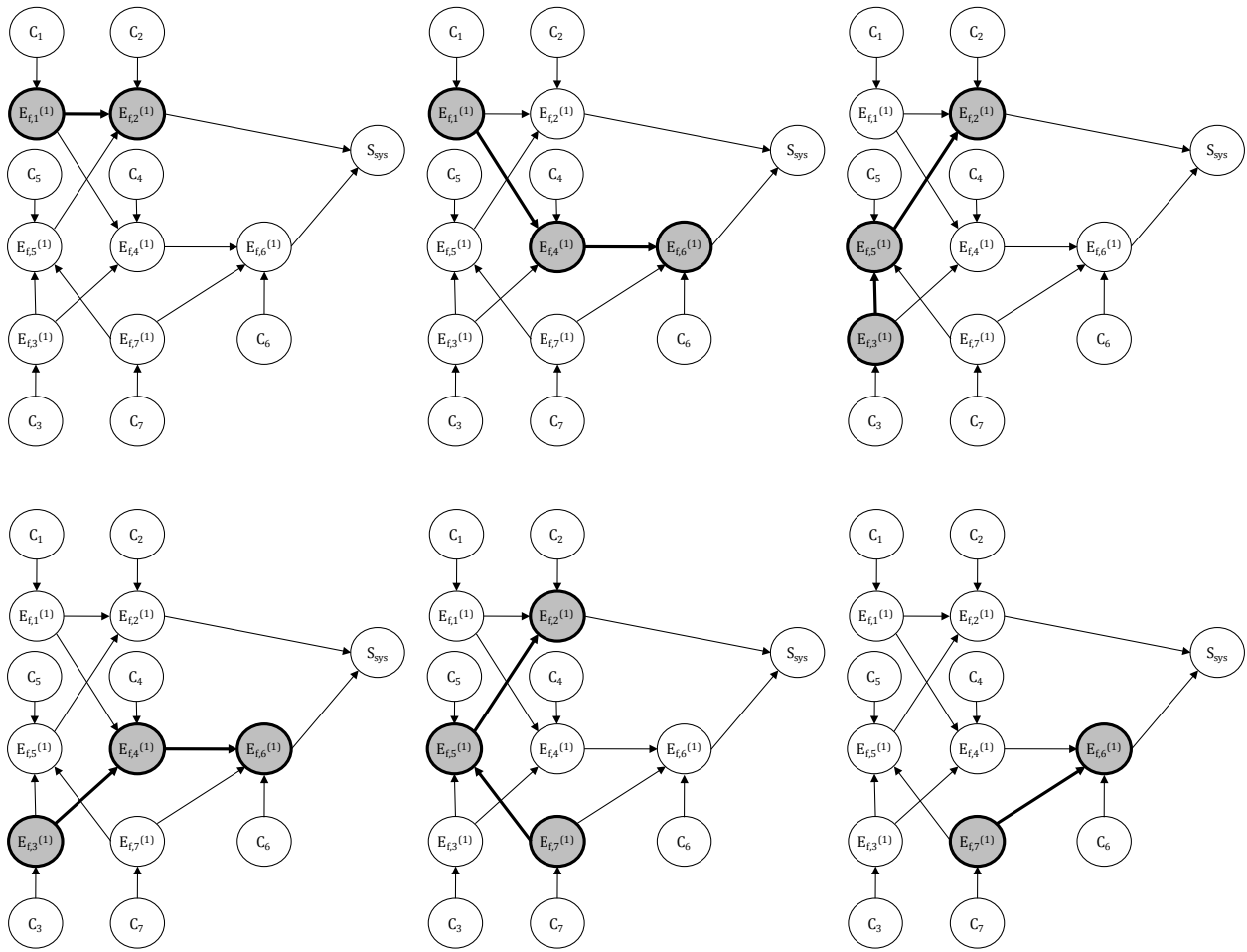


Figure 6.36: Illustration of FPSs corresponding to MCSs for example application 1

6.8.2 Example application 2

Next consider the structural system in Figure 6.37 consisting of 10 labeled components that can fail. The system has 11 MCSs: {1,2}, {3,4}, {1,3,10}, {1,4,10}, {2,3,10}, {2,4,10}, {5}, {6}, {7}, {8}, and {9}. The BN obtained using the optimization algorithm is shown in Figure 6.38. Figure 6.39 explicitly shows the FPSs corresponding to each of the multiple component MCSs. This solution relies on the super component heuristic. MCSs containing a single elementary component (components 5–9) are grouped into a super component in which the nodes form a series system; that is, if any component 5–9 fails, the system will be in the failure state. The total clique table size associated with this BN is 184. Note that the system node in Figure 6.39 has four parents. Replacing the converging structure with a chain structure, as shown by dotted lines in Figure 6.40, reduces the total clique table size to 164. The total clique table size of the standard MLS BN formulation with the converging structure is 5140 without use of intermediate nodes. When intermediate nodes are introduced to ensure that no node has more than three parents, the total clique table size falls to 804 but remains substantially higher than the topology resulting from the optimization algorithm. Thus, the efficient MCS BN obtained through optimization is significantly more efficient.

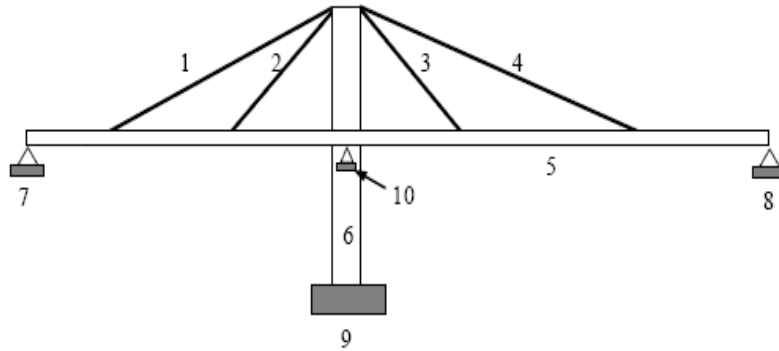


Figure 6.37: Example application 2

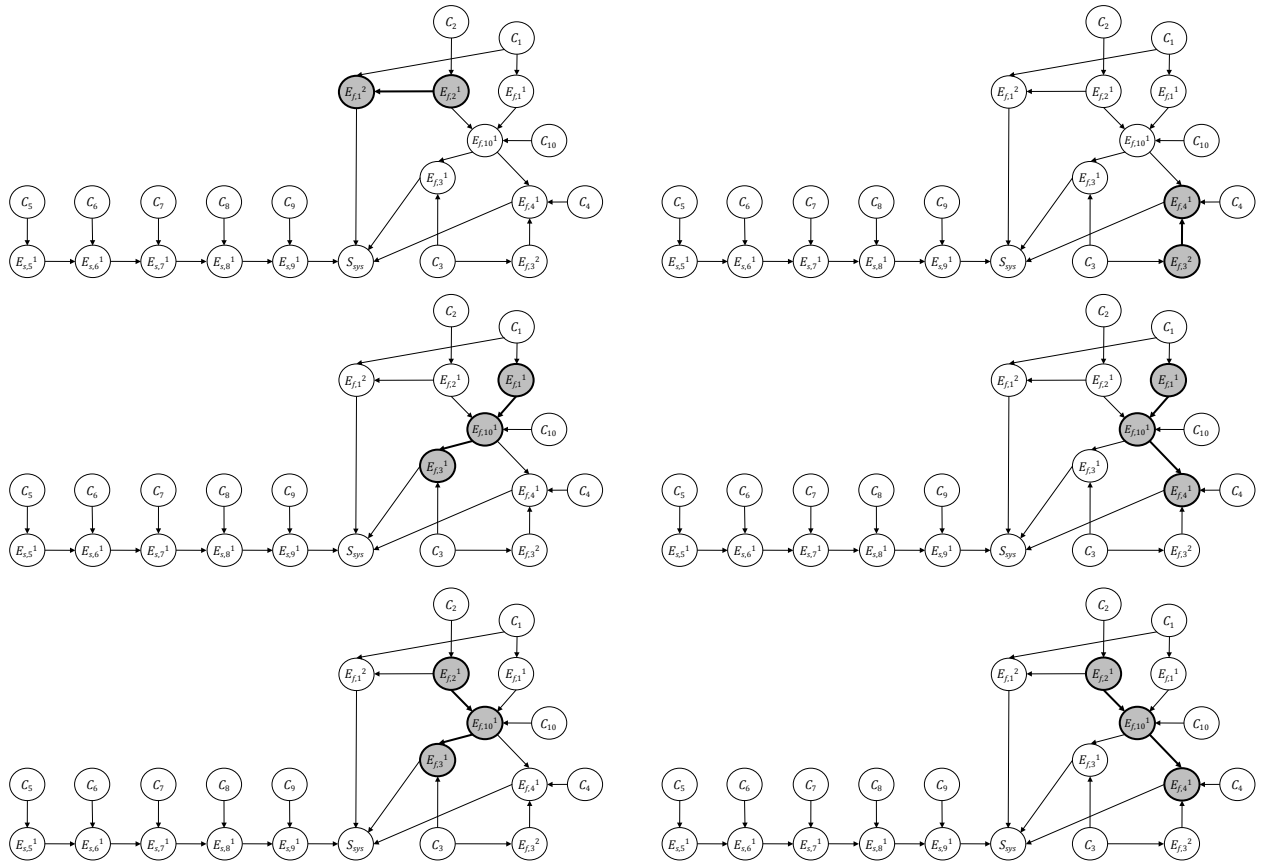


Figure 6.39: Illustration of FPSs corresponding to MCSs for example application 2

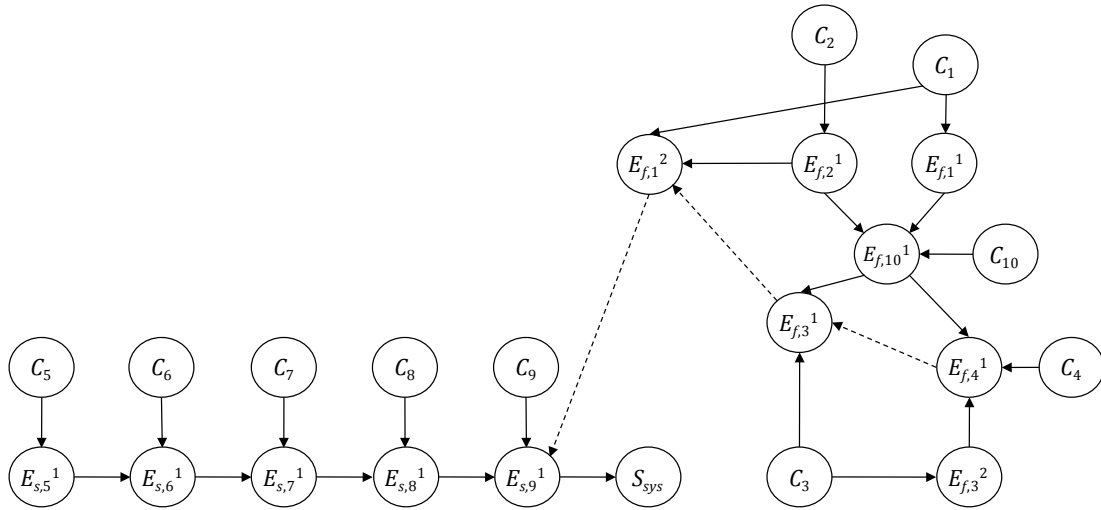


Figure 6.40: Efficient MCS formulation obtained using optimization algorithm with chain structure

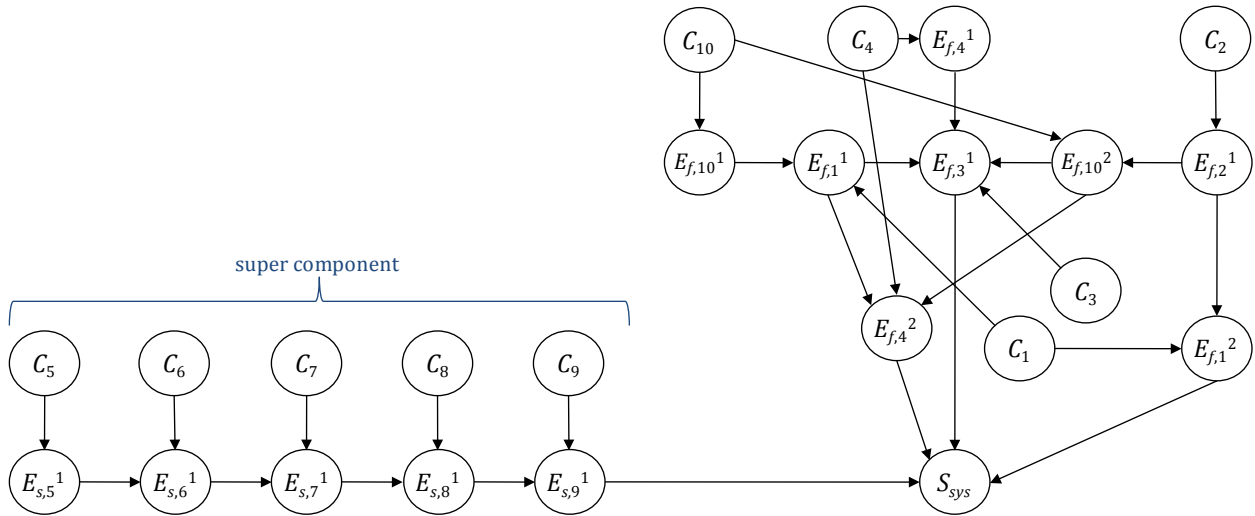


Figure 6.41: Efficient MCS formulation obtained using optimization algorithm with both heuristics

Given a sufficiently large M , any values of x_1 and x_2 will satisfy the modified constraint e_1' . It is thus an inactive constraint. Similarly, when a large number is added to constraint e_2 , it becomes inactive.

Next, we introduce a binary design variable y in conjunction with the arbitrarily large number M to achieve two new modified constraints, e_1'' and e_2'' , which achieve the desired behavior:

$$e_1'': a_1x_1 + a_2x_2 \leq a_3 + M * y$$

$$e_2'': b_1x_1 + b_2x_2 \leq b_3 + M * (1 - y).$$

When $y = 0$, constraint e_1'' must hold and e_2'' is inactive. Conversely, when $y = 1$, constraint e_2'' must hold and e_1'' is inactive. Thus the “either-or” behavior is achieved.

A similar procedure can be used for the case in which “ k -out-of- n ” constraints must hold. Consider n possible constraints:

$$e_1: f_1(x) \leq c_1$$

$$\vdots$$

$$e_n: f_N(x) \leq c_n$$

Introduce n binary design/selection variables y_i in conjunction with arbitrarily large number M to each constraint:

$$e_1'': f_1(x) \leq c_1 + M * y_1$$

$$\vdots$$

$$e_n'': f_N(x) \leq c_N + M * y_N$$

Constraint e_i'' is active when $y_i = 0$ and inactive when $y_i = 1$. To achieve the desired “ k -out-of- n ” behavior, we must satisfy the constraint on the integer variables:

$$\sum_{i=1}^n y_i = n - k.$$

7. Decision Support

7.1 Introduction

Decision theory provides a rational basis for solving a wide range of practical decision problems encountered in civil engineering. Examples include structural system selection (e.g., the decision to construct a steel versus concrete bridge); choice and timing of maintenance, rehabilitation, and retrofit actions; and inspection prioritization. Associated with these decisions are costs and benefits. For example, costs associated with performing a retrofit include materials and labor. Benefits associated with the retrofit include increased reliability and service life. Decision theory provides a rational basis for weighing the costs and benefits associated with a set of alternative choices and for selecting the best among them in accordance with the preferences of the decision-maker (Kübler 2007). However, the eventual outcome and, therefore, the costs and benefits associated with decision alternatives are not deterministic. For example, a seismic retrofit may be expected to improve the reliability of a component, but there is no guarantee that it will prevent damage to the component in a future earthquake. Several theories provide solutions to decision problems under uncertainty, but we use the paradigm in which the optimal decision is the one associated with the maximum expected utility. The concept of expected utility is described below.

Consider an arbitrary decision problem in which a decision-maker must select among alternative actions a_i , $i = 1, \dots, m$. Each alternative action can lead to one of multiple potential outcomes b_j , $j = 1, \dots, n$. Associated with decision alternative a_i and outcome b_j is a utility $u_{ij} = u(a_i, b_j)$, which maps the relative desirability of this pair on the value scale of the decision maker. Usually a positive utility indicates a benefit and a negative utility indicates a cost. Let $p_{ij} = \Pr(b_j|a_i)$ be

the probability of outcome b_j given alternative a_i is chosen. The expected utility associated with decision alternative a_i is

$$E(u|a_i) = \sum_{j=1}^n p_{ij}u_{ij}. \quad (7.1)$$

The best decision alternative is the one that achieves the maximum expected utility u^* (Kübler 2007):

$$u^* = \max_{i=1,\dots,m} E(u|a_i) \quad (7.2)$$

Methods for solving decision problems under uncertainty include conventional methods such as decision trees and the more compact representation resulting from influence diagrams. The goal of this chapter is to demonstrate how BNs can be extended by decision and utility nodes to solve decision problems. Once decision and utility nodes have been added to a BN, the resulting graphical model is known as an influence diagram. We focus on developing preliminary influence diagrams to solve a specific problem involving the post-earthquake inspection and shutdown of components. Consider a post-earthquake scenario in which an earthquake has placed seismic demands on the components of an infrastructure system. Immediately after the earthquake, the owner/decision-maker must quickly decide, for each component, whether to keep it open, shut it down, or conduct an inspection before deciding on the fate of the component. Because of finite resources, the owner cannot simultaneously inspect all components. Therefore, for components that require inspection, the owner must choose the order in which to perform the inspections.

This chapter first gives a brief overview of decision trees, then presents an introduction to influence diagrams, including perfect recall and limited memory influence diagrams. We next develop an influence diagram for the inspection-shutdown decision at the component level. Then we consider the decision at the system level and develop a prioritization heuristic based on a value-of-information criterion. Finally, we provide illustrative results for an example system.

7.2 Introduction to decision trees and influence diagrams

Decision trees are a classical method for solving decision problems under uncertainty. In a decision tree, all possible sequences of alternatives, observations, and outcomes are expanded in a tree-like structure containing decision, chance, and utility nodes. Each path from the root of the tree to a leaf represents a possible set of decision alternatives, observations, and outcomes—a *sequence*. An optimal decision strategy is found by finding the sequence(s) resulting in the highest expected utility. Because the tree must list all possible combinations of decision alternatives, observations, and outcomes, decision trees quickly become impracticably large for problems with many variables, especially in scenarios in which the order of decisions is not known a priori. For example, in the inspection prioritization problem, the order in which inspections are to be performed is not known when the decision problem is formulated; indeed, that order is an outcome of the decision problem. A decision tree for this problem must consider all permutations of the order in which components can be inspected, in addition to considering whether or not to shut down components with or without first making an inspection. For any realistic number of components, the large number of decision alternatives makes a decision tree impractical. Additional details on decision trees can be found in a number of sources (Benjamin and Cornell 1970; Raiffa 1997; Jordaan 2005).

An *influence diagram* (ID) can generally be viewed as a compact representation of the same information contained in the decision tree. The following brief description of IDs is taken from Kjaerulff and Madsen (2008) and Jensen and Nielsen (2007), which present more details.

An ID is a probabilistic network used to aid decision-making under uncertainty. It encodes both the probability model and the decision problem structure, which includes a set of observations, outcomes, and decision alternatives. Solving a decision problem with an ID amounts to (1) calculating the expected utility associated with each decision alternative and (2) selecting the decision alternative that maximizes the expected utility from the perspective of the decision-maker.

In general, there are two types of decision alternatives: (1) action decisions, which proactively “change the state of the world” through some activity, and (2) test decisions, i.e., decisions to look for more evidence that can be included in the model before an action decision is made

(Raiffa and Schlaifer 1970; Friis-Hansen 2000). The inspection alternative described above is an example of a test decision. The shutdown alternative represents an action decision.

Like a BN, an ID consists of nodes representing discrete random variables (hereafter called chance nodes) that are connected by directed links and are associated with CPTs. An ID differs from a BN by additionally having utility and decision nodes. A utility node represents the value associated with a specific decision(s) and/or the outcome of a chance node(s). A utility node is commonly represented by a diamond, though some authors and software applications use other shapes. A utility node has no states, but instead is assigned a utility value (e.g., monetary units) as a function of the states of its parent variables. A utility node cannot have children.

A decision node encodes alternative actions available to the decision-maker. It is represented by a rectangle and is defined by a finite set of states corresponding to the decision alternatives. To define an order for observations and decisions in the ID, *information* and *precedence links* are added to the graphical model. An information link goes from a chance node to a decision node and indicates that the value of the chance node is observed before the decision is made. A precedence link connects decision nodes and represents an order of decisions, with the parent decision being made before the child decision. It is important to emphasize that the links going into a decision node are not associated with quantitative requirements; they strictly specify the information that is available to the decision-maker at the time the decision is made. By specifying a required order for decisions and observations, information and precedence links reduce the solution space that must be searched to find an optimal decision (Jensen 2001a).

The *perfect recall ID* is the conventional form of an ID. It is associated with a structural requirement in which the ID describes a temporal sequence on all decisions. In other words, there must be a directed path through the ID that contains all decision nodes. Several challenges arise when constructing IDs with a directed path between all decision nodes: (1) not all decision problems can be reasonably formulated with a known ordering; and (2) considering all preceding decisions may result in an intractably large number of decision sequences. Perfect recall IDs are based on a “no forgetting” assumption (Jensen and Nielsen 2007), which means that there is only one order in which decisions can be made and that when making each decision the decision-maker remembers all preceding observations, outcomes, and decisions. A decision problem with

these properties is called *symmetric* because it is possible to formulate it as a symmetric decision tree, one in which all paths from a root node to a leaf node include all variables in the problem. A decision problem is asymmetric if a decision tree representation of the problem exists in which not all paths from a root node to a leaf node include all variables in the problem (Shenoy 1996).

Three types of asymmetry exist in decision problems: (1) functional asymmetry, in which outcomes and decision options may vary as a function of the past, (2) structural asymmetry, in which the occurrence of an observation or decision in the network is a function of the past, and (3) order asymmetry, in which the ordering of decisions and observations in the network does not follow a predefined sequence, i.e., the order is not known when the ID is constructed. The inspection-shutdown problem described previously contains decisions that can be performed in any order, e.g., the owner can decide to inspect bridge i before bridge j or vice versa. Indeed, the order in which the inspections are performed is a desired outcome of the decision formulation. The problem as formulated in this report is order asymmetric.

Order asymmetric problems cannot be modeled using perfect recall IDs. However, two more-general classes of IDs called *limited memory influence diagrams* (LIMID) and *unconstrained influence diagrams* (UID) relax the requirement that there be an explicit order on decisions. A LIMID drops the no-forgetting assumption and instead assumes that only nodes that are explicitly represented as parents to a decision node are known at the time the decision is made. The LIMID thus solves decision problems with a smaller domain, and therefore the solution of a LIMID is an approximation of the solution of a perfect recall ID (Jensen 2001b). UIDs permit decision problems in which not only the optimal choice for each decision but also the best ordering of those decisions are of concern. The result is an exponential growth in complexity when using exact solution algorithms. Additional details on UIDs can be found in a variety of sources (Jensen and Vomlelova 2002; Jensen and Nielsen 2007; Luque et al. 2008). In this study we utilize LIMIDs, which use an iterative approximate algorithm for solution and are supported in popular commercial BN software such as Hugin (Hugin Expert A/S 2008).

7.2.1 Overview of limited memory influence diagrams

A LIMID differs from a perfect recall ID in that the no-forgetting assumption is relaxed. Rather than considering that all preceding decisions are known at the time a decision is made, only the states of nodes that are direct parents to the decision node are assumed to be known. The types of links found in a LIMID are shown in Figure 7.1. Diagram (a) in Figure 7.1 shows a link between two chance nodes, which as in previous chapters indicates that the distribution of X_2 is defined conditionally on X_1 . Diagram (b) has a chance node X that is dependent on a decision node D , indicating that the distribution of X depends on the selected alternative of D . The link between decision nodes in Figure 7.1c indicates temporal precedence, which is necessary for the solution algorithm. It does not define a conditional distribution as with the links in (a) and (b). Figure 7.1d shows an information link from chance node X to decision node D , which implies that the state of X is known before making decision D and may influence its outcome. Figure 7.1e shows a utility node U that is a child of chance node X and decision node D . This relationship indicates that the decision-makers' utility is dependent on the outcome of random variable X and the selected decision alternative. Recall that a utility node cannot have children. These connections are referenced later to provide specific examples of each type.

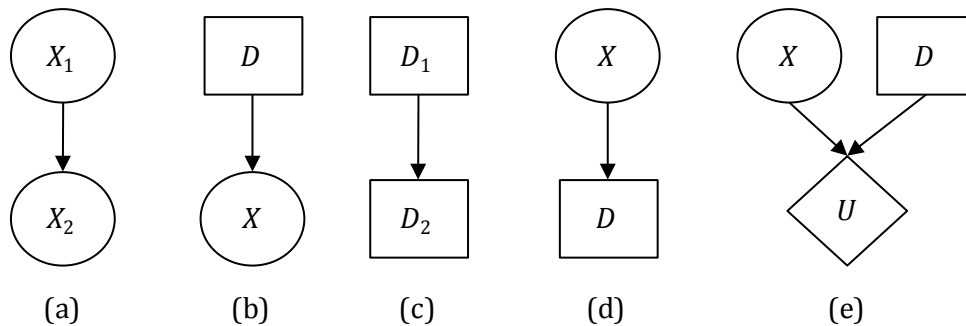


Figure 7.1: Types of links in limited memory influence diagrams

7.2.2 Computations in limited memory influence diagrams

Computations in LIMIDs are explained here using a simplified adaptation of a detailed description by Lauritzen and Nilsson (2001), which presents details of mathematics and specifics

of the algorithm. When solving either a perfect recall ID or a LIMID, the goal is to determine a *policy* for each decision node that maximizes the expected utility for any given configuration of its precedent nodes. In a LIMID, this policy is defined for each combination of the states of the direct parents of the decision node, i.e., it specifies a preferred action for any given combination of states of the parents of decision node D . Note that a policy may be deterministic or stochastic. The set of utility-maximizing policies for all decision nodes in an ID or LIMID is referred to as a *strategy*. For a perfect recall ID, this strategy is a global optimum.

Because LIMIDs do not require a temporal ordering of decisions, the possible combinations of orders for decision alternatives can be extremely large. Rather than explicitly considering all combinations and possible orders of decision alternatives, locally optimal solutions are determined using an iterative procedure known as *single policy updating*. The algorithm begins with an initial strategy that can be and typically should be random. A *cycle* of the algorithm updates policies for all decision nodes in the LIMID. Let q_i be the current strategy. Begin a cycle by updating the first decision D_1 to yield a new strategy, q_{i+1} . Strategy q_{i+1} is computed by finding the local maximum policy for q_i for decision D_1 . The algorithm next computes a locally optimal policy for decision D_2 . When all policies for all decisions have been updated, the cycle is complete. The algorithm converges when the expected utilities associated with successive cycles are the same (Lauritzen and Nilsson 2001). Because single policy updating works locally, it is not guaranteed to give a globally optimal solution.

In computing optimal strategies for the inspection-shutdown decision considered in this chapter (described in detail later), occasionally convergence to solutions that were not optimal at the system (global) level were encountered. Because the structure of the example problem is predictable, it was possible to recognize these situations and modify strategies accordingly.

7.3 Post-earthquake inspection and closure decision

Within the context of the example inspection-shutdown decision, we consider two decision problems. First we consider decision-making at the component level without addressing system-level effects. Second we consider decision-making when accounting for the effects of the decisions at the system level.

7.3.1 Component-level decision-making

The decision to shut down or reduce the capacity of a component is made under competing objectives: on the one hand the owner does not want to lose revenue by unnecessarily shutting down or reducing the operating level of a component that may not have experienced serious damage, while on the other hand the owner does not want to incur a liability by making an unsafe decision, keeping a component operating that may have sustained serious damage. To reduce the uncertainty associated with this decision, the owner may elect to conduct an inspection of the component, incurring a certain cost, that will yield information about the state of the component. The decision to close or not close the component is then made after receiving information gained from the inspection. To develop an ID for the component-level joint inspection-shutdown decision, we first individually consider three specific decision scenarios: (a) decide whether to shut down or continue operation of the component without the option to conduct an inspection; (b) make the shutdown/operation decision knowing the damage state of the component with certainty; and (c) make the shutdown/operation decision with imperfect information gained from an inspection of the component. For the moment we neglect costs associated with the inspection.

The ID corresponding to the component shutdown/operation decision without consideration of inspection is shown in Figure 7.2a. We do not distinguish between IDs and LIMIDs here because there is only one decision being made. In Figure 7.2a, the true damage state of component i is modeled by node C_i , which is defined conditionally on the ground motion intensity at the site, node S_i . Node S_i has mutually exclusive, collectively exhaustive interval states spanning the range of possible ground motion intensities at the site of the component. Node C_i has states corresponding to component damage levels (e.g., not damaged, slightly damaged, moderately damaged, severely damaged). The decision node *Shutdown?* corresponds to the decision whether or not to shut down or reduce the operating level of the component. Although for brevity this node is labeled *Shutdown?*, it need not be binary and can include decision alternatives that change a component's operating level without shutting it down. Utility node L_i is a child of nodes C_i and *Shutdown?*. This is an example of connection type (e) shown in Figure 7.1. The utility node L_i models potential loss associated with outcomes of the true component damage

state and the shutdown decision. It assigns a value to every combination of the states of its parent nodes. A liability is associated with making an unsafe decision, i.e., keeping the component open when it is damaged. A revenue loss is incurred whenever the decision is made to shut down or reduce the operating level of the component, regardless of its damage state. If the component is undamaged and remains in operation, no loss is incurred.

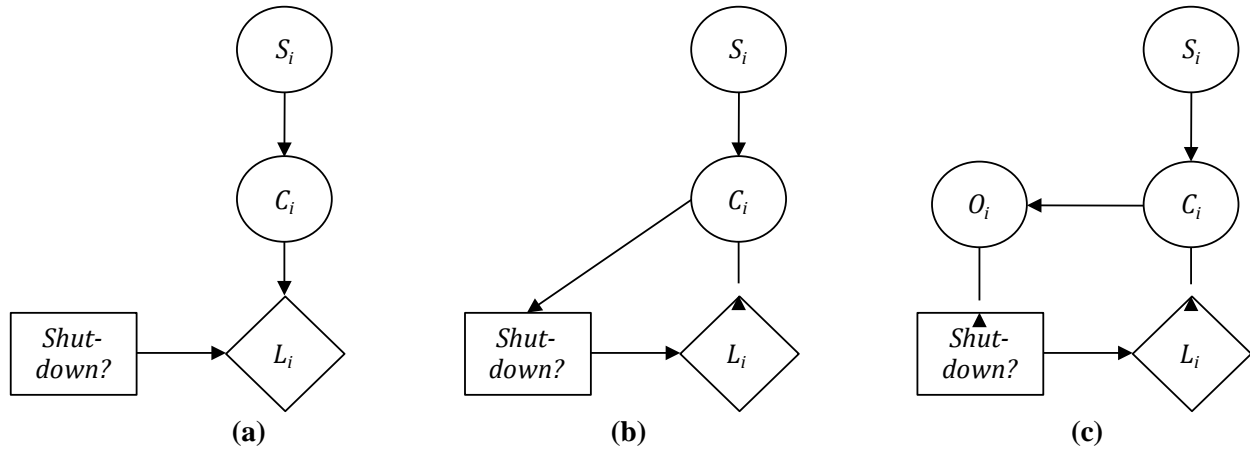


Figure 7.2: IDs modeling shutdown/operation decision based on (a) no information, (b) perfect information, and (c) imperfect information about damage state of component i

Next, consider the decision scenario in which the owner has perfect information about the damage state of the component, representing a case in which a high-quality and thorough inspection of the component is performed. The ID corresponding to this decision scenario is shown in Figure 7.2b. The information link between node C_i and decision node *Shut-down?* corresponds to link type (d) in Figure 7.1 and indicates that the true damage state of the component is known prior to making the decision. Thus, the optimal policy will be defined for each true component damage state.

However, inspections do not always yield accurate results, particularly when a cursory or visual inspection is performed. In the absence of a perfect inspection, the true component damage state is a latent variable. The ID corresponding to the shutdown decision when an inspection provides imperfect information is shown in Figure 7.2c. The flow of information between C_i and the decision node is mediated by node O_i corresponding to the observed damage state. The conditional relationship between C_i and O_i reflects the accuracy of the inspection method and is

commonly described by the test likelihood, i.e., conditional probabilities of each observation given the true state of the component. The solution of this ID yields a decision policy for each observed damage state. However, because the observed damage state is an uncertain proxy for the true damage state, the shutdown decision is made while the true damage state remains unknown. The three formulations in Figure 7.2 correspond to common forms of IDs used to model decisions made under no information, perfect information, and imperfect information.

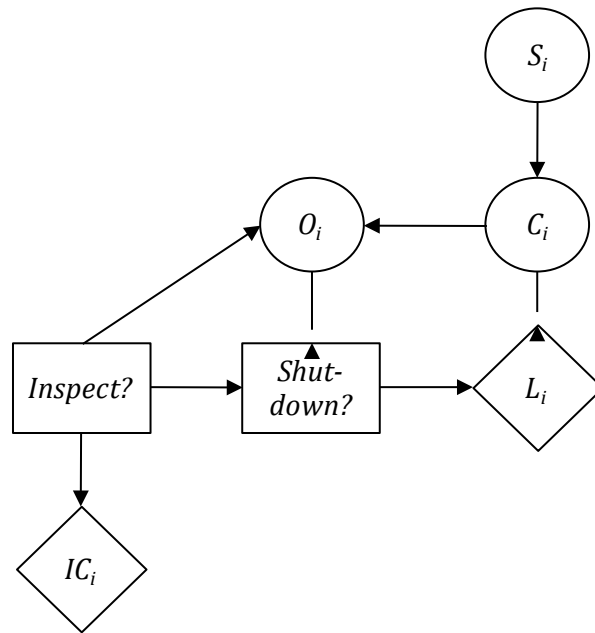


Figure 7.3: ID modeling an inspection-shutdown decision at component level

The IDs in Figure 7.2 must be coalesced onto one ID to solve the inspection-shutdown decision at the component level. The decision-maker first decides whether to inspect the component (and what inspection quality to use), and then decides whether to shut down the component based on the inspection results, if an inspection was performed. The coalesced ID must behave as Figure 7.2a when an inspection is not performed, as Figure 7.2b when perfect information is available, and as Figure 7.2c when an imperfect inspection is performed. The ID in Figure 7.3 achieves the desired behavior by adding a node that defines the inspection type (no inspection, imperfect inspection, perfect inspection). It assumes that the inspection decision choice, and the associated outcome if an inspection is made, is known before a decision is made regarding component shut

down. The precedence link between *Inspect?* and *Shutdown?* is of the type in Figure 7.1c. It encodes an ordering on these decisions. Defining this order encodes the value of the information obtained from the inspection. The link from *Inspect?* to O_i is of the type in Figure 7.1b. This link differentiates the three decision scenarios in Figure 7.2. It also encodes the inspection quality relationship. If a decision is made not to inspect the component (i.e., *Inspect?* = no inspection), the distribution of O_i is uniform over all its states regardless of the state of its other parent node C_i , indicating that the true component damage state remains a latent variable. If *Inspect?* = perfect inspection, the state of O_i is set equal to the state of C_i . In the case of an imperfect inspection, the distribution of O_i given C_i is equal to the test likelihood.

In the above, we neglected inspection costs. Associated with the inspection choice is a cost that depends on the inspection type. In Figure 7.3, the utility node IC_i is functionally dependent on the inspection decision node and represents the cost of performing an inspection, which normally increases as the inspection quality improves. Again, as a function of the shutdown decision and the true component damage state, there is a utility node that represents the potential losses associated with the outcomes of the shutdown decision and the true component damage state, i.e., losses due to shutting down the component as well as due to liability. This perfect recall ID (designated perfect recall because it contains a total order on decisions) can now be used to make decisions at the component level. The formulation can be solved using exact procedures that yield a global optimum.

7.3.2 System-level decision-making

Although the previous description focuses on immediate post-event decisions made at the component level, decisions regarding post-event inspection and closure of components should ideally be made at the system level. This requires creation of an ID that contains a decision model, of the form in Figure 7.3, for each component. The result is a LIMID as shown in Figure 7.4. Because there is no longer an explicit order among all the decision nodes, the LIMID must be solved using the single policy updating procedure, which provides an approximate solution. To account for correlations among demands placed on the components, the seismic demand model is included. Consequences of shutting down or reducing the capacity of the component

(e.g., lost revenue) should be calculated by considering the effect of the operating level of the component on the performance of the system. This is achieved by introducing the system performance model into the LIMID, as shown near the bottom of Figure 7.4. A utility node representing lost revenue at the system level is attached to node S_{sys} . If the system state is defined as a binary node, then the utility is defined as a loss associated with system closure and no loss associated with system operation. If the system has multiple states, then each state below full capacity is associated with a loss. Consideration of losses at the system level allows the decision framework to account for redundancies in the system.

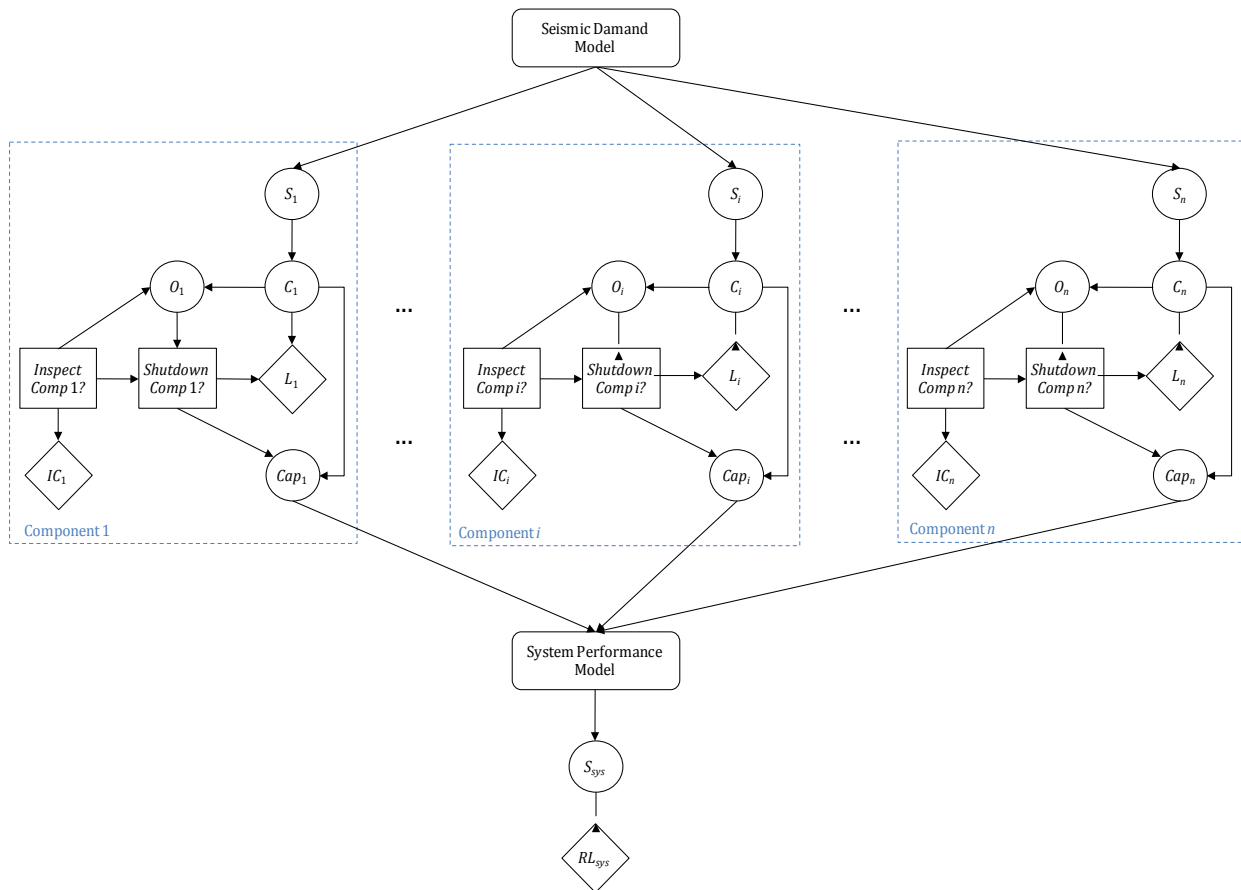


Figure 7.4: ID modeling joint inspection-shutdown decision at system level

To account for multiple operating levels, node Cap_i is introduced at the component level as a child of the node representing the true damage state and node $Shutdown\ comp\ i?$. Node Cap_i represents the component capacity or operating level, which is functionally dependent on the damage state of the component and the actions of the decision-maker. This allows for a

multistate mapping between the component damage state C_i and the operating state of the component, Cap_i . Accordingly, the component operates at reduced or zero capacity if it is damaged or if a decision is made to shut it down. The system node in Figure 7.4 is a child of nodes Cap_i , which represents the dependence of the system performance on the operating levels of the components.

For a given post-earthquake scenario, the solution for a particular component obtained from the LIMID may indicate that the component should be kept in full operation or have its operating level reduced or shut down *without* first making an inspection, while other components may require an inspection before making the shutdown decision. The LIMID indicates that a component should be kept in operation without inspection if the expected loss due to liability is less than the expected loss at the system level due to the shutdown of the component, regardless of the information that can be gained through inspection. Conversely, the LIMID indicates that a component should be shut down or have its operating level reduced, without inspection, if the expected loss due to liability exceeds the expected value of the component to the system, regardless of what information can be gained by inspection. For components for which there is value to be gained through inspection, a method is needed of prioritizing the order in which inspections are performed. In this study, inspection prioritization is based on a value-of-information heuristic, as described in the following section. This heuristic represents a first attempt at solving post-earthquake decision problems involving component shutdown and inspection using the proposed BN-based methodology. Development of a more sophisticated decision framework based on the preferences of actual decision-makers remains an area warranting further study.

7.4 Value-of-information heuristic

The value of information is a common concept in decision analysis that quantifies the benefit a decision maker obtains from acquiring more information before making a decision. In the context of the joint inspection-shutdown decision, examples of the values of perfect and imperfection information at the component level are given in Appendix 7.1.

We first consider the component-level problem. Let $EU|NI$ be the maximum expected utility associated with the available decision options given no information, i.e., the maximum expected utility associated with the ID in Figure 7.3 when decision node *Inspect?* is set equal to the no-inspection option. Define $EU|PI$ as the expected utility associated with making the optimal decision given perfect information, excluding the cost of the information, i.e., the optimal strategy when decision node *Inspect?* is set equal to the perfect inspection option and IC_i is set to zero. Finally, define $EU|II$ as the expected utility associated with making the optimal decision given imperfect information, excluding the cost of the information, i.e., the expected utility when decision node *Inspect?* is set equal to the imperfect inspection option and IC_i is set to zero. Then, the expected value of perfect information is

$$EVPI = EU|PI - EU|NI \quad (7.3)$$

and the expected value of imperfect information is

$$EVII = EU|II - EU|NI. \quad (7.4)$$

To help prioritize post-earthquake inspections of components at the infrastructure system level, we use a value-of-information heuristic. The heuristic assumes that, at each stage, the decision-maker is looking for the next best component to inspect, given that only one inspector is available. It asks, if only one more component can be inspected, which component should it be? Furthermore, the heuristic does not account for issues related to the time it takes to inspect a component, which is important in post-earthquake applications and should be addressed in further studies. The LIMID in Figure 7.4 is used to determine the optimal inspection decision for each component. For components not needing inspection, the optimal shutdown decision maximizes the expected utility. For these components, the policy on *Shutdown Comp i?* is a deterministic policy indicating whether, in absence of additional information, it is locally optimal to keep the component open or shut. In contrast, when an inspection is performed, the shutdown policy is stochastic depending on the outcome of the inspection.

For the components for which an inspection is recommended, the value of information is computed as follows. First, the total system-level expected utility, neglecting inspection costs, is computed using the LIMID and assuming that all components requiring inspection are inspected

according to the optimal inspection type indicated. This is analogous to quantities $EU|PI$ and $EU|II$, depending on the type of inspection, as described above. Then, for component i requiring inspection, the inspection decision node is set to the “no inspection” state. The remaining components are left at their optimal decisions. Then, the system-level utility when the component inspection is disregarded (output from the LIMID) is recorded, not including inspection costs. This is analogous to $EU|NI$, which was described above for the component-level problem. The value of information is computed as the difference between the two quantities. The value of information gained from the inspection is thus the difference between (1) the system-level expected utility when inspecting all recommended components and (2) the system-level expected utility when the inspection of component i is disregarded. The procedure is repeated until the values of information for all components for which an inspection is recommended are evaluated. The component with the highest value of information, i.e., the component for which neglecting to perform an inspection has the most adverse impact on the system-level expected utility, is inspected first. In the event that multiple inspectors are able to visit n components simultaneously, the above procedure is modified to select the n components for which the value of information is highest at each stage.

Using the LIMID methodology, the inspection prioritization order evolves as new information becomes available. Sources of information may include measurements of ground motion intensity and data from structural health monitoring sensors. As inspections are performed and decisions are made regarding the shutdown of components, this information is also entered into the LIMID. The information propagates through the LIMID to provide an up-to-date probabilistic characterization of the system model and decision structure. At any stage, the recommendations for component inspections may differ from those made previously; e.g., a component previously deemed to require an inspection may no longer need one, and vice versa. Thus, the LIMID provides the decision-maker with guidance on optimal decisions relating to inspection and component closure, at any point in time, based on all available information up to that time. Note that the above heuristic does not consider all possible orderings of the inspection and shutdown decisions explicitly, a task that is computationally expensive and possibly intractable. Therefore, the proposed approach may arrive at a suboptimal solution.

7.4.1 Example application

To illustrate the methodology just described, consider the simple infrastructure system shown in Figure 7.5. It has a predictable topology that facilitates intuitive interpretation of results obtained from the LIMID analysis. The system contains a source node and a sink node and eight components. It is assumed that, when operational, components 1–6 each carry 25 units of capacity and components 7 and 8 each have a capacity of 100 units. Components 7 and 8 form a system bottleneck. Thus, when all components are fully operational the system carries a maximum of 100 units from the source to the sink. Each component is assumed to have binary states, either full capacity or zero. The performance of the system is defined considering multiple states corresponding to the total capacity of the system. Let Cap_i indicate the operating capacity of component i at a given time. The system operating capacity is computed as a function of the individual component operating capacities using the expression:

$$Cap_{sys} = \min[\min(Cap_7, Cap_8), Cap_1 + Cap_2 + Cap_3 + \min(Cap_4, Cap_5, Cap_6)]. \quad (7.5)$$

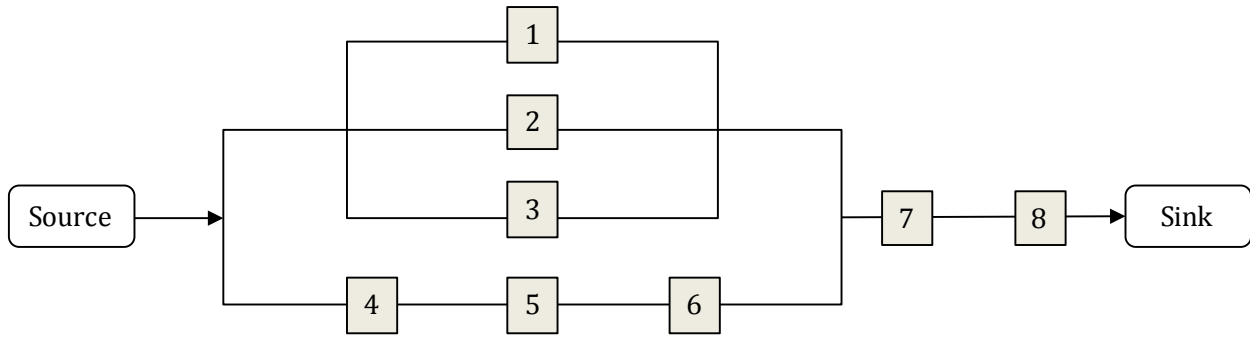


Figure 7.5: Example infrastructure system

LIMIDs are constructed for the system and the above inspection prioritization procedure is executed considering varying conditions: (1) assuming all components have identical versus heterogeneous reliabilities; (2) accounting for statistical dependence in the performance of components of the same class versus neglecting it; and (3) accounting for or neglecting the effect of system performance on the optimal decisions, i.e., ignoring the system object in Figure 7.4. The result is eight combinations of cases under which the above methodology is carried out. These cases are described in greater detail below.

In the cases in which all system components have identical reliabilities, each component has a probability 0.05 of failure (reliability = 0.95). When components are treated as heterogeneous, they are grouped into five classes with reliabilities given in Table 7.1.

Table 7.1: Component classes

Component	Class	Reliability
1	1	0.95
2	2	0.96
3	2	0.96
4	3	0.99
5	1	0.95
6	3	0.99
7	4	0.96
8	5	0.98

For the sake of clarity, we consider a simple and intuitive statistical dependence structure instead of a seismic demand model. In the cases in which dependence is considered, it is modeled through a common parent node that has binary states. Components of the same class are connected through a common parent node with its marginal PMF defined according to the corresponding reliability in Table 7.1. The CPTs of the child nodes, which represent the states of the individual components in the same class, are defined such that there is a 0.8 probability that the component has the same state as its parent node and a 0.2 probability that it does not.

Table 7.2: System configurations for example inspection-shutdown decisions

Case	System effects	Components	Demand correlation
1	Neglected	Identical	Independent
2	Neglected	Identical	Correlated
3	Neglected	Heterogenous	Independent
4	Neglected	Heterogenous	Correlated
5	Included	Identical	Independent
6	Included	Identical	Correlated
7	Included	Heterogenous	Independent
8	Included	Heterogenous	Correlated

The eight cases that arise from considering combinations of identical/heterogeneous components, including/neglecting statistical dependence, and including/neglecting system effects are listed in Table 7.2. The IDs for these cases are shown in Figure 7.6, where the component-level IDs are hidden behind objects. Colors and line textures are used to distinguish component classes.

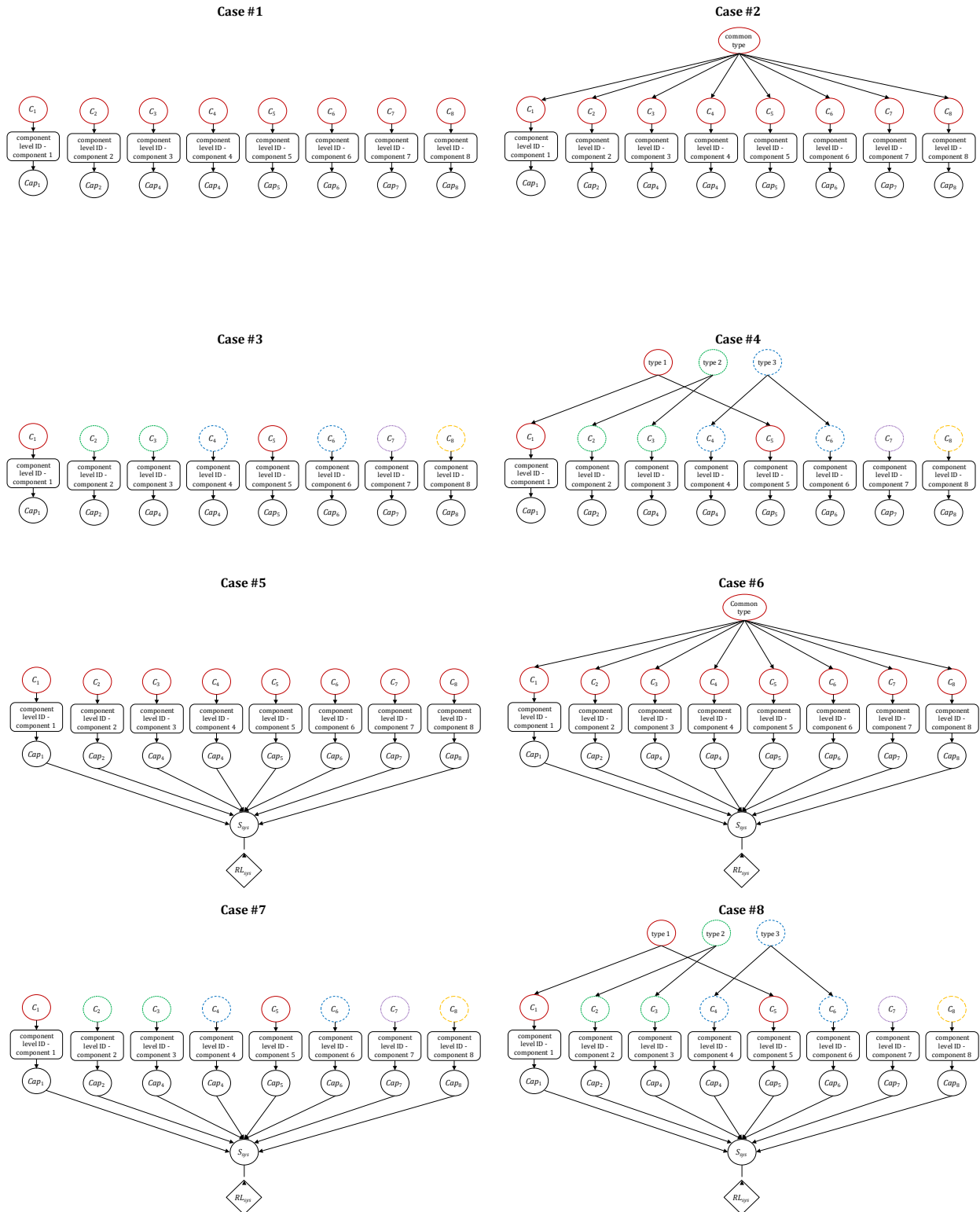


Figure 7.6: System configurations for example inspection-shutdown decisions

For all cases, the test likelihood associated with an imperfect inspection is defined by the following probabilities:

	Component undamaged	Component damaged
Component observed to be undamaged	0.9	0.25
Component observed to be damaged	0.1	0.75

7.4.2 Assumed utilities

In addition to defining the CPTs of nodes, it is necessary to specify utility values. For cases 1–4, the assumed utility values are given in Table 7.3. In the cases that components have identical reliabilities (cases 1 and 2), all components are assumed to have the same utility values. For the cases in which system effects are neglected and components are heterogeneous (cases 3 and 4), the assumed utility values depend on the component classes. Because components 7 and 8 carry a higher capacity, they are assumed to be associated with higher losses at the component level than components 1–6.

Table 7.3: Assumed utility values for cases 1–4

Utility type	Components 1-8 for cases 1 & 2 Components 1-6 for cases 3 & 4	Components 7 & 8 for cases 3 & 4
Liability	-250 cost units/component	-1000 cost units/component
Loss due to component being non-operational	-25 cost units/component	-100 cost units/component
Perfect (imperfect) inspection cost	-5 (-2.5) cost units/component	-10 (-5) cost units/component

The utilities associated with cases 5–8 are given in Table 7.4. Note that there are no explicit costs associated with an individual component being nonoperational; instead costs are incurred at the system level as a function of the system operating capacity.

The utility values in the above tables are arbitrary, but we selected them to produce interesting results in which the recommended decision actions are not always the same. To achieve this effect, we needed to modify the liability values for the cases in which system effects are included. Because the assumed utilities are significantly different when system effects are included, the computed values of information should not be compared between cases 1–4 and cases 5–8. However, the prioritization orders can be reasonably compared.

Table 7.4: Assumed utility values for cases 5–8

Utility type	Components 1-8 for cases 5 & 6 Components 1-6 for cases 7 & 8	Components 7 & 8 for cases 7 & 8
Liability	-2500 cost units/component	-10000 cost units/component
Perfect (imperfect) inspection cost	-5 (-2.5) cost units/component	-10 (-5) cost units/component
System cost function	$Cap_{svs} = 0$: -400 cost units $Cap_{svs} = 25$: -300 cost units $Cap_{svs} = 50$: -200 cost units $Cap_{svs} = 75$: -100 cost units $Cap_{svs} = 100$: 0 cost units	

7.4.3 Numerical results

For cases 1–4, the value of information associated with making a perfect inspection of each component as well as the prioritization orders are shown in Table 7.5a, assuming no inspections have yet been performed. Table 7.5b presents the same results, but considers that component 1 was perfectly inspected and found to be damaged. Although the possibility of performing imperfect inspections was included in the model, it was never recommended as the optimal choice. Therefore, in this section a recommended inspection is taken to mean a perfect inspection. For outcomes for which the no-inspection choice is recommended, abbreviated “No Ins,” the shutdown decision that is prescribed in lieu of inspection is shown in parentheses with “SD” indicating component shutdown and “O” indicating the component remains operational.

For the unconditional scenario in which no inspections have yet been performed (Table 7.5a), cases 1 and 2 indicate that all components have equal importance. This is expected because all components have identical reliabilities and system effects are not included. The difference between cases 1 and 2 is due to the inclusion of dependence among the components. This inclusion is only important when information becomes available about the state of a component, as shown in Table 7.5b. In the absence of information about the states of other components, the inclusion of statistical dependence only has the effect of increasing the value of information; however, it does not alter the prioritization order. Note that when dependence is included, inspecting one component provides partial information about other components.

Table 7.5: Value of information and prioritization rankings for cases 1–4 given (a) no evidence and (b) component 1 has been perfectly inspected and found to be damaged (VoI = value of information)

(a)

Component	Case 1		Case 2		Case 3		Case 4	
	VoI	Ranking by VoI	VoI	Ranking by VoI	VoI	Ranking by VoI	VoI	Ranking by VoI
1	11.25	1	19.25	1	11.25	3	19.25	4
2	11.25	1	19.25	1	9	4	19.4	3
3	11.25	1	19.25	1	9	4	19.4	3
4	11.25	1	19.25	1	No Ins (0)	-	19.85	2
5	11.25	1	19.25	1	11.25	3	19.25	4
6	11.25	1	19.25	1	No Ins (0)	-	19.85	2
7	11.25	1	19.25	1	36	1	36	1
8	11.25	1	19.25	1	18	2	18	5

(b)

Component	Case 1		Case 2		Case 3		Case 4	
	VoI	Ranking by VoI	VoI	Ranking by VoI	VoI	Ranking by VoI	VoI	Ranking by VoI
1	-	-	-	-	-	-	-	-
2	11.25	1	17.4	1	9	4	19.4	3
3	11.25	1	17.4	1	9	4	19.4	3
4	11.25	1	17.4	1	No Ins (0)	-	19.85	2
5	11.25	1	17.4	1	11.25	3	17.4	5
6	11.25	1	17.4	1	No Ins (0)	-	19.85	2
7	11.25	1	17.4	1	36	1	36	1
8	11.25	1	17.4	1	18	2	18	4

Cases 3 and 4 have heterogeneous components. For case 3, components 4 and 6, which have the highest reliability, do not require an inspection and can be kept in operation. An inspection is recommended for the remaining components. Among these, component 7 is deemed the most critical, followed by component 8. This is expected because these components are associated with the highest liability. Component 7 has a reliability of 0.96, the same as components 2 and 3, but because of the difference in potential liability it should be inspected before the other two. Although components 7 and 8 have the same liability associated with making an unsafe decision, component 7 is recommended to be inspected before component 8 because component 8 is more

reliable. When evidence is observed about the state of component 1, there is no effect on component values of information in case 3 because statistical dependence between components is not included in this case.

Case 4 adds statistical dependence to the case 3 model. The inclusion of dependence increases the value of information for any component that is in a class with another component, i.e., all but components 7 and 8. In the absence of dependence, it was not recommended that components 4 and 6 be inspected, but when dependence is included the recommendation changes and there is value in inspecting these components. Furthermore, the inspection-prioritization order of the components changes from the order recommended in case 3. When the observation has been made about the performance of component 1, all values of information remain unchanged except for component 5, which is in the same class as component 1. The inspection of component 1 provides information not only about component 1, but also about the likely state of component 5. Therefore, the value of information associated with an inspection of component 5 decreases. It is now lowest in the prioritization order.

Next, we consider the system-level problem (cases 5–8). Case 5 assumes that all components have identical reliabilities and liabilities. The results shown in Table 7.6a for case 5 reflect the importance of each component to the system. Components 7 and 8 are part of the system bottleneck and are therefore given first priority. Components 1–3 exist in parallel, and operation of any one of them allows some flow through the system. Furthermore, because they have the same reliabilities and utility values, and provide the same function to the system, there is no differentiation between them with regard to prioritization. Components 4–6 exist in series and have the same reliabilities, and all three must be operational for the link to be operational. Because of the relatively low probability that the link will be operable ($0.95 * 0.95 * 0.95 = 0.86$), they are given lowest priority. An observation of the state of component 1 has no effect on the recommended prioritization order or the values of information because this case assumes no statistical dependence between the component states.

Table 7.6: Value of information and prioritization rankings for cases 5–8 given (a) no evidence and (b) component 1 has been perfectly inspected and found to be damaged (VoI = Value of information)

(a)

Component	Case 5		Case 6		Case 7		Case 8	
	VoI	Ranking by VoI						
1	86	2	49	2	89	4	72	4
2	86	2	49	2	90	3	73	3
3	86	2	49	2	90	3	73	3
4	77	3	31	3	25	6	46	5
5	77	3	31	3	88	5	46	5
6	77	3	31	3	25	6	46	5
7	125	1	177	1	358	1	264	1
8	125	1	177	1	200	2	200	2

(b)

Component	Case 5		Case 6		Case 7		Case 8	
	VoI	Ranking by VoI						
1	-	-	-	-	-	-	-	-
2	86	2	42	2	90	3	73	2
3	86	2	42	2	90	3	73	2
4	77	3	27	3	25	5	42	3
5	77	3	27	3	88	4	42	3
6	77	3	27	3	25	5	42	3
7	125	1	112	1	268	1	188	1
8	125	1	112	1	200	2	188	1

The inclusion of statistical dependence in case 6 with identical component reliabilities has the effect of increasing the values of information associated with components 7 and 8 and decreasing those associated with components 1–3. This is because components 7 and 8 are in series and form the system bottleneck, while components 1–3 are in a parallel configuration. However, the prioritization order remains unchanged. The observation of component 1 being damaged reduces the value of information associated with all components for this case, although the prioritization order is unaltered. This is because the observation decreases the reliability of all components due to the common dependence structure. Therefore, when an inspection is made, it is less likely that the component will be observed to be undamaged and thus able to be kept in operation. In the

absence of an inspection, the optimal decision is to shut the component down rather than risk a liability. Therefore, there is a smaller difference between the maximum expected utility when the component is and is not inspected, due to the revised reliability estimate of the components, given the observation of damage to component 1.

Cases 7 and 8 consider heterogeneous components as well as system effects. Case 7 neglects dependence between components. Thus component importance is governed jointly by the component reliabilities/liabilities as well as the importance of the component to the system. As expected, component 7 is given first priority followed by component 8 (recall that component 7 is less reliable than component 8). Note that the value of information for component 5 is higher than the value of information associated with components 4 and 6, even though the three components lie in series. This is because, in the absence of the inspection of component 4 or 6, the optimal decision is to keep these components in operation due to their relatively high reliabilities and low liability. However, when inspection of component 5 is disregarded, the optimal action is to shut down that component (due to its low reliability), and thus the entire link becomes inoperable. Consequently, there is a relatively high value of information in inspecting component 5.

In cases 7 and 8, the values of information associated with components 2 and 3 are the same. This is expected, because they have the same reliabilities/liabilities and importance to the system. The value of information associated with component 1 is less than that associated with components 2 and 3. In the absence of an inspection of any of the components 1–3, the optimal decision is to shut it down. Components 2 and 3 are more reliable than component 1. Therefore, since the three components are in parallel, it is preferable to shut down component 1 than components 2 and 3. Thus component 1 is given lower priority. In comparing the results of case 7 before and after observing component 1 is damaged, it is found that the values of information of all but component 7 are unchanged.

Case 8 includes heterogeneous components with statistical dependence and system effects included. It is thus the most comprehensive case considered. Like in case 7, component 7 is given higher priority than component 8 when no observation has been made about the state of component 1. Components 2 and 3 are given priority over component 1 for the reason described

above. Components 4–6 are given lowest priority. The observation of component 1 being damaged has no effect on the value of information associated with components 2 and 3 for the number of significant digits reported. However, the observation reduces the value of information associated with components 7 and 8 as well as components 4–6, for the following reason. In the absence of an inspection of component 7 (or 8), the optimal decision is to shut down the component and thus the system. This results in a revenue loss of 400 units, regardless of the operating levels of the remaining components. Before the observation of damage to component 1 is made, the expected system level utility is higher than after the observation because damage to component 1 implies the system can, at best, operate at 75% of its full operating level. Therefore, the maximum expected utility when component 7 (or 8) is inspected, for the case in which component 1 is not observed to be damaged, is larger than that after the damage is observed. The value of information for component 7 (or 8) is computed as the difference between the maximum expected utility assuming the component is inspected and the maximum expected utility when it is not inspected. This difference turns out to be smaller when component 1 is observed to be damaged. A similar argument applies to components 4–6 and the shutdown of the link.

7.5 Appendix: Example calculation of the value of perfect and imperfect information

The following calculations illustrate the value of information for the joint inspection-shutdown decision problem at the component level. With the help of software such as Hugin (Hugin Expert A/S 2008), these calculations are easily performed once the ID is defined.

Example: Calculating expected value of perfect information

Consider the IDs in Figure 7.2a and b, which respectively model the cases that no information and perfect information are available about the state of the component before a decision is made. We now demonstrate calculation of the value of perfect information. Assume the component state is binary (damaged/undamaged) and set the prior probability that the component is damaged to be 0.05. Assign liability and cost-of-closure utilities according to the following table:

<i>Shut-down?</i>	No (Open)		Yes (Shut-down)		
	<i>C_i</i>	undamaged	damaged	undamaged	damaged
Utility		0	-1000	-100	-100

In the absence of information about the component damage state (Figure 7.2a), the expected utility, EU , associated with each decision is:

$$EU(open) = 0.95(0) + 0.05(-1000) = -50$$

$$EU(closed) = 0.95(-100) + 0.05(-100) = -100.$$

It follows that in the absence of additional information, the optimal decision is to keep the component open. Define $EU|NI$ as the maximum expected utility associated with the available decision options, given no information other than prior probabilities. Based on the above calculation, $EU|NI = -50$ units.

Having perfect information (Figure 7.2b) implies the optimal decision is made for any outcome of C_i . If C_i is in the damaged state, the optimal decision is to shut down the component for a loss of 100 units. If C_i is in the undamaged state, the optimal decision is to keep the component open and thus incur no penalty. Thus, given perfect information (PI), the expected utility is

$$EU|PI = 0.05(-100) + 0.95(0) = -5.$$

It follows that the value of obtaining perfect information, $EVPI$, is

$$EVPI = EU|PI - EU|NI = -5 - (-50) = 45.$$

The value of performing an inspection capable of providing perfect information is 45 units of utility.

Example: Calculating the expected value of imperfect information

Consider the prior damage probabilities and utility values defined above. Also, consider the following test likelihood table to define the mapping between nodes C_i and O_i :

	<i>C_i</i>	undamaged	damaged
<i>O_i</i>	observe no damage	0.9	0.2
	observe damage	0.1	0.8

Let c_i denote the event that component i is not damaged and \bar{c}_i denote the damaged state. Similarly, let o_i denote the event that component i is observed not to be damaged and \bar{o}_i indicate that damage is observed. The expected utility associated with imperfect information is computed as follows.

- Compute the probability that a component is damaged/undamaged given that damage/no damage is observed:

$$\Pr(c_i|o_i) = \frac{\Pr(o_i|c_i) \Pr(c_i)}{\Pr(o_i)} = \frac{0.9(0.95)}{0.9(0.95) + 0.2(0.05)} = 0.988$$

$$\Pr(c_i|\bar{o}_i) = \frac{\Pr(\bar{o}_i|c_i) \Pr(c_i)}{\Pr(\bar{o}_i)} = \frac{0.1(0.95)}{0.1(0.95) + 0.8(0.05)} = 0.704$$

$$\Pr(\bar{c}_i|o_i) = \frac{0.2(0.05)}{0.2(0.05) + 0.9(0.95)} = 0.011$$

$$\Pr(\bar{c}_i|\bar{o}_i) = \frac{0.8(0.05)}{0.8(0.05) + 0.1(0.95)} = 0.296.$$

- Compute the expected utility associated with each decision alternative given that damage/no damage is observed:

$$EU(Open|o_i) = -1000 * \Pr(\bar{c}_i|o_i) + 0 * \Pr(c_i|o_i) = -11$$

$$EU(Closed|o_i) = -100 * \Pr(\bar{c}_i|o_i) - 100 * \Pr(c_i|o_i) = -100$$

$$EU(Open|\bar{o}_i) = -1000 * \Pr(\bar{c}_i|\bar{o}_i) + 0 * \Pr(c_i|\bar{o}_i) = -296$$

$$EU(Closed|\bar{o}_i) = -100 * \Pr(\bar{c}_i|\bar{o}_i) - 100 * \Pr(c_i|\bar{o}_i) = -100.$$

Given that no damage is observed, the optimal decision is to keep the facility open with an expected loss of -11 units. Given that damage is observed, the optimal decision is to close the facility with an expected loss of -100 units. These conclusions are intuitive, but their quantitative values lead to the more interesting result of the expected utility given imperfect information ($EU|II$):

$$EU|II = -11 * \Pr(o_i) - 100 * \Pr(\bar{o}_i) = -23.$$

Note that the quantity $EU|II$ is the utility associated with the optimal policy corresponding to the ID in Figure 7.2c. It is therefore direct output from the ID, and the calculations shown above need not be performed manually.

- Compute the expected value of imperfect information:

$$EVII = EU|II - EU^*|NI = -23 - (-50) = 27.$$

As expected, the value associated with imperfect information is less than the value associated with perfect information.

8. Example Applications

8.1 Introduction

As emphasized in previous chapters, the capacity of Bayesian networks to facilitate near-real-time updating makes them useful for post-earthquake decision support. However, BNs are also useful for performing conventional probabilistic seismic hazard assessment (PSHA). The BN framework described in Chapter 3 naturally provides the output of conventional PSHA: the probability that the ground motion intensity at a site exceeds a given level in a specified time period. The output of this BN can thus be used to construct hazard curves. BNs can also be used to perform hazard deaggregation. However, BNs go beyond conventional PSHA by (1) providing insight into the most-probable earthquake scenarios to affect a site, (2) making it feasible to consider hazards for many different post-earthquake situations, and (3) allowing system hazard assessments to incorporate random field effects and measures of component and system performance.

Two illustrative examples are presented in this chapter. The first example considers a simple transportation system and demonstrates how BNs can be applied to perform, and go beyond, conventional PSHA. The second example is based on an idealized portion of the proposed California High-Speed Rail system and emphasizes post-earthquake information updating. Both examples show the capabilities and advantages of the BN framework for seismic hazard assessment and risk management of infrastructure systems.

8.2 Example 1: Connectivity of a transportation network

Consider the simple, hypothetical transportation network in Figure 8.1. Four cities, represented by circles labeled A through D, are connected to a hospital (circle H) by roadways. These roadways must cross a river in six places on six identical bridges, represented by numbered squares. The transportation network is located near three active faults, as shown in Figure 8.2. This figure shows the fault-specific coordinate system associated with earthquake source 1. The fault lengths are 65, 83.5, and 105 km for sources 1, 2, and 3, respectively. We want to know the probability that any city will be disconnected from the hospital after an earthquake due to damage to the bridges. It is assumed that the roadways are not prone to earthquake damage.

8.2.1 Using BN for conventional site-specific PSHA

The goal of PSHA is to quantify the probability of exceeding a given level of ground motion intensity. For a given earthquake occurrence, this probability is defined by:

$$\Pr(S_i > s_i) = \sum_{n=1}^{N_{sc}} \Pr(E_{sc,n}) \int_M \int_R \int_{\epsilon} \Pr(S_i > s_i | m, r, \epsilon) f_{M,R}(m, r) f_{\epsilon}(\epsilon) dm dr d\epsilon, \quad (8.1)$$

where $\Pr(S_i > s_i)$ is the probability that the ground motion intensity at site i exceeds level s_i in the event of the earthquake occurring on one of the faults; $\Pr(E_{sc,n})$ is the probability of the earthquake occurring on source n ; $\Pr(S_i > s_i | m, r, \epsilon)$ is the conditional probability that the ground motion intensity at site i resulting from the earthquake on source n exceeds level s_i for the given magnitude, source-to-site distance, and ϵ value; $f_{M,R}(m, r)$ is the joint distribution of the magnitude (M) and source-to-site distance (R); $f_{\epsilon}(\epsilon)$ is the distribution of the error on the attenuation model; and N_{sc} ($= 3$ in this example) is the number of sources in the vicinity of the site. The integral in Equation (8.1) is a common form used in PSHA, though it does not explicitly show the effects of finite rupture length and directivity, discussed in Chapter 3. It also combines the inter- and intra-earthquake error terms in the attenuation model, which is reasonable when considering a single site.

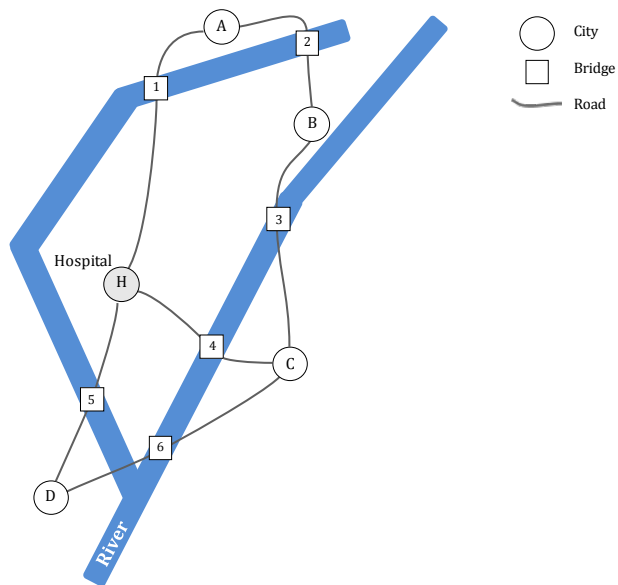


Figure 8.1: Example transportation network

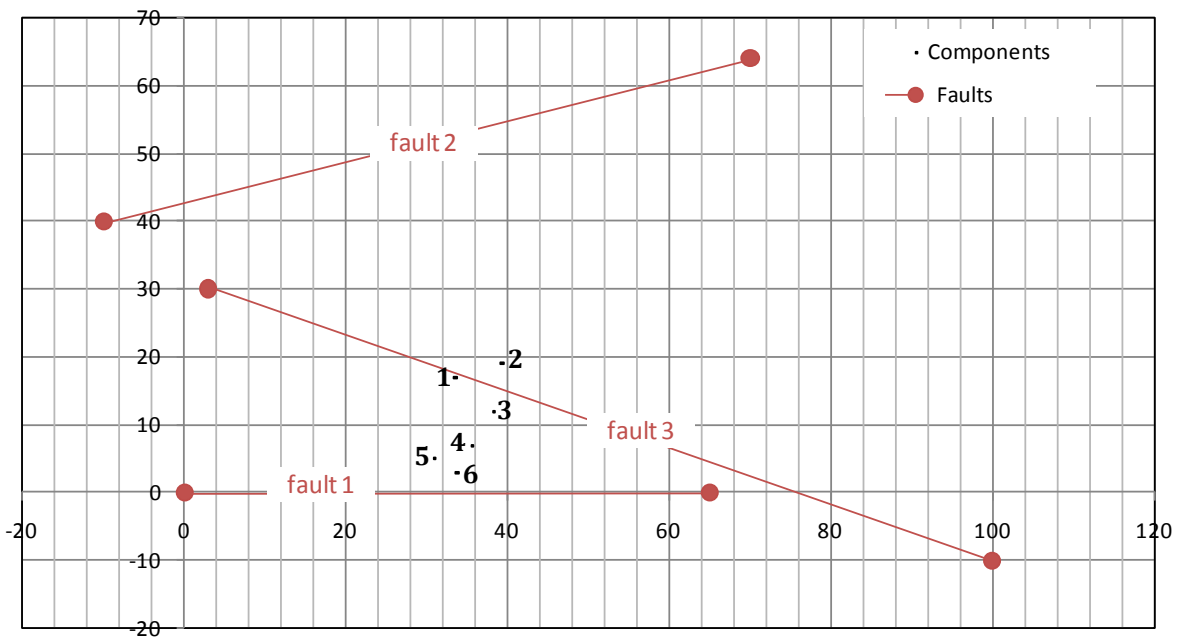


Figure 8.2: Location of transportation system relative to three active faults

Often PSHA expresses the hazard at a site as an annual rate at which the ground motion intensity level s_i is exceeded. Denoted $\nu_i(s_i)$, this rate is computed as

$$\nu_i(s_i) = \sum_{n=1}^{N_{sc}} \nu_n \int_M \int_R \int_{\epsilon} \Pr(S_i > s_i | m, r, \epsilon) f_{M,R}(m, r) f_{\epsilon}(\epsilon) dm dr d\epsilon, \quad (8.2)$$

where ν_n is the mean rate at which earthquakes occur on source n .

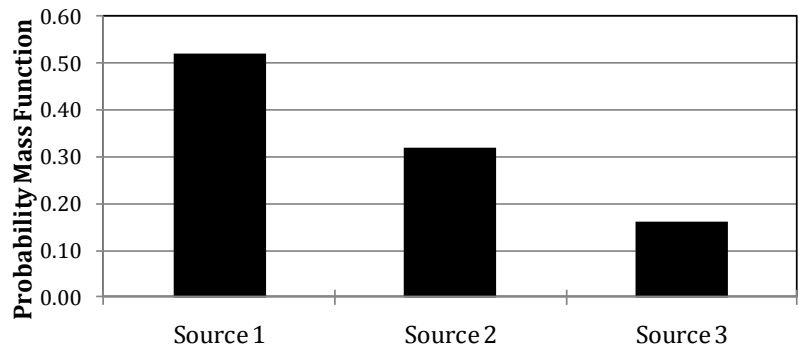
The BN in Figure 3.22 is used to model the seismic demand on a component in the example system. The modeling assumptions used to construct the CPTs of this BN, consistent with the methodology described in Chapter 3, are described below. All modeling assumptions made in this example are for illustrative purposes only.

Figure 8.3a shows the assumed relative likelihoods of an earthquake occurring on each source. These probabilities are proportional to the mean occurrence rates ν_n defined above. The distribution of the magnitude follows the truncated Gutenberg-Richter law (Gutenberg and Richter 1944) with source-specific parameters. The assumed prior discretized distribution of the magnitude for each source is shown in Figure 8.3b. The distribution of the location of the epicenter in each fault-specific coordinate system is assumed to be uniform along the fault length, as shown in a discretized form in Figure 8.3c. Note that, for source 2, the probability mass associated with the state 80–85 is slightly less than that associated with other states because source 2 is assumed to be 83.5 units in length, which falls near the middle of the state 80–85.

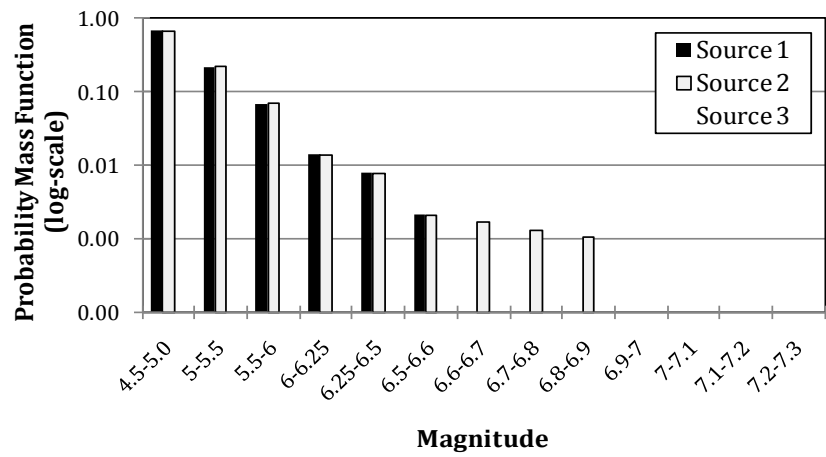
The magnitude–rupture length relationship is given by (Wells and Coppersmith 1994):

$$\log R_L = a + b * M + \epsilon_L. \quad (8.3)$$

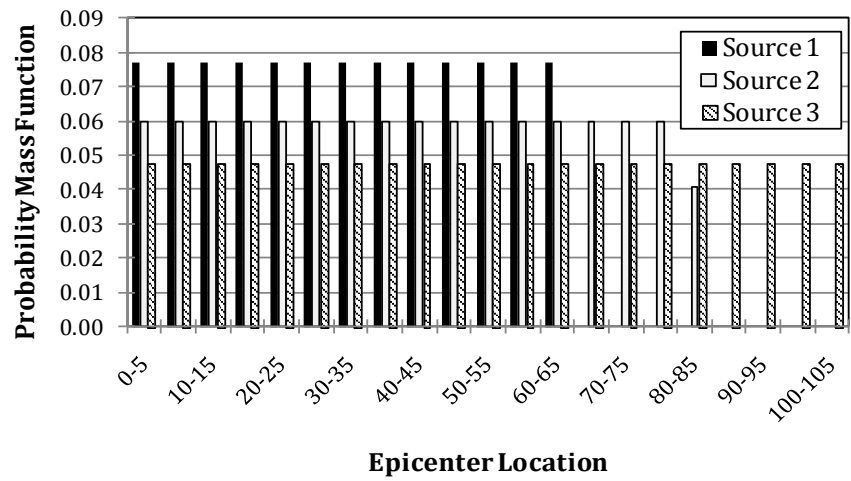
Statistical uncertainty in the values of parameters a and b as well as the model error (ϵ_L) are accounted for when defining the distribution of the rupture length for a given magnitude. For all faults, a and b are assumed to be normally distributed with means of -3.55 and 0.74 and standard deviations of 0.37 and 0.05 , respectively. ϵ_L is normally distributed with zero mean and standard deviation of 0.23 . The distributions of the rupture reference coordinate X_r and source-to-site distance R are defined using the expressions defined in Chapter 3.



(a)



(b)



(c)

Figure 8.3: Prior probability mass functions of (a) source, (b) magnitude, and (c) epicenter location

The Shahi and Baker (2010) directivity model is used to define the probability of experiencing a directivity pulse at a site and to determine the distribution of the variance reduction term R_f . The ground motion intensity is measured in terms of spectral acceleration at 1 second. The Campbell and Bozorgnia (2007) NGA relationship is used to define the spectral acceleration at a site as a function of source and site characteristics. All faults are assumed to be strike-slip faults that crop out at the ground surface, and all sites have a soil shear wave velocity of 600 m/s. For simplicity, all fault parameters required in the attenuation model ($Z_{1.0} = 1$, $F_{RV} = 0$, $F_{NM} = 0$, $Z_{tor} = 0$, $Dip = 90$), other than fault length, are assumed to be identical for all sources. These simplifying assumptions are made to ensure that the illustrative results obtained from the BN are intuitive and predictable.

The BN described in Chapter 3 yields the discretized distribution of ground motion intensity at a site (referred to as a ground motion prediction point, GMPP, in Chapter 3) as the output of node S_i in Figure 3.22. For the unconditional case in which no evidence has been entered in the BN, summation of the probability masses above a given threshold yields the prior probability that the ground motion intensity at the site exceeds the given threshold in a future earthquake; this is the standard output of PSHA in Equation (8.1). Conversely, to obtain this quantity, a binary node can be added to the BN that is in the true state if the ground motion intensity at the site exceeds the threshold and is in the false state otherwise.

The remainder of this section describes the site-specific hazard assessment for site 1. Unless noted otherwise, the results are obtained using exact inference with the Hugin application (Hugin Expert A/S 2008). The distribution of spectral acceleration for site 1, for a random earthquake occurring on one of the faults, is shown in Figure 8.4. This figure also demonstrates how this distribution changes when the earthquake is known to have occurred on each of the faults. The updated source-dependent distributions are obtained by entering evidence at node S_c in Figure 3.22 corresponding to an earthquake on each fault. Because the faults are assumed to be identical with the exception of length, the longest fault (source 3), which is capable of producing the largest earthquake, is associated with the distribution of ground motion intensity that is shifted farthest to the right.

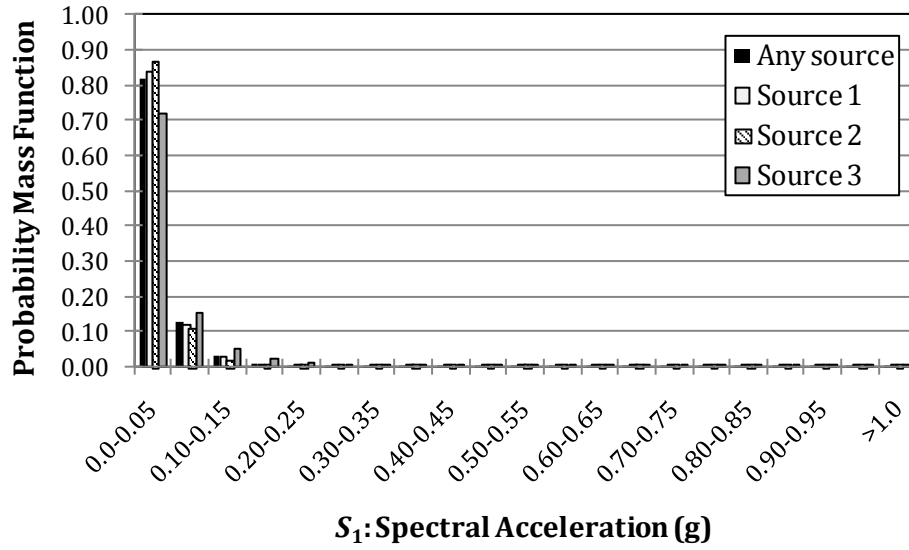


Figure 8.4: Distribution of ground motion intensity at site 1

The distribution in Figure 8.4 facilitates the construction of the site-specific hazard curve. A hazard curve gives the annual frequency (y -axis) that the ground motion intensity at a site will exceed a given level (x -axis). Earthquakes occur on each fault with rate ν_n , and they occur on any fault near the example system with rate $\nu_1 + \nu_2 + \nu_3$. The rate at which earthquakes occur on any fault with ground motion intensity greater than s_i is $\Pr(S_i > s_i) * (\nu_1 + \nu_2 + \nu_3)$, where $\Pr(S_i > s_i)$ is obtained by summing the probability masses for all states greater than s_i in Figure 8.4 when considering all sources. Assuming that earthquakes occur according to a homogeneous Poisson process, the annual probability that the ground motion intensity at site i will exceed the level s_i due to earthquakes occurring on one of the N_{sc} faults is

$$\begin{aligned} & \Pr(\text{at least one earthquake with } S_i > s_i \text{ in one year}) \\ & = 1 - \exp(-\Pr(S_i > s_i) * (\nu_1 + \nu_2 + \nu_3)). \end{aligned} \quad (8.4)$$

To produce a hazard curve for an individual fault, $(\nu_1 + \nu_2 + \nu_3)$ in the above expression is replaced with the fault-specific rate ν_n and $\Pr(S_i > s_i)$ is computed using the corresponding distribution in Figure 8.4. This leads to the hazard curves for site 1 shown in Figure 8.5.

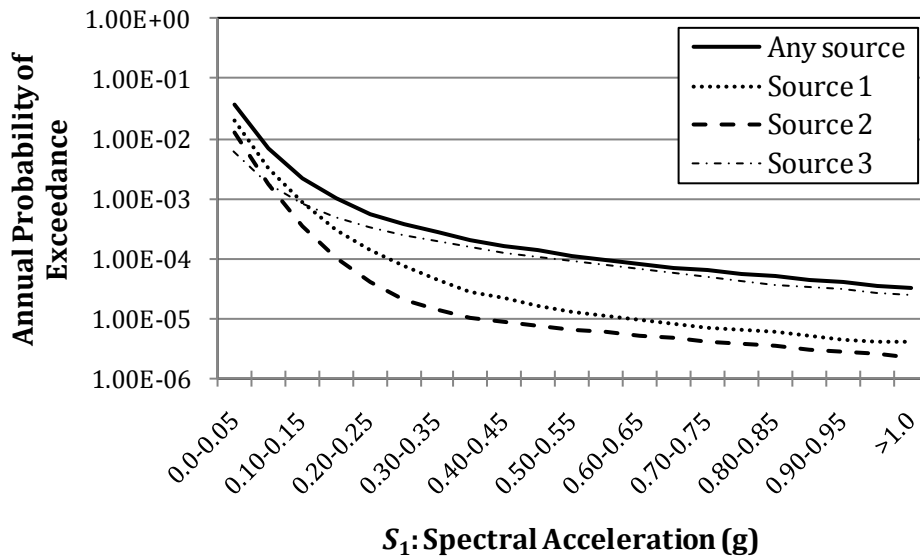


Figure 8.5: Example hazard curve for site 1

Source 3 produces the largest earthquakes but at the lowest rate whereas source 1 produces the smallest earthquakes but at the highest rate. Therefore, at low intensity thresholds (high levels of annual probability of exceedance and short return periods), source 1 provides the largest contribution to hazard. At high intensity thresholds (low annual probabilities of exceedance and long return periods), source 3 dominates the hazard.

The hazard curve gives the probability of exceeding a level of ground motion intensity when considering all possible combinations of earthquake magnitude and location (and thus source-to-site distance). From such an aggregated curve, it is difficult to gain insight into the combinations of magnitude and location (source-to-site distance) that govern the hazard. Ground motion records required for structural analysis are commonly selected based on the magnitude of the earthquake associated with the ground motion record and the distance between the earthquake source and the recording instrument. To gain insight into the combinations of magnitude and source-to-site distance that dominate the hazard, a process known as hazard *deaggregation* is used. Deaggregation breaks down the hazard curves into contributions from different earthquake scenarios, which most commonly are defined by combinations of magnitude and source-to-site distance. The hazard deaggregation gives the fractional contribution of a particular combination to the total hazard at a site and is computed according to Bayes' rule:

$$\begin{aligned}
& P(M^{(1)} \leq M \leq M^{(2)}, R^{(1)} \leq R \leq R^{(2)} | S_i > s_i) \\
= & \frac{P(S_i > s_i | M^{(1)} \leq M \leq M^{(2)}, R^{(1)} \leq R \leq R^{(2)}) * P(M^{(1)} \leq M \leq M^{(2)}, R^{(1)} \leq R \leq R^{(2)})}{P(S_i > s_i)}. \tag{8.5}
\end{aligned}$$

where the superscripted values indicate lower and upper limits of intervals on the magnitude and source-to-site distance. It is seen that the conditional joint distribution of M and R given the hazard is proportional to the product of the conditional hazard and the unconditional joint distribution of M and R . Deaggregation is performed for a specific hazard level. In this example, we use the ground motion intensity in the hazard curve that corresponds to an annual probability of exceedance of 10^{-4} . For the hazard curve in Figure 8.5, the discrete S_A state with ground motion in the range 0.55–0.6 g at site 1 has a probability of exceedance of approximately 10^{-4} .

The unconditional joint PMF of magnitude and source-to-site distances for site 1 is shown in Figure 8.6. In the three-dimensional space, the depth-wise axis has the low magnitudes located close to the reader. As expected, low-magnitude events at moderate source-to-site distances are most likely. The conditional probability that spectral acceleration at the site is in the state (0.55–0.6 g) or higher at various combinations of magnitude and source-to-site distances is shown in Figure 8.7. This exceedance event is most likely to result from a high-magnitude event at a close distance. The distributions in Figure 8.6 and Figure 8.7 can be obtained directly from the BN. Finally, multiplying the conditional distribution times the unconditional joint distribution and dividing by the hazard level yields the deaggregation shown in Figure 8.8 according to Equation (8.5). Conversely, the discretized joint distribution of M and R for a given evidence scenario (e.g., $S_i > s_i$) can be obtained directly as output from the BN by entering the evidence as the appropriate node. Thus, the intermediate quantities in Figure 8.6 and Figure 8.7 need not be computed. Instead, Figure 8.8 can be obtained directly as natural output from the BN. Figure 8.8 shows that the hazard at site 1 is dominated by low- to moderate-magnitude events located close to the site.

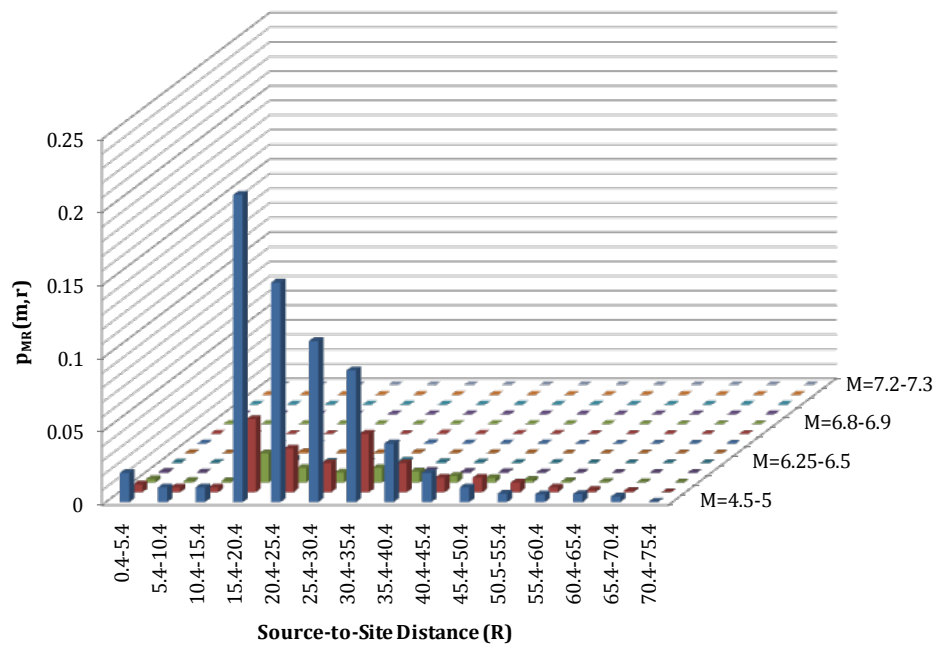


Figure 8.6: Joint distribution of magnitude and source-to-site distance

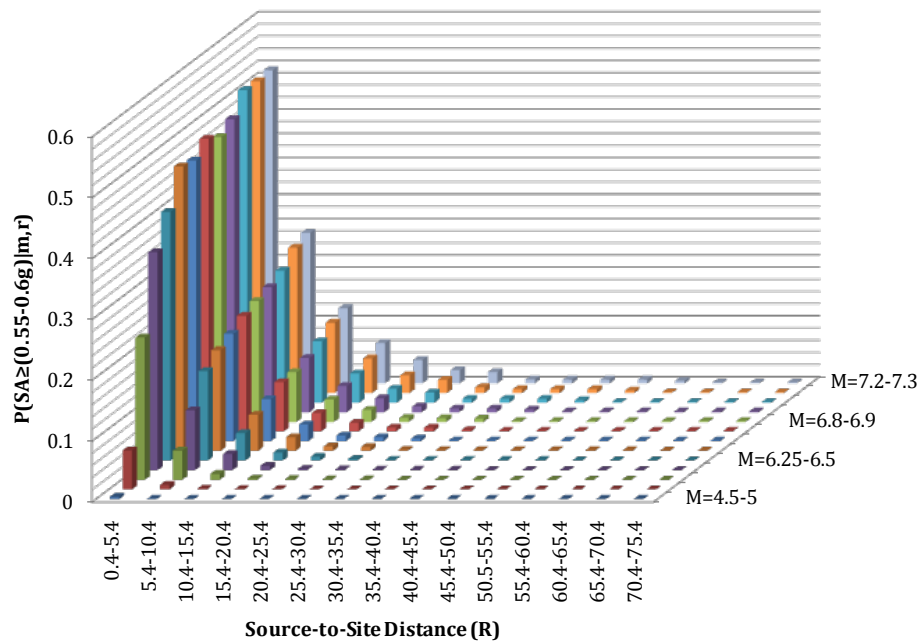


Figure 8.7: Conditional probability that spectral acceleration is equal to the state (0.55–0.6 g) or greater at site 1 for various magnitudes and source-to-site distances

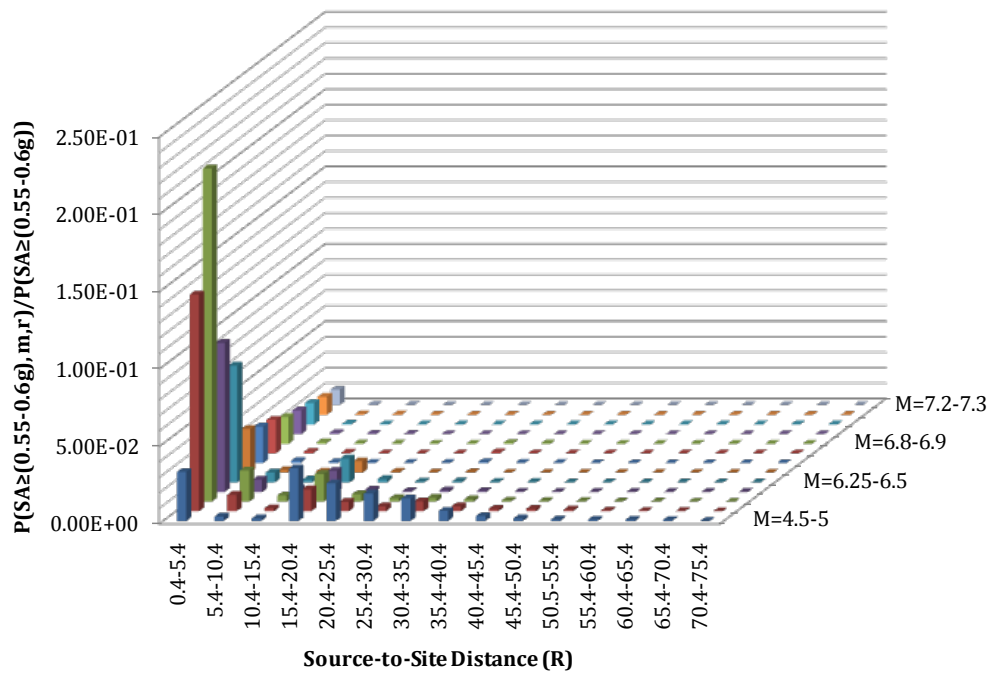


Figure 8.8: Hazard deaggregation for site 1

Many available applications (e.g., see <http://earthquake.usgs.gov/hazards/apps/>) provide site-specific deaggregation. However, the BN framework is particularly useful for helping understand the hazard at a site in addition to performing deaggregation. By entering evidence at any node in the BN, it is possible to identify its influence on the hazard at the site. For example, Figure 8.9 shows the distribution of ground motion intensity at site 1 for several evidence cases (ECs): (1) an event with magnitude in the range 6.5–6.6 has occurred on one of the faults; (2) the 6.5–6.6 magnitude event has occurred on source 2; and (3) the 6.5–6.6 magnitude event has occurred on source 2 with its epicenter at the center of the fault, but with unknown rupture length and direction. All evidence cases shift the distribution of ground motion intensity to the right relative to the unconditional case.

The ease with which BNs help calculate updated distributions for all nodes in the BN is useful in understanding the hazard at a site. For example, the updated distributions of node S_C for a magnitude 6.5–6.6 event on any source as well as for events producing intensities of 0.3–0.35 g

and 0.55–0.60 g at site 1 are shown in Figure 8.10a. The updated distributions of node M for the latter two evidence case are shown in Figure 8.10b.

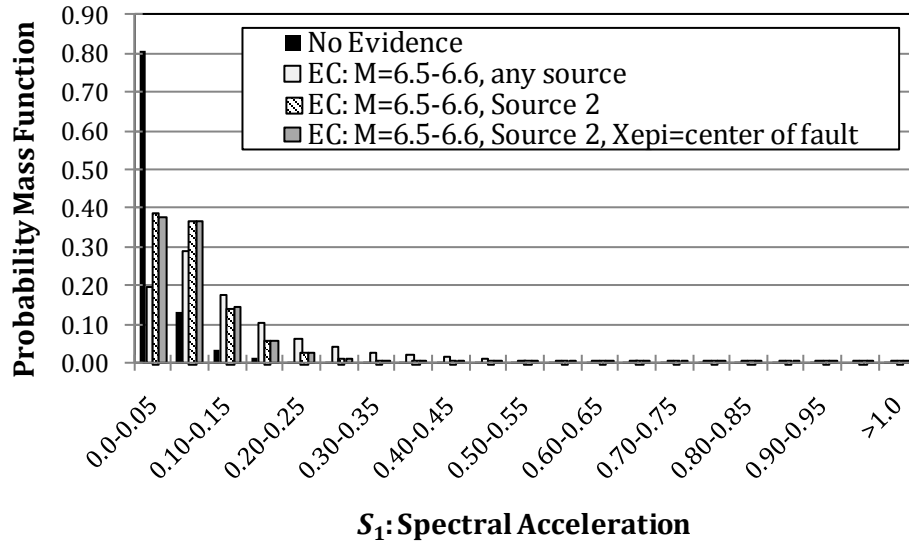


Figure 8.9: Distribution of spectral acceleration at site 1 given evidence cases

Another useful application of BNs for understanding the hazard at a site is the *max-propagation algorithm*, which provides the most-probable configuration of node states for a given evidence scenario. The algorithm can be applied to find the most likely configuration for any subset of nodes in the BN given evidence on a different subset. The exact version of the algorithm (in contrast to an approximate algorithm described later) is carried out using the inference procedures described in Chapter 2, but with summations over random variables replaced by maximization operators (Jensen and Nielson 2007). To differentiate the inference methods described in Chapter 2 from the max-propagation algorithm, the methods in Chapter 2 are generally referred to as *sum-propagation* algorithms.

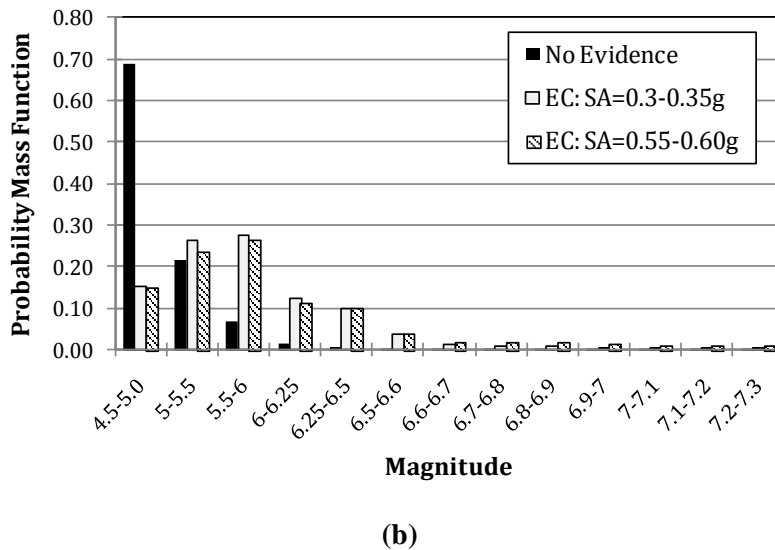
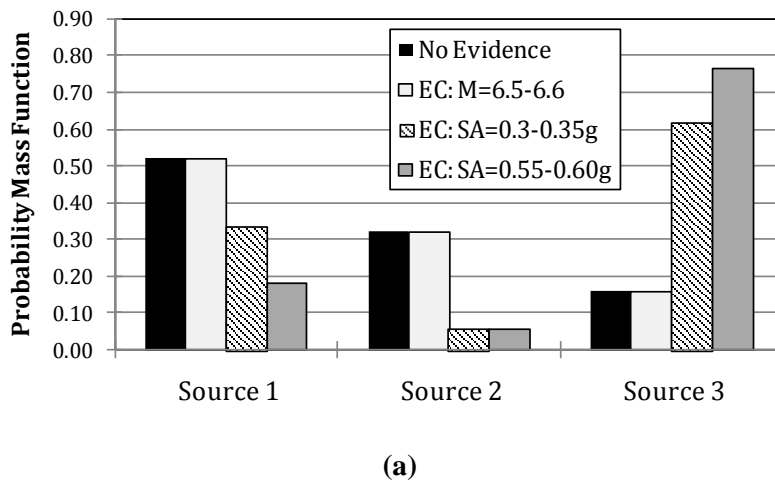


Figure 8.10: Updated distributions of (a) earthquake source and (b) magnitude given evidence cases

To illustrate the value of the max-propagation algorithm, consider that ground motion intensity at site 1 is in the state 0.55–0.6 g or greater, consistent with the hazard level considered previously. To help specify this evidence case, a node is added to the BN as a child of node S_A corresponding to the binary event $S_A \geq (0.55-0.6 g)$. This binary node is then set equal to the “true” state to reflect the evidence. The resulting most-probable configuration of source node states in the BN for this evidence scenario is shown in Table 8.1. The larger-than-expected ground motion intensity is most likely to result from a moderate-magnitude event with its epicenter about one-third from the left end of source 3.

Table 8.1: Most-probable source node state configuration corresponding to evidence scenario in which spectral acceleration is in the state 0.55–0.6 g or greater

Node	State
Source	Source 3
Magnitude	5.0-5.5
Rupture length	0-5 km
Epicenter location	30-35 km
Rupture reference coordinate	30-35 km

The results described above are obtained using an approximate algorithm in GeNIe developed by Yuan et al. (2004). It is important to note that the discretization intervals used with continuous random variables can strongly influence results obtained with max propagation. Recall that the algorithm seeks to find the most probable joint combination of node states. If a continuous random variable is discretized into unequal bins, the algorithm may identify certain states as being the most probable simply because they are associated with a large amount of probability mass, regardless of the physical meaning of the combination of states.

8.2.2 Using BN for system-level PSHA

The previous section focused on site-specific hazard; however, with infrastructure systems it is necessary to consider the hazard at multiple sites. Analysis of seismic hazard at multiple sites requires consideration of ground motion intensities that vary in space and must be considered as a random field. For further analysis of the example of the four cities and six bridges, the size and complexity of the BN renders exact inference intractable on a workstation with 32 GB of RAM. Thus, we use the importance sampling-based algorithm EPIS-BN (Yuan and Druzdzel 2003), available in GeNIe (DSL 2007), for sum propagation. The hazard at the site of each bridge in Figure 8.1 differs depending on the distance to the earthquake source as well as site effects. For simplicity, all sites are assumed to be identical, and differences in hazard are thus due to source location and wave propagation effects only. Hazard curves for the different sites in Figure 8.11 show that site 6 has the highest hazard level and site 2 the lowest. These results can be explained by the relative distances of these sites to the three faults and the mean rates of earthquake events on these faults.

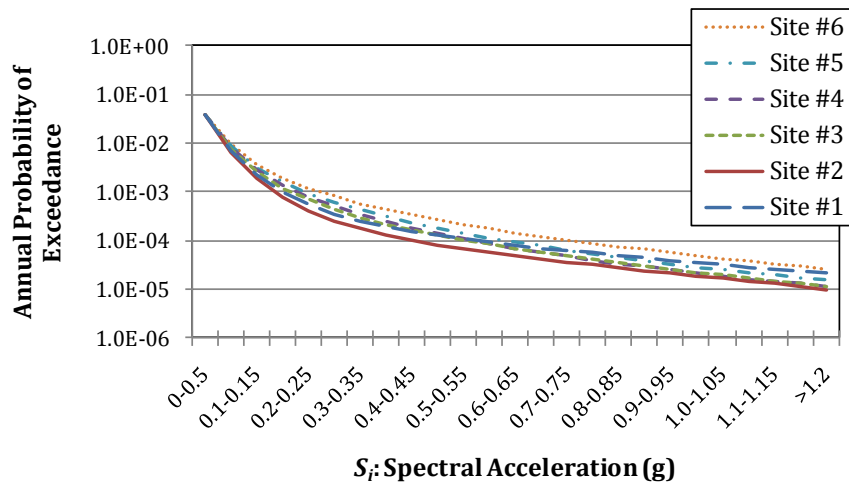


Figure 8.11: Hazard curves for all sites for unconditional case

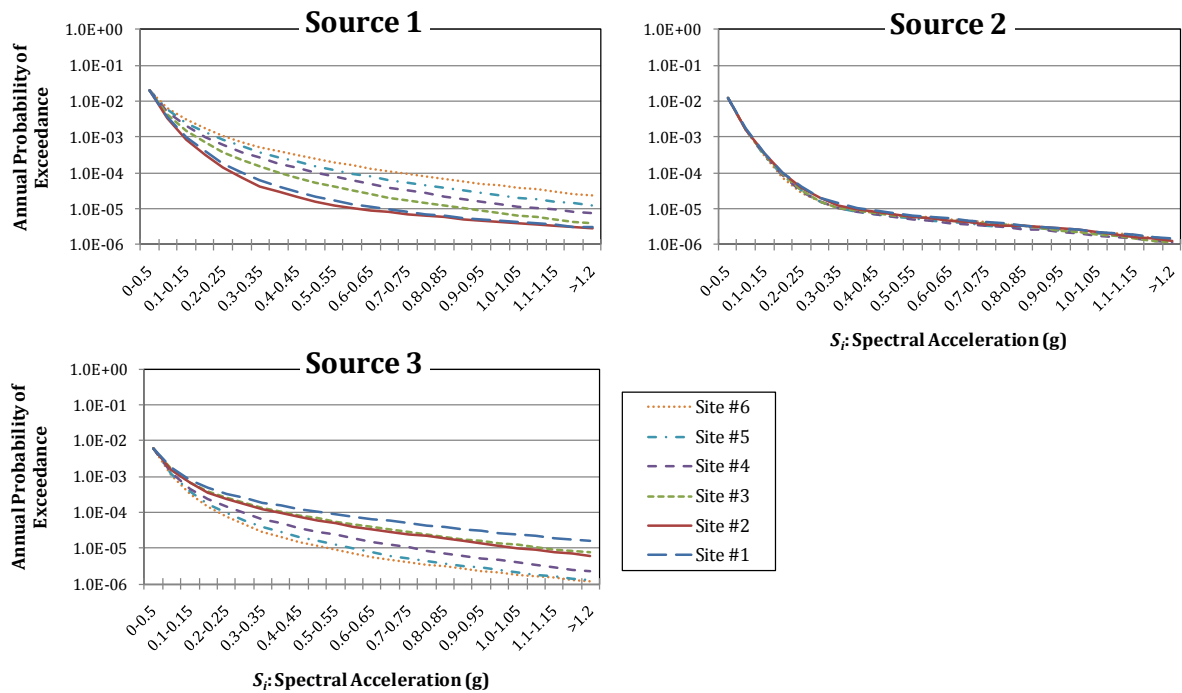


Figure 8.12: Hazard curves for all sites for earthquakes on each source

Figure 8.12 shows how the hazard curves differ depending on the earthquake source. These curves are obtained by entering evidence at node S_C specifying the source. The resulting distribution of ground motion intensity at each site is then used to construct the hazard curve.

The hazard curves associated with sources 1 and 3 are more dispersed from site to site. For source 1, site 6, which is located closest to the source, is associated with the highest hazard. However, this site is located farthest from source 3 and is, therefore, associated with the lowest hazard for the source 3 hazard curve. The hazards for source 2 are similar for all sites because the distances of the sites from the fault are all similar. Figure 8.13 shows site-specific hazard curves given an earthquake on each source as well as for the unconditional evidence case, i.e., considering all earthquake sources. Consistent with previous observations, for all sites hazard at low intensities is dominated by source 1. For sites close to source 3 (sites 1–3), the hazard at large intensity values is dominated by source 3. For sites 4–6, source 1 dominates the hazard at all intensities. For all sites, source 2 provides the smallest contribution to hazard.

8.2.3 Incorporating component performance in assessing system seismic risk

The sites for which hazard curves were calculated correspond to the locations of bridges in the example transportation system. Consistent with Chapter 5, the performance of each bridge is defined as a function of the seismic demands placed upon it. For simplicity and predictability, we assume that all bridges are identical. The fragility model used takes the form in Equation (5.7), with $\lambda = 0.6$ and $\zeta = 0.4$. Statistical uncertainty in the value of the parameters is neglected. The component of model error that is common to all bridges is arbitrarily assumed to have a standard deviation of 0.1. The uncertainty associated with the site-specific component of model error is assumed to be incorporated in ζ . Figure 8.14 shows the fragility function for different realizations of the common component of model error.

Component failure probabilities associated with the unconditional case in which an earthquake occurs on an unknown source, as well as the conditional cases in which the source is known, are shown in Figure 8.15. For the unconditional case, the failure probabilities are more homogeneous than when considering earthquakes on sources 1 and 3. For the unconditional case, the highest failure probabilities are associated with components 5 and 6, which are located closest to fault 1 (the most active fault). Component 1, located less than 1 km from fault 3 (which is capable of producing the largest earthquake), and component 4, located between faults 1 and 3, have failure probabilities of similar magnitude.

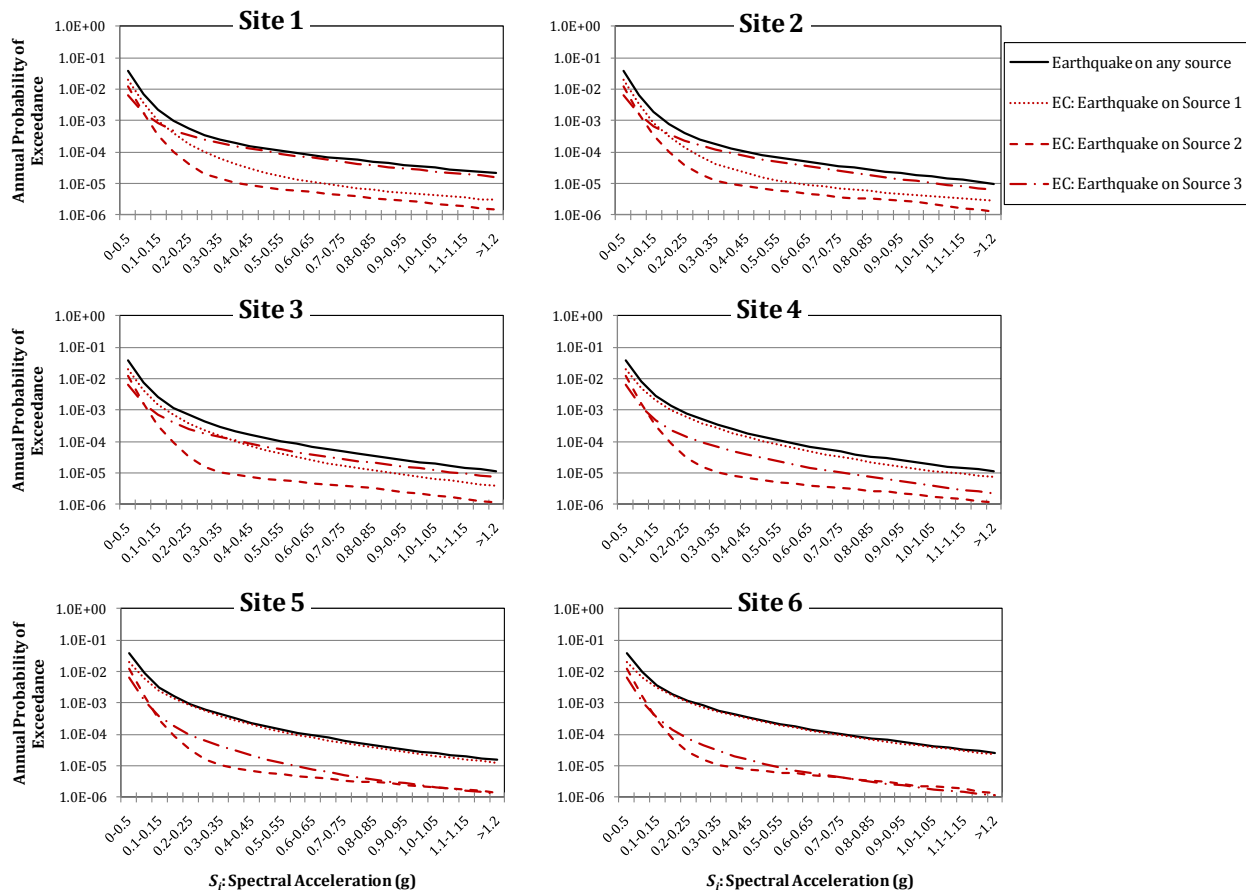


Figure 8.13: Site-specific hazard curves for earthquakes on each source

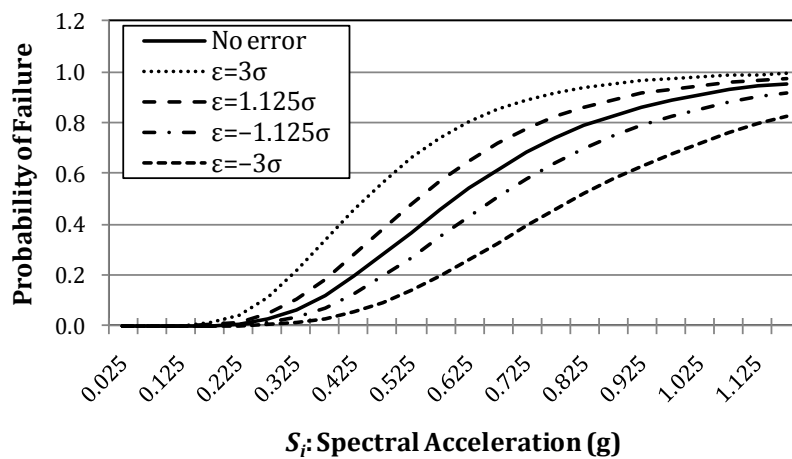


Figure 8.14: Fragility function for different realizations of model error

For the source-specific cases, the failure probabilities increase with proximity to the fault. Because source 3 is associated with the largest events, the associated failure probabilities are higher. The component failure probabilities associated with source 2 are the lowest and relatively homogeneous because all sites are located farther (at least 34 km) from the fault.

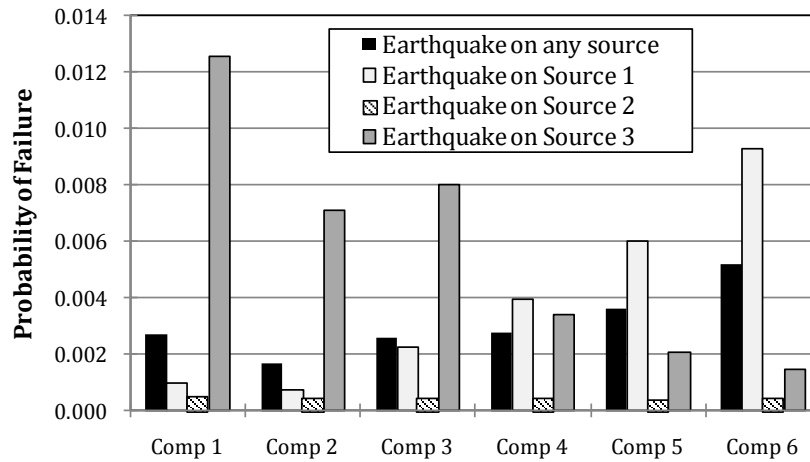


Figure 8.15: Probability of component failure given an earthquake

8.2.4 Incorporating system performance in assessing system seismic risk

The next step in assessing the seismic risk to the example system is incorporating a measure of system performance. The transportation system is classified in the failure state if any city is cut off from the hospital after an earthquake as a result of bridge failures. A city is disconnected from the hospital if a connectivity path does not exist between the city and the hospital. Treating a city as a source and the hospital as a sink, MLSs can be defined representing these connectivity paths. The MLSs corresponding to the source at city A and the sink at the hospital are {1}, {2,3,4}, and {2,3,6,5}. For the source at city B the MLSs are {2,1}, {3,4}, and {3,5,6}; for city C they are {4}, {3,2,1}, {5,6}; and for City D they are {5}, {4,6}, and {1,2,3,6}.

The portion of the BN used to model system performance is shown in Figure 8.16 using an MLS formulation. Node S_{sys} is defined as a child of nodes “city” $\rightarrow H$, which represent the event that a city is able to reach the hospital. S_{sys} is in the survival state only if all nodes “city” $\rightarrow H$ are in the survival state. Parents of nodes “city” $\rightarrow H$ are nodes that represent the MLSs for

connectivity between each city and the hospital. The MLS nodes are defined as children of their respective constitutive components. The BN in Figure 8.16 is not optimum for computational efficiency as converging connections are used instead of a chain structure. This BN structure is shown here for illustrative purposes because it is easier to interpret than the more efficient chain structure. For comparison, the efficient formulation is shown in Figure 8.17. In that BN, the formulations corresponding to each source-sink pair are hidden behind objects. The BNs behind the objects are included below the system BN. The total clique table sizes associated with the converging and efficient MLS formulations, neglecting correlation in demands are 2624 and 1440 respectively.

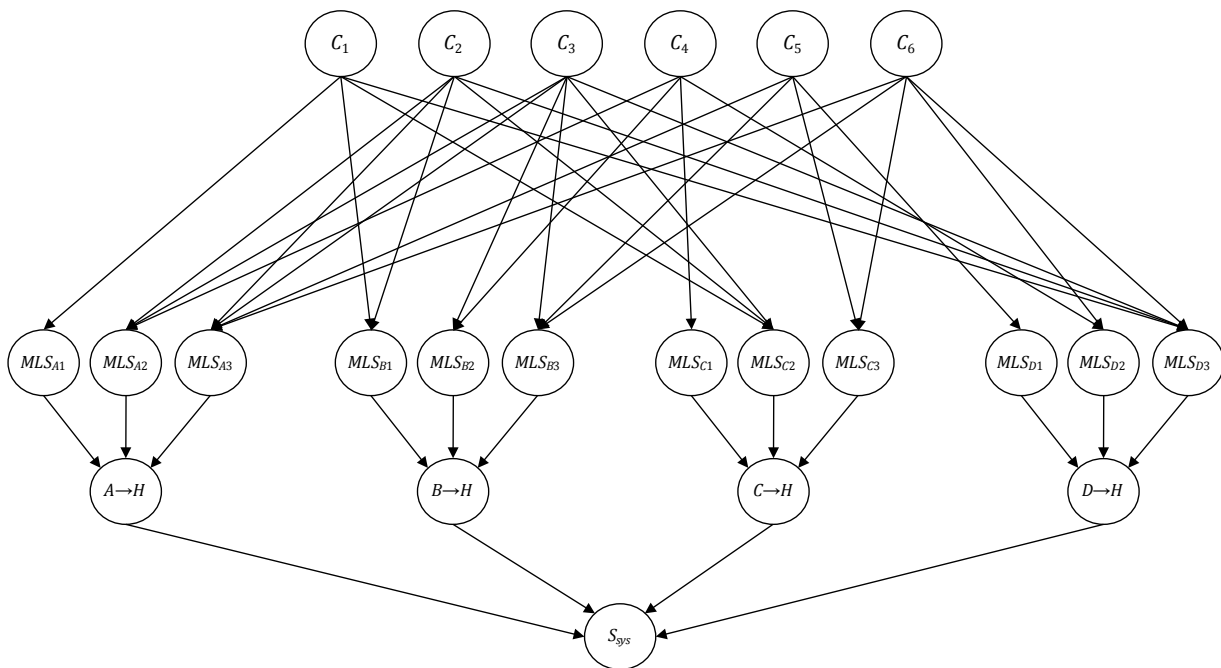


Figure 8.16: BN modeling system performance in example 1 using converging MLS formulation

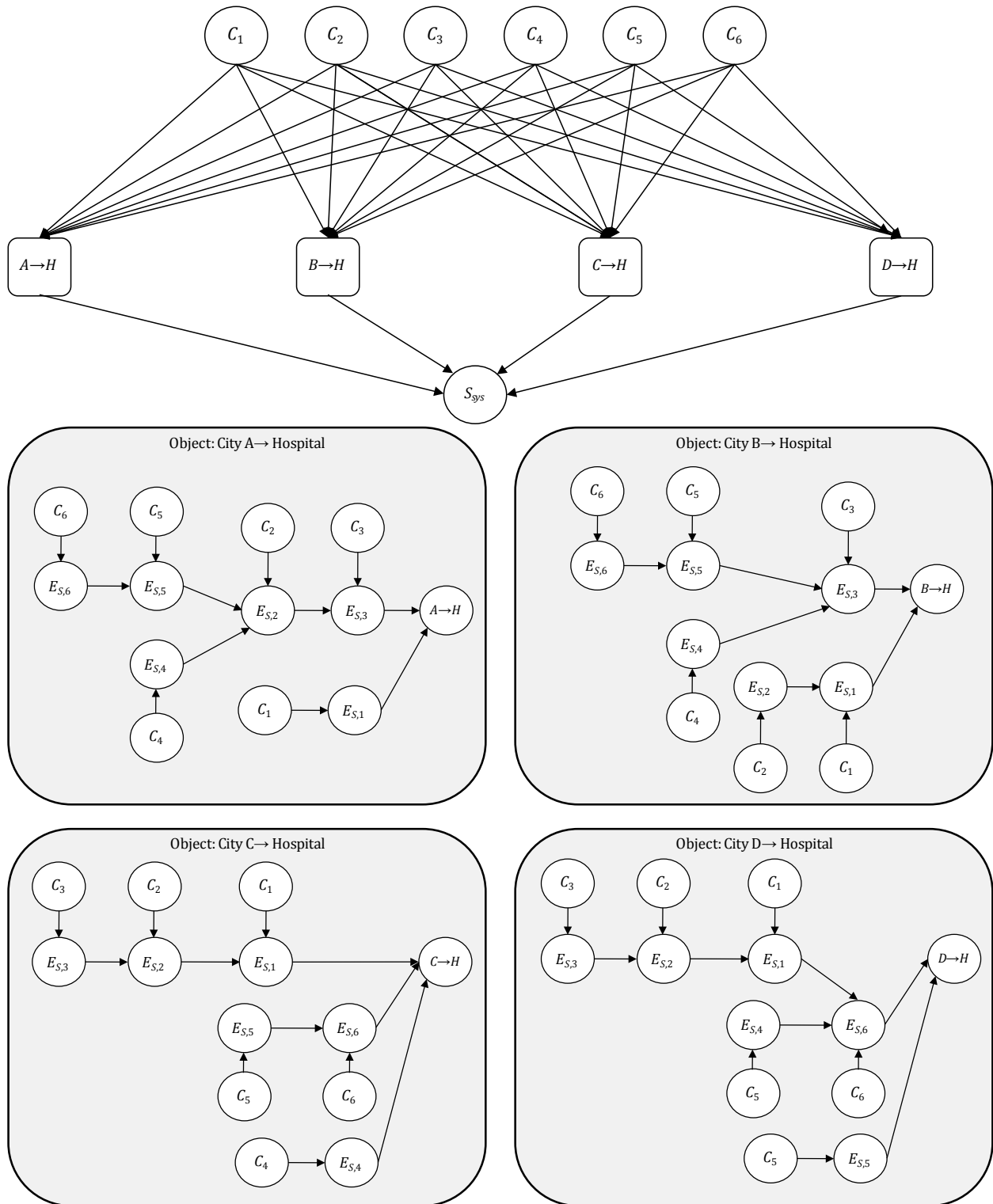


Figure 8.17: BN modeling system performance in example 1 using efficient MLS formulation

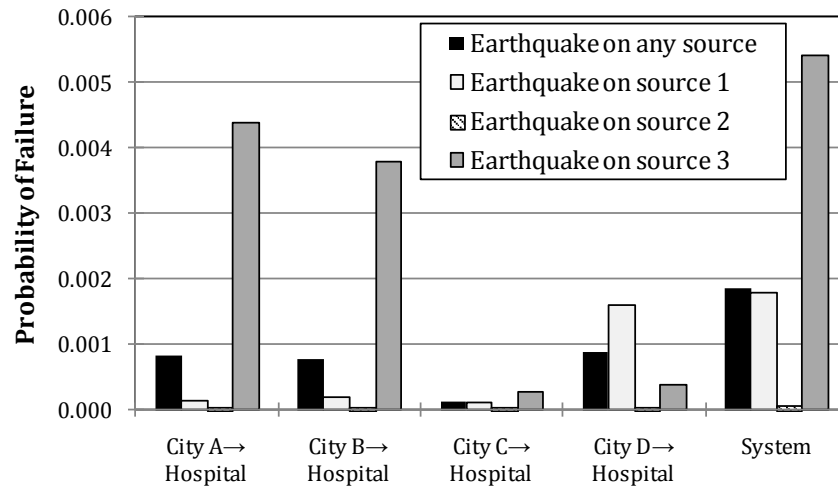


Figure 8.18: System failure probabilities for example 1

Figure 8.18 shows the system failure probability as well as the probability that each city is disconnected from the hospital in the event of an earthquake on one or on any of the faults. For an earthquake on source 1, city D, which is located closest to the source and is disconnected if bridges 5 and 6 fail, has the highest probability of disconnect. For an earthquake on source 3, cities A and B, which are located closest to the source, have the highest probabilities of disconnect. Source 3 is likely to produce the largest magnitude earthquakes and therefore the highest levels of ground motion intensity. As shown in Figure 8.15, the failure probabilities of bridges 1–3 are significantly higher for earthquakes on source 3 than for earthquakes on other sources. These bridges are important for maintaining connectivity between cities A and B and the hospital.

Max-propagation is also useful for system identification. Table 8.2a shows the most probable configuration of component states corresponding to the case where node $A \rightarrow H$ is in the failure state, i.e., city A is disconnected from the hospital. It implies that disconnect of city A from the hospital is mostly likely to result from the failure of bridges 1 and 3. This result is based on the approximate max propagation algorithm in GeNIe (Yuan et al. 2004). The most probable configuration is useful in identifying the most vulnerable components or subsystems to cause failure of the infrastructure system in a future earthquake. Furthermore, Table 8.2b shows the

most probable joint configuration of the nodes that describe the source: the most probable event to disconnect city A from the hospital is a 5.5–6.0 magnitude event on source 3 with epicenter located 30–35 km from the end of the fault and rupturing 0–5 km to the right. This rupture is located near the bridges whose failures are the most likely to result in disconnect of city A from the hospital. Such information is useful in identifying system vulnerabilities and dangerous earthquake scenarios.

Table 8.2: Most probable node state configuration of (a) component states and (b) source characteristics for evidence scenario in which city A is disconnected from the hospital

(a)	
Component	State
1	Failure
2	Survival
3	Failure
4	Survival
5	Survival
6	Survival

(b)	
Node	State
Source	Source 3
Magnitude	5.5-6.0
Rupture length	0-5 km
Epicenter location	30-35 km
Rupture reference coordinate	30-35 km

8.2.5 Using BNs in post-event applications

We have demonstrated the value of using the information-updating capabilities of BNs for understanding hazards at individual sites as well as at the system level. Next, we demonstrate how the information-updating capabilities are useful in near-real-time applications. (We consider post-earthquake decision-making more extensively in example 2.) To illustrate the information-updating capabilities of BNs, we consider seven post-earthquake evidence cases (ECs):

- EC 1: No evidence
- EC 2: $S_{A,1} = 0.3\text{--}0.35 g$
- EC 3: $S_{A,1} = 0.55\text{--}0.60 g$
- EC 4: Earthquake on source 2, $M = 6.5\text{--}6.6$, $X_{epi} = \text{center of fault}$
- EC 5: Earthquake on source 2, $M = 6.5\text{--}6.6$, $X_{epi} = \text{center of fault}$, $S_{A,1} = 0.3\text{--}0.35 g$
- EC 6: Earthquake on source 2, $M = 6.5\text{--}6.6$, $X_{epi} = \text{center of fault}$, $S_{A,1} = 0.55\text{--}0.60 g$
- EC 7: Earthquake on source 2, $M = 6.5\text{--}6.6$, $X_{epi} = \text{center of fault}$, C_1 in failure state

where $S_{A,1}$ is the spectral acceleration at site 1. The first evidence case is the baseline unconditional scenario in which no information is available other than the occurrence of the earthquake. Evidence cases 2 and 3 correspond to the situation in which an observation has been made of ground motion intensity at site 1 (e.g., from a recording instrument), but no source information is available about the earthquake. Evidence cases 4–6 include information about the earthquake source and, in cases 5 and 6, additional information about the ground motion intensity at site 1. Evidence case 7 replaces the measurement of ground motion intensity with an observation of structural performance. Figure 8.19 shows the distributions of spectral accelerations at sites 2, 4, and 6 under evidence cases 1–3.

In Figure 8.19, the distributions of ground motion intensity for all three sites are shifted toward higher values when the intensity is observed at site 1. However, the observation has the strongest influence on site 2, which is near site 1. This pronounced influence results from the way in which the observation updates the distributions of earthquake location parameters as well as the random field model. The observation of ground motion intensity at site 1 updates the BN in the backwards direction. The observed intensity at node S_1 updates the probability distributions of the unobserved source terms (X_e , X_r , and R_L) as well as the random field model. Figure 8.20 shows the updated distribution of the location parameters given information about the ground motion intensity at site 1. Evidence case 2 shifts the distribution of node S_C to reflect the increased likelihood that the earthquake occurs on source 3 (the source nearest site 1). The shift is more pronounced for the third evidence case than the second evidence case. Furthermore, for evidence cases 2 and 3, the distributions of the epicenter location and the rupture reference coordinate reduce in entropy and become more peaked at values near the center of the fault. The distribution of the rupture length also shifts toward higher values.

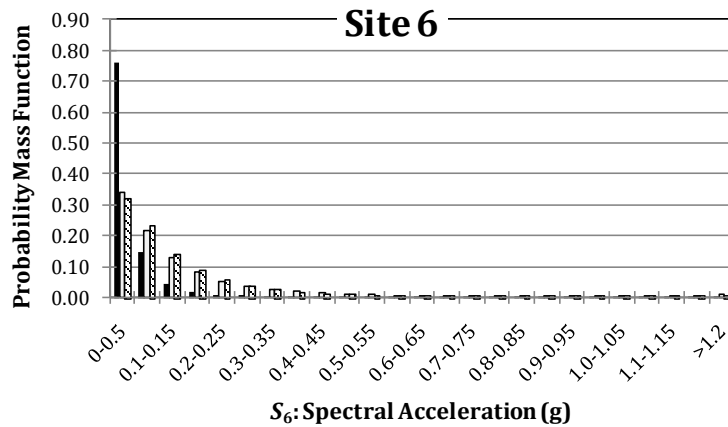
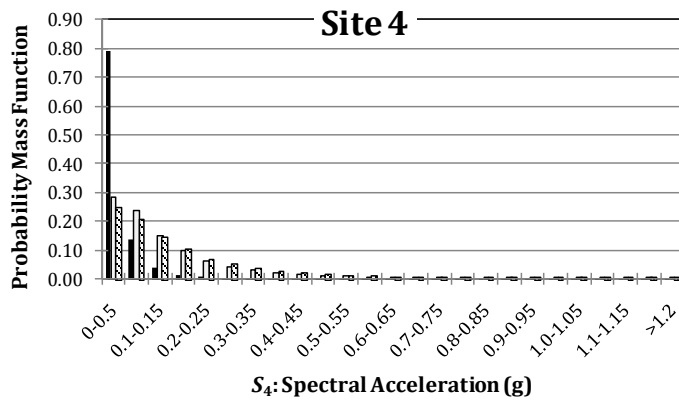
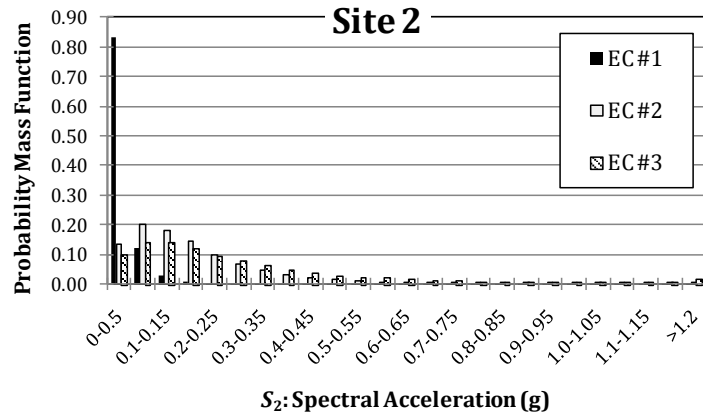


Figure 8.19: Distribution of spectral acceleration at sites 2, 4, and 6 for evidence cases 1–3

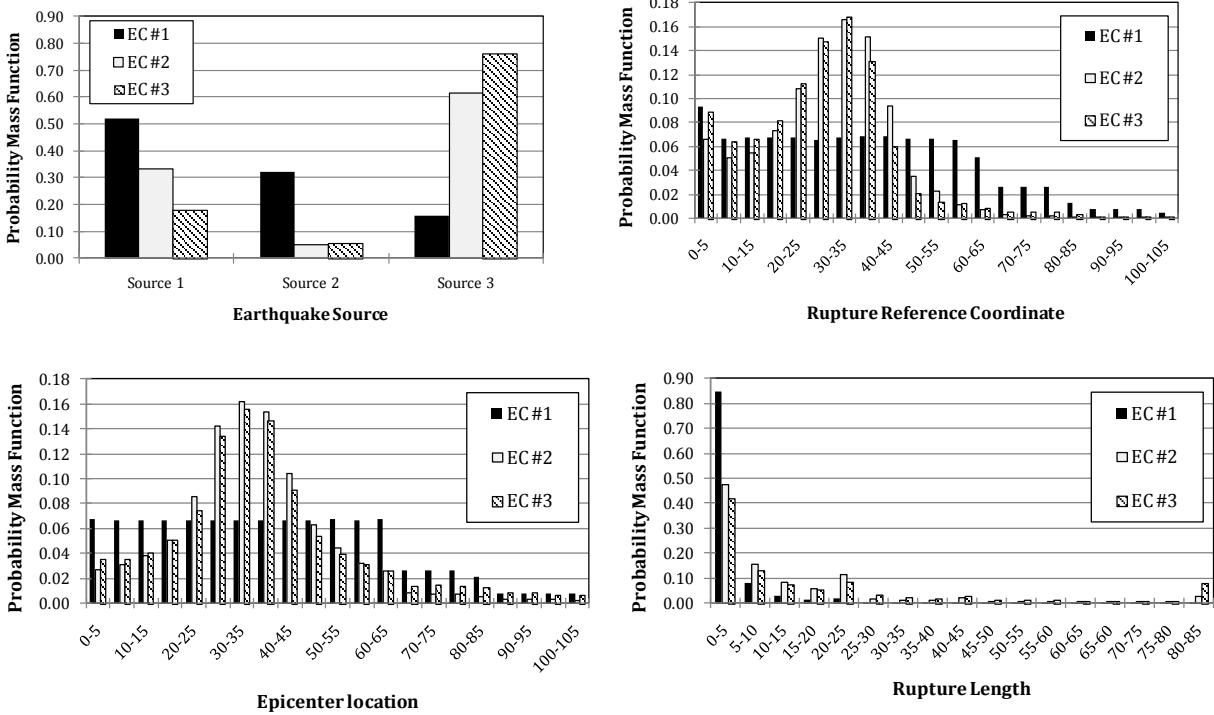


Figure 8.20: Distributions of earthquake location parameters for evidences cases 1–3

The effect of the observation of ground motion intensity at site 1 on the intra-event error terms of the random field for sites 1, 2, 4, and 6 is shown in Figure 8.21. The distribution of $\varepsilon_{r,1}$ shifts strongly to the right as a result of the observed high level of ground motion intensity at site 1. A similar though less pronounced trend is observed for $\varepsilon_{r,2}$. The effect of the observation on the distribution of $\varepsilon_{r,4}$ and $\varepsilon_{r,6}$ is negligible. The approximate random field model is shown in Figure 8.22. Note that sites 1–3 are linked by a common U -node, as are sites 5 and 6. All sites are linked by node U_2 . Obviously, an observation at site 1 has a stronger effect on the intensity at sites with which it shares multiple U -nodes than at sites linked to it by only one information path.

Figure 8.23 shows the updated distributions of ground motion intensities at sites 2, 4, and 6 for evidence cases 4–7. The distribution at all sites shifts to the right based on the observation of only source characteristics (EC 4). The distribution shifts further to the right when the ground motion intensity at site 1 is observed to be larger than expected (ECs 5 and 6). Observation of failure of component 1 (EC 7) shifts the distribution to the right relative to EC 4, though not as

far as for EC 6. The updated distribution of ground motion intensity at site 1, given that component 1 fails, is shown in Figure 8.24. The peak of this distribution is at a value lower than the state 0.55–0.6 g . Recall that the mapping between component performance and ground motion intensity is uncertain. Therefore, the observation of component performance is less informative to the seismic demand model than a direct observation of ground motion intensity.

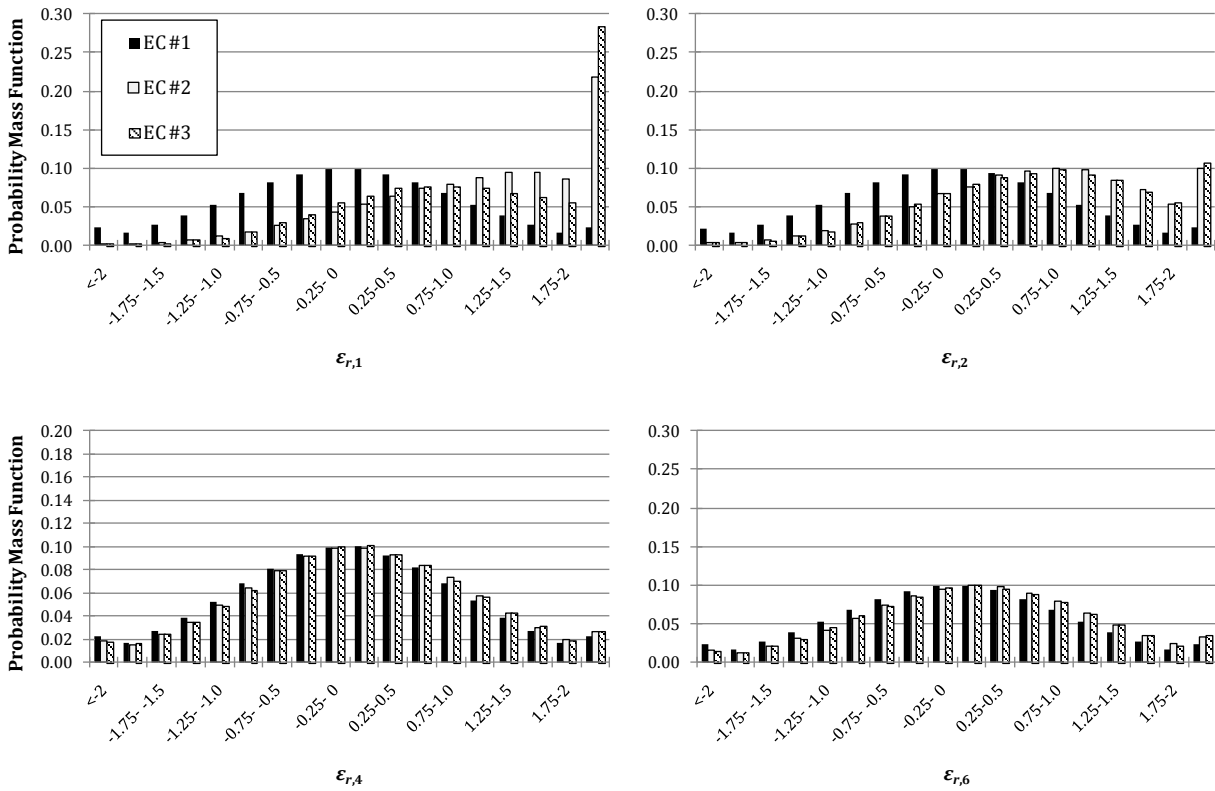


Figure 8.21: Distributions of random field intra-event error terms for evidence cases 1–3

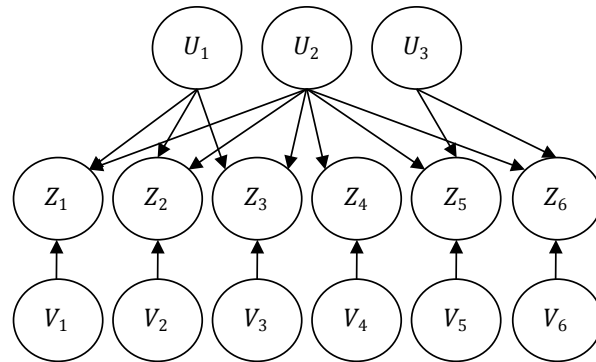


Figure 8.22: Approximate random field model

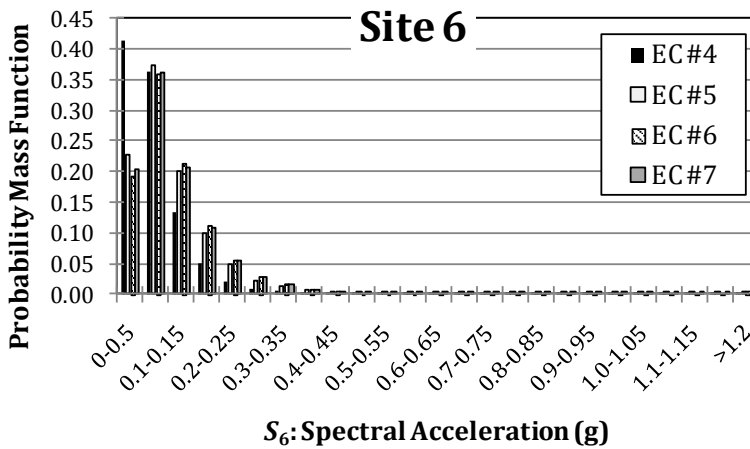
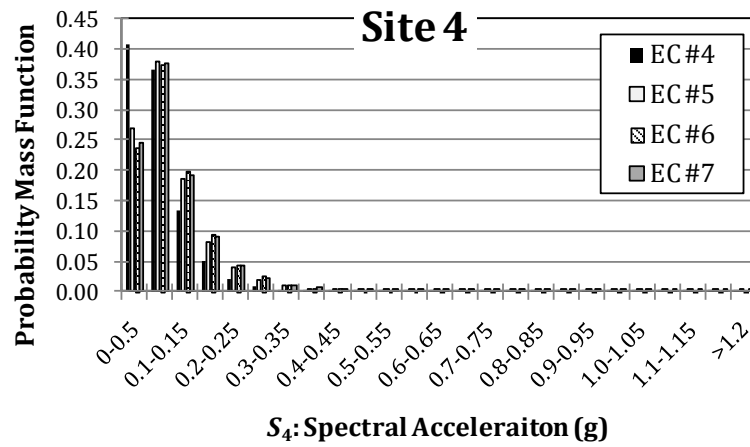
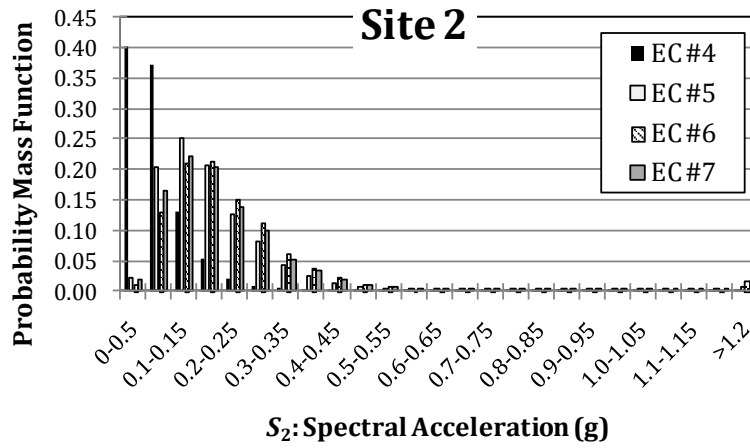


Figure 8.23: Distributions of spectral accelerations at sites 2, 4, and 6 for evidence cases 4–7

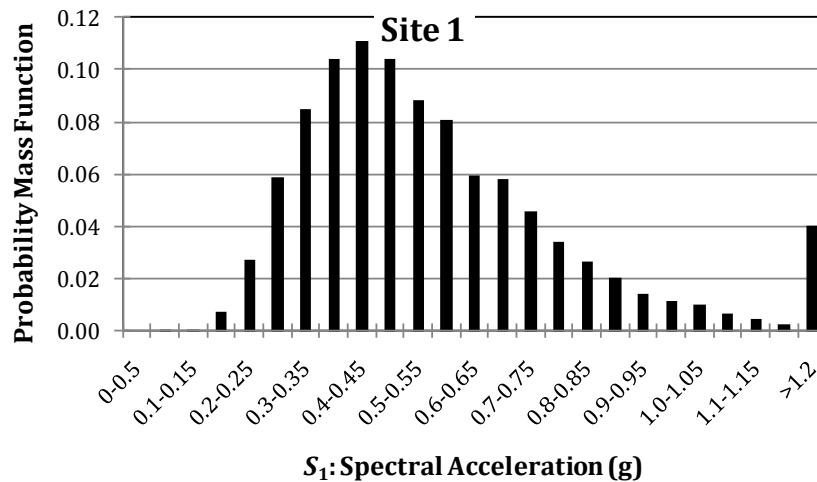


Figure 8.24: Distribution of spectral acceleration at site 1 for evidence case 7

8.3 Example 2: Proposed California high-speed rail system

The proposed California high-speed rail (HSR) system is currently in the early stages of development under the guidance of the California High-Speed Rail Authority (CA HSR 2010). The proposed system will initially link San Francisco and Los Angeles in approximately 2.5 hours and connect intermediate cities along the route. It will later be expanded to other major cities, such as San Diego and Sacramento. The system is situated in a highly seismic region, and thus earthquakes pose a significant risk to the system. Figure 8.25 shows the proposed alignment of the northern portion of the HSR system (in blue) as well as known faults in the region (in red) (Bryant 2005). In this example, we focus on the portion of the system between San Francisco and Gilroy, California.

Through sound engineering and decision-making, it is possible to mitigate risks posed to the HSR system by seismic hazard. In this example we focus on hazard assessment and decision-making in the immediate aftermath of an earthquake. Often, at this stage, emphasis is placed on life safety (e.g., stopping the train to avoid derailment) and restoration of critical services (e.g., providing electricity to ensure trains can reach stations to aid evacuees). Post-event decisions include the dispatching of rescue, inspection, and repair crews as well as decisions to shut down

or continue component and system operations. These decisions are made under the competing demands to maintain operability (to prevent revenue loss), while not sacrificing safety (to avoid deaths and injury and consequent liability). In the environment of the post-event decision phase, information is both uncertain and quickly evolving. Sources of information at this phase may include ground motion intensity measurements, structural health monitoring sensors, inspection results, and observations reported by various people. This section provides an overview of the BN models developed for this purpose and their preliminary application to the proposed California HSR project.

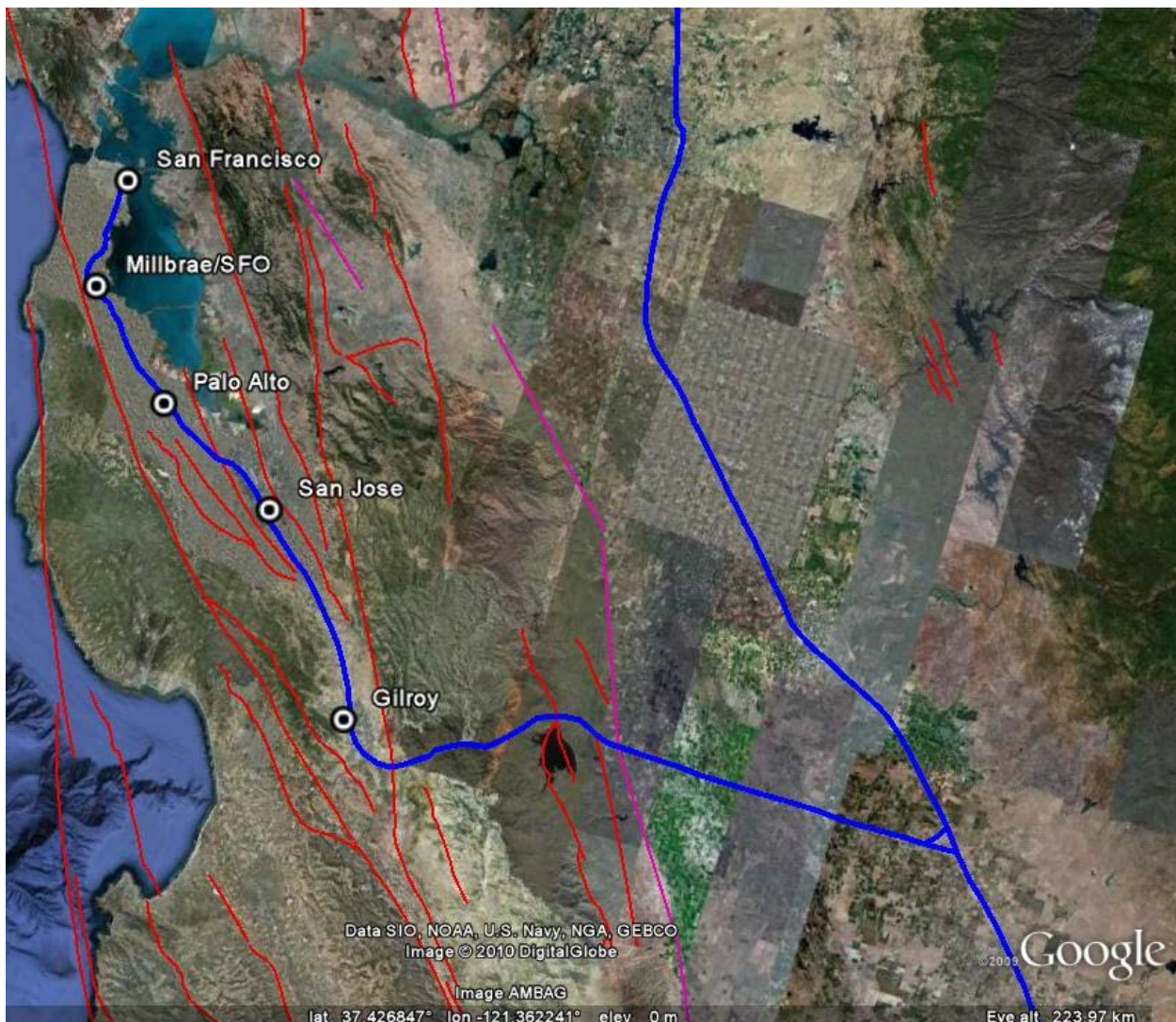


Figure 8.25: Google Earth map of northern California portion of proposed California High-Speed Rail system route (blue) (CA HSR 2010) and nearby faults (red and pink) (Bryant 2005)

Because the HSR system is in an early stage of design, data about the system (including specific component types, ground conditions, and finalized alignment) are not available. The analysis here is largely based on assumptions about the system, and all results must be treated as hypothetical. All assumptions contained in this report should be considered preliminary “placeholders” that are used because information is currently scarce. Nonetheless, the study illustrates the power of the BN approach for infrastructure seismic risk assessment and provides a general framework that can be adapted when more specific information becomes available. This example also draws attention to areas where further research and development are needed.

8.3.1 Model assumptions

There are three major faults in the vicinity of the portion of the HSR system under consideration in this study: the Hayward fault, the Calaveras fault, and a portion of the San Andreas fault. The faults are idealized as straight or broken line segments, as shown in Figure 8.26. If more detailed fault geometry is available and required, the framework can be extended to include it. In that case, modifications need only be made to the evaluation of the CPTs, which are generated external to the BN using Monte Carlo simulation, as described in Chapter 2. All calculations performed in this section are based on exact inference using Hugin (Hugin Expert A/S 2008).

For each fault, source-dependent distributions of magnitudes and epicenter locations are assumed. Fault parameters are available in the Caltrans fault parameter database (Caltrans 2007). The Wells and Coppersmith (1994) model is used to define the rupture length on the fault as a function of the earthquake magnitude and source characteristics. The Campbell and Bozorgnia (2007) NGA attenuation relationship is used to describe the ground motion intensity at each site as a function of source and site characteristics. Various components in the system are sensitive to different measures of ground motion intensity. The seismic demand BN model thus has nodes representing spectral acceleration, peak ground acceleration, and peak ground velocity. We use the model by Shahi and Baker (2010) to describe the directivity effects on spectral acceleration. For peak ground velocity, we use a prediction equation developed by Bray and Rodriguez-Marek (2004), which incorporates the effect of directivity. The site shear velocity for all sites is in the range 250–325 m/s.

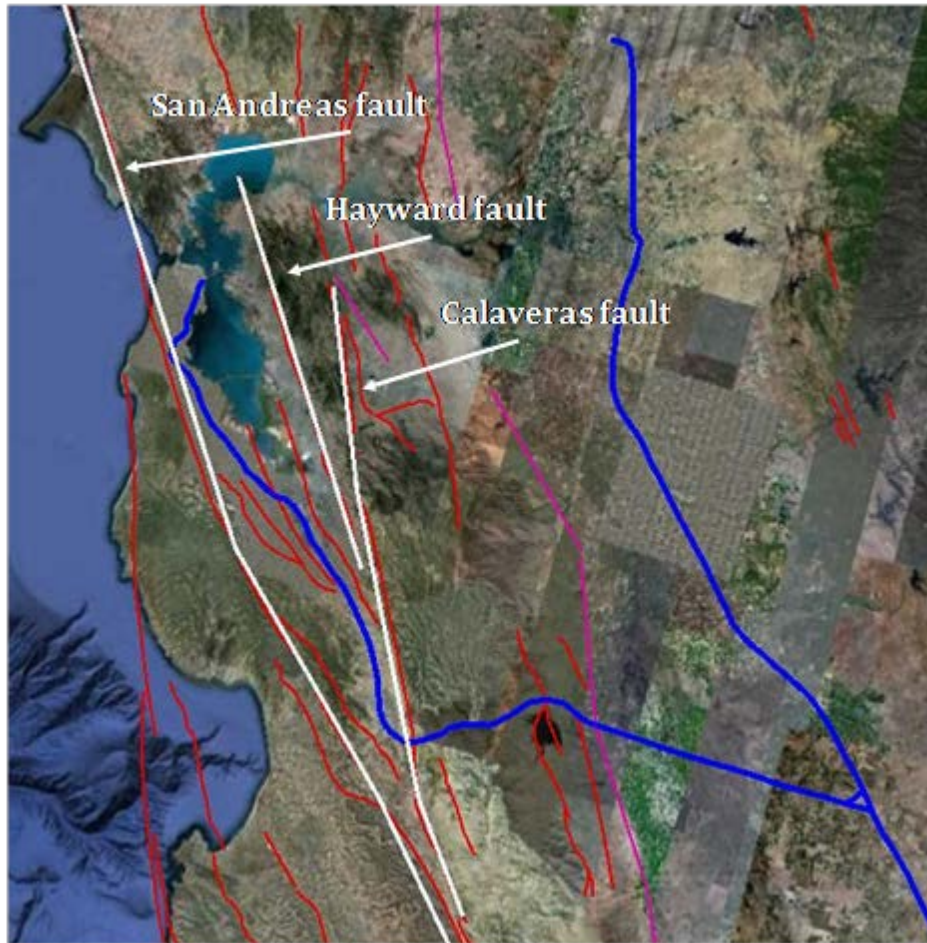


Figure 8.26: Google Earth map with idealizations of Calaveras, Hayward, and a portion of the San Andreas faults

For each fault, the geometry of the geographic region and of the infrastructure system is defined within a local coordinate system with the origin at one end of the fault and the x -axis oriented along its first linear segment. In this coordinate system, the epicenter is defined as a point along the fault. The rupture is assumed to occur anywhere along the fault with uniform likelihood, while containing the epicenter and not extending beyond the known ends of the fault. For a given rupture on a fault, the source-to-site distance R_i is obtained as described in Chapter 3. Site and fault coordinates are considered deterministic.

The 18 GMPPs in the HSR system are shown in Figure 8.27, and the approximated random field BN model is shown in Figure 8.28. We use an approximated model with few links to ensure

computational tractability. Because the HSR is a series system, its reliability is relatively insensitive to approximations in the correlation matrix, so that we are able to eliminate many nodes and links (see Chapter 4). Thus, in the resulting BN, only relatively closely spaced GMPPs are linked through common U -nodes.

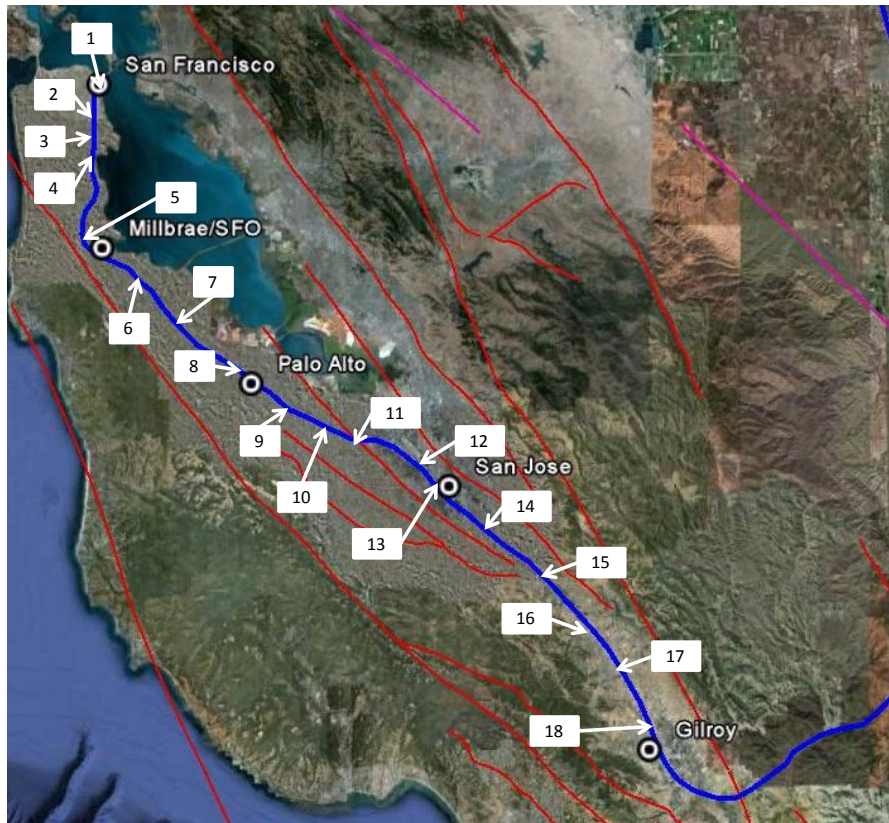


Figure 8.27: Ground motion prediction points along HSR alignment

Aside from ground shaking, other earthquake-related hazards potentially affecting the HSR system include fault rupture where segments cross active faults; liquefaction and lateral spreading of saturated sandy soils; stability of slopes, embankments, retaining structures, and tunnels that are affected by various aspects of the ground motion; and the spatial variability of the ground motion on extended components such as the rail line or long-span bridges. BN models in this example focus on ground shaking; models for some of the other hazards are briefly discussed in Chapter 3, but their full development and application are left as areas warranting future study.

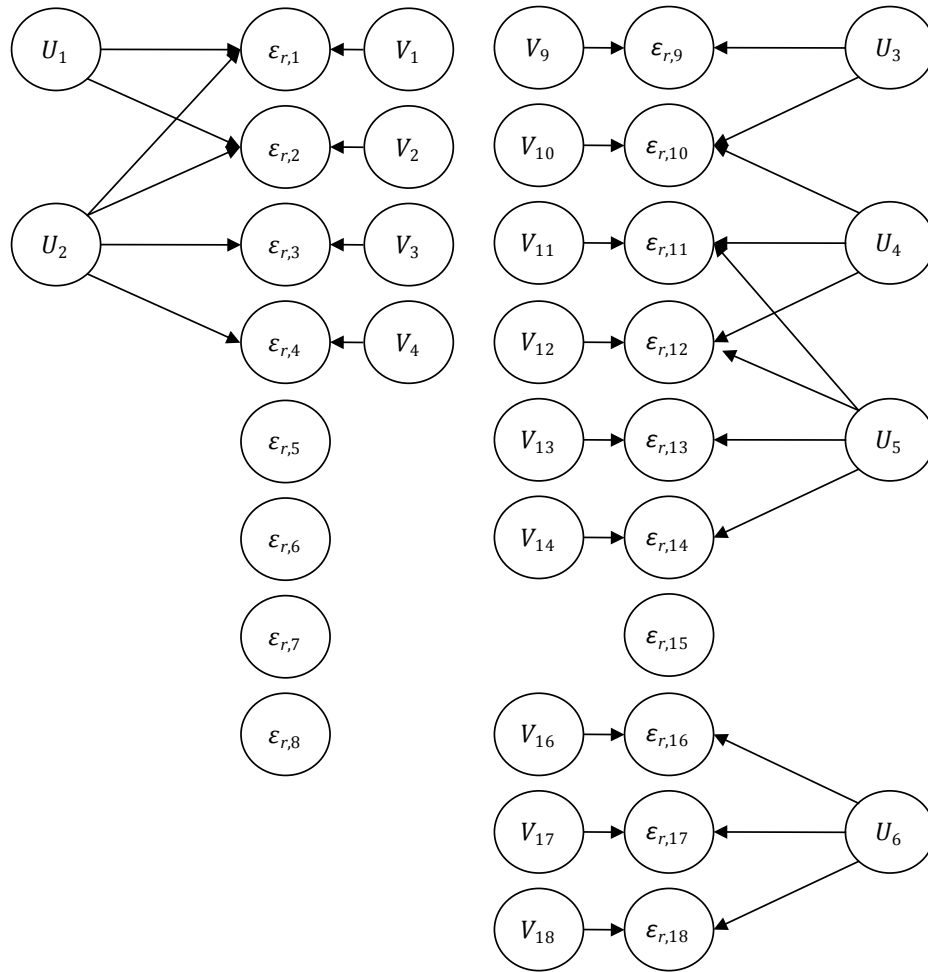


Figure 8.28: Approximated random field model for HSR

The HSR system consists of two general classes of components. Point-site components include short-span bridges over small waterways or roads, culverts, and station buildings; distributed-site components include rail tracks, long embankments, aerial structures, and tunnels. At this stage, little is known about the locations of the point-site components in the system, and we have only crude estimates of the locations of the distributed components, as shown in Figure 8.29. The assumed discretized component types are listed in Table 8.3 along with their estimated length and associated GMPPs. The idealizations contained in this table are extremely crude. Significant modification and expansion will be necessary when more detailed information becomes available.

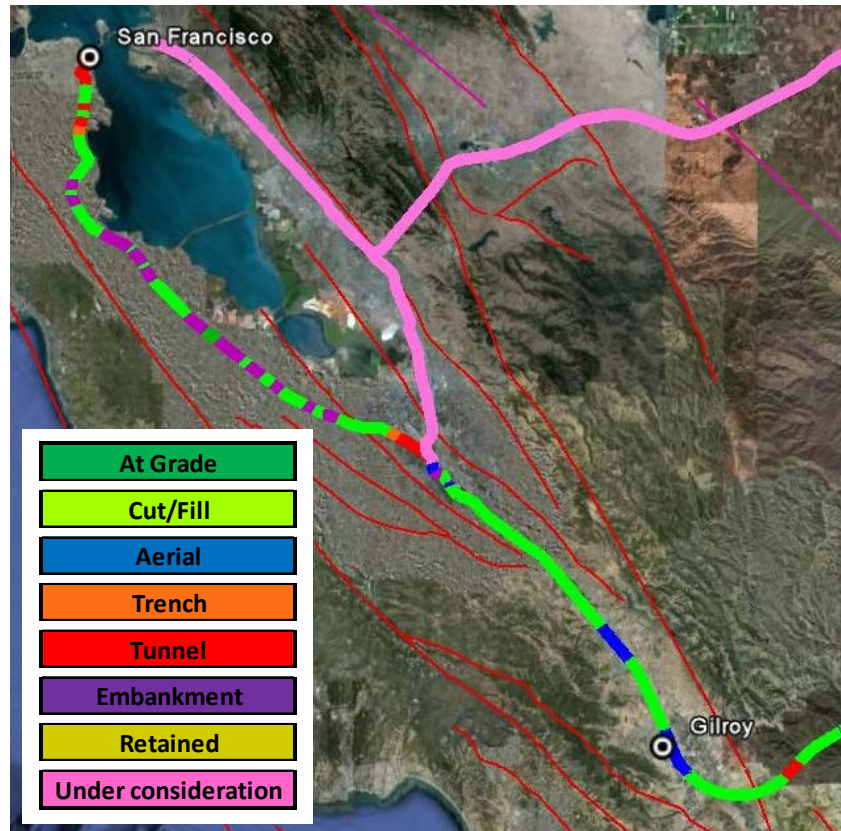


Figure 8.29: Locations of major distributed components of HSR alignment (CA HSR 2010)

As little is known about the final structural or geotechnical systems to be employed for the HSR system, broad assumptions are made about the fragility/performance functions for the components listed in Table 8.3. Thus, the functions used in this example should be regarded as placeholders that must be replaced when more specific component descriptions and corresponding fragility/performance models become available. Simple fragility models for the structural systems (tunnels and aerial structures) are adapted from HAZUS^{MH} (DHS 2003). The HAZUS^{MH} fragility functions are developed for standard highway systems; however, the HSR system will be designed with more rigorous performance criteria. Furthermore, the HAZUS^{MH} fragility functions include a large amount of uncertainty to account for the broad class of structural systems to which they are applied. As such, the associated fragility functions are not directly applicable to the HSR. To account for the more rigorous design standards and quality control of the HSR, HAZUS^{MH} fragility functions are modified by increasing the median resistance and reducing the standard deviation.

Table 8.3: Assumed component types, length, and associated GMPPs of the HSR

Component	Type	Length (km)	GMPP(<i>i</i>)	GMPP(<i>i</i>+1)
1	Tunnel	4.0	1	2
2	Embankment	2.7	2	3
3	Tunnel	3.5	3	4
4	Embankment	8.8	4	5
5	Embankment	8.7	5	6
6	Embankment	8.4	6	7
7	Embankment	8.8	7	8
8	Embankment	8.8	8	9
9	Embankment	7.7	9	10
10	Embankment	6.9	10	11
11	Tunnel	6.0	11	12
12	Aerial	point	12	-
13	Embankment	2.7	12	13
14	Aerial	point	13	-
15	Embankment	8.1	13	14
16	Embankment	9.0	14	15
17	Embankment	8.9	15	16
18	Aerial	5.5	16	17
19	Embankment	9.5	17	18

Most fragility functions developed for bridges and tunnels are applicable only to point-site structures and do not account for spatial variability of the ground motion intensity along the structure. Analysis of structures subjected to differential ground motions is an area of developing research (Kim and Feng 2003; Konakli and Der Kiureghian 2010). Absent fragility curves specifically for the structures employed by the HSR system, we must make simplifying assumptions to develop the overall framework and produce illustrative (though hypothetical) results. For the present analysis, we estimate the performance of tunnels and aerial structures distributed between GMPPs i and $i + 1$ as

$$p_{i,i+1}^k(s_i, s_{i+1}) = F_k^i(\max(s_i, s_{i+1})) - F_{k+1}^i(\max(s_i, s_{i+1})), \quad (8.6)$$

where $p_{i,i+1}^k(s_i, s_{i+1})$ denotes the probability that the component between GMPPs i and $i + 1$ will experience damage of state k , and $F_k^i(\cdot)$ is the fragility model associated with damage state

k (see Chapter 5). The embankment segments are PGV-sensitive and are modeled using fragility functions adapted from the literature (Mizuno et al. 2008). These models provide conditional rates of damage per unit length, from which fragility functions are developed by use of the nonhomogeneous Poisson model as described in Chapter 5. In the absence of fragility functions for the cut-fill geotechnical systems, we use embankment fragility functions for these components.

Neglecting infrastructure interdependencies (e.g., the dependence of the HSR system on the electrical grid) and assuming that tracks going in either direction are associated with the same supporting structures, the HSR can be considered as a series system. We provisionally assume that components of the system have three states: not damaged, slightly damaged, and moderately to severely damaged. Components that are not damaged are assumed to be fully operational. Slight damage is associated with reduced performance (e.g., the trains must slow down when traversing the component), and moderate to severe damage is associated with complete component closure.

In this analysis, the system failure event is defined as the inability to reach Gilroy from San Francisco. However, we assume that if a portion of the alignment is not passable, passengers use alternative transportation to bypass the damaged segment and board the train further down the line to complete the journey to Southern California. With this in mind, four intermediate failure events are considered: Inability to travel from (1) San Jose to Gilroy, (2) Palo Alto to Gilroy, (3) Millbrae to Gilroy, and (4) San Francisco to Gilroy. The train is unable to travel from San Jose to Gilroy at normal speed if any component along this segment is damaged, and connectivity is completely lost if any component experiences moderate or severe damage. Connectivity between Palo Alto and Gilroy is lost if any component between Palo Alto and San Jose is moderately or severely damaged or connectivity is lost between San Jose and Gilroy. By extension to the other segments, connectivity between San Francisco and Gilroy is possible if no component between San Francisco and Millbrae (or Millbrae and Palo Alto) is moderately or severely damaged and connectivity is not lost somewhere farther down the line. The resulting BN for modeling the HSR system performance shown in Figure 8.30. Because this is a series system, the efficient formulation is constructed directly as described in Section 6.5.1 without requiring use of the optimization algorithm.

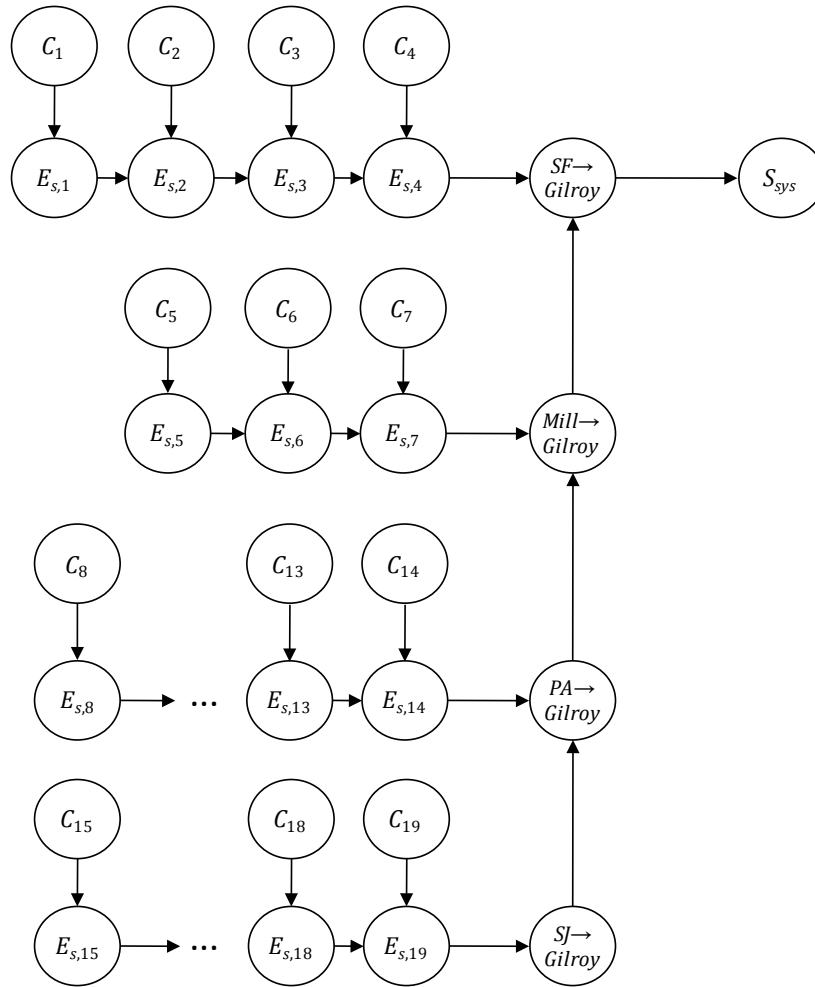


Figure 8.30: BN modeling system performance of HSR

In Figure 8.30, nodes “city-name” → *Gilroy* indicate whether connectivity exists between the indicated city and *Gilroy*. Node *SJ* [San Jose] → *Gilroy* is in an open (reduced/closed) state if node $E_{s,19}$ is in open (reduced/closed) state. Node *PA* [Palo Alto] → *Gilroy* indicates full capacity connectivity between Palo Alto and *Gilroy* only if node *SJ* → *Gilroy* and $E_{s,14}$ both are in the open (full capacity) state. Similarly node *PA* → *Gilroy* indicates loss of connectivity if node *SJ* → *Gilroy* or $E_{s,14}$ are in the closed state. Otherwise, node *PA* → *Gilroy* indicates the reduced capacity state. The CPTs of nodes *Mill*[brae] → *Gilroy* and *SF* → *Gilroy* are constructed similarly.

Next, we extend the BN by decision and utility nodes to begin to address the post-earthquake inspection-shutdown decision problem, as described in Chapter 7. When more information becomes available about the HSR system and the preferences of the system decision-makers, the decision framework described here must be modified and expanded. For now, we present a first attempt at developing a post-earthquake decision-framework for the HSR system. Preliminarily, it is assumed that the shutdown decision will happen at the link level, where a link is the set of components located between stations. Link 1 connects San Francisco to Millbrae and contains components 1–4, link 2 extends from Millbrae to Palo Alto and includes components 5–7, link 3 connects Palo Alto and San Jose and contains components 8–14, and link 4 is between San Jose and Gilroy and contains components 15–19. For reference in the following description, the LIMID corresponding to the decision model for link 1 is shown in Figure 8.31. LIMIDs for the other links are similar and are thus not shown here. Note that the decision problem described here considers each link as a separate system rather than considering the entire system simultaneously. Inspection decisions are made at the link as well as component levels. Decision-making at the entire system level proved to be computationally impossible with the Hugin software application and our computing resources. In any case, decision-making at the link level is reasonable because a given earthquake is likely to affect only one link, and because it is likely that separate inspection and repair crews will be available for the separate links and, hence, decisions can be made locally.

The decision framework described in Chapter 7 is applied to the LIMID for link 1 with a few modifications. In the modified decision framework, the component-level inspection-shutdown decision is replaced by a link-level decision, as shown by the nodes *Shutdown Link 1?* and *Inspect Link 1?*. Node *Shutdown Link 1?* is a parent of the link performance object with conditional relationships defined such that link 1 is closed (has reduced operating level) if any component is moderately or severely damaged (slightly damaged), or a decision is made to shut down (reduce the operating level of) the link. The decision node is also a parent of nodes L_i , which model component liabilities. Node *Inspect Link 1?* is a parent of the node that represents the link-level shutdown decision to indicate decision precedence. It is also a parent of nodes *Inspect Comp $i?$* , $i = 1, \dots, 4$, which represent component-level inspection decisions. Here, we assume that component-level inspections are prioritized after a link has been chosen for

inspection. (Alternative heuristics for prioritizing component inspections can be easily considered.) Nodes O_i and IC_i are children of the component-level inspection decisions, consistent with the descriptions in Chapter 7.

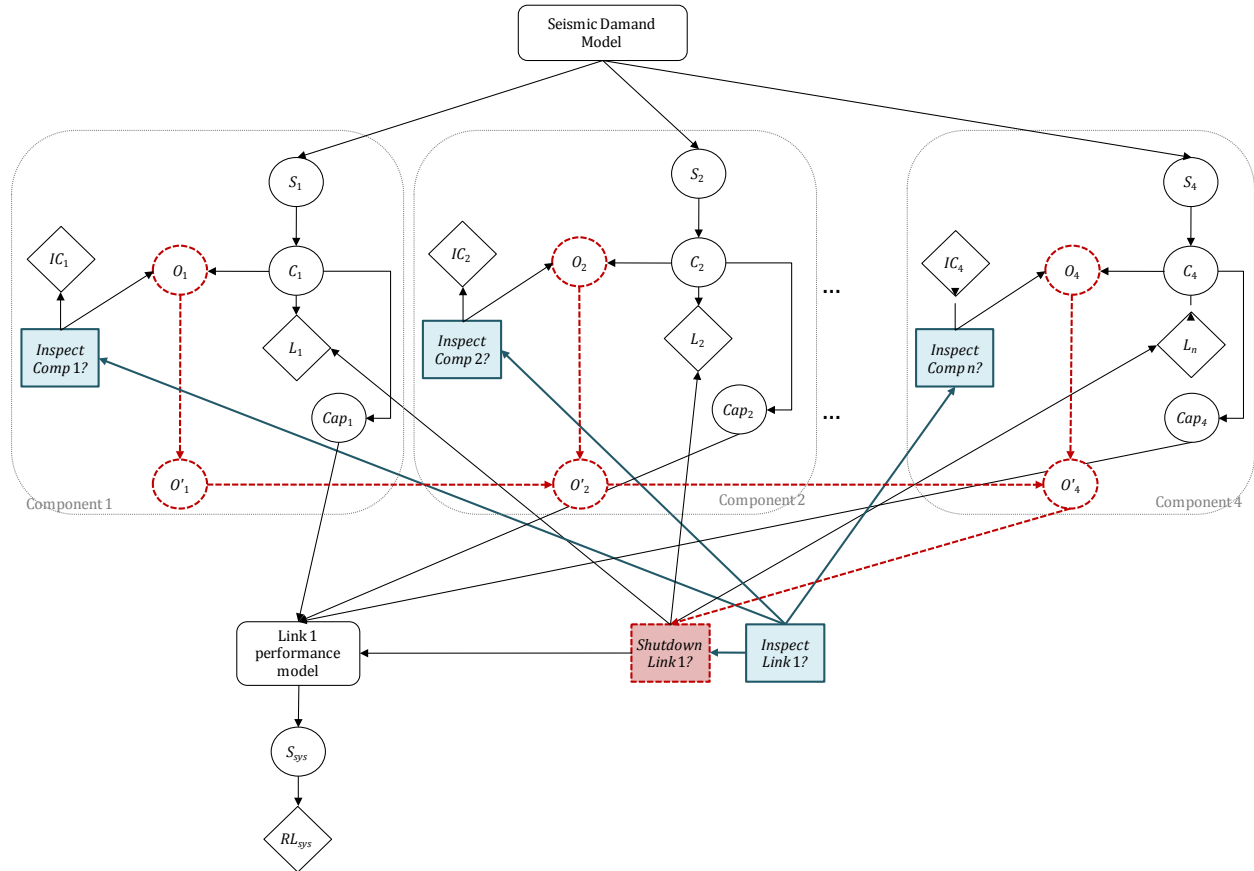


Figure 8.31: LIMID for solving inspection-shutdown decision for link 1 of HSR system

To indicate information precedence, it is necessary to include links that signify that, if inspections are made, the inspection results (i.e., the outcomes of nodes O_i) are known before the shutdown decision is made. Including all nodes O_i as parents of node *Shutdown Link 1?* results in an inefficient converging structure. Instead, the converging structure is replaced by a chain structure of nodes O'_i as shown in dashed lines in Figure 8.31. Each node of the chain indicates the worst damage state that is observed along the link up to that node, analogous to the logic used to construct the efficient MLS formulation in Chapter 6.

For this example, inspection costs and liabilities (in an arbitrary unit of utility) are defined as a function of component type and length and are summarized in Table 8.4. The penalties

associated with closing a link are defined as a function of the number of components along the link. This is a proxy for revenue lost as a function of shutting down the component, e.g., due to lost passengers, and costs such as running a bus bridge around the closed link. The link closure costs are defined as 10 times the number of components located along the link. The penalty associated with reducing the capacity of the link is assumed to be 10 units, regardless of the number of components comprising the link.

Table 8.4: Assumed component inspection costs and liabilities

Component	Type	Length (km)	Inspection Cost (imperfect)	Inspection Cost (perfect)	Liability (open when damage is slight)	Liability (open when damage is moderate or worse)	Liability (reduced when damage is moderate or worse)
1	Tunnel	4.0	0.080	0.160	6.00	600	60.0
2	Embankment	2.7	0.027	0.054	1.35	135	13.5
3	Tunnel	3.5	0.070	0.140	5.25	525	52.5
4	Embankment	8.8	0.088	0.176	4.40	440	44.0
5	Embankment	8.7	0.087	0.174	4.35	435	43.5
6	Embankment	8.4	0.084	0.168	4.20	420	42.0
7	Embankment	8.8	0.088	0.176	4.40	440	44.0
8	Embankment	8.8	0.084	0.168	4.40	440	44.0
9	Embankment	7.7	0.077	0.154	3.85	385	38.5
10	Embankment	6.9	0.069	0.138	3.45	345	34.5
11	Tunnel	6.0	0.120	0.240	9.00	900	90.0
12	Aerial	point	0.0005	0.001	2.50	250	25.0
13	Embankment	2.7	0.027	0.054	1.35	135	13.5
14	Aerial	point	0.0005	0.001	2.50	250	25.0
15	Embankment	8.1	0.081	0.162	4.05	405	40.5
16	Embankment	9.0	0.090	0.180	4.50	450	45.0
17	Embankment	8.9	0.089	0.178	4.45	445	44.5
18	Aerial	5.5	0.905	1.810	13.75	1375	137.5
19	Embankment	9.5	0.095	0.190	4.75	475	47.5

8.3.2 Illustrative results

To illustrate the value of using BNs for immediate post-earthquake decision support, we consider the evolution of information following the occurrence of an earthquake. The result is a series of hypothetical results that are strongly influenced by the preliminary model assumptions. Consequently, the results may not accurately reflect the true system and hazard environment.

Suppose a 6.8 magnitude earthquake occurs with the epicenter located 30 km from the northern end of the Hayward fault. Following the earthquake, information becomes incrementally available to the decision-maker. For illustration, we show how predictions by the BN model evolve as three pieces of evidence become available. For reference, we refer to each stage of information acquisition as an evidence case (EC):

- EC 1: $M = 6.8$, $X_e = 30$ km (the base case)
- EC 2: EC 1 + spectral acceleration at GMPP 2 = 0.45–0.50 g
- EC 3: EC 2 + pulse-like ground motion at GMPP 9
- EC 4: EC 3 + extensive damage of C_{17}

We consider each of these ECs individually below.

Evidence case 1 corresponds to the information that will (likely) be available to the decision-maker from a source such as the United States Geological Survey almost immediately following the occurrence of an earthquake. The values reported initially are not certain, but in this example we treat these estimates of the magnitude and epicenter as deterministic quantities. (Uncertainty can be easily incorporated by adding two nodes in Figure 3.22.) In evidence case 2, a sensor at GMPP 2 indicates that the ground motion intensity (spectral acceleration) at that site was in the range 0.45–0.50 g (larger than expected for this event). This evidence is entered at the corresponding node and the information propagates throughout the BN. The observation updates the model in a forward direction: the known ground motion intensity provides a more accurate estimate of the failure probabilities of the associated components and therefore updates the system failure probabilities. This observation also provides information updating in the backward direction, updating the error terms in the ground motion intensity model, which in turn update the ground motion intensity distributions at GMPPs for which observations are not available. The distributions of ground motion intensities at GMPPs 1, 6, 11, and 16 are shown in Figure 8.32. At site 1, the distribution is shifted to the right relative to the distribution predicted for evidence case 1. This is due to the updating of the intra-event error random field ϵ_r and the common event error ϵ_m , shown in Figure 8.33. The distribution of the intra-event deviation for GMPP 1 (which is near the point of observation) is significantly shifted, but the distributions for more distant sites remain relatively unchanged due to loss of correlation of the random field with distance.

Also, note that the distribution of the intra-event error for GMPP 6 does not change in response to any observation at other GMPPs because it is independent of other sites in the approximated random field model (see Figure 8.28).

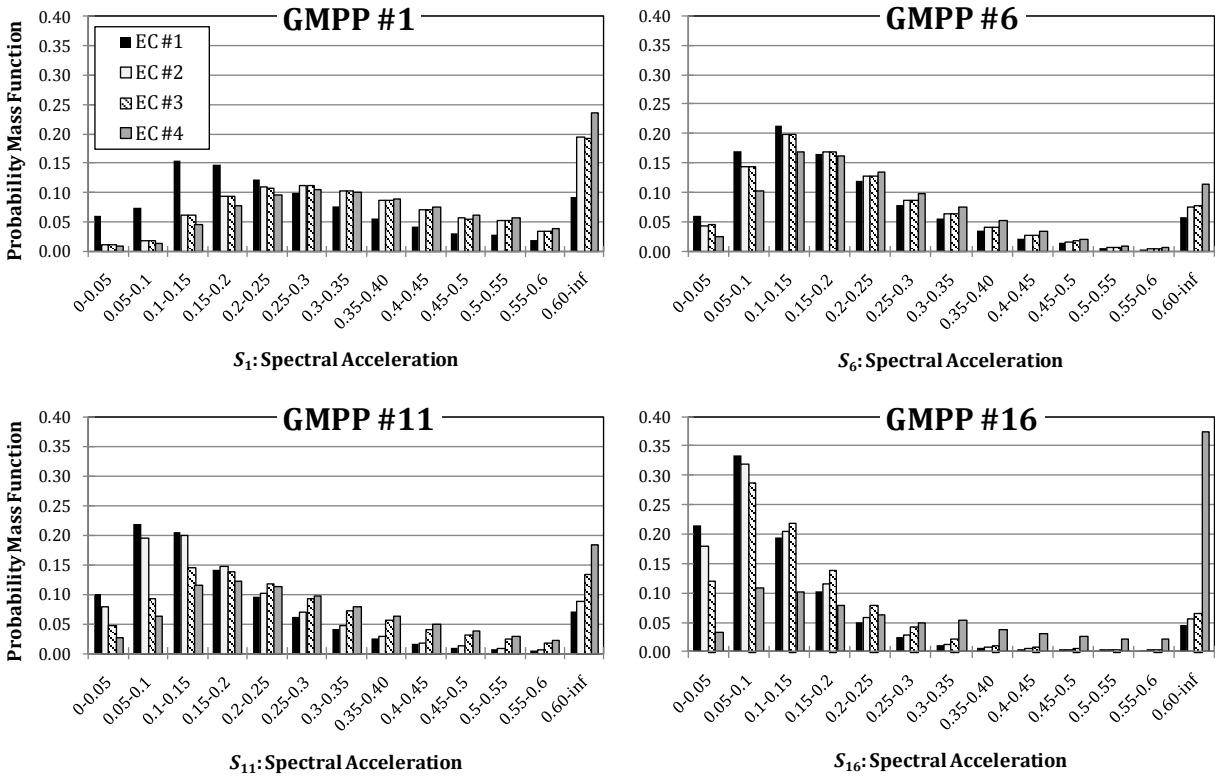


Figure 8.32: Distributions of ground motion intensities at GMPPs 1, 6, 11, and 16 for four evidence cases

In the third evidence case a partially processed ground motion record at GMPP 9 indicates the existence of a directivity pulse at that site, although the intensity could not be determined. In light of this information, the distributions of ground motion intensities at GMPPs 11 and 16 in Figure 8.32 shifted to larger values, and the distributions of the intra- and inter-event error terms were unchanged. The observation also updated the distributions of the parameters defining the location of the rupture on the fault (see Figure 8.34). The shifted distributions suggest a rupture that is longer (though assumed bounded at one-half the fault length) and that propagates more toward GMPP 9 than away from it. In turn, these updated distributions of source geometry

increase the probability that the ground motion at the southern sites in the system experienced directivity effects.

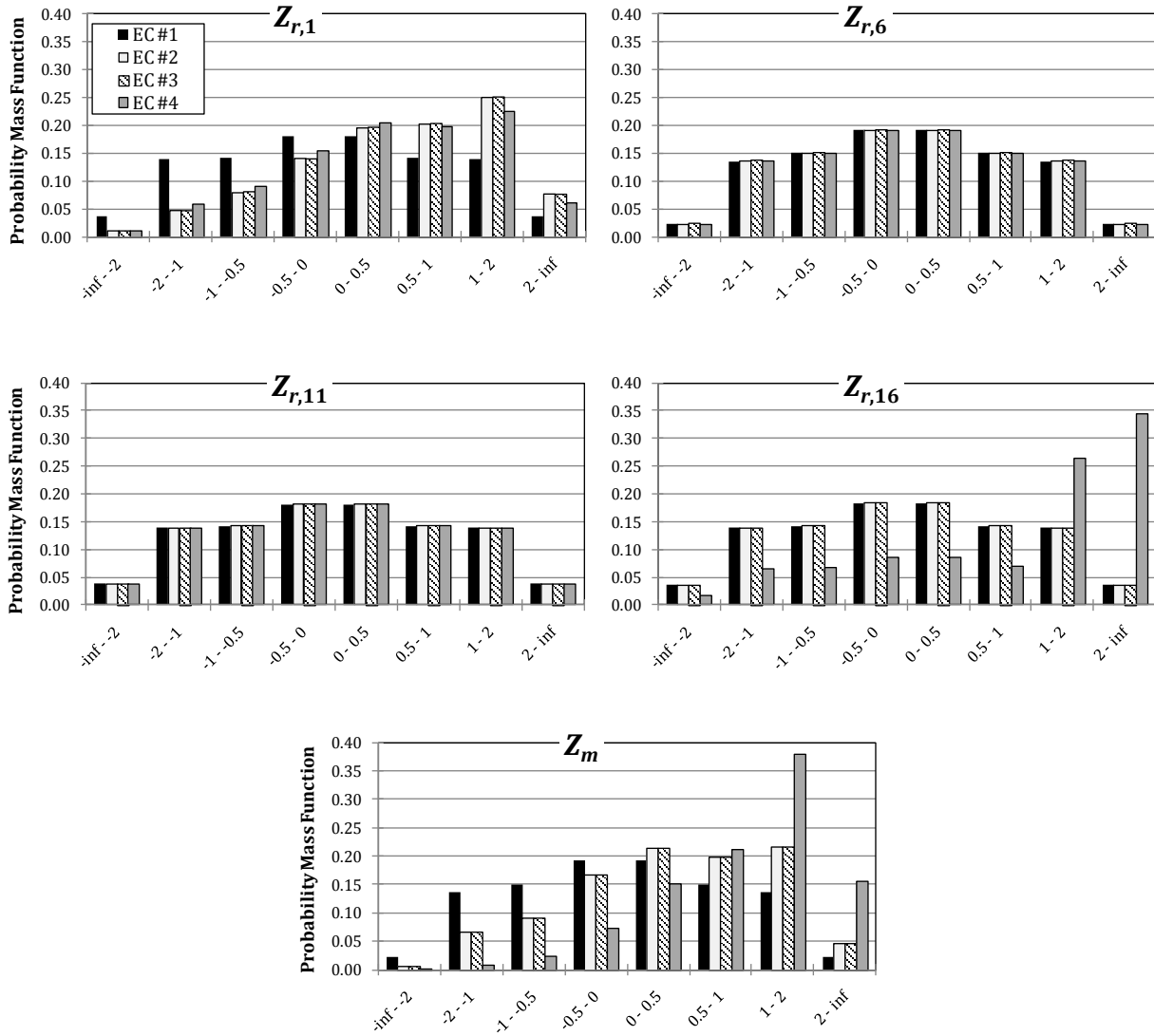


Figure 8.33: Distributions of normalized intra-event error terms ($z_{r,i} = \varepsilon_{r,i}/\sigma_{r,i}$) for GMPPs 1, 6, 11, and 16 and the normalized inter-event error term ($z_m = \varepsilon_m/\sigma_m$)

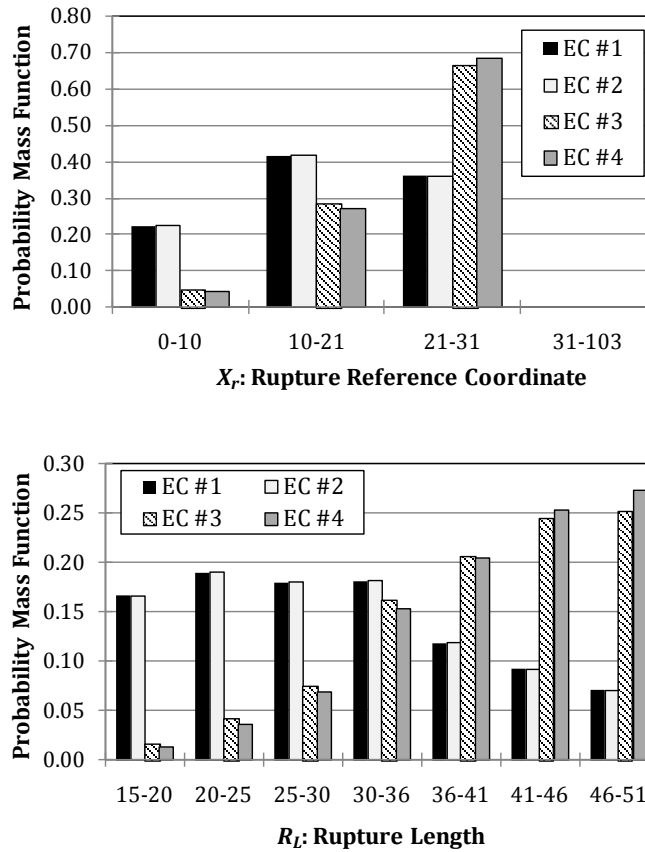


Figure 8.34: Distributions of parameters defining rupture location (X_r, R_L) for four evidence cases

Evidence case 4 represents a situation in which, for example, a structural health monitoring sensor or an inspector reports that component 19 (the aerial structure located closest to Gilroy) is extensively damaged. This information is entered in the BN and updates the probabilistic model in several ways. First, it provides forward updating by decreasing the system reliability in light of evidence that a component has failed. For this particular evidence scenario, the system reliability is zero because the damaged component interrupts connectivity between all cities and Gilroy. The observation also updates the model in the backward direction by shifting the distributions of ground motion intensities of GMPPs at either end of the component toward larger values. This in turn updates the complete seismic demand model providing updated distributions of ground motion intensities at other sites in the system. In particular, the observation updates the intra-event error terms at sites near the failed component, consistent with

the random field model. The inter-event error distribution is also updated in a significant way as the accumulation of evidence suggests higher than expected ground motion intensities at geographically dispersed locations. Consequently, the common inter-event error distribution shifts to the right to indicate that the ground motion prediction equations are systematically underpredicting intensities for all sites for this particular earthquake.

Table 8.5 shows the component state probabilities for the no-damage and moderate or severe damage states. (The probability of slight damage is computed as 1 minus the sum of these two probabilities.) Table 8.6 shows the system failure probabilities for the four evidence cases. When the BN framework is extended with decision and utility nodes, these updated probabilities are important for accurately determining optimal decisions based on expected utilities.

Table 8.5: Component state probabilities for states no damage and moderate or severe damage under different evidence cases

Component	EC #1		EC #2		EC #3		EC #4	
	No damage	Moderate or severe damage						
1	0.94	0.06	0.89	0.10	0.89	0.10	0.86	0.13
2	0.95	0.05	0.91	0.08	0.91	0.08	0.89	0.11
3	0.95	0.05	0.90	0.10	0.90	0.10	0.86	0.13
4	0.95	0.05	0.91	0.08	0.91	0.08	0.88	0.12
5	0.96	0.04	0.95	0.05	0.95	0.05	0.92	0.08
6	0.96	0.04	0.95	0.05	0.94	0.05	0.91	0.09
7	0.96	0.04	0.94	0.05	0.94	0.06	0.91	0.09
8	0.96	0.04	0.95	0.05	0.93	0.06	0.90	0.10
9	0.95	0.05	0.94	0.06	0.92	0.07	0.88	0.11
10	0.95	0.05	0.93	0.07	0.90	0.09	0.85	0.14
11	0.96	0.04	0.95	0.05	0.93	0.07	0.89	0.10
12	0.95	0.03	0.94	0.04	0.92	0.06	0.88	0.08
13	0.96	0.04	0.95	0.05	0.93	0.06	0.90	0.10
14	0.97	0.02	0.96	0.03	0.94	0.04	0.91	0.07
15	0.96	0.04	0.95	0.05	0.94	0.06	0.91	0.09
16	0.97	0.03	0.96	0.04	0.95	0.05	0.51	0.49
17	0.97	0.03	0.96	0.04	0.95	0.05	0.00	1.00
18	0.95	0.03	0.93	0.04	0.92	0.06	0.67	0.24
19	0.98	0.02	0.97	0.03	0.96	0.04	0.90	0.09

Table 8.6: System state probabilities under different evidence cases

	State	EC #1	EC #2	EC #3	EC #4
SF→ Gilroy	<i>Open</i>	0.64	0.50	0.46	0.00
	<i>Reduced/Closed</i>	0.36	0.50	0.54	1.00
Millbrae → Gilroy	<i>Open</i>	0.71	0.64	0.58	0.00
	<i>Reduced/Closed</i>	0.29	0.36	0.42	1.00
Palo Alto → Gilroy	<i>Open</i>	0.75	0.69	0.63	0.00
	<i>Reduced/Closed</i>	0.25	0.31	0.38	1.00
San Jose → Gilroy	<i>Open</i>	0.88	0.84	0.81	0.00
	<i>Reduced/Closed</i>	0.12	0.16	0.19	1.00

Next, we examine how the inspection prioritization changes under each evidence scenario. Preliminary (and hypothetical) prioritization orders for each evidence case are shown in Table 8.7. Under the first evidence case, link 3 is given highest priority, followed by links 1 and 2. Link 4 is located farthest from the epicenter and has components with generally the lowest probability of moderate or severe damage. Therefore, link 4 is not recommended for inspection; however, it is recommended that the link operate at reduced capacity. The prioritization order for the remaining links, under evidence case 1, is strongly influenced by the liabilities and system shutdown penalties. Link 3 has the largest number of components, and thus the potential liability associated with making an unsafe decision is highest for this link. The prioritization of links 1 and 2 follows similar logic. The prioritization order changes when the ground motion intensity is observed at GMPP 2. This GMPP lies along link 1 and, thus, the evidence of a high intensity there increases the probability that components along the link have experienced damage. Therefore, even though link 3 is a longer link with more components and thus higher potential liability, it is second in the prioritization order. Evidence case 3 provides observation of a pulse-like ground motion at GMPP 9, which lies along link 3. Interestingly, this observation reduces the value of information associated with inspecting the components along link 3, and an inspection is no longer required. Instead, the recommendation is to simply reduce the operating level of the link without inspection, because this recommendation is not sufficiently likely to change, based on the results of an inspection, to warrant the cost of making inspections. Given knowledge that component 17 is extensively damaged, the prioritization order returns to the

order suggested under evidence case 1, however the values of information associated with each link are higher. This reflects the accumulation of evidence that suggests higher ground motion intensities than expected everywhere. Therefore, the prioritization order is once again controlled by the potential liabilities. Note, however, that link 4 still does not require an inspection. This is because the observation of extensive damage of component 17 implies that the link must be shut down, and thus there is no value in inspecting the other components along link 4.

Table 8.7: Prioritization order associated with each links under evidence cases

Link	EC #1	EC #2	EC #3	EC #4
1	2	1	1	2
2	3	3	2	3
3	1	2	No Insp	1
4	No Insp	No Insp	No Insp	No Insp

Once a link has been chosen for inspection, the individual components along the link are prioritized, based on the assumed heuristic described in Chapter 7. For illustration, Table 8.8 provides a preliminary prioritization order for link 1 under evidence case 2. The tunnels (components 1 and 3) require inspection first, followed by the embankment segments (components 2 and 4).

Table 8.8: Value of information and prioritization order associated with components along link 1 under evidence case 2

Comp	VoI	Order
1	27	1
2	14	3
3	18	2
4	18	2

9. Conclusions

9.1 Summary of major contributions

This study outlines a comprehensive Bayesian network methodology for seismic infrastructure risk assessment and decision support. BNs have a variety of characteristics that make them well suited for the proposed application, including their graphical nature and especially the ease with which they facilitate modeling and information updating in complex problems. We primarily focus on the use of BNs to facilitate near-real-time updating of models of seismic hazard as well as component and system performance in the immediate aftermath of an earthquake. Sources of information that can be incorporated in the model include measurements of ground motion intensity from seismic recording instruments, data received from structural health monitoring sensors, and observations of component and system states.

The BN methodology contained in this study is composed of several components, described below and summarized in Figure 9.1:

- (1) A seismic demand model of ground motion intensity as a spatially distributed Gaussian random field accounting for multiple seismic sources with uncertain characteristics and including finite fault rupture and directivity effects.
- (2) A model of the performance of point-site and distributed components under seismic loading.
- (3) Models of system performance as a function of component performances.
- (4) Extensions of the BN to include decision and utility nodes to aid post-earthquake decision-making.

Chapter 3 and 4 address the first component of the framework. Components 2 and 3 are the subjects of Chapters 5 and 6, respectively. Chapter 7 describes component 4.

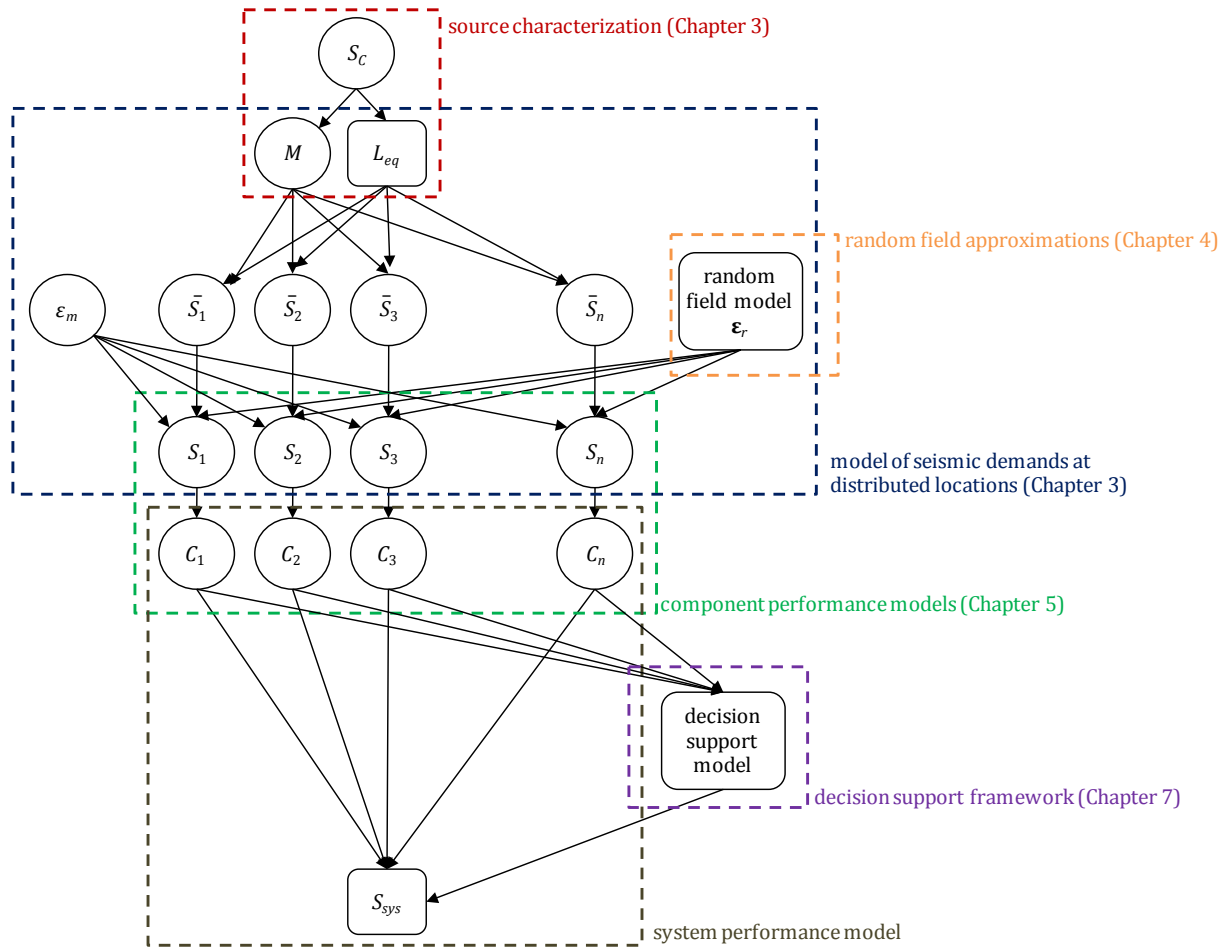


Figure 9.1: Summary of Bayesian network methodology for seismic infrastructure risk assessment and decision support

The BN is a powerful tool for modeling risks posed to infrastructure systems both before and after a hazard event. Although the use of BNs in civil engineering remains limited, this study shows the power of this framework to aid post-event decisions for emergency response and recovery of infrastructure systems. The study develops a methodology for using BNs to perform seismic infrastructure hazard assessment and provide decision support. This represents a novel approach to assessing and responding to seismic risk that integrates knowledge from a range of disciplines including computer science, hazard modeling, structural engineering, and system analysis methods. The result is a fully updateable probabilistic methodology that goes well

beyond the capabilities of existing tools. In addition to demonstrating the value of using BNs for seismic infrastructure risk assessment and decision support, this study develops models necessary to construct efficient BNs for that purpose. These models are developed with the goal of minimizing computational demands while accurately reflecting the full probabilistic characterization of the problem. Although the hazard, component, system, and decision models in this report have been developed for earthquake engineering applications, many of them are useful in a broader context. Thus the methodology described in this study provides the foundation for a new and innovative computational tool for performing risk assessment and providing decision support for infrastructures subjected to a variety of hazards.

9.2 Future research and development

The methodology outlined here lays the groundwork for a comprehensive seismic infrastructure risk assessment and decision support system. The framework can be extended and refined in many ways. Examples for future extensions and refinements are discussed below.

Expanded models:

- The seismic demand model in Chapter 3 considers line-idealizations of faults. More complex finite-rupture plane formulations and seismologically based formulations may yield improved source characterizations.
- The liquefaction and fault rupture seismic demand models in Chapter 3 are not fully developed, and hazards such as landslide have not been addressed. To comprehensively model seismic hazard to infrastructure systems, models of these and other hazards must be developed with a level of detail that is consistent with the ground-shaking model.
- The component performance models developed in this study use fragility functions. For some infrastructure system components, this idealization may be insufficient. Development of discipline-specific component performance formulations remains an area warranting further effort.
- Chapter 6 presents a heuristically augmented optimization algorithm to automate construction of efficient BN formulations for modeling system performance. New

heuristics that further reduce problem size and increase efficiency should be developed to allow consideration of larger systems.

- The methodology described in Chapter 6 considers generic system connectivity and flow problems. Discipline-specific BN models are needed, for example for transportation demand and travel time models, or hydrological models for water distribution systems. Furthermore, it is known that system interdependency can strongly affect system reliability. New formulations should be developed to capture system interdependency.
- Chapter 7 demonstrates the value of extending the BN framework with utility and decision nodes to solve decision problems. However, the example application to the post-earthquake inspection-shutdown decisions used gross assumptions and simplifications relating to economic consequences. Research is needed to define utility values more accurately, particularly at the system level. Furthermore, the current formulation does not address the amount of time required to carry out actions, e.g., time to inspect a component, nor such issues as the effect of downtime or loss of service. The formulation needs to be expanded to consider time effects, which are critical in immediate post-earthquake applications.
- Decision formulations are needed for additional applications such as the dispatch of rescue personnel after an earthquake and allocation of resources for repair and reconstruction. Models should ideally be formulated in collaboration with actual decision-makers.

Computational issues:

- Applying the framework developed in this study to large and complex infrastructure systems requires a multi-scale modeling approach. Guidance on multi-scale modeling is not contained in this study. Ideas, such as those contained in Der Kiureghian and Song (2008) should be explored for application in conjunction with BNs.
- This study focuses on the use of exact and some sampling-based algorithms (e.g., Yuan and Druzdzel 2006) for performing probabilistic inference. Work is needed to examine the accuracy of the sampling-based methods as well as the viability, precision, and

convergence in time of Markov-chain Monte Carlo and other methods. Sensitivities to discretization of continuous variables should be examined.

- Computational efficiency is crucial in near-real-time applications. Inference algorithms are needed to handle the challenges of modeling large infrastructure systems with BNs. Variational and sampling-based approaches specifically developed for the topology of the BN for seismic infrastructure risk assessment may significantly increase computational efficiency in time and space.

Integration with external information sources:

- For practical applications, the methodology described in this study must be integrated directly with tools that process data from external sources, such as structural health monitoring sensors and ground motion recording instruments. Data should be fed directly into the BN without external action by the operator, requiring an application that links these sources with the BN. Furthermore, an interface that processes the probabilistic output of the BN to create charts and graphs that provide hazard curves, prioritization lists, and other decision guidance would be valuable.

Additional applications:

- The proposed framework is useful for modeling hazards other than earthquakes. Because the methodology developed in this study is modular, it can be expanded to consider hazards such as hurricanes and fire. Models for other hazards can be substituted in place of the seismic demand model. The mapping between the demands and component performance must also be modified. However, the system performance model likely does not need to be changed. The development of models for additional hazards will increase the usefulness of the proposed framework.
- It is envisioned that the BN methodology can be used to aid decision-making under normal operating conditions, e.g., maintenance and rehabilitation planning. Decisions that improve system reliability under normal operating conditions as well as resilience to extreme loads should ideally be made in tandem. Special decision models are necessary to consider issues related to normal operating conditions.

- Seismic events provide information about seismic hazard and component and system performance. This information should be used to update the hazard models, component fragilities, and system characterizations that are used in BNs. The methodology described here should be extended to facilitate this updating.

References

- Abrahamson, N. (2000). "Effects of rupture directivity on probabilistic seismic hazard analysis." *Proceedings of the 6th International Conference on Seismic Zonation*, Earthquake Engineering Research Institute, Palm Springs.
- Abrahamson, N., Atkinson, G., Boore, D., Bozorgnia, Y., Campbell, K., Chiou, B., Idriss, I. M., Silva, W., and Youngs, R. (2008). "Comparisons of the NGA Ground-Motion Relations." *Earthquake Spectra*, 24(1), 45-66.
- Adachi, T., and Ellingwood, B. R. (2008). "Serviceability of earthquake-damaged water systems: Effects of electrical power availability and power backup systems on system vulnerability." *Reliability Engineering & System Safety*, 93(1), 78-88.
- Agostinelli, C., and Rotondi, R. (2003). "Using Bayesian belief networks to analyse the stochastic dependence between interevent time and size of earthquakes." *Journal of Seismology*, 7(3), 281-299.
- Andersen, S. K., Olesen, K. G., and Jensen, F. V. (1989). "HUGIN—a shell for building Bayesian belief universes for expert systems." *Proceedings of the 11th International Joint Conference on Artificial Intelligence*, Morgan Kaufmann Publishers Inc., Detroit, Michigan, 1080-1085.
- Ang, A. H., Pires, J. A., and Villaverde, R. (1996). "A model for the seismic reliability assessment of electric power transmission systems." *Reliability Engineering & System Safety*, 51(1), 7-22.
- Basoz, N. I., Kiremidjian, A. S., King, S. A., and Law, K. H. (1999). "Statistical Analysis of Bridge Damage Data from the 1994 Northridge, CA, Earthquake." *Earthquake Spectra*, 15(1), 25-54.

- Bayes Nets. (2007). "D-seperation." <<http://www.bayesnets.com/D-seperation.html>> (Dec. 30, 2008).
- Bayraktarli, Y. Y. (2006). "Application of Bayesian probabilistic networks for liquefaction of soil." *6th International PhD Symposium in Civil Engineering*, Institute of Structural Engineering ETH Zurich.
- Bayraktarli, Y. Y., Ulfkjaer, J., Yazgan, U., and Faber, M. (2005). "On the application of Bayesian probabilistic networks for earthquake risk management." *Proceedings of the 9th International Conference on Structural Safety and Reliability*, Rome, Italy.
- Bayraktarli, Y. Y., Yazgan, U., Dazio, A., and Faber, M. (2006). "Capabilities of the Bayesian probabilistic networks approach for earthquake risk management." *Proceedings of First European Conference on Earthquake Engineering and Seismology*, Geneva, Switzerland.
- Benjamin, J. R., and Cornell, C. A. (1970). *Probability, Statistics, and Decision for Civil Engineers*. McGraw-Hill, New York.
- Berahman, F., and Behnamfar, F. (2007). "Seismic Fragility Curves for Un-Anchored On-Grade Steel Storage Tanks: Bayesian Approach." *Journal of Earthquake Engineering*, 11(2), 166-192.
- Blaser, L., Ohrnberger, M., Riggelsen, C., and Scherbaum, F. (2009). "Bayesian Belief Network for Tsunami Warning Decision Support." *Lecture Notes In Artificial Intelligence; Proceedings of the 10th European Conference on Symbolic and Quantitative Approaches to Reasoning with Uncertainty*, Springer-Verlag Berlin Heidelberg, Verona, Italy, 757-768.
- Bobbio, A., Portinale, L., Minichino, M., and Ciancamerla, E. (2001). "Improving the analysis of dependable systems by mapping fault trees into Bayesian networks." *Reliability Engineering & System Safety*, 71(3), 249-260.
- Boore, D. M., Joyner, W. B., and Fumal, T. E. (1997). "Equations for estimating horizontal response spectra and peak acceleration from western North American earthquakes: A summary of recent work." *Seismological Research Letters*, 68(1), 128-153.

- Boore, D. M., Gibbs, J. F., Joyner, W. B., Tinsley, J. C., and Ponti, D. J. (2003). "Estimated Ground Motion From the 1994 Northridge, California, Earthquake at the Site of the Interstate 10 and La Cienega Boulevard Bridge Collapse, West Los Angeles, California." *Bulletin of the Seismological Society of America*, 93(6), 2737-2751.
- Bowers, M. E. (2007). "Seismic fragility curves for a typical highway bridge in Charleston, SC considering soil-structure interaction and liquefaction effects." M.S., Clemson University.
- Box, G., and Tiao, G. (1971). *Bayesian Methods, Forecasting and Control in Statistics and Operations Analysis*. Defense Technical Information Center.
- Box, G., and Tiao, G. (1992). *Bayesian Inference in Statistical Analysis*. Wiley, New York.
- Bray, J. D., and Rodriguez-Marek, A. (2004). "Characterization of forward-directivity ground motions in the near-fault region." *Soil Dynamics and Earthquake Engineering*, 24, 815-828.
- Bryant, W. A. (2005). *Digital Database of Quaternary and Younger Faults from the Fault Activity Map of California, version 2.0*,
<http://www.consrv.ca.gov/CGS/information/publications/QuaternaryFaults_ver2.htm>.
- CA HSR. (2010). "California High-Speed Rail Authority Website."
<<http://www.cahighspeedrail.ca.gov/>> (Mar. 29, 2010).
- Campbell, K.W., and Bozorgnia, Y. (2007) "Campbell-Bozorgnia NGA Ground Motion Relations for the Geometric Mean Horizontal Component of Peak and Spectral Ground Motion Parameters." *PEER Report 2007/02*, Pacific Earthquake Engineering Research Center, University of California, Berkeley, CA, May.
- Caltrans. (2007). "Fault Parameter Database (Excel Spreadsheet) from ARS Online (by California Department of Transportation Division of Engineering Services)."
<http://dap3.dot.ca.gov/shake_stable/references/2007_Fault_Database_120309.xls> (May 13, 2010).
- Castelletti, A., and Soncini-Sessa, R. (2007). "Bayesian networks in water resource modelling and management." *Environmental Modelling & Software*, 22(8), 1073-1074.

- Cetin, K., Der Kiureghian, A., and Seed, R. B. (2002). "Probabilistic models for the initiation of seismic soil liquefaction." *Structural Safety*, 24(1), 67-82.
- Cheng, J., and Druzdzel, M. (2000). "AIS-BN: An adaptive importance sampling algorithm for evidential reasoning in large Bayesian networks." *Journal of Artificial Intelligence Research*, 13, 155-188.
- Clynch, J. R. (2006). "Earth Coordinates."
 <http://www.gmat.unsw.edu.au/snap/gps/clynch_pdfs/coorddef.pdf> (May 31, 2010).
- Congdon, P. (2003). *Applied Bayesian Modelling*. John Wiley and Sons, West Sussex, England.
- Cooper, G. F. (1990). "The computational complexity of probabilistic inference using Bayesian belief networks." *Artificial Intelligence*, 42(2-3), 393-405.
- Dechter, R. (1996). "Bucket Elimination: A unifying framework for probabilistic inference." *Uncertainty in Artificial Intelligence*, UA1996, 211-219.
- Dechter, R., and Rish, I. (2003). "Mini-buckets: A general scheme for approximating inference." *Journal of ACM*, 50(2), 1-61.
- Der Kiureghian, A. (2002). "Bayesian methods for seismic fragility assessment of lifeline components." *Acceptable Risk Processes: Lifelines and Natural Hazards*, ASCE, 61-77.
- Der Kiureghian, A. (2005). "Chapter 14: First- and second-order reliability methods.." *Engineering Design Reliability Handbook*, CRC Press, Boca Raton, Florida.
- Der Kiureghian, A. (2006). "System reliability revisited." *Proceedings, 3rd ASRANet International Colloquium*, Glasgow, U.K., CD-ROM.
- Der Kiureghian, A. (2009). "Seismic risk assessment and management of infrastructure systems: Review and new perspectives. Keynote Lecture.." *Proc. 10th Int. Conf. On Structural Safety and Reliability*, CRC Press, Osaka, Japan, 27-37.
- Der Kiureghian, A., Haukaas, T., and Fujimura, K. (2006). "Structural reliability software at the University of California, Berkeley." *Structural Safety*, 28(1-2), 44-67.

- Der Kiureghian, A., and Song, J. (2008). "Multi-scale reliability analysis and updating of complex systems by use of linear programming." *Reliability Engineering & System Safety*, 93(2), 288-297.
- DHS. (2003). *HAZUS-MH MR4 Technical Manual*. Department of Homeland Security, Emergency Preparedness and Response Directorate, FEMA, Mitigation Division, Washington D.C.
- Ditlevsen, O., and Madsen, H. O. (1996). *Structural reliability methods (First edition: 1996, Internet edition: 2005)*. first edition: John Wiley & Sons Ltd, Internet edition: <http://www.mek.dtu.dk/staff/od/books.htm>.
- DoD. (2000). "Department of Defense World Geodetic System 1984 - Technical Report Third Edition Amendment 1." <<http://earth-info.nga.mil/GandG/publications/tr8350.2/wgs84fin.pdf>> (Jun. 1, 2010).
- Doguc, O., and Ramirez-Marquez, J. E. (2009). "A generic method for estimating system reliability using Bayesian networks." *Reliability Engineering & System Safety*, 94(2), 542-550.
- DSL. (2007). *GeNIe 2.0 by Decision Systems Laboratory* (<http://genie.sis.pitt.edu/>).
- Dunnett, C. W., and Sobel, M. (1955). "Approximations to the Probability Integral and Certain Percentage Points of a Multivariate Analogue of Student's t-Distribution." *Biometrika*, 42(1/2), 258-260.
- Eidinger, J. M., Avila, E. A., Ballantyne, D. B., Cheng, L., Der Kiureghian, A., Maison, B. F., O'Rourke, T. D., and Power, M. S. (2001). *Seismic fragility formulations for water systems, Part 1: Guideline*. American Lifelines Alliance.
- Elias, P., Feinstein, A., and Shannon, C. (1956). "A note on the maximum flow through a network." *Information Theory, IRE Transactions on*, 2(4), 117-119.
- Ellingwood, B. R. (2001). "Earthquake risk assessment of building structures." *Reliability Engineering & System Safety*, 74(3), 251-262.

- Fabbrocino, G., Iervolino, I., Orlando, F., and Salzano, E. (2005). "Quantitative risk analysis of oil storage facilities in seismic areas." *Journal of Hazardous Materials*, 123(1-3), 61-69.
- Faizian, M., Schalcher, H. R., and Faber, M. (2005). "Consequence assessment in earthquake risk management using damage indicators." *9th International Conference on Structural Safety and Reliability (ICOSSAR 05)*, 19–23.
- Fard, N. S. (1997). "Determination of minimal cut sets of a complex fault tree." *Computers & Industrial Engineering*, 33(1-2), 59-62.
- Farrell, J., and Barth, M. (1999). *The Global Positioning System and Inertial Navigation*. McGraw-Hill Professional, New York.
- FEMA. (2008). "HAZUS-MH Website." <www.fema.gov/plan/prevent/hazus> (Jul. 23, 2010).
- Fink, D. (1997). "A Compendium of Conjugate Priors." Environmental Statistics Group Department of Biology Montana State University.
- Ford, L. R., and Fulkerson, D. R. (1956). "Maximal flow through a network." *Canadian Journal of Mathematics*, 8(3), 399-404.
- Friis-Hansen, A. (2000). "Bayesian networks as a decision support tool in marine applications." Department of Naval Architecture and Offshore Engineering, Technical University of Denmark.
- Friis-Hansen, P. (2004). "Structuring of complex systems using Bayesian Networks (with additional material from the unpublished extension to the paper, 2008)." *Proceedings of Two Part Workshop at DTU*, O. Ditlevsen and P. Friis-Hansen, eds., Technical University of Denmark.
- Fung, R. M., and Chang, K. (1990). "Weighing and Integrating Evidence for Stochastic Simulation in Bayesian Networks." *Proceedings of the Fifth Annual Conference on Uncertainty in Artificial Intelligence*, North-Holland Publishing Co., Windsor, Ontario, 209-220.
- Gamerman, D., and Lopes, H. F. (2006). *Markov chain Monte Carlo: stochastic simulation for Bayesian inference*. CRC Press, Boca Raton, Florida.

- Gardoni, P., Der Kiureghian, A., and Mosalam, K. M. (2002). *Probabilistic Models and Fragility Estimates for Bridge Components and Systems - PEER Report 2002/13*. Pacific Earthquake Engineering Research Center, University of California, Berkeley.
- Gardoni, P., and Rosowsky, D. (2009). “Seismic fragility increment functions for deteriorating reinforced concrete bridges.” *Structure and Infrastructure Engineering*, (1–11, iFirst article).
- GHI. (2009). “(Geohazards International) RADIUS - Risk Assessment Tools for Diagnosis of Urban Areas against Seismic Disasters.” <<http://www.geohaz.org/projects/radius.html>> (Jun. 13, 2010).
- Gill, J. (2002). *Bayesian Methods: A Social and Behavioral Sciences Approach*. CRC press, Boca Raton, Florida.
- Grêt-Regamey, A., and Straub, D. (2006). “Spatially explicit avalanche risk assessment linking Bayesian networks to a GIS.” *Natural Hazards and Earth System Sciences*, 6, 911-926.
- Grigoriu, M. (2000). “Non-Gaussian models for stochastic mechanics.” *Probabilistic Engineering Mechanics*, 15(1), 15-23.
- Grigoriu, M., and Turkstra, C. (1979). “Safety of structural systems with correlated resistances.” *Applied Mathematical Modelling*, 3(2), 130-136.
- Gutenberg, B., and Richter, C. F. (1944). “Frequency of earthquakes in California.” *Bulletin of the Seismological Society of America*, 34(4), 185-188.
- Heckerman, D. (2008). “A tutorial on learning with Bayesian networks.” *Innovations in Bayesian Networks*, Springer-Verlag Berlin Heidelberg, 33-82.
- Holmström, K. (2008). *Tomlab Optimization Environment* (<http://tomopt.com/tomlab/>).
- Horvitz, E. J., Suermondt, H. J., and Cooper, G. F. (1989). “Bounded conditioning: Flexible inference for decisions under scarce resources.” *Proceedings of the Fifth Workshop on Uncertainty in Artificial Intelligence*, Windsor, Ontario, 182–193.
- Hugin Expert A/S. (2008). *Hugin Researcher API 7.0* (www.hugin.com). Hugin Expert A/S, Denmark.

- International Code Council. (2006). *International Building Code 2006*. Cengage Learning.
- Ishihara, K., and Yoshimine, M. (1992). "Evaluation of settlements in sand deposits following liquefaction during earthquakes." *Soils and Foundations*, 32(1), 173-188.
- Jacobson, A., and Grigoriu, M. (2005). "Fragility analysis of water supply systems." *MCEER*, <<http://mceer.buffalo.edu/publications/resaccom/03-SP06/webpdfs/16Jacobson.pdf>>.
- Jensen, F. V. (2001a). "Graphical Models as Languages for Computer Assisted Diagnosis and Decision Making." *Symbolic and Quantitative Approaches to Reasoning with Uncertainty (ECSQARU 2001, LNAI 2143)*, Springer-Verlag, Berlin Heidelberg.
- Jensen, F. V. (2001b). *Bayesian Networks and Decision Graphs*. Springer-Verlag, New York.
- Jensen, F. V., and Nielson, T. D. (2007). *Bayesian Networks and Decision Graphs*. Springer-Verlag, New York.
- Jensen, F. V., and Vomlelova, M. (2002). "Unconstrained influence diagrams." *Proc. of the 18th International Conference on Uncertainty in Artificial Intelligence (UAI-02)*, 234–241.
- Jha, M. (2006). "Applying Bayesian Networks to Assess Vulnerability of Critical Transportation Infrastructure." *Applications of Advanced Technology in Transportation - Proceedings of 9th International Conference*, ASCE.
- Jolliffe, I. T. (2002). *Principal Component Analysis*. Springer-Verlag, New York.
- Jordaan, I. J. (2005). *Decisions Under Uncertainty: Probabilistic Analysis for Engineering Decisions*. Cambridge University Press, Cambridge.
- Jordan, M., Ghahramani, Z., Jaakkola, T., and Saul, L. (1999). "An Introduction to Variational Methods for Graphical Models." *Machine Learning*, 37, 183-233.
- Karim, K. R., and Yamazaki, F. (2003). "A simplified method of constructing fragility curves for highway bridges." *Earthquake Engineering & Structural Dynamics*, 32(10), 1603-1626.
- Kennedy, R., and Ravindra, M. (1984). "Seismic fragilities for nuclear power plant risk studies." *Nuclear Engineering and Design*, 79(1), 47-68.
- Kim, S., and Feng, M. Q. (2003). "Fragility analysis of bridges under ground motion with spatial variation." *International Journal of Non-Linear Mechanics*, 38(5), 705-721.

- Kim, S., and Shinozuka, M. (2004). "Development of fragility curves of bridges retrofitted by column jacketing." *Probabilistic Engineering Mechanics*, 19(1-2), 105-112.
- Kjaerulff, U. B., and Madsen, A. L. (2008). *Bayesian Networks and Influence Diagrams: A Guide to Construction and Analysis*. Information Science and Statistics, Springer Science+Business Media, LLC, New York.
- Konakli, K., and Der Kiureghian, A. (2010). "Extended MSRS rule for Seismic Analysis of Bridges subjected to Differential Support Motions." *Under Review*.
- Koop, G. (2003). *Bayesian Econometrics*. Wiley-Interscience, Hoboken, N.J.
- Kramer, S. L. (1996). *Geotechnical Earthquake Engineering*. Prentice Hall, New Jersey.
- Kübler, O. (2007). *Applied Decision-Making in Civil Engineering*. vdf Hochschulverlag AG, ETH Zurich.
- Kuehn, N. M., Riggelsen, C., and Scherbaum, F. (2009). "Facilitating Probabilistic Seismic Hazard Analysis Using Bayesian Networks." *Seventh Annual Workshop on Bayes Applications (in conjunction with UAI/COLT/ICML 2009)*.
- Kurian, S. A., Deb, S. K., and Dutta, A. (2006). "Seismic vulnerability assessment of a railway overbridge using fragility curves." *ICEE 2006: 4th International Conference on Earthquake Engineering*, National Center for Research on Earthquake Engineering.
- Lampis, M., and Andrews, J. D. (2009). "Bayesian belief networks for system fault diagnostics." *Quality and Reliability Engineering International*, 25(4), 409-426.
- Langseth, H., Nielsen, T. D., Rumí, R., and Salmerón, A. (2009). "Inference in hybrid Bayesian networks." *Reliability Engineering & System Safety*, 94(10), 1499-1509.
- Lauritzen, S. L. (1992). "Propagation of probabilities, means and variances in mixed graphical association models." *Journal of the American Statistical Association*, 87, 1098-1108.
- Lauritzen, S. L., and Jensen, F. V. (2001). "Stable local computation with conditional Gaussian distributions." *Statistics and Computing*, 11(2), 191-203.
- Lauritzen, S. L., and Nilsson, D. (2001). "Representing and Solving Decision Problems with Limited Information." *Management Science*, 47(9), 1235-1251.

- Lewis, E. E. (1987). *Introduction to Reliability Engineering*. John Wiley & Sons Inc.
- Li, D., Liu, H., and Wu, S. (2009). "Reliability analysis of embankment dams using Bayesian network." *Geotechnical Safety and Risk*, CRC Press, Leiden, The Netherlands.
- Liam Finn, W., Ledbetter, R., and Wu, G. (1994). "Liquefaction in Silty Soils: Design and Analysis." *Ground Failures Under Seismic Conditions (GSP 44)*, 51-76.
- Lin, L., and Adams, J. (2007). "Lessons for the fragility of Canadian hydropower components under seismic loading." *Proceedings of 9th Canadian Conference on Earthquake Engineering*, Ottawa, Ontario, Canada.
- Liu, X., Li, H., and Li, L. (2008). "Building method of diagnostic model of Bayesian networks based on fault tree." *Seventh International Symposium on Instrumentation and Control Technology: Sensors and Instruments, Computer Simulation, and Artificial Intelligence*, SPIE, Beijing, China, 71272C-6.
- Luque, M., Nielsen, T. D., and Jensen, F. V. (2008). "An anytime algorithm for evaluating unconstrained influence diagrams." *Proc. 4th European Workshop on Probabilistic Graphical Models*, Hirtshals, Denmark, 177-184.
- MacKay, D. J. C. (1999). "Introduction to Monte Carlo methods." *Learning in graphical models*, MIT Press, Cambridge, MA.
- Mackie, K.R., and Stojadinovic, B. (2004). "Fragility curves for reinforced concrete overpass bridges." *Proceedings of 13th World Conference on Earthquake Engineering*, Vancouver, B.C., Canada.
- Mackie, K. R., and Stojadinovic, B. (2006). "Post-earthquake functionality of highway overpass bridges." *Earthquake Engineering & Structural Dynamics*, 35(1), 77-93.
- Madsen, A. L. (2008). "Belief update in CLG Bayesian networks with lazy propagation." *International Journal of Approximate Reasoning*, 49(2), 503-521.
- Mahadevan, S., Zhang, R., and Smith, N. (2001). "Bayesian networks for system reliability reassessment." *Structural Safety*, 23(3), 231-251.

- Medina Oliva, G., Weber, P., Simon, C., and Iung, B. (2009). "Bayesian networks applications on dependability, risk analysis and maintenance." *Proceedings of 2nd IFAC Workshop on Dependable Control of Discrete System, DCDS'09*, Bari, Italy.
- Mizuno, K., Maruyama, Y., Yamazaki, F., Tsuchiya, Y., and Yogai, H. (2008). "Construction of the fragility curves of expressway embankment based on actual earthquake data." *Proceedings of Eleventh East Asia-Pacific Conference on Structural Engineering & Construction (EASEC-11)*, Taipei, Taiwan.
- Moon, T. K. (1996). "The expectation-maximization algorithm." *IEEE Signal Processing Magazine*, 13(6), 47-60.
- Moss, R. E. S., Seed, R. B., Kayen, R. E., Stewart, J. P., Der Kiureghian, A., and Cetin, K. O. (2006). "CPT-Based Probabilistic and Deterministic Assessment of In Situ Seismic Soil Liquefaction Potential." *Journal of Geotechnical and Geoenvironmental Engineering*, 132(8), 1032-1051.
- Mouroux, P., and Brun, B. (2006). "Presentation of RISK-UE Project." *Bulletin of Earthquake Engineering*, 4(4), 323-339.
- Murphy, K. (2007). "Software for graphical models: A review." *International Society for Bayesian Analysis Bulletin*, 14(4), 13-15.
- Murphy, K. (2010). "Software Packages for Graphical Models / Bayesian Networks." <<http://people.cs.ubc.ca/~murphyk/Software/bnsoft.html>> (May 4, 2010).
- Nakamura, N., Akita, S., Suzuki, T., Koba, M., Nakamura, S., and Nakano, T. (2010). "Study of ultimate seismic response and fragility evaluation of nuclear power building using nonlinear three-dimensional finite element model." *Nuclear Engineering and Design*, 240(1), 166-180.
- Neil, M., Tailor, M., and Marquez, D. (2007). "Inference in hybrid Bayesian networks using dynamic discretization." *Statistics and Computing*, 17(3), 219-233.
- Nielsen, B. G., and DesRoches, R. (2007). "Seismic fragility methodology for highway bridges using a component level approach." *Earthquake Engineering & Structural Dynamics*, 36(6), 823-839.

- Nishijima, K., and Faber, M. (2007). "A Bayesian framework for typhoon risk management." *Proceedings of 12th International Conference on Wind Engineering (12ICWE)*, Cairns, Australia.
- NRC. (1981). "Fault Tree Handbook (NUREG-0492)." Systems and Reliability Research, Office of Nuclear Regulatory Research, U.S. Nuclear Regulatory Commission.
- Ordonez, G. (2009). *SHAKE2000* (www.shake2000.com).
- O'Rourke, M. J., and So, P. (2000). "Seismic Fragility Curves for On-Grade Steel Tanks." *Earthquake Spectra*, 16(4), 801-815.
- Padgett, J. E., and DesRoches, R. (2009). "Retrofitted Bridge Fragility Analysis for Typical Classes of Multispan Bridges." *Earthquake Spectra*, 25(1), 117-141.
- Pagès, A., and Gondran, M. (1986). *System Reliability*. Springer-Verlag, New York.
- Park, J., Bazzurro, P., and Baker, J. W. (2007). "Modeling spatial correlation of ground motion Intensity Measures for regional seismic hazard and portfolio loss estimation." *Applications of Statistics and Probability in Civil Engineering*, Taylor & Francis Group, Tokyo, Japan.
- Park, J., Towashiraporn, P., Craig, J. I., and Goodno, B. J. (2009). "Seismic fragility analysis of low-rise unreinforced masonry structures." *Engineering Structures*, 31(1), 125-137.
- Paskin, M. (2003). "A Short Course on Graphical Models: 3. The Junction Tree Algorithms." Short Course notes <<http://ai.stanford.edu/~paskin/gm-short-course/lec3.pdf>> (May 30, 2010).
- Pearl, J. (2000). "d-Separation without Tears." <<http://bayes.cs.ucla.edu/BOOK-2K/d-sep.html>> (Dec. 28, 2008).
- PEER. (2005). "Pacific Earthquake Engineering Research Center: NGA Database." <<http://peer.berkeley.edu/nga/>> (May. 5, 2010).
- Rackwitz, R. (2001). "Reliability analysis-a review and some perspectives." *Structural Safety*, 23(4), 365-395.

- Raiffa, H. (1997). *Decision Analysis: Introductory Readings on Choices Under Uncertainty*. McGraw-Hill.
- Raiffa, H., and Schlaifer, R. (1970). *Applied Statistical Decision Theory*. M.I.T. Press, Cambridge, MA.
- Rauch, A. F. (1997). "An Empirical Method for Predicting Surface Displacements Due to Liquefaction-Induced Lateral Spreading in Earthquakes." PhD, Virginia Tech.
- Rojahn, C., and Sharpe, R. L. (1985). "ATC 13: Earthquake Damage Evaluation Data for California." Applied Technology Council.
- Rota, M., Penna, A., and Magenes, G. (2010). "A methodology for deriving analytical fragility curves for masonry buildings based on stochastic nonlinear analyses." *Engineering Structures*, 32(5), 1312-1323.
- Ryu, H., Luco, N., Baker, J. W., and Karaca, E. (2008). "Converting HAZUS capacity curves to seismic hazard-compatible building fragility functions: effect of hysteric models." *Proceedings of 14th World Conference on Earthquake Engineering*, International Association for Earthquake Engineering, Beijing, China.
- Sarker, R. A., and Newton, C. S. (2008). *Optimization Modelling: a Practical Approach*. CRC Press, Taylor and Francis Group, LLC, Boca Raton, Florida.
- Seed, R. B., and Bray, J. D. (1997). "Site-dependent seismic response including recent strong motion data." *Seismic behavior of ground and geotechnical structures: proceedings of a discussion special technical session on earthquake geotechnical engineering during fourteenth International Conference on Soil Mechanics and Foundation Engineering*, Taylor & Francis, 125-134.
- Seed, R. B., Cetin, K. O., Moss, R. E. S., Kammerer, A. M., Wu, J., Pestana, J. M., Riemer, M. F., Sancio, R. B., Bray, J. D., and Kayen, R. E. (2003). "Recent advances in soil liquefaction engineering: a unified and consistent framework." *Proceedings of 26th Annual ASCE Los Angeles Geotechnical Spring Semester*, Long Beach, CA.

- Shachter, R. D., and Peot, M. A. (1990). "Simulation Approaches to General Probabilistic Inference on Belief Networks." *Proceedings of the Fifth Annual Conference on Uncertainty in Artificial Intelligence*, North-Holland Publishing Co., 221-234.
- Shahi, S. K., and Baker, J. W. (2010). "An empirically calibrated framework for including the effects of near-fault directivity in Probabilistic Seismic Hazard Analysis (manuscript in preparation)."
- Shenoy, P. P. (1996). "Representing and Solving Assymmetric Decision Problems Using Valuation Networks." *Learning from data: artificial intelligence and statistics V*, Springer-Verlag, New York.
- Shenoy, P. P. (2006). "Inference in hybrid Bayesian networks using mixtures of Gaussians." *Proceedings of the 22nd Conference on Uncertainty in Artificial Intelligence*, 428-436.
- Shih, B., and Chang, C. (2006). "Damage Survey of Water Supply Systems and Fragility Curve of PVC Water Pipelines in the Chi-Chi Taiwan Earthquake." *Natural Hazards*, 37(1-2), 71-85.
- Shin, Y., and Koh, J. (1998). "An algorithm for generating minimal cutsets of undirected graphs." *Journal of Applied Mathematics and Computing*, 5(3), 681-693.
- Shinozuka, M., Feng, M. Q., Lee, J., and Naganuma, T. (2000). "Statistical Analysis of Fragility Curves." *Journal of Engineering Mechanics*, 126(12), 1224-1231.
- Shumuta, Y., Takahashi, K., and Matsumoto, T. (2009). "Development of a Damage Estimation System for Electric Power Distribution Equipment Using the Bayesian Network." *Proceedings of the 2009 ASCE Technical Council on Lifeline Earthquake Engineering Conference*, A. K. K. Tang and S. Werner, eds., ASCE, Oakland, California, 197-208.
- Smith, M. (2006). "Dam Risk Analysis Using Bayesian Networks." *Proceedings of 2006 ECI Conference of GeoHazards*, Lillehammer, Norway.
- Somerville, P. G., Smith, N. F., Graves, R. W., and Abrahamson, N. (1997). "Modification of Empirical Strong Ground Motion Attenuation Relations to Include the Amplitude and Duration Effects of Rupture Directivity." *Seismological Research Letters*, 68, 199-222.

- Song, J., and Kang, W. (2009). "System reliability and sensitivity under statistical dependence by matrix-based system reliability method." *Structural Safety*, 31(2), 148-156.
- Song, J., and Ok, S. (2009). "Multi-scale system reliability analysis of lifeline networks under earthquake hazards." *Earthquake Engineering & Structural Dynamics*, 39(3), 259-279.
- Straub, D. (2005). "Natural hazards risk assessment using Bayesian networks." *Proceedings of 9th International Conference on Structural Safety and Reliability (ICOSSAR 05)*, Rome, Italy.
- Straub, D. (2009). "Stochastic Modeling of Deterioration Processes through Dynamic Bayesian Networks." *Journal of Engineering Mechanics*, 135(10), 1089-1099.
- Straub, D., and A. Der Kiureghian (2008). "Improved seismic fragility modeling from empirical data." *Structural Safety*, 30, 320-336.
- Straub, D., and Der Kiureghian, A. (2010a). "Bayesian Network Enhanced with Structural Reliability Methods: Methodology." *Journal of Engineering Mechanics*, 136(10), 1248-1258.
- Straub, D., and Der Kiureghian, A. (2010b). "Bayesian Network Enhanced with Structural Reliability Methods: Application." *Journal of Engineering Mechanics*, 136(10), 1259-1270.
- Straub, D., Bensi, M., and Der Kiureghian, A. (2008). "Spatial Modeling of Earthquake Hazard and Infrastructure System Performance Through Bayesian Network." *Proceedings of Inaugural International Conference of the Engineering Mechanics Institute (EM08)*, Engineering Mechanics Institute, Minneapolis, Minnesota.
- Suh, H., and Chang, C. K. (2000). "Algorithms for the minimal cutsets enumeration of networks by graph search and branch addition." *Proceedings of the 25th Annual IEEE Conference on Local Computer Networks*, IEEE Computer Society, 100.
- Sung, Y., and Su, C. (2009). "Time-dependent seismic fragility curves on optimal retrofitting of neutralised reinforced concrete bridges." *Structure and Infrastructure Engineering*.

- Tokimatsu, K., and Seed, H. B. (1987). "Evaluation of settlements in sands due to earthquake shaking." *Journal of Geotechnical Engineering*, 113(8), 861-878.
- Toprak, S., and Taskin, F. (2007). "Estimation of Earthquake Damage to Buried Pipelines Caused by Ground Shaking." *Natural Hazards*, 40(1), 1-24.
- Torres-Toledano, J., and Sucar, L. (1998). "Bayesian Networks for Reliability Analysis of Complex Systems." *Lecture Notes in Computer Science: Progress in Artificial Intelligence (IBERAMIA '98, LNAI 1484)*, Springer-Verlag Berlin Heidelberg, 195-206.
- Tothong, P., Cornell, A., and Baker, J. W. (2007). "Explicit Directivity-Pulse Inclusion in Probabilistic Seismic Hazard Analysis." *Earthquake Spectra*, 23(4), 867-891.
- Trefethen, L. N., and Bau, D. (1997). *Numerical Linear Algebra*. Society for Industrial and Applied Mathematics, Philadelphia.
- USGS. (2007). "ShakeCast Fact Sheet 2007-3086,"
<<http://pubs.usgs.gov/fs/2007/3086/pdf/FS07-3086.pdf>> (Dec. 4, 2008).
- USGS. (2008). "ShakeMaps." *USGS Earthquake Hazard Program*,
<<http://earthquake.usgs.gov/eqcenter/shakemap/>> (Dec. 4, 2008).
- Vanzi, I. (1996). "Seismic reliability of electric power networks: methodology and application." *Structural Safety*, 18(4), 311-327.
- Wainwright, M. J., and Jordan, M. (2008). *Graphical Models, Exponential Families, and Variational Inference*. now Publishers Inc, Hanover, MA.
- Wells, D., and Coppersmith, K. (1994). "New empirical relationships among magnitude, rupture length, rupture width, rupture area, and surface displacement." *Bulletin of the Seismological Society of America*, 84(4), 974-1002.
- Werner, S. D., Taylor, C. E., Cho, S., Lavoie, J., Huyck, C., Eitzel, C., Chung, H., and Eguchi, R. (2006). *REDARS 2 Methodology and Software for Seismic Risk Analysis of Highway Systems*. MCEER, University of Buffalo, The State University of New York.
- Wilson, C. (2010). "Life is (NP-) Hard." *Bugs Are Easy*,
<<http://bugsareeasy.wordpress.com/2010/01/19/life-is-np-hard/>> (May 30, 2010).

- Yeh, W. (2006). "A new algorithm for generating minimal cut sets in k-out-of-n networks." *Reliability Engineering & System Safety*, 91(1), 36-43.
- Yoshikawa, H., Ohtaki, T., Hattori, H., Maeda, Y., Noguchi, A., and Okada, H. (2007). "Seismic Risk Assessment and Expected Damage for a Railway Viaduct." *Proceedings of 10th International Conference on Applications of Statistics and Probability in Civil Engineering*, Taylor & Francis Group, Tokyo, Japan.
- Youd, T. L., Hansen, C. M., and Bartlett, S. F. (2002). "Revised Multilinear Regression Equations for Prediction of Lateral Spread Displacement.." *Journal of Geotechnical & Geoenvironmental Engineering*, 128(12), 1007-1017.
- Youngs, R. R., and Coppersmith, K. (1985). "Implications of fault slip rates and earthquake recurrence models to probabilistic seismic hazard estimates." *Bulletin of the Seismological Society of America*, 75(4), 939-964.
- Yuan, C., and Druzdzel, M. (2003). "An importance sampling algorithm based on evidence pre-propagation." *In Proceedings of the 19th Annual Conference on Uncertainty in Artificial Intelligence (UAI03)*.
- Yuan, C., and Druzdzel, M. (2006). "Importance sampling algorithms for Bayesian networks: Principles and performance." *Mathematical and Computer Modelling*, 43(9-10), 1189-1207.
- Yuan, C., Lu, T., and Druzdzel, M. (2004). "Annealed MAP." *Proceedings of the 20th conference on Uncertainty in artificial intelligence*, AUAI Press, Banff, Canada, 628-635.
- Zhang, J., Huo, Y., Brandenberg, S., and Kashighandi, P. (2008). "Effects of structural characterizations on fragility functions of bridges subject to seismic shaking and lateral spreading." *Earthquake Engineering and Engineering Vibration*, 7(4), 369-382.

PEER REPORTS

PEER reports are available individually or by yearly subscription. PEER reports can be ordered at http://peer.berkeley.edu/publications/peer_reports.html or by contacting the Pacific Earthquake Engineering Research Center, 325 Davis Hall mail code 1792, Berkeley, CA 94720. Tel.: (510) 642-3437; Fax: (510) 665-1655; Email: peer_editor@berkeley.edu

- PEER 2011/02** *A Bayesian Network Methodology for Infrastructure Seismic Risk Assessment and Decision Support.* Michelle T. Bensi, Armen Der Kiureghian, and Daniel Straub. March 2011.
- PEER 2011/01** *Demand Fragility Surfaces for Bridges in Liquefied and Laterally Spreading Ground.* Scott J. Brandenberg, Jian Zhang, Pirooz Kashighandi, Yili Huo, and Minxing Zhao. March 2011.
- PEER 2010/05** *Guidelines for Performance-Based Seismic Design of Tall Buildings.* Developed by the Tall Buildings Initiative. November 2010.
- PEER 2010/04** *Application Guide for the Design of Flexible and Rigid Bus Connections between Substation Equipment Subjected to Earthquakes.* Jean-Bernard Dastous and Armen Der Kiureghian. September 2010.
- PEER 2010/03** *Shear Wave Velocity as a Statistical Function of Standard Penetration Test Resistance and Vertical Effective Stress at Caltrans Bridge Sites.* Scott J. Brandenberg, Naresh Bellana, and Thomas Shantz. June 2010.
- PEER 2010/02** *Stochastic Modeling and Simulation of Ground Motions for Performance-Based Earthquake Engineering.* Sanaz Rezaeian and Armen Der Kiureghian. June 2010.
- PEER 2010/01** *Structural Response and Cost Characterization of Bridge Construction Using Seismic Performance Enhancement Strategies.* Ady Aviram, Božidar Stojadinović, Gustavo J. Parra-Montesinos, and Kevin R. Mackie. March 2010.
- PEER 2009/03** *The Integration of Experimental and Simulation Data in the Study of Reinforced Concrete Bridge Systems Including Soil-Foundation-Structure Interaction.* Matthew Dryden and Gregory L. Fenves. November 2009.
- PEER 2009/02** *Improving Earthquake Mitigation through Innovations and Applications in Seismic Science, Engineering, Communication, and Response. Proceedings of a U.S.-Iran Seismic Workshop.* October 2009.
- PEER 2009/01** *Evaluation of Ground Motion Selection and Modification Methods: Predicting Median Interstory Drift Response of Buildings.* Curt B. Haselton, Ed. June 2009.
- PEER 2008/10** *Technical Manual for Strata.* Albert R. Kottke and Ellen M. Rathje. February 2009.
- PEER 2008/09** *NGA Model for Average Horizontal Component of Peak Ground Motion and Response Spectra.* Brian S.-J. Chiou and Robert R. Youngs. November 2008.
- PEER 2008/08** *Toward Earthquake-Resistant Design of Concentrically Braced Steel Structures.* Patxi Uriz and Stephen A. Mahin. November 2008.
- PEER 2008/07** *Using OpenSees for Performance-Based Evaluation of Bridges on Liquefiable Soils.* Stephen L. Kramer, Pedro Arduino, and HyungSuk Shin. November 2008.
- PEER 2008/06** *Shaking Table Tests and Numerical Investigation of Self-Centering Reinforced Concrete Bridge Columns.* Hyung IL Jeong, Junichi Sakai, and Stephen A. Mahin. September 2008.
- PEER 2008/05** *Performance-Based Earthquake Engineering Design Evaluation Procedure for Bridge Foundations Undergoing Liquefaction-Induced Lateral Ground Displacement.* Christian A. Ledezma and Jonathan D. Bray. August 2008.
- PEER 2008/04** *Benchmarking of Nonlinear Geotechnical Ground Response Analysis Procedures.* Jonathan P. Stewart, Annie On-Lei Kwok, Youssef M. A. Hashash, Neven Matasovic, Robert Pyke, Zhiliang Wang, and Zhaohui Yang. August 2008.
- PEER 2008/03** *Guidelines for Nonlinear Analysis of Bridge Structures in California.* Ady Aviram, Kevin R. Mackie, and Božidar Stojadinović. August 2008.
- PEER 2008/02** *Treatment of Uncertainties in Seismic-Risk Analysis of Transportation Systems.* Evangelos Stergiou and Anne S. Kiremidjian. July 2008.
- PEER 2008/01** *Seismic Performance Objectives for Tall Buildings.* William T. Holmes, Charles Kircher, William Petak, and Nabih Youssef. August 2008.
- PEER 2007/12** *An Assessment to Benchmark the Seismic Performance of a Code-Conforming Reinforced Concrete Moment-Frame Building.* Curt Haselton, Christine A. Goulet, Judith Mitrani-Reiser, James L. Beck, Gregory G. Deierlein, Keith A. Porter, Jonathan P. Stewart, and Ertugrul Taciroglu. August 2008.
- PEER 2007/11** *Bar Buckling in Reinforced Concrete Bridge Columns.* Wayne A. Brown, Dawn E. Lehman, and John F. Stanton. February 2008.

- PEER 2007/10** *Computational Modeling of Progressive Collapse in Reinforced Concrete Frame Structures.* Mohamed M. Talaat and Khalid M. Mosalam. May 2008.
- PEER 2007/09** *Integrated Probabilistic Performance-Based Evaluation of Benchmark Reinforced Concrete Bridges.* Kevin R. Mackie, John-Michael Wong, and Božidar Stojadinović. January 2008.
- PEER 2007/08** *Assessing Seismic Collapse Safety of Modern Reinforced Concrete Moment-Frame Buildings.* Curt B. Haselton and Gregory G. Deierlein. February 2008.
- PEER 2007/07** *Performance Modeling Strategies for Modern Reinforced Concrete Bridge Columns.* Michael P. Berry and Marc O. Eberhard. April 2008.
- PEER 2007/06** *Development of Improved Procedures for Seismic Design of Buried and Partially Buried Structures.* Linda Al Atik and Nicholas Sitar. June 2007.
- PEER 2007/05** *Uncertainty and Correlation in Seismic Risk Assessment of Transportation Systems.* Renee G. Lee and Anne S. Kiremidjian. July 2007.
- PEER 2007/04** *Numerical Models for Analysis and Performance-Based Design of Shallow Foundations Subjected to Seismic Loading.* Sivapalan Gajan, Tara C. Hutchinson, Bruce L. Kutter, Prishati Raychowdhury, José A. Ugalde, and Jonathan P. Stewart. May 2008.
- PEER 2007/03** *Beam-Column Element Model Calibrated for Predicting Flexural Response Leading to Global Collapse of RC Frame Buildings.* Curt B. Haselton, Abbie B. Liel, Sarah Taylor Lange, and Gregory G. Deierlein. May 2008.
- PEER 2007/02** *Campbell-Bozorgnia NGA Ground Motion Relations for the Geometric Mean Horizontal Component of Peak and Spectral Ground Motion Parameters.* Kenneth W. Campbell and Yousef Bozorgnia. May 2007.
- PEER 2007/01** *Boore-Atkinson NGA Ground Motion Relations for the Geometric Mean Horizontal Component of Peak and Spectral Ground Motion Parameters.* David M. Boore and Gail M. Atkinson. May 2007.
- PEER 2006/12** *Societal Implications of Performance-Based Earthquake Engineering.* Peter J. May. May 2007.
- PEER 2006/11** *Probabilistic Seismic Demand Analysis Using Advanced Ground Motion Intensity Measures, Attenuation Relationships, and Near-Fault Effects.* Polsak Tothong and C. Allin Cornell. March 2007.
- PEER 2006/10** *Application of the PEER PBEE Methodology to the I-880 Viaduct.* Sashi Kunnath. February 2007.
- PEER 2006/09** *Quantifying Economic Losses from Travel Forgone Following a Large Metropolitan Earthquake.* James Moore, Sungbin Cho, Yue Yue Fan, and Stuart Werner. November 2006.
- PEER 2006/08** *Vector-Valued Ground Motion Intensity Measures for Probabilistic Seismic Demand Analysis.* Jack W. Baker and C. Allin Cornell. October 2006.
- PEER 2006/07** *Analytical Modeling of Reinforced Concrete Walls for Predicting Flexural and Coupled-Shear-Flexural Responses.* Kutay Orakcal, Leonardo M. Massone, and John W. Wallace. October 2006.
- PEER 2006/06** *Nonlinear Analysis of a Soil-Drilled Pier System under Static and Dynamic Axial Loading.* Gang Wang and Nicholas Sitar. November 2006.
- PEER 2006/05** *Advanced Seismic Assessment Guidelines.* Paolo Bazzurro, C. Allin Cornell, Charles Menun, Maziar Motahari, and Nicolas Luco. September 2006.
- PEER 2006/04** *Probabilistic Seismic Evaluation of Reinforced Concrete Structural Components and Systems.* Tae Hyung Lee and Khalid M. Mosalam. August 2006.
- PEER 2006/03** *Performance of Lifelines Subjected to Lateral Spreading.* Scott A. Ashford and Teerawut Juirnarongrit. July 2006.
- PEER 2006/02** *Pacific Earthquake Engineering Research Center Highway Demonstration Project.* Anne Kiremidjian, James Moore, Yue Yue Fan, Nesrin Basoz, Ozgur Yazali, and Meredith Williams. April 2006.
- PEER 2006/01** *Bracing Berkeley. A Guide to Seismic Safety on the UC Berkeley Campus.* Mary C. Comerio, Stephen Tobriner, and Ariane Fehrenkamp. January 2006.
- PEER 2005/16** *Seismic Response and Reliability of Electrical Substation Equipment and Systems.* Junho Song, Armen Der Kiureghian, and Jerome L. Sackman. April 2006.
- PEER 2005/15** *CPT-Based Probabilistic Assessment of Seismic Soil Liquefaction Initiation.* R. E. S. Moss, R. B. Seed, R. E. Kayen, J. P. Stewart, and A. Der Kiureghian. April 2006.
- PEER 2005/14** *Workshop on Modeling of Nonlinear Cyclic Load-Deformation Behavior of Shallow Foundations.* Bruce L. Kutter, Geoffrey Martin, Tara Hutchinson, Chad Harden, Sivapalan Gajan, and Justin Phalen. March 2006.
- PEER 2005/13** *Stochastic Characterization and Decision Bases under Time-Dependent Aftershock Risk in Performance-Based Earthquake Engineering.* Gee Liek Yeo and C. Allin Cornell. July 2005.

- PEER 2005/12** *PEER Testbed Study on a Laboratory Building: Exercising Seismic Performance Assessment.* Mary C. Comerio, editor. November 2005.
- PEER 2005/11** *Van Nuys Hotel Building Testbed Report: Exercising Seismic Performance Assessment.* Helmut Krawinkler, editor. October 2005.
- PEER 2005/10** *First NEES/E-Defense Workshop on Collapse Simulation of Reinforced Concrete Building Structures.* September 2005.
- PEER 2005/09** *Test Applications of Advanced Seismic Assessment Guidelines.* Joe Maffei, Karl Telleen, Danya Mohr, William Holmes, and Yuki Nakayama. August 2006.
- PEER 2005/08** *Damage Accumulation in Lightly Confined Reinforced Concrete Bridge Columns.* R. Tyler Ranf, Jared M. Nelson, Zach Price, Marc O. Eberhard, and John F. Stanton. April 2006.
- PEER 2005/07** *Experimental and Analytical Studies on the Seismic Response of Freestanding and Anchored Laboratory Equipment.* Dimitrios Konstantinidis and Nicos Makris. January 2005.
- PEER 2005/06** *Global Collapse of Frame Structures under Seismic Excitations.* Luis F. Ibarra and Helmut Krawinkler. September 2005.
- PEER 2005/05** *Performance Characterization of Bench- and Shelf-Mounted Equipment.* Samit Ray Chaudhuri and Tara C. Hutchinson. May 2006.
- PEER 2005/04** *Numerical Modeling of the Nonlinear Cyclic Response of Shallow Foundations.* Chad Harden, Tara Hutchinson, Geoffrey R. Martin, and Bruce L. Kutter. August 2005.
- PEER 2005/03** *A Taxonomy of Building Components for Performance-Based Earthquake Engineering.* Keith A. Porter. September 2005.
- PEER 2005/02** *Fragility Basis for California Highway Overpass Bridge Seismic Decision Making.* Kevin R. Mackie and Božidar Stojadinović. June 2005.
- PEER 2005/01** *Empirical Characterization of Site Conditions on Strong Ground Motion.* Jonathan P. Stewart, Yoojoong Choi, and Robert W. Graves. June 2005.
- PEER 2004/09** *Electrical Substation Equipment Interaction: Experimental Rigid Conductor Studies.* Christopher Stearns and André Filiatrault. February 2005.
- PEER 2004/08** *Seismic Qualification and Fragility Testing of Line Break 550-kV Disconnect Switches.* Shakhzod M. Takhirov, Gregory L. Fenves, and Eric Fujisaki. January 2005.
- PEER 2004/07** *Ground Motions for Earthquake Simulator Qualification of Electrical Substation Equipment.* Shakhzod M. Takhirov, Gregory L. Fenves, Eric Fujisaki, and Don Clyde. January 2005.
- PEER 2004/06** *Performance-Based Regulation and Regulatory Regimes.* Peter J. May and Chris Koski. September 2004.
- PEER 2004/05** *Performance-Based Seismic Design Concepts and Implementation: Proceedings of an International Workshop.* Peter Fajfar and Helmut Krawinkler, editors. September 2004.
- PEER 2004/04** *Seismic Performance of an Instrumented Tilt-up Wall Building.* James C. Anderson and Vitelmo V. Bertero. July 2004.
- PEER 2004/03** *Evaluation and Application of Concrete Tilt-up Assessment Methodologies.* Timothy Graf and James O. Malley. October 2004.
- PEER 2004/02** *Analytical Investigations of New Methods for Reducing Residual Displacements of Reinforced Concrete Bridge Columns.* Junichi Sakai and Stephen A. Mahin. August 2004.
- PEER 2004/01** *Seismic Performance of Masonry Buildings and Design Implications.* Kerri Anne Taeko Tokoro, James C. Anderson, and Vitelmo V. Bertero. February 2004.
- PEER 2003/18** *Performance Models for Flexural Damage in Reinforced Concrete Columns.* Michael Berry and Marc Eberhard. August 2003.
- PEER 2003/17** *Predicting Earthquake Damage in Older Reinforced Concrete Beam-Column Joints.* Catherine Pagni and Laura Lowes. October 2004.
- PEER 2003/16** *Seismic Demands for Performance-Based Design of Bridges.* Kevin Mackie and Božidar Stojadinović. August 2003.
- PEER 2003/15** *Seismic Demands for Nondeteriorating Frame Structures and Their Dependence on Ground Motions.* Ricardo Antonio Medina and Helmut Krawinkler. May 2004.
- PEER 2003/14** *Finite Element Reliability and Sensitivity Methods for Performance-Based Earthquake Engineering.* Terje Haukaas and Armen Der Kiureghian. April 2004.

- PEER 2003/13** *Effects of Connection Hysteretic Degradation on the Seismic Behavior of Steel Moment-Resisting Frames.* Janise E. Rodgers and Stephen A. Mahin. March 2004.
- PEER 2003/12** *Implementation Manual for the Seismic Protection of Laboratory Contents: Format and Case Studies.* William T. Holmes and Mary C. Comerio. October 2003.
- PEER 2003/11** *Fifth U.S.-Japan Workshop on Performance-Based Earthquake Engineering Methodology for Reinforced Concrete Building Structures.* February 2004.
- PEER 2003/10** *A Beam-Column Joint Model for Simulating the Earthquake Response of Reinforced Concrete Frames.* Laura N. Lowes, Nilanjan Mitra, and Arash Altoontash. February 2004.
- PEER 2003/09** *Sequencing Repairs after an Earthquake: An Economic Approach.* Marco Casari and Simon J. Wilkie. April 2004.
- PEER 2003/08** *A Technical Framework for Probability-Based Demand and Capacity Factor Design (DCFD) Seismic Formats.* Fatemeh Jalayer and C. Allin Cornell. November 2003.
- PEER 2003/07** *Uncertainty Specification and Propagation for Loss Estimation Using FOSM Methods.* Jack W. Baker and C. Allin Cornell. September 2003.
- PEER 2003/06** *Performance of Circular Reinforced Concrete Bridge Columns under Bidirectional Earthquake Loading.* Mahmoud M. Hachem, Stephen A. Mahin, and Jack P. Moehle. February 2003.
- PEER 2003/05** *Response Assessment for Building-Specific Loss Estimation.* Eduardo Miranda and Shahram Taghavi. September 2003.
- PEER 2003/04** *Experimental Assessment of Columns with Short Lap Splices Subjected to Cyclic Loads.* Murat Melek, John W. Wallace, and Joel Conte. April 2003.
- PEER 2003/03** *Probabilistic Response Assessment for Building-Specific Loss Estimation.* Eduardo Miranda and Hesameddin Aslani. September 2003.
- PEER 2003/02** *Software Framework for Collaborative Development of Nonlinear Dynamic Analysis Program.* Jun Peng and Kincho H. Law. September 2003.
- PEER 2003/01** *Shake Table Tests and Analytical Studies on the Gravity Load Collapse of Reinforced Concrete Frames.* Kenneth John Elwood and Jack P. Moehle. November 2003.
- PEER 2002/24** *Performance of Beam to Column Bridge Joints Subjected to a Large Velocity Pulse.* Natalie Gibson, André Filiatrault, and Scott A. Ashford. April 2002.
- PEER 2002/23** *Effects of Large Velocity Pulses on Reinforced Concrete Bridge Columns.* Greg L. Orozco and Scott A. Ashford. April 2002.
- PEER 2002/22** *Characterization of Large Velocity Pulses for Laboratory Testing.* Kenneth E. Cox and Scott A. Ashford. April 2002.
- PEER 2002/21** *Fourth U.S.-Japan Workshop on Performance-Based Earthquake Engineering Methodology for Reinforced Concrete Building Structures.* December 2002.
- PEER 2002/20** *Barriers to Adoption and Implementation of PBEE Innovations.* Peter J. May. August 2002.
- PEER 2002/19** *Economic-Engineered Integrated Models for Earthquakes: Socioeconomic Impacts.* Peter Gordon, James E. Moore II, and Harry W. Richardson. July 2002.
- PEER 2002/18** *Assessment of Reinforced Concrete Building Exterior Joints with Substandard Details.* Chris P. Pantelides, Jon Hansen, Justin Nadauld, and Lawrence D. Reaveley. May 2002.
- PEER 2002/17** *Structural Characterization and Seismic Response Analysis of a Highway Overcrossing Equipped with Elastomeric Bearings and Fluid Dampers: A Case Study.* Nicos Makris and Jian Zhang. November 2002.
- PEER 2002/16** *Estimation of Uncertainty in Geotechnical Properties for Performance-Based Earthquake Engineering.* Allen L. Jones, Steven L. Kramer, and Pedro Arduino. December 2002.
- PEER 2002/15** *Seismic Behavior of Bridge Columns Subjected to Various Loading Patterns.* Asadollah Esmaeily-Gh. and Yan Xiao. December 2002.
- PEER 2002/14** *Inelastic Seismic Response of Extended Pile Shaft Supported Bridge Structures.* T.C. Hutchinson, R.W. Boulanger, Y.H. Chai, and I.M. Idriss. December 2002.
- PEER 2002/13** *Probabilistic Models and Fragility Estimates for Bridge Components and Systems.* Paolo Gardoni, Armen Der Kiureghian, and Khalid M. Mosalam. June 2002.
- PEER 2002/12** *Effects of Fault Dip and Slip Rake on Near-Source Ground Motions: Why Chi-Chi Was a Relatively Mild M7.6 Earthquake.* Brad T. Aagaard, John F. Hall, and Thomas H. Heaton. December 2002.

- PEER 2002/11** *Analytical and Experimental Study of Fiber-Reinforced Strip Isolators.* James M. Kelly and Shakhzod M. Takhirov. September 2002.
- PEER 2002/10** *Centrifuge Modeling of Settlement and Lateral Spreading with Comparisons to Numerical Analyses.* Sivapalan Gajan and Bruce L. Kutter. January 2003.
- PEER 2002/09** *Documentation and Analysis of Field Case Histories of Seismic Compression during the 1994 Northridge, California, Earthquake.* Jonathan P. Stewart, Patrick M. Smith, Daniel H. Whang, and Jonathan D. Bray. October 2002.
- PEER 2002/08** *Component Testing, Stability Analysis and Characterization of Buckling-Restrained Unbonded Braces™.* Cameron Black, Nicos Makris, and Ian Aiken. September 2002.
- PEER 2002/07** *Seismic Performance of Pile-Wharf Connections.* Charles W. Roeder, Robert Graff, Jennifer Soderstrom, and Jun Han Yoo. December 2001.
- PEER 2002/06** *The Use of Benefit-Cost Analysis for Evaluation of Performance-Based Earthquake Engineering Decisions.* Richard O. Zerbe and Anthony Falit-Baiamonte. September 2001.
- PEER 2002/05** *Guidelines, Specifications, and Seismic Performance Characterization of Nonstructural Building Components and Equipment.* André Filiatrault, Constantin Christopoulos, and Christopher Stearns. September 2001.
- PEER 2002/04** *Consortium of Organizations for Strong-Motion Observation Systems and the Pacific Earthquake Engineering Research Center Lifelines Program: Invited Workshop on Archiving and Web Dissemination of Geotechnical Data, 4–5 October 2001.* September 2002.
- PEER 2002/03** *Investigation of Sensitivity of Building Loss Estimates to Major Uncertain Variables for the Van Nuys Testbed.* Keith A. Porter, James L. Beck, and Rustem V. Shaikhutdinov. August 2002.
- PEER 2002/02** *The Third U.S.-Japan Workshop on Performance-Based Earthquake Engineering Methodology for Reinforced Concrete Building Structures.* July 2002.
- PEER 2002/01** *Nonstructural Loss Estimation: The UC Berkeley Case Study.* Mary C. Comerio and John C. Stallmeyer. December 2001.
- PEER 2001/16** *Statistics of SDF-System Estimate of Roof Displacement for Pushover Analysis of Buildings.* Anil K. Chopra, Rakesh K. Goel, and Chatpan Chintanapakdee. December 2001.
- PEER 2001/15** *Damage to Bridges during the 2001 Nisqually Earthquake.* R. Tyler Ranf, Marc O. Eberhard, and Michael P. Berry. November 2001.
- PEER 2001/14** *Rocking Response of Equipment Anchored to a Base Foundation.* Nicos Makris and Cameron J. Black. September 2001.
- PEER 2001/13** *Modeling Soil Liquefaction Hazards for Performance-Based Earthquake Engineering.* Steven L. Kramer and Ahmed-W. Elgamal. February 2001.
- PEER 2001/12** *Development of Geotechnical Capabilities in OpenSees.* Boris Jeremić. September 2001.
- PEER 2001/11** *Analytical and Experimental Study of Fiber-Reinforced Elastomeric Isolators.* James M. Kelly and Shakhzod M. Takhirov. September 2001.
- PEER 2001/10** *Amplification Factors for Spectral Acceleration in Active Regions.* Jonathan P. Stewart, Andrew H. Liu, Yoojoong Choi, and Mehmet B. Baturay. December 2001.
- PEER 2001/09** *Ground Motion Evaluation Procedures for Performance-Based Design.* Jonathan P. Stewart, Shyh-Jeng Chiou, Jonathan D. Bray, Robert W. Graves, Paul G. Somerville, and Norman A. Abrahamson. September 2001.
- PEER 2001/08** *Experimental and Computational Evaluation of Reinforced Concrete Bridge Beam-Column Connections for Seismic Performance.* Clay J. Naito, Jack P. Moehle, and Khalid M. Mosalam. November 2001.
- PEER 2001/07** *The Rocking Spectrum and the Shortcomings of Design Guidelines.* Nicos Makris and Dimitrios Konstantinidis. August 2001.
- PEER 2001/06** *Development of an Electrical Substation Equipment Performance Database for Evaluation of Equipment Fragilities.* Thalia Agnanos. April 1999.
- PEER 2001/05** *Stiffness Analysis of Fiber-Reinforced Elastomeric Isolators.* Hsiang-Chuan Tsai and James M. Kelly. May 2001.
- PEER 2001/04** *Organizational and Societal Considerations for Performance-Based Earthquake Engineering.* Peter J. May. April 2001.
- PEER 2001/03** *A Modal Pushover Analysis Procedure to Estimate Seismic Demands for Buildings: Theory and Preliminary Evaluation.* Anil K. Chopra and Rakesh K. Goel. January 2001.

- PEER 2001/02** *Seismic Response Analysis of Highway Overcrossings Including Soil-Structure Interaction.* Jian Zhang and Nicos Makris. March 2001.
- PEER 2001/01** *Experimental Study of Large Seismic Steel Beam-to-Column Connections.* Egor P. Popov and Shakhzod M. Takhirov. November 2000.
- PEER 2000/10** *The Second U.S.-Japan Workshop on Performance-Based Earthquake Engineering Methodology for Reinforced Concrete Building Structures.* March 2000.
- PEER 2000/09** *Structural Engineering Reconnaissance of the August 17, 1999 Earthquake: Kocaeli (Izmit), Turkey.* Halil Sezen, Kenneth J. Elwood, Andrew S. Whittaker, Khalid Mosalam, John J. Wallace, and John F. Stanton. December 2000.
- PEER 2000/08** *Behavior of Reinforced Concrete Bridge Columns Having Varying Aspect Ratios and Varying Lengths of Confinement.* Anthony J. Calderone, Dawn E. Lehman, and Jack P. Moehle. January 2001.
- PEER 2000/07** *Cover-Plate and Flange-Plate Reinforced Steel Moment-Resisting Connections.* Taejin Kim, Andrew S. Whittaker, Amir S. Gilani, Vitelmo V. Bertero, and Shakhzod M. Takhirov. September 2000.
- PEER 2000/06** *Seismic Evaluation and Analysis of 230-kV Disconnect Switches.* Amir S. J. Gilani, Andrew S. Whittaker, Gregory L. Fenves, Chun-Hao Chen, Henry Ho, and Eric Fujisaki. July 2000.
- PEER 2000/05** *Performance-Based Evaluation of Exterior Reinforced Concrete Building Joints for Seismic Excitation.* Chandra Clyde, Chris P. Pantelides, and Lawrence D. Reaveley. July 2000.
- PEER 2000/04** *An Evaluation of Seismic Energy Demand: An Attenuation Approach.* Chung-Che Chou and Chia-Ming Uang. July 1999.
- PEER 2000/03** *Framing Earthquake Retrofitting Decisions: The Case of Hillside Homes in Los Angeles.* Detlof von Winterfeldt, Nels Roselund, and Alicia Kitsuse. March 2000.
- PEER 2000/02** *U.S.-Japan Workshop on the Effects of Near-Field Earthquake Shaking.* Andrew Whittaker, ed. July 2000.
- PEER 2000/01** *Further Studies on Seismic Interaction in Interconnected Electrical Substation Equipment.* Armen Der Kiureghian, Kee-Jeung Hong, and Jerome L. Sackman. November 1999.
- PEER 1999/14** *Seismic Evaluation and Retrofit of 230-kV Porcelain Transformer Bushings.* Amir S. Gilani, Andrew S. Whittaker, Gregory L. Fenves, and Eric Fujisaki. December 1999.
- PEER 1999/13** *Building Vulnerability Studies: Modeling and Evaluation of Tilt-up and Steel Reinforced Concrete Buildings.* John W. Wallace, Jonathan P. Stewart, and Andrew S. Whittaker, editors. December 1999.
- PEER 1999/12** *Rehabilitation of Nonductile RC Frame Building Using Encasement Plates and Energy-Dissipating Devices.* Mehrdad Sasani, Vitelmo V. Bertero, James C. Anderson. December 1999.
- PEER 1999/11** *Performance Evaluation Database for Concrete Bridge Components and Systems under Simulated Seismic Loads.* Yael D. Hose and Frieder Seible. November 1999.
- PEER 1999/10** *U.S.-Japan Workshop on Performance-Based Earthquake Engineering Methodology for Reinforced Concrete Building Structures.* December 1999.
- PEER 1999/09** *Performance Improvement of Long Period Building Structures Subjected to Severe Pulse-Type Ground Motions.* James C. Anderson, Vitelmo V. Bertero, and Raul Bertero. October 1999.
- PEER 1999/08** *Envelopes for Seismic Response Vectors.* Charles Menun and Armen Der Kiureghian. July 1999.
- PEER 1999/07** *Documentation of Strengths and Weaknesses of Current Computer Analysis Methods for Seismic Performance of Reinforced Concrete Members.* William F. Cofer. November 1999.
- PEER 1999/06** *Rocking Response and Overturning of Anchored Equipment under Seismic Excitations.* Nicos Makris and Jian Zhang. November 1999.
- PEER 1999/05** *Seismic Evaluation of 550 kV Porcelain Transformer Bushings.* Amir S. Gilani, Andrew S. Whittaker, Gregory L. Fenves, and Eric Fujisaki. October 1999.
- PEER 1999/04** *Adoption and Enforcement of Earthquake Risk-Reduction Measures.* Peter J. May, Raymond J. Burby, T. Jens Feeley, and Robert Wood.
- PEER 1999/03** *Task 3 Characterization of Site Response General Site Categories.* Adrian Rodriguez-Marek, Jonathan D. Bray, and Norman Abrahamson. February 1999.
- PEER 1999/02** *Capacity-Demand-Diagram Methods for Estimating Seismic Deformation of Inelastic Structures: SDF Systems.* Anil K. Chopra and Rakesh Goel. April 1999.
- PEER 1999/01** *Interaction in Interconnected Electrical Substation Equipment Subjected to Earthquake Ground Motions.* Armen Der Kiureghian, Jerome L. Sackman, and Kee-Jeung Hong. February 1999.

- PEER 1998/08** *Behavior and Failure Analysis of a Multiple-Frame Highway Bridge in the 1994 Northridge Earthquake.* Gregory L. Fenves and Michael Ellery. December 1998.
- PEER 1998/07** *Empirical Evaluation of Inertial Soil-Structure Interaction Effects.* Jonathan P. Stewart, Raymond B. Seed, and Gregory L. Fenves. November 1998.
- PEER 1998/06** *Effect of Damping Mechanisms on the Response of Seismic Isolated Structures.* Nicos Makris and Shih-Po Chang. November 1998.
- PEER 1998/05** *Rocking Response and Overturning of Equipment under Horizontal Pulse-Type Motions.* Nicos Makris and Yiannis Roussos. October 1998.
- PEER 1998/04** *Pacific Earthquake Engineering Research Invitational Workshop Proceedings, May 14–15, 1998: Defining the Links between Planning, Policy Analysis, Economics and Earthquake Engineering.* Mary Comerio and Peter Gordon. September 1998.
- PEER 1998/03** *Repair/Upgrade Procedures for Welded Beam to Column Connections.* James C. Anderson and Xiaojing Duan. May 1998.
- PEER 1998/02** *Seismic Evaluation of 196 kV Porcelain Transformer Bushings.* Amir S. Gilani, Juan W. Chavez, Gregory L. Fenves, and Andrew S. Whittaker. May 1998.
- PEER 1998/01** *Seismic Performance of Well-Confined Concrete Bridge Columns.* Dawn E. Lehman and Jack P. Moehle. December 2000.

ONLINE REPORTS

The following PEER reports are available by Internet only at http://peer.berkeley.edu/publications/peer_reports.html

- PEER 2011/101** *Report of the Eighth Planning Meeting of NEES/E-Defense Collaborative Research on Earthquake Engineering.* Convened by the Hyogo Earthquake Engineering Research Center (NIED), NEES Consortium, Inc. February 2011.
- PEER 2010/111** *Modeling and Acceptance Criteria for Seismic Design and Analysis of Tall Buildings.* Task 7 Report for the Tall Buildings Initiative - Published jointly by the Applied Technology Council. October 2010.
- PEER 2010/110** *Seismic Performance Assessment and Probabilistic Repair Cost Analysis of Precast Concrete Cladding Systems for Multistory Buildings.* Jeffrey P. Hunt and Božidar Stojadinovic. November 2010.
- PEER 2010/109** *Report of the Seventh Joint Planning Meeting of NEES/E-Defense Collaboration on Earthquake Engineering. Held at the E-Defense, Miki, and Shin-Kobe, Japan, September 18–19, 2009.* August 2010.
- PEER 2010/108** *Probabilistic Tsunami Hazard in California.* Hong Kie Thio, Paul Somerville, and Jascha Polet, preparers. October 2010.
- PEER 2010/107** *Performance and Reliability of Exposed Column Base Plate Connections for Steel Moment-Resisting Frames.* Ady Aviram, Božidar Stojadinovic, and Armen Der Kiureghian. August 2010.
- PEER 2010/106** *Verification of Probabilistic Seismic Hazard Analysis Computer Programs.* Patricia Thomas, Ivan Wong, and Norman Abrahamson. May 2010.
- PEER 2010/105** *Structural Engineering Reconnaissance of the April 6, 2009, Abruzzo, Italy, Earthquake, and Lessons Learned.* M. Selim Günay and Khalid M. Mosalam. April 2010.
- PEER 2010/104** *Simulating the Inelastic Seismic Behavior of Steel Braced Frames, Including the Effects of Low-Cycle Fatigue.* Yuli Huang and Stephen A. Mahin. April 2010.
- PEER 2010/103** *Post-Earthquake Traffic Capacity of Modern Bridges in California.* Vesna Terzic and Božidar Stojadinović. March 2010.
- PEER 2010/102** *Analysis of Cumulative Absolute Velocity (CAV) and JMA Instrumental Seismic Intensity (I_{JMA}) Using the PEER–NGA Strong Motion Database.* Kenneth W. Campbell and Yousef Bozorgnia. February 2010.
- PEER 2010/101** *Rocking Response of Bridges on Shallow Foundations.* Jose A. Ugalde, Bruce L. Kutter, Boris Jeremic
- PEER 2009/109** *Simulation and Performance-Based Earthquake Engineering Assessment of Self-Centering Post-Tensioned Concrete Bridge Systems.* Won K. Lee and Sarah L. Billington. December 2009.
- PEER 2009/108** *PEER Lifelines Geotechnical Virtual Data Center.* J. Carl Stepp, Daniel J. Ponti, Loren L. Turner, Jennifer N. Swift, Sean Devlin, Yang Zhu, Jean Benoit, and John Bobbitt. September 2009.
- PEER 2009/107** *Experimental and Computational Evaluation of Current and Innovative In-Span Hinge Details in Reinforced Concrete Box-Girder Bridges: Part 2: Post-Test Analysis and Design Recommendations.* Matias A. Hube and Khalid M. Mosalam. December 2009.
- PEER 2009/106** *Shear Strength Models of Exterior Beam-Column Joints without Transverse Reinforcement.* Sangjoon Park and Khalid M. Mosalam. November 2009.
- PEER 2009/105** *Reduced Uncertainty of Ground Motion Prediction Equations through Bayesian Variance Analysis.* Robb Eric S. Moss. November 2009.
- PEER 2009/104** *Advanced Implementation of Hybrid Simulation.* Andreas H. Schellenberg, Stephen A. Mahin, Gregory L. Fenves. November 2009.
- PEER 2009/103** *Performance Evaluation of Innovative Steel Braced Frames.* T. Y. Yang, Jack P. Moehle, and Božidar Stojadinovic. August 2009.
- PEER 2009/102** *Reinvestigation of Liquefaction and Nonliquefaction Case Histories from the 1976 Tangshan Earthquake.* Robb Eric Moss, Robert E. Kayen, Liyuan Tong, Songyu Liu, Guojun Cai, and Jiaer Wu. August 2009.
- PEER 2009/101** *Report of the First Joint Planning Meeting for the Second Phase of NEES/E-Defense Collaborative Research on Earthquake Engineering.* Stephen A. Mahin et al. July 2009.
- PEER 2008/104** *Experimental and Analytical Study of the Seismic Performance of Retaining Structures.* Linda Al Atik and Nicholas Sitar. January 2009.

- PEER 2008/103** *Experimental and Computational Evaluation of Current and Innovative In-Span Hinge Details in Reinforced Concrete Box-Girder Bridges. Part 1: Experimental Findings and Pre-Test Analysis.* Matias A. Hube and Khalid M. Mosalam. January 2009.
- PEER 2008/102** *Modeling of Unreinforced Masonry Infill Walls Considering In-Plane and Out-of-Plane Interaction.* Stephen Kadysiewski and Khalid M. Mosalam. January 2009.
- PEER 2008/101** *Seismic Performance Objectives for Tall Buildings.* William T. Holmes, Charles Kircher, William Petak, and Nabih Youssef. August 2008.
- PEER 2007/101** *Generalized Hybrid Simulation Framework for Structural Systems Subjected to Seismic Loading.* Tarek Elkhoraibi and Khalid M. Mosalam. July 2007.
- PEER 2007/100** *Seismic Evaluation of Reinforced Concrete Buildings Including Effects of Masonry Infill Walls.* Alidad Hashemi and Khalid M. Mosalam. July 2007.

The Pacific Earthquake Engineering Research Center (PEER) is a multi-institutional research and education center with headquarters at the University of California, Berkeley. Investigators from over 20 universities, several consulting companies, and researchers at various state and federal government agencies contribute to research programs focused on performance-based earthquake engineering.

These research programs aim to identify and reduce the risks from major earthquakes to life safety and to the economy by including research in a wide variety of disciplines including structural and geotechnical engineering, geology/seismology, lifelines, transportation, architecture, economics, risk management, and public policy.

PEER is supported by federal, state, local, and regional agencies, together with industry partners.



PEER reports can be ordered at http://peer.berkeley.edu/publications/peer_reports.html or by contacting

Pacific Earthquake Engineering Research Center
University of California, Berkeley
325 Davis Hall, mail code 1792
Berkeley, CA 94720-1792
Tel: 510-642-3437
Fax: 510-642-1655
Email: peer_editor@berkeley.edu

ISSN 1547-0587X